

Axiomatic Design of Customizable Automotive Suspension Systems

by

Hrishikesh V Deo
B.Tech., Mechanical Engineering
Indian Institute of Technology, 2001

Submitted to the Department of Mechanical Engineering in partial fulfillment of the
requirements for the degree of

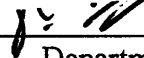
Doctor of Philosophy in Mechanical Engineering


at the


MASSACHUSETTS INSTITUTE OF TECHNOLOGY

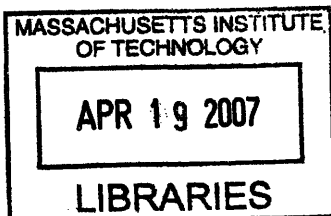
February 2007

© Massachusetts Institute of Technology 2006. All rights reserved

Author _____ 
Department of Mechanical Engineering
October 25, 2006

Certified by _____ 
Nam P Suh
Ralph E. and Eloise F. Cross Professor of Mechanical Engineering

Accepted by _____ 
Lallit Anand
Professor of Mechanical Engineering
Chairman, Department Committee on Graduate Students



ARCHIVES

Axiomatic Design of Customizable Automotive Suspension Systems

by

Hrishikesh V Deo

Submitted to the Department of Mechanical Engineering
on October 25, 2006 in partial fulfillment of the requirements for the degree of
Doctor of Philosophy in Mechanical Engineering

Abstract

The design of existing suspension systems typically involves a compromise solution for the conflicting requirements of comfort and handling. For instance, cars need a soft suspension for better comfort, whereas a stiff suspension leads to better handling. Cars need high ground clearance on rough terrain, whereas a low center of gravity (CG) height is desired for swift cornering and dynamic stability at high speeds. It is advantageous to have low damping for low force transmission to vehicle frame, whereas high damping is desired for fast decay of oscillations. To eliminate these trade-offs, a novel design for a customizable automotive suspension system with independent control of stiffness, damping and ride-height is proposed in this thesis. This system is capable of providing the desired performance depending on user preference, vehicle speed, road conditions and maneuvering inputs. The design, fabrication and control of the customizable suspension prototype are discussed. The application of variable stiffness and variable ride-height suspension system to achieve improved vehicle dynamics is studied. Application to control of vehicle dynamics parameters required bandwidth and power input beyond the capability of the first prototype. To eliminate the bandwidth restrictions of the prototype, a variable-stiffness pneumatic suspension system capable of instantaneous stiffness change with essentially no power input and no ride-height change, is developed. This is done by supporting the vehicle on air springs and connecting each air spring volume to multiple auxiliary volumes through On-Off valves. By adequately choosing N unequal auxiliary volumes, this system can achieve 2^N stiffness settings. This suspension has been incorporated in a car suspension. The design, fabrication, and testing of the suspension system are reported in this thesis. A detailed frequency-domain model for the air-spring with auxiliary volumes is developed. Based on this modeling and testing, the performance limits and practical applicability of this system are discussed. The proposed variable stiffness isolator is capable of instantaneous stiffness change with no power input and no dimension change; moreover the isolator is inexpensive, robust and light. As a result, it is readily applicable to several other vibration isolation applications with conflicting stiffness requirements (such as a precision motion stages) or time-varying stiffness requirements (such as prosthetic limbs) and these applications are discussed.

Thesis Committee:

Professor Nam P Suh (Thesis Supervisor), Department of Mechanical Engineering, MIT

Professor Samir Nayfeh, Department of Mechanical Engineering, MIT

Professor Kamal Youcef-Toumi, Department of Mechanical Engineering, MIT

Acknowledgements

First and foremost, I would like to thank my advisor and mentor Professor Nam Suh for all the guidance, support and sound advice- academic as well as personal. Most importantly, I would like to thank him for the confidence and trust he placed in me and my capabilities. Professor Suh has been a constant source of inspiration for me and I will truly miss working with him closely. I could not have asked for a better mentor.

I would like to thank my committee member Professor Kamal Youcef-Toumi for very carefully reading my thesis. His comments and suggestions were extremely helpful in improving the manuscript. I am grateful for his help on modeling and controls aspects of the thesis, and in particular for the inspiration through his dedication and work-ethic. I would like to thank Professor Samir Nayfeh for his advice and direction. His thoughtful suggestions and constructive criticism, during the many “walk and talk” discussion sessions, have helped to shape my research.

The funding for this research was provided by the Park Center for Complex Systems (PCCS), which was set up by the generous support of Dr. B J Park. I am grateful to Dr. B J Park for creating the Park Fellowship that supported my graduate studies. I would also like to thank the Ford MIT Alliance for supporting the initial part of this research. .

I would like to thank Dr. Richard Perdichizzi for going out of the way to let me use the Aero-Astro hanger to work on the car suspension prototype.

I consider myself fortunate to get an opportunity to work with an extremely talented research group over the last five years. Dr. Jason Melvin and Dr. Taesik Lee have been my mentors and close friends and I have often gone to them for advice. AJ Schrauth, Stephen Bathurst, Ishan Barman, Peter Jeziorek, Beto Peliks, Dr. Jeffery Thomas, Dr. Gyunyoung Heo, Dr. Christian

Habitch have also been my talented labmates and close friends. They helped to keep me motivated and moving.

Special thanks to Jason Melvin, Stephen Bathurst, Lawrence Maligaya, AJ Schrauth and Jordan Etra for all the help with fabrication. I would like to thanks Mark Belanger and Gerry Wentworth for helping me build the prototypes for my designs.

A number of friends at MIT have been instrumental in keeping me sane during my research and writing- including Binayak Roy, Ajay Somani, Brandy Worthington, Ashish Shah, Vickram Mangalgi, Jason Melvin, Steve Bathurst, AJ Schrauth, Saif Khan, Sadaf Ansari, Waleed Farahat, Wayne Hsiao, Kyungyoon Noh, Jason Lapenta, and Blaise Gassend. Special thanks to Brandy for carefully reading and editing my thesis and all the help, support and encouragement during the most stressful stages of my thesis.

Finally, I would like to thank my Mom and Dad for all their love, support, encouragement and patience.

Contents

1	Introduction	13
1.1	Introduction to Axiomatic design	14
1.2	Introduction to existing suspension systems	15
1.2.1	Suspension kinematics	17
1.2.1.1	Dependent suspension systems	17
1.2.1.2	Independent suspension systems	18
1.2.2	Springs	20
1.2.3	Dampers	21
1.2.4	Suspension dynamics models	22
1.2.5	Prior art on active suspension systems	24
1.3	Thesis summary	26
2	Proposal of a novel Six-Bar Suspension	31
2.1	Introduction	31
2.1.1	Wheel Alignment Parameters	32
2.2	FRDP decomposition of vehicle system	33
2.2.1	Existing designs: Identification of coupling	36
2.2.2	Existing suspension systems: Four-bar linkages	37
2.2.3	Manifestation of coupling in existing systems	39
2.3	Proposed New Design	40
2.3.1	Proposed Design of a Suspension System	40
2.3.2	Dimensional synthesis of Watt-I linkage for the suspension	42

2.3.3	Application to suspension design	43
2.3.4	Proposed design of steering system	45
2.4	Evaluation of the proposed design	49
2.4.1	Advantages	49
2.4.2	Limitations	50
2.5	Summary	51
3	Customizable Automotive Suspension System	53
3.1	Introduction	54
3.2	Motivation for customizable suspension	56
3.2.1	Need for variable stiffness: Effect of stiffness on suspension performance	56
3.2.2	Need for variable ride-height	60
3.2.3	Prior art on variable stiffness and ride height	61
3.3	Proposed design for customizable suspension	61
3.3.1	Concept development	61
3.3.2	Prototype design and development	64
3.4	Control system design	66
3.4.1	Stiffness control	66
3.4.2	Ride-height control	66
3.5	Limitations: Motivation for instantaneous stiffness change	70
3.6	Summary	71
4	Design, Modeling and Fabrication of a Customizable Pneumatic Suspension System	73
4.1	Basic cylinder and piston air-spring	74
4.1.1	Adiabatic stiffness	74
4.1.2	Isothermal stiffness	75
4.1.3	Polytropic stiffness	75
4.2	Proposed modifications to achieve independent control of stiffness and ride-height	77

4.2.1	Advantages of proposed design (Strategy 4)	81
4.2.2	Other potential applications	82
4.3	Reinforced flexible member springs construction	84
4.3.1	Convolute/Bellows type air-spring	84
4.3.2	Rolling lobe or reversible sleeve type air-spring	86
4.3.3	Modified stiffness due to the effect of air-spring membrane	86
4.4	Detailed thermodynamic model to determine the frequency response of an air-spring with auxiliary volumes	92
4.4.1	Thermodynamic modeling to estimate Damping due to the valve flow resistance	94
4.4.2	Effect of valve damping on road noise isolation	99
4.4.3	Implementation issues with the solenoid valve arrangement	102
4.4.4	Modeling of effective inertia in the tubing	105
4.4.4.1	Incompressible flow assumption in pipe	106
4.4.4.2	Thermodynamic equations for air-spring and auxiliary volume	107
4.4.4.3	Pipe flow equation	110
4.4.4.4	Estimates of the effective parameters in the model	116
4.4.4.5	Simulation of air-spring with complex stiffness model	117
4.4.4.6	Comparison with experimental results	119
4.4.5	Effect of inertia of air in pipe on road noise isolation for a quarter-car SDOF model	120
4.4.6	Effect of inertia of air in pipe on road noise isolation for a quarter-car 2DOF model	123
4.5	Suspension prototype	125
4.5.1	Fabrication/Implementation	125
4.5.2	Sensors and data acquisition	126
4.6	Experiments	130
4.6.1	Determination of lateral acceleration from body-mounted accelerometers	131
4.6.2	Front suspension deflection trends	132

4.6.3	Rear suspension deflection trends	135
4.6.4	Nonlinear force-deflection analysis for the air-spring	137
4.6.5	Cross-coupling between the two stiffness components	140
4.7	Limitations	142
4.7.1	Limited stiffness change and packaging issues	142
4.7.2	Time and power input requirements for stiffness change	144
4.7.3	Ride-height change due to unequal pressures in chambers	145
4.7.4	Modified stiffness control strategy	146
4.8	Summary	147
4.9	List of abbreviations and car parameters	149
5	Application to Improved Vehicle Dynamics	153
5.1	User customization of comfort and handling	154
5.1.1	Stiffness customization	154
5.1.2	Ride-height customization	155
5.1.3	Low-frequency attitude control: Ride-height change to uncouple comfort and handling	155
5.1.4	Optimum performance over the entire speed range	156
5.2	Handling: Response to maneuvering inputs	157
5.2.1	Instantaneous stiffening change on hard braking, acceleration or cornering to limit wheel attitude changes	157
5.3	Alteration of anti-dive and anti-pitch characteristics	159
5.4	Alteration of Understeer-Oversteer behavior	162
5.4.1	Cornering behavior of a simplified bicycle model	163
5.4.2	Suspension effects on cornering	166
5.4.3	Demonstration of capability to change understeer-oversteer behavior on the fly	168
5.5	Alteration of pitch and bounce frequencies and the pitch and bounce motion centers	169
5.6	Summary	171

6	Ride-Height Control and Stiffness Scheduling for Pneumatic Suspension	173
6.1	Ride-height control	174
6.1.1	Model for ride-height control	174
6.1.2	Control law	177
6.2	Stiffness scheduling	180
6.2.1	Determination of disturbance source from state measurements exploiting phase relations	180
6.2.2	Scaling	184
6.2.3	Exponential forgetting	185
6.2.4	Stiffness scheduling based on $r(T)$	186
6.3	Summary	190
7	Conclusions	191
	Bibliography	195

Chapter 1

Introduction

Suspension and steering systems have been in existence for centuries and they appeared on horse carriages long before the automobile was invented. As expected, this is a very mature field and there is a significant body of literature that deals with suspension and steering systems. Significant advances in design, modeling and analysis techniques, as well as materials and manufacturing technology have led to significant improvement in suspension performance over the decades. In spite of these advances, the main challenge in the design of suspension and steering systems still remains, and that is the trade-off that exists between the conflicting requirements of comfort and handling.

In the past few decades, due to advances in sensing, computation and actuator technology, active suspension systems have emerged as a very active field of research to eliminate this coupling between the comfort and handling requirements. This can be seen from the vast amount of literature in the field. There have been at least a dozen review papers that outline the state-of-art in the field (Elbeheiry et al., 1995; Hedrick & Wormely, 1975; Sharp & Crolla, 1987; Karnopp, 1995; Hrovat, 1997). In spite of the volume of this literature, the practical implementation of these ideas in automobiles has been limited. This is primarily due to the fact that the high actuator bandwidth requirements, power requirements, weight and cost increments, and reduced reliability are not justified by the limited incremental benefit to the passenger.

Our approach was to eliminate this trade-off by coming up with a very simple design that does not add significantly to the cost and complexity of the system, but at the same time provides perceptible benefit to the passenger. Axiomatic Design Theory (Suh, 1990; Suh, 2001) is used to identify the coupling that causes this trade-off and to come up with novel designs to eliminate this coupling.

1.1 Introduction to Axiomatic design

Axiomatic design is a structured design method created to improve design activities by establishing criteria on which potential designs may be evaluated and by developing tools for implementing these criteria. Axiomatic design discusses the existence of four domains in the design world- customer domain, functional domain, physical domain and process domains. Customer attributes {CAs}, functional requirements {FRs}, design parameters {DPs}, and process variables {PVs} are the characteristic vectors of these domains. Design of products involves mapping from the functional domain to the physical domain and design of processes involves mapping from the physical domain to the process domain.

The axiomatic design process is centered on the satisfaction of functional requirements, which are defined as the minimum set of independent requirements that completely characterize the functional need of the product. Given a minimum set of independent FRs, the designer conceives a physical embodiment or a design containing a set of DPs, which are key physical variables in the physical domain that characterize the design that satisfies the specified FRs. The design and the choice of DPs are guided by the two design axioms.

- Axiom 1 (Independence Axiom): Maintain the independence of all functional requirements.
- Axiom 2 (Information Axiom): Minimize the information content of the design.

The design matrix (DM) is used to note the effect of DPs on FRs as follows:

$$\begin{Bmatrix} \text{FR 1} \\ \text{FR 2} \end{Bmatrix} = \begin{bmatrix} A_{11} & O \\ A_{21} & A_{22} \end{bmatrix} \begin{Bmatrix} \text{DP 1} \\ \text{DP 2} \end{Bmatrix} \quad (1.1)$$

where A_{11} denotes the effect of DP 1 on FR 1, A_{21} denotes the effect of DP 1 on FR 2, etc. When the design equations represent conceptual design levels, it is common for the elements in the matrix A_{ij} to be replaced with an 'X' if there is an effect and with an 'O' if there is not effect. To satisfy the Independence Axiom, the DM must be either diagonal or triangular. In an uncoupled design, the DM is diagonal and each of the FRs can be satisfied independently by adjusting one DP. In a decoupled design, the matrix is triangular and the independence of FRs can be guaranteed only if the DPs are determined in a proper sequence. In the case shown, we

need to set the DPs in the order: DP 1 followed by DP 2. A full design matrix leads to a coupled design and the satisfaction of FRs becomes difficult.

The Information Axiom guides the designer to maximize the probability of satisfaction of the FRs. It becomes increasingly difficult to satisfy FRs when FRs are coupled by the chosen DPs. This is because the allowable tolerance for DPs decreases with the increase in the number of FRs and the number of off-diagonal elements in the design matrix.

Axiomatic design begins with the most general requirements of the system, and decomposes these into sub-requirements. The goal of decomposition is the specification of a set of elements that will result in the parent. This involves moving back and forth between the functional and physical domains, and progressing from a general to a detailed description, and is referred to as zigzagging.

A direct consequence of Axiom 1 is Theorem 1 (Coupling due to insufficient number of DPs): “When the number of DPs is less than the number of FRs, either a coupled design results or the FRs cannot be satisfied”. This coupling can be removed by addition of another DP.

1.2 Introduction to existing suspension systems

In this section, a basic overview of existing suspension systems and suspension components is presented. In a practical suspension system, the wheel is connected to the car chassis through various links, which permit an approximately vertical motion of the wheel relative to the body. The motion of the wheel is controlled by the forces applied by the springs and dampers in passive suspension system. In active suspension systems, the springs and dampers are replaced by actuators which act as force producers according to some control law, using feedback from the vehicle. According to Gillespie (1992), the primary functions of a suspension system are to:

1. Provide vertical compliance so that the wheels can follow the uneven road, isolating the chassis from roughness in the road.
2. Maintain wheel attitude (characterized by wheel alignment parameters such camber, caster, toe etc.)
3. React to the longitudinal (acceleration and braking) and lateral (cornering) forces produced by the tires, as well as the braking and driving torques.

4. Maintain body alignment by minimizing roll and pitch motions of the car chassis
5. Maintain the tires in contact with the road with minimum load variations.

The corresponding FR/DP decomposition of the suspension system is given in Table 1.1.

Table 1.1: FR/DP decomposition of suspension systems

	Functional Requirements	Design Parameters
Parent	Ensure comfortable ride	Suspension system
1	Limit maximum relative motion	Suspension stiffness
2	Dissipate energy	Suspension damping coefficient
3	Set equilibrium position	Spring initial length
4	Maintain wheel alignment	Suspension kinematics
5	Maintain tire-road contact	Suspension travel

DP 4: Suspension Kinematics is responsible for FR 4: Maintaining wheel alignment; while permitting an approximately vertical motion of the wheel. Wheel alignment is characterized by wheel alignment parameters (WAP) such as camber, caster, toe, steering axis inclination, caster offset, kingpin offset etc., which are shown in Figure 1-1 and will be explained in greater detail along with their effect on handling in Chapter 2.

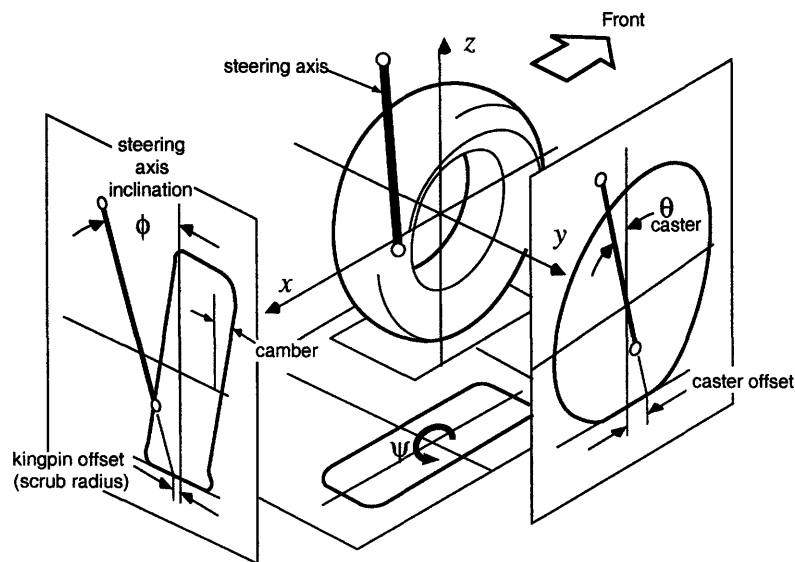


Figure 1-1: Wheel alignment parameters

1.2.1 Suspension kinematics

Suspension kinematics are generally categorized into two groups- dependant suspensions (also known as solid axles) and independent suspensions.

1.2.1.1 Dependant suspension systems

In a dependant suspension system (solid axle suspension), the two wheels are mounted at either end of a rigid beam. The most common form of solid-axle suspension is the Hotchkiss drive as shown in Figure 1-2. As the two wheels are connected to each other, motion of one wheel is transmitted to the other wheel, and hence the name- dependant suspension system. Solid drive axles are used on the rear wheels of most trucks and on the front wheels of many four-wheel drive trucks. The drive axle is clamped to the leaf springs, and is driven through a longitudinal driveshaft with universal joints at the transmission and the axle. The leaf springs are mounted longitudinally and connect to the chassis at their ends.

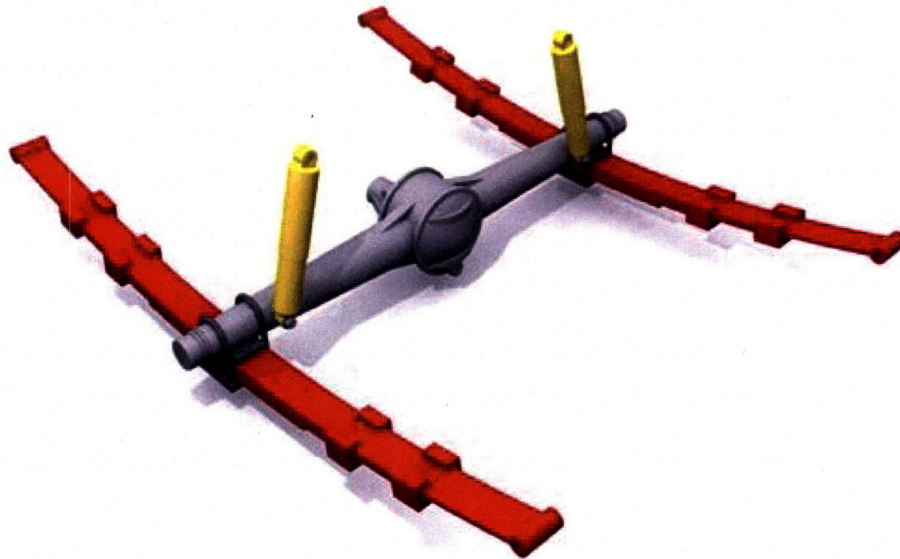


Figure 1-2: Solid-axle leaf-spring rear suspension (Figure from Longhurst 2006)

Advantages of solid-axle suspensions are simplicity and fewer components, ease of assembly and manufacturing, high load capacity and insensitivity of camber to body roll. Disadvantages of solid-axle suspensions include higher unsprung weight and packaging constraints due to the large beam connecting the two wheels. The higher unsprung weight deteriorates suspension performance- comfort as well as handling. Moreover, the solid-axle makes it difficult to locate

the steering correctly and most solid-axle suspensions exhibit large bump steer, which is discussed in greater detail in Chapter 2. Other forms of solid axle suspensions include the four-link suspension system and the beam-axle suspension system.

1.2.1.2 Independent suspension systems

Independent Suspensions allow each wheel to move independent of the other wheel. Nearly all passenger cars and light trucks use independent front suspensions, because they provide more room for the engine in the front, and because of better resistance to steering vibrations (known as wobble and shimmy). They also provide higher roll stiffness relative to the vertical spring rate as compared to solid axles. Another major advantage is the significant reduction in unsprung weight, which leads to significant improvements in ride-quality. The most common types of independent suspension systems are the short long arm (SLA) suspension and the MacPherson strut. Other examples include the swing axle suspension, trailing arm suspension, and multi-link rear suspension.

Swing Axle Suspension

Swing axles have universal joints connecting the driveshafts to the differential, which is attached to the chassis. They do not have universal joints at the wheels, and as a result the wheels are always perpendicular to the driveshafts. The swing radius is small and as a result they exhibit excessive camber change and tire-scrub (side-to-side motion of the tire-patch during the motion of the wheel) due to suspension travel as shown in Figure 1-3. This suspension also suffers from the problem of jacking. Jacking is caused during cornering when both tires are developing cornering forces, with the outer tire contributing greater cornering force and this inward force causes the vehicle CG to lift and reduces its rollover resistance. Due to these disadvantages, these were soon replaced by SLA suspensions.

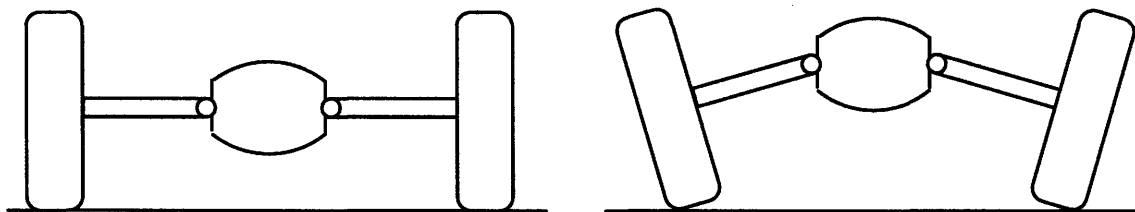


Figure 1-3: Swing-Axle Suspension showing significant camber change due to suspension travel

Short Long Arm Suspension

The most common independent suspension is the short long arm (SLA) suspension, also known as the double wishbone suspension. This uses two lateral control arms (A-arms or wishbones) of unequal lengths to hold a wheel as shown in Figure 1-4, and hence the name short long arm suspension. A simplified kinematic representation as planar four-bar linkage is also illustrated in Figure 1-4. The upper control arm is shorter than the lower control arm, to reduce the tire-scrub and to improve camber at the outside wheel by counteracting camber due to body-roll. It provides for excellent packaging for longitudinally oriented engines in front-engine rear-wheel-drive cars. Design of the geometry for an SLA is full of trade-offs and hence requires careful refinement to give good performance.

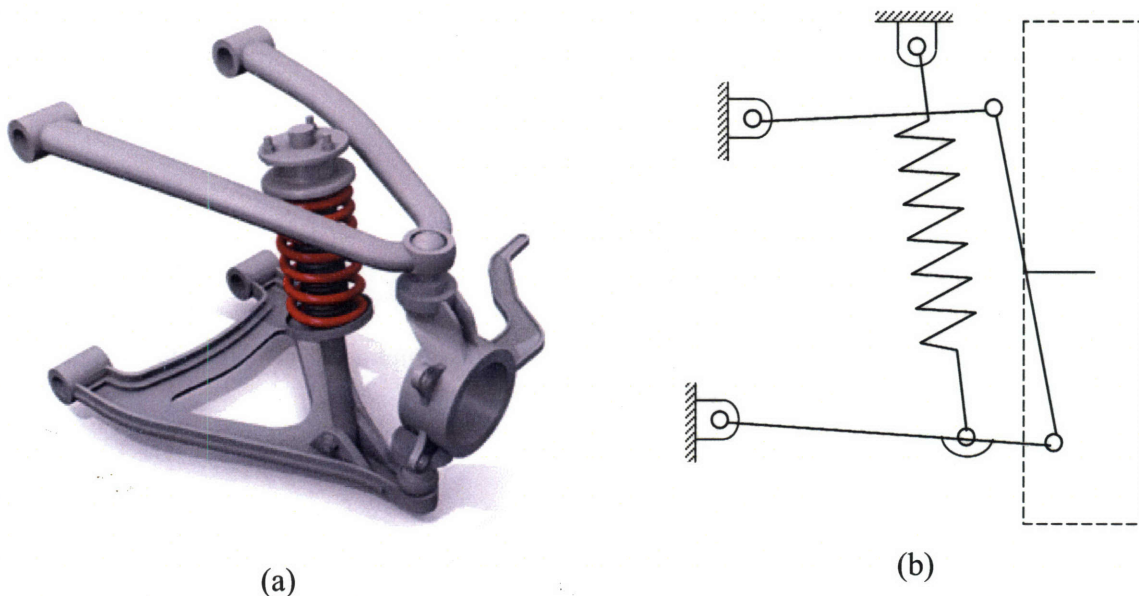


Figure 1-4: Short long arm suspension system (a) 3D model (Figure from Longhurst 2006) and (b) Simplified representation as a planar mechanism

MacPherson Strut

The MacPherson strut is a telescoping member incorporating the spring and the damper with the wheel rigidly attached at its lower end as shown in Figure 1-5. The figure also shows a simplified kinematic representation as a planar four-bar linkage. The upper end of the strut is fixed to the chassis, and the lower end is located by linkages which pick up the lateral and longitudinal forces. The MacPherson strut, in addition to having fewer parts, provides major advantages in packaging for transverse engines and this is widely used for front-wheel-drive cars. As in the case of SLA

suspension systems, design of the geometry for a MacPherson strut system is full of trade-offs and hence requires careful refinement to give good performance

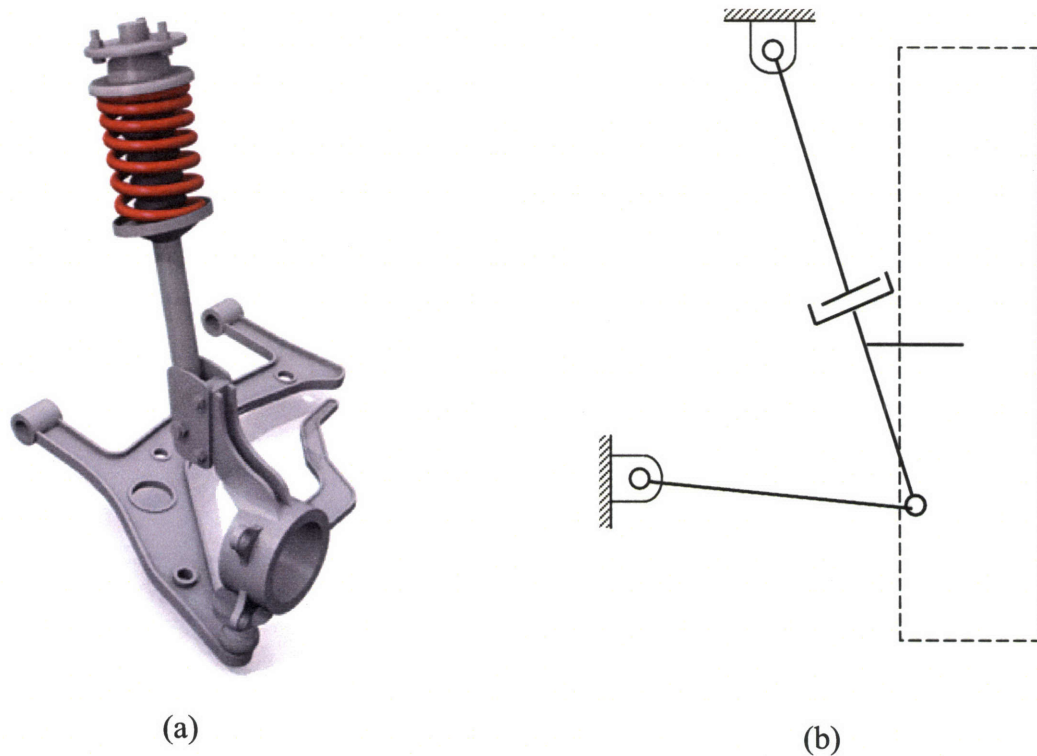


Figure 1-5: MacPherson Strut (a) 3D model (Longhurst 2006) and (b) Simplified kinematic representation as a planar mechanism

1.2.2 Springs

A variety of springs have been employed on existing suspension systems to achieve the desired DP 1: Suspension stiffness. These include leaf springs, coil springs, air springs, and torsion bar springs.

Leaf springs are simple, robust and inexpensive. They were used on early automotive suspensions such as the Hotchkiss suspension, and they are still common on some solid-axle suspensions on large trucks. The coulomb friction (stiction) in the individual leaves of the leaf spring leads to hysteresis and a much higher effective stiffness for small deflections (Sayers & Gillespie, 1982). This leads to a much harsher ride on smooth roads as compared to rough roads. Elongation of the leaf springs to lower spring rate, results in loss of side stability of the springs. Because of these disadvantages, they are not used on passenger cars anymore.

Coil springs are the most common type of spring on passenger cars for their simplicity, cost, compact size and performance.

Torsion bar springs have been used on certain cars, where packaging constraints prohibit the use of coil springs.

The use of *pneumatic springs* was first demonstrated in experimental car suspensions in 1935, but they have made inroads into commercial suspensions very recently. Some of their advantages are adjustable stiffness, adjustable ride-height, reduction of friction and nearly constant frequency with respect to load variations. A major portion of this thesis deals with the design and modeling of pneumatic springs and application of pneumatic springs to design a customizable automotive suspension with independent control of suspension stiffness and suspension ride-height.

1.2.3 Dampers

A variety of damper constructions have been employed on existing suspension systems to achieve DP 2: Damping Coefficient. Damping in suspension systems typically comes from viscous friction that results from the flow of fluid through a restriction in telescoping hydraulic dampers. Coulomb friction in the joints and bushings, and aerodynamic damping force on the body also contribute to the damping, but for analytical simplicity the damper is typically assumed to be a simple linear element with force proportional to velocity. The linear force-velocity relation is actually achieved with much difficulty in hydraulic dampers through suitable valving. In practice, the damping is linear but asymmetric, i.e., the damping in suspension rebound (extension) is typically two or three times the damping in suspension jounce (compression). This is achieved by using a piston that contains two orifices with one-way valves which provide different damping during jounce and rebound.

1.2.4 Suspension dynamics models

The effect of the DP 1: Suspension stiffness and DP 2: Suspension damping coefficient, on the comfort and handling performance of the car is the subject of suspension dynamics. In this section, we look at the different dynamic models used to study the effect of these parameters on the performance of passive suspension systems and the effect of the control law on the performance of active suspension systems. Several dynamic models have been used in literature to study the design and dynamic behavior of active and passive suspension systems. The choice of the model used depends on the vibration mode and frequency range of interest and the simplicity of analysis involved. Basic vehicle models that have appeared in the literature and

have been used in the design of suspension systems are quarter car 1-DOF model to study the bounce mode, quarter car 2-DOF model to study the bounce mode with wheel-hop, half car 4-DOF model to study bounce and pitch modes, and the full car 7-DOF model to study the bounce, pitch and roll modes. These models are described below:

1. Quarter car 1-DOF model: This is the simplest representation of an automotive suspension system at each wheel and captures the motion of the vehicle body at one wheel as shown in Figure 1-6 (a). The suspension is shown to have stiffness K_s , damping B and possibly an actuator (for active suspension) in parallel. The sprung mass M_s represents the quarter-car equivalent of the vehicle body mass, This model can be used to study only the vehicle bounce mode and fails to capture the wheel-hop mode.
2. Quarter car 2-DOF model: This model is shown in Figure 1-6 (b) and represents the automotive suspension at each wheel, i.e., the motion of the axle and of the vehicle body at one wheel. The suspension is shown to have stiffness K_s , damping B and possibly an actuator (for active suspension) in parallel. The sprung mass M_s represents the quarter-car equivalent of the vehicle body mass, and the unsprung mass M_{us} represents the equivalent mass due to the wheel. The tire stiffness is represented by K_t . This model can be used to study the modes of vehicle bounce and wheel-hop. X_s , X_{us} , and X_r , represent the sprung mass displacement, unsprung mass displacement and the road deflection respectively.
3. Half car 4-DOF model: This model included the front and rear wheel to study bounce and pitch mode. In Figure 1-6 (c), X_s and θ represent the sprung mass bounce and pitch motions; X_{usf} and X_{usr} represents the unsprung mass displacement for the front and rear wheels respectively and X_{rf} and X_{rr} represents road deflection at the front and rear wheels respectively. The spring stiffness, damping and tire stiffness are denoted by K , B and K_t respectively.
4. Full car 7-DOF model: The models above can similarly be extended to a four wheel 7-DOF model to study the bounce, pitch and roll modes. The roll of the car is indicated by ϕ in Figure 1-7. Working with this model may become computationally expensive, so very often designers start with the simpler models and use the full car model to verify the design.

This thesis primarily deals with coming up with means to change suspension stiffness to eliminate the trade-off involved in the conflicting requirements of comfort and handling. We will primarily use the quarter car 1-DOF and 2-DOF models to study the effect of DP 1: Suspension stiffness and DP 2: Suspension damping on the comfort and handling performance of a car. The half car models will be used to study anti-pitch and anti-dive characteristics as well as understeer-oversteer behavior of the car.

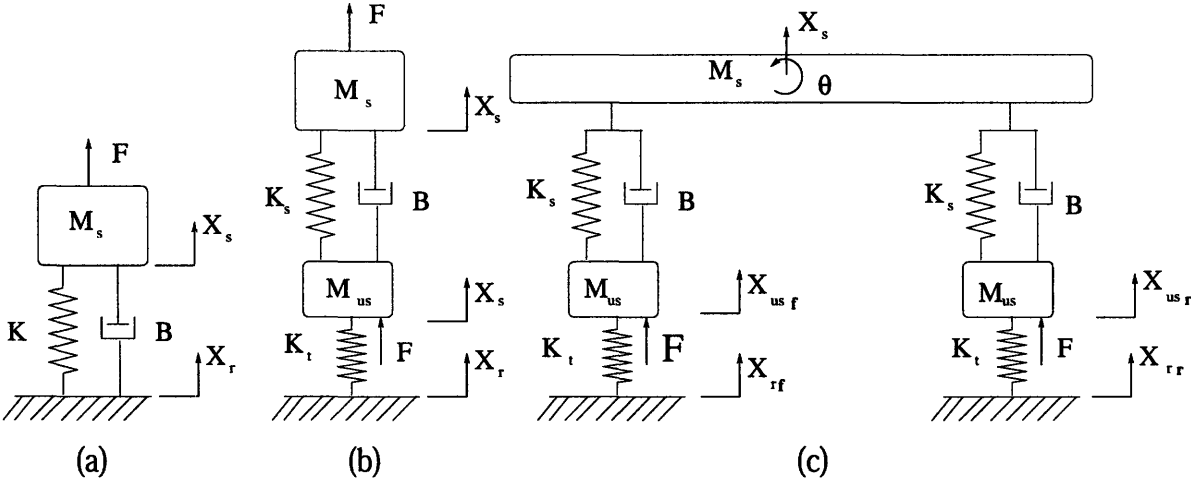


Figure 1-6 : Suspension dynamics models (a) Quarter car 1-DOF model; (b) Quarter car 2-DOF model; and (c) Half car 4-DOF model

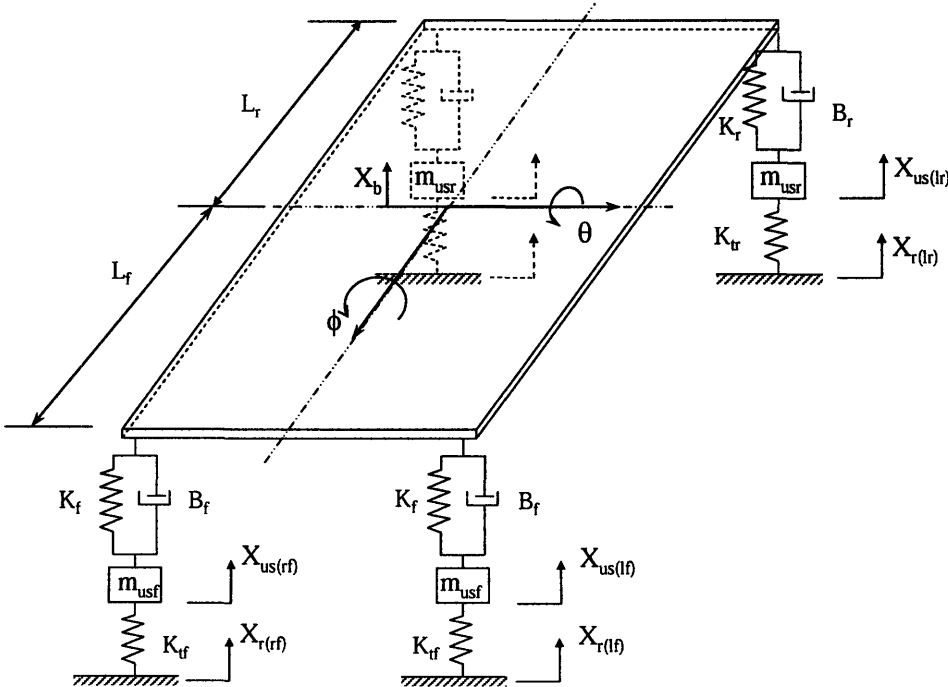


Figure 1-7 : Full car 7-DOF model to study the bounce, pitch and roll modes

1.2.5 Prior art on active suspension systems

Active vehicle suspensions have attracted a large number of researchers in the past few decades and comprehensive surveys on related research can be found in the papers by Elbeheiry et al (1995), Hedrick and Wormely (1975), Sharp and Crolla (1987), Karnopp (1995), and Hrovat (1997). These review papers classify various suspension systems discussed in the literature as passive, active, semi-active, slow-active, self-leveling and adaptive systems.

- *Passive suspension systems:* In passive suspension systems, the vehicle chassis is supported by only springs and dampers, which apply forces proportional to suspension displacement and suspension velocity respectively.
- *Active suspension systems:* Active suspension systems (fully active or high frequency active) replace, in part or full, the springs and dampers of passive systems by actuators. These actuators act as force producing elements according to some control law, using feedback from the vehicle. The actuator control bandwidth is assumed to extend beyond the wheel hop frequency, which is typically 8-10 Hz.
- *Semi-active suspension systems:* Semi-active suspension systems are considered to be derived from active systems, with the actuator replaced by controllable damper and a passive spring in parallel. It is assumed that the force-velocity relation can be modulated at relatively high frequencies. These systems employ feedback control to track the force demand signal which is similar to a corresponding active system, except that in circumstances where the active system would supply work, the force demanded of the damper is zero.
- *Slow-active suspension systems:* Slow-active suspension systems (also known as “low frequency active”) use actuator bandwidths in the range of body resonant frequencies in bounce, pitch and roll, and the frequency range of interest as far as responses to steering control are concerned, but lower than the wheel hop frequency. Actuators may be of one of the two basic types. They can be flexible like a spring when they become inactive in a control sense beyond the bandwidth, in which case they can support the body weight or act in parallel with the spring. Or they can be rigid when inactive in which case they must be mounted in series with the spring. Pneumatic actuators belong to the first category. Hydraulic actuator, electric motor or irreversible lead screw actuators belong to the

second category and are typically modeled as a displacement producer rather than a force producer.

- *Preview suspension systems*: Preview suspension systems involve acquisition and use of information of the road profile ahead of the vehicle wheels for actuator control purpose. These typically rely on high bandwidth actuators and accurate sensors; and have achieved limited success.
- *Adaptive suspension systems*: Adaptive suspension systems are essentially passive systems in which the parameters of the system can be changed in response to some information.
- Dynamic vibration absorbers have also been used in passive as well as active (Hrovat, 1997; Hrovat, 1990) suspension systems to get improved performance.

The applicability of fully active suspensions is restricted as the size, weight, power requirements and cost increase prohibitively with the bandwidth of the actuators. Semi-active suspensions have only dissipative elements and slow-active suspensions are band-limited; and hence are limited in their capabilities. In this thesis, we will focus on adaptive suspension systems. These are essentially passive systems in which the parameters of the system can be changed on the fly. Karnopp and Margolis (1984) have discussed the effects of parameter variation on frequency response and proposed that suspensions with adaptive stiffness and damping coefficient have potential in improvement of ride comfort and handling. Damping control, typically achieved through orifice control, is an established technology in existing vehicles (Crosby & Karnopp, 1973; Karnopp, 1983). Several road vehicles with pneumatic springs are capable of achieving variable ride-height (Esmailzadeh, 1979; Chance, 1984). Although advantages of variable stiffness have been illustrated in literature (Karnopp & Margolis, 1984), no system with independent control of stiffness has been proposed so far. In Chapters 3 and 4, we have proposed designs for novel customizable automotive suspension system with independent control of stiffness, damping and ride-height, which is capable of providing the desired performance depending on user preference, road conditions, vehicle speed, and maneuvering inputs.

In automotive suspension optimization literature, road noise is considered as a disturbance input. Different performance metrics such as sprung mass velocity, suspension deflection and tire-deflection are included in the cost as measures of comfort, suspension rattle-space and road-

holding. Different optimization techniques (predominantly LQG) are used to determine the control law for fully active suspensions. These techniques have been modified for application to optimization of passive suspension system parameters. Inertial forces due to maneuvering inputs are never included as they are difficult to model as stochastic disturbances. But this is not a reasonable assumption as the inclusion of inertial forces is the most important factor for handling performance optimization. In Chapter 6, we have presented stiffness scheduling for the variable-stiffness suspension systems proposed in Chapters 3 and 4, including both road noise and inertial forces caused by maneuvering inputs in the optimization formulation.

1.3 Thesis Summary

In this thesis, we have investigated the application of Axiomatic Design approach to eliminate the coupling that causes the trade-off between the conflicting comfort and handling requirements. Road noise isolation is defined as a performance metric for comfort; and the extent of lateral destabilizing forces caused due to wheel alignment parameter changes is defined as a performance metric for handling.

The first coupling in the suspension system that has been addressed in this thesis manifests itself through the wheel alignment parameter changes caused by suspension travel. Wheel alignment parameter changes lead to lateral destabilizing forces and increased tire-wear. The four-bar linkages used in the existing independent suspension systems (namely the SLA suspension and the MacPherson strut) are not capable of avoiding the wheel alignment parameter changes due to suspension travel. In Chapter 2, a six-bar Watt-I linkage suspension is proposed which is capable of making the wheel alignment parameters independent of suspension travel thereby eliminating lateral destabilizing forces and tire-wear. As a result a softer suspension may be used without affecting handling adversely. A formulation for kinematic synthesis of the suspension system using the six-bar Watt-I linkage is outlined and a new steering system compatible with the new suspension system is proposed. This design has great promise for improved comfort and handling and reduced tire-wear on straight-ahead driving conditions, but exhibits unfavorable camber change on cornering. This indicates that changing single degree of freedom suspension kinematics may have limited benefit in eliminating this coupling.

The second coupling, addresses in this thesis, is caused due the fact that the same DP: *Suspension stiffness* affects the two functional requirements of comfort and handling. This leads

to coupling as handling requires a stiff suspension, whereas comfort requires a soft suspension. In this thesis, we eliminate this coupling by separating the DP: *Suspension stiffness* in time. This can be done by designing a suspension system with time-varying stiffness, such that the vehicle has low stiffness when comfort is of primary importance, and has high stiffness when handling is of primary importance. Moreover, the tradeoffs in selection of ride-height and damping are also considered. Cars need high ground clearance on rough terrain, whereas a low center of gravity (CG) height is desired for swift cornering and dynamic stability at high speeds. It is advantageous to have low damping for low force transmission to vehicle frame, whereas high damping is desired for fast decay of oscillations. To avoid these trade-offs, a novel design for a customizable automotive suspension system with independent control of stiffness, damping and ride-height is proposed in Chapter 3. This system is capable of providing the desired performance depending on user preference, road conditions and maneuvering inputs. A prototype has been designed and fabricated to demonstrate the concept. The structure of the design matrix is shown in Equation (1.2).

$$\left\{ \begin{array}{l} \text{FR1: Control Stiffness} \\ \text{FR2: Control Ride-height} \end{array} \right\} = \begin{bmatrix} X & O \\ X & X \end{bmatrix} \left\{ \begin{array}{l} \text{DP1} \\ \text{DP2} \end{array} \right\} \quad (1^{\text{st}} \text{ Design}) \quad (1.2)$$

The proposed system employs a linear stage to move the lower spring pivot along the lower control arm to achieve the desired stiffness change. This system presents cost, robustness and unsprung mass issues. Moreover this system is designed for slow changes in stiffness to satisfy the constraint of low power requirement. But application of variable stiffness suspension system to improved vehicle dynamics suggested that much greater benefit could be derived if the stiffness change is instantaneous (rapid) and if stiffness change does not affect ride-height. The design matrix for the existing suspension system shows that stiffness change affects ride-height change. Although this can be compensated for by DP 2, the compensation involves energy input and time-delay. Hence it is preferable to have an uncoupled design as shown in Equation (1.3). In case an uncoupled design is not possible a decoupled design with the design matrix structure as shown in Equation (1.4) is preferable over a design matrix structure as shown in Equation (1.2).

$$\left\{ \begin{array}{l} \text{FR1: Control Stiffness} \\ \text{FR2: Control Ride-height} \end{array} \right\} = \begin{bmatrix} X & O \\ O & X \end{bmatrix} \left\{ \begin{array}{l} \text{DP1 A} \\ \text{DP2 A} \end{array} \right\} \quad (\text{Ideal Design}) \quad (1.3)$$

$$\begin{Bmatrix} \text{FR1: Control Stiffness} \\ \text{FR2: Control Ride-height} \end{Bmatrix} = \begin{bmatrix} X & X \\ O & X \end{bmatrix} \begin{Bmatrix} \text{DP1 B} \\ \text{DP2 B} \end{Bmatrix} \quad (\text{Preferred over 1}^{\text{st}} \text{ Design}) \quad (1.4)$$

In chapter 4, we have investigated the possibility of using pneumatic and hydro-pneumatic suspension systems to create a customizable automotive suspension with independent control of stiffness, damping and ride-height; preferably with instantaneous (or rapid) stiffness change, with no (or limited) power input and no (or limited) effect on ride-height change as described in the design matrix in Equation (1.4). One of the proposed designs employs auxiliary volumes connected to the air-spring volume through On-Off valves for changing the stiffness of the system. The stiffness of an air-spring is inversely proportional to the volume of air in the air-spring. When the valve is opened, the air-spring stiffness reduces due to increase in effective volume. By adequately choosing N unequal auxiliary volumes, this system can achieve 2^N stiffness settings. This system shows the potential of instantaneous stiffness change, with no power input, and no ride-height change due to stiffness change. Moreover, the proposed variable stiffness isolator is inexpensive, robust and light. As a result, it is readily applicable to several other vibration isolation applications with conflicting stiffness requirements (such as a precision motion stages) or time-varying stiffness requirements (such as prosthetic limbs). These applications are also discussed in Chapter 4.

A customizable pneumatic suspension system prototype has been designed and incorporated in a car and it demonstrates the concept well. A data acquisition system has been designed and incorporated in the car for testing the performance of the pneumatic suspension system. The design, fabrication, and testing of the suspension system is discussed in Chapter 4. A detailed thermodynamic model of the air-spring with auxiliary volumes is developed to predict the frequency response of the system for small displacements. For large displacements, the linear stiffness model is no longer valid. This may lead to counter-intuitive behavior such as increase in stiffness when valves are opened. The nonlinear force-displacement relations are derived for an air-spring with auxiliary volumes and they explain the observed data well. Based on this modeling and testing, the performance limits and practical applicability of this system are discussed.

The capability to change stiffness instantaneously and with no power input, allows us to employ a soft suspension on rough roads during straight-ahead driving conditions, and to instantaneously

increase stiffness on hard braking, hard acceleration or cornering to limit the wheel attitude changes and vehicle attitude changes. In Chapter 5, the applications of the customizable suspension systems, capable of low bandwidth stiffness change and high bandwidth (instantaneous) stiffness change, are discussed. Here high bandwidth stiffness change refers to stiffness change that is much faster than the time constants associated with the relevant rigid-body modes of the system, namely bounce, pitch, roll and yaw modes. The application of variable stiffness to achieve real-time alteration of pitch and bounce motion centers, and real time alteration of anti-pitch characteristics is demonstrated. The possibility of ensuring stability through real-time alteration of understeer-oversteer characteristics is explored and demonstrated on the pneumatic customizable suspension system. The suspension geometries (kinematics) and stiffness settings required for achieving the desired vehicle dynamic characteristics (such as anti-pitch/anti-dive characteristics, understeer-oversteer characteristics or pitch and bounce motion center locations) are well known. But the geometries required for the different characteristics are very often contradictory and this leads to a trade-off solution for the suspension kinematics. The capability of rapid real-time alteration of these characteristics allows us to eliminate the design coupling involved.

In Chapter 6, ride-height control of a constant area pneumatic suspension system is discussed. The response of this nonlinear system to the valve On-Off control is modeled and it is observed that a feedback control law using only position feedback leads to a limit cycle. A modified state feedback control law using position and pressure feedback is proposed to ensure convergence to the equilibrium point.

In automotive suspension optimization literature using LQG/H2 techniques, road noise is considered as a disturbance input, and sprung mass velocity, suspension deflection and tire-deflection are included in the cost as measures of comfort, suspension rattle-space and road-holding. Inertial forces due to maneuvering inputs are never included as they are difficult to model as filtered white noise. But this is not a reasonable assumption as the inclusion of inertial forces is the most important factor for handling performance optimization as was seen from the six-bar example. The second part of Chapter 6 discusses stiffness scheduling based on the hypothesis that the optimum stiffness depends on the source of disturbance- road noise or inertial forces due to maneuvering inputs. In this chapter, an attempt is made to determine the source of

disturbance from state measurements by exploiting phase relations, and to schedule the stiffness to the optimum value based on the source of disturbance.

Chapter 2

Proposal of a novel Six-Bar Suspension

2.1 Introduction

Existing vehicle suspension and steering system designs exhibit a high level of coupling. For instance, the coupling in suspension and steering systems manifests itself through the change in wheel alignment parameters (WAP) due to suspension travel. This change in the wheel alignment parameters causes directional instability and tire-wear. The approach of the industry to solve this problem has been twofold. The first approach has been the optimization of suspension link lengths to reduce the change in wheel alignment parameters to zero. Since this is not possible with the existing architecture, the solution used is the optimization of the spring stiffness to get a compromise solution for comfort (which requires soft suspension for good road-noise isolation) and directional stability (which requires a stiff suspension for minimizing wheel travel to reduce wheel alignment parameters variation).

In this chapter, an axiomatic design solution to this problem is presented and an attempt is made to remove the coupling in the steering and suspension systems by making the wheel alignment parameters independent of suspension travel. The four-bar linkages used in the existing independent suspension systems are incapable of satisfying their FRs independently and cause coupling at a higher level. The proposed solution uses a six-bar Watt-I linkage suspension, which eliminates this coupling. It also offers other advantages such as the hardening characteristics for the suspension. A new steering system conformal to the new suspension system has been proposed.

FR/DP decomposition of the vehicle systems is presented. This indicates other couplings and DP redundancies in the vehicle system and also provides the framework for design of novel vehicles.

2.1.1 Wheel Alignment Parameters

As mentioned earlier, the extent of lateral destabilizing forces caused by wheel alignment parameter changes is defined as a performance metric for handling. In this section we define the wheel alignment parameter and their effect on handling. Orientation of the wheels and steering axes with respect to the vehicle frame and with respect to the terrain changes due to suspension travel (Gillespie, 1992; Bastow, 1987; Dixon, 1996). Figure 2-1 shows the wheel alignment parameters which describe the orientation of the wheel and the wheel axis.

Camber: Camber is defined as the angle the wheel makes with respect to the vertical as seen in the front view. Camber tends to lift up one side of the tire and the higher load on one side of the tire leads to increased tire-wear. The tire assumes the shape of a base of the cone during rotation leading to a lateral force known as camber thrust. As a result camber spread (unequal camber on left and right wheels) causes directional instability.

Toe angle: Toe angle is the angle between the wheel and the vehicle longitudinal axis as seen in the top-view (denoted by ψ in Figure 2-1), and is used to steer the vehicle. In existing suspension systems, toe changes due to suspension travel, leading to *Bump Steer* as shown in Figure 2-10. Excess toe causes tire-wear.

Caster: Caster is the angle the steering axis makes with respect to the vertical as seen in the side view. Caster spread (unequal caster on left and right) causes directional instability.

Steering Axis Inclination: Steering Axis Inclination (SAI) is the angle the steering axis makes with respect to the vertical as seen in the front view. The forces acting on the wheel create a moment of the steering linkage which depends on the SAI and the kingpin offset. These determine the stability of a vehicle in high speed straight-ahead driving situations. Changes in steering axis inclination and the kingpin offset, due to suspension travel, cause directional instability.

As a result of these factors, vehicles exhibit tire-wear and directional instability due to wheel alignment parameter changes caused by suspension travel under conditions of overload, offset load or road undulations. Our approach to solve this problem is to perform a FR/DP

decomposition of the system, identify the coupling that causes the problem and to eliminate the coupling through proposal of a new design.

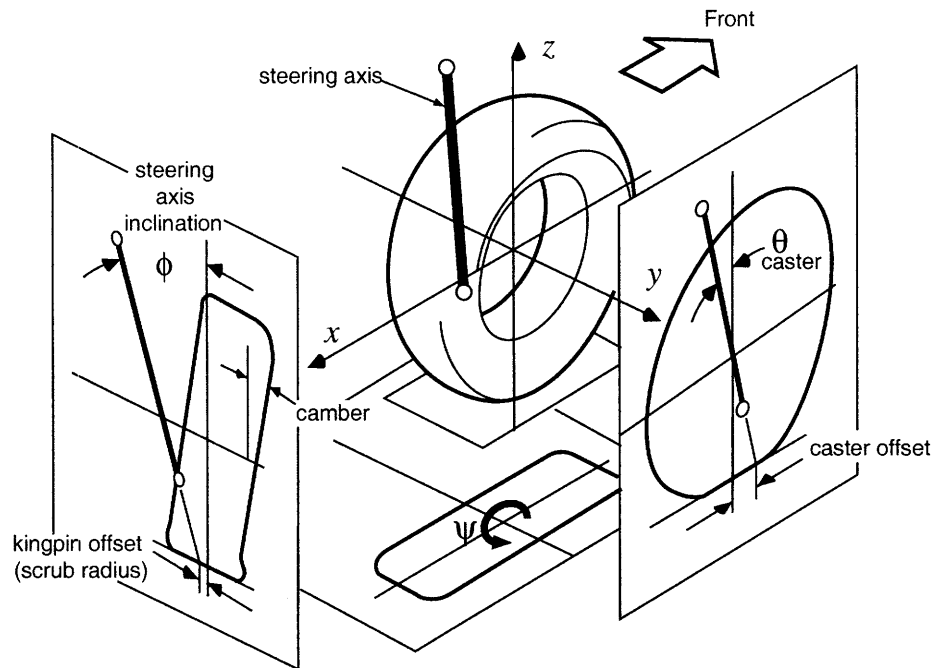


Figure 2-1: Wheel Alignment Parameters

2.2 FRDP decomposition of vehicle system

The top level FR/DP decomposition for the vehicle system is shown in Table 2.1 and the corresponding design matrix (DM) is shown in Equation (2.1). The DM indicates two sets of couplings- coupling between FR 3 and FR 5 and coupling between FR 4 and FR 5. The effect of DP 5 on FR 3 is small, as indicated by x in the DM in Equation (2.1). The design works in spite of this coupling, due to the presence of a feedback control system- the driver. Identification and removal of the coupling between FR 4 and FR 5 is the subject matter of this chapter. These two FRs have been decomposed further to understand this coupling better.

FR 4: Hold passengers can be further decomposed as shown in Table 2.2. As indicated in the decomposition, the passenger compartment must provide safety, comfort and pleasure to the passenger. Further decomposition of FR 42: Ensure comfortable ride is shown in Table 2.3. The corresponding design matrix is given in Equation (2.2).

Table 2.1 : Top level FR/DP decomposition of vehicle system

	Functional Requirements	Design Parameters
Parent	Need for transportation	Vehicle system
1	Allow low resistance motion	Rolling motion (Wheels)
2	Hold cargo	Cargo space
3	Control speed	Wheel rotation speed
4	Hold passengers	Passenger space
5	Control direction	Turning torque
6	Attractive appearance	Exterior Bodywork

$$\begin{matrix} \text{FR 1} \\ \text{FR 2} \\ \text{FR 3} \\ \text{FR 4} \\ \text{FR 5} \\ \text{FR 6} \end{matrix} = \begin{bmatrix} X & O & O & O & O & O \\ X & X & O & O & O & O \\ X & O & X & O & x & O \\ X & O & X & X & X & O \\ X & O & X & X & X & O \\ X & X & O & X & X & X \end{bmatrix} \begin{matrix} \text{DP 1} \\ \text{DP 2} \\ \text{DP 3} \\ \text{DP 4} \\ \text{DP 5} \\ \text{DP 6} \end{matrix} \quad (2.1)$$

Table 2.2 : FR/DP decomposition of FR 4 (Hold passengers)

	Functional Requirements	Design Parameters
4	Hold passenger	Passenger compartment
41	Provide crash protection	Impact strength
42	Ensure comfortable ride	Suspension dynamics
43	Provide pleasing environment	Interior design

Table 2.3 : FR/DP decomposition of FR 42 (Ensure comfortable ride)

	Functional Requirements	Design Parameters
42	Ensure comfortable ride	Suspension dynamics
421	Limit maximum relative motion	Spring rate
422	Dissipate energy	Damping coefficient
423	Set equilibrium position	Spring initial length

$$\begin{Bmatrix} \text{FR 1421} \\ \text{FR 1422} \\ \text{FR 1423} \end{Bmatrix} = \begin{bmatrix} \text{X} & \text{O} & \text{O} \\ \text{X} & \text{X} & \text{O} \\ \text{X} & \text{O} & \text{X} \end{bmatrix} \begin{Bmatrix} \text{DP 1421} \\ \text{DP 1422} \\ \text{DP 1423} \end{Bmatrix} \quad (2.2)$$

FR 5 (Control direction) can be further decomposed as shown in Table 2.4 and the corresponding design matrix is given in Equation (2.3).

Table 2.4 : FR/DP decomposition of FR 5 (Control direction)

	Functional Requirements	Design Parameters
5	Control direction	Turning torque
51	Maintain wheel alignment	Suspension kinematics
52	Maintain tire-road contact	Suspension travel
53	Adjust desired torque	Wheel angle

$$\begin{Bmatrix} \text{FR 51} \\ \text{FR 52} \\ \text{FR 53} \end{Bmatrix} = \begin{bmatrix} \text{X} & \text{O} & \text{O} \\ \text{X} & \text{X} & \text{O} \\ \text{X} & \text{O} & \text{X} \end{bmatrix} \begin{Bmatrix} \text{DP 51} \\ \text{DP 52} \\ \text{DP 53} \end{Bmatrix} \quad (2.3)$$

In several complex systems, the design matrix (DM) may be coupled at the highest level as shown in Equation (2.4), which on further decomposition of FR_{ex1} and FR_{ex2} can be expressed as Equation (2.5).

$$\begin{Bmatrix} \text{FR}_{\text{ex}1} \\ \text{FR}_{\text{ex}2} \end{Bmatrix} = \begin{bmatrix} \text{X} & \text{X} \\ \text{X} & \text{X} \end{bmatrix} \begin{Bmatrix} \text{DP}_{\text{ex}1} \\ \text{DP}_{\text{ex}2} \end{Bmatrix} \quad (2.4)$$

$$\begin{Bmatrix} \text{FR}_{\text{ex}11} \\ \text{FR}_{\text{ex}12} \\ \text{FR}_{\text{ex}21} \\ \text{FR}_{\text{ex}22} \end{Bmatrix} = \begin{bmatrix} \text{X} & \text{O} & \text{O} & \text{O} \\ \text{X} & \text{X} & \text{X} & \text{X} \\ \text{X} & \text{O} & \text{X} & \text{O} \\ \text{X} & \text{O} & \text{O} & \text{X} \end{bmatrix} \begin{Bmatrix} \text{DP}_{\text{ex}11} \\ \text{DP}_{\text{ex}12} \\ \text{DP}_{\text{ex}21} \\ \text{DP}_{\text{ex}22} \end{Bmatrix} \quad (2.5)$$

The structure of the design matrix in Equation (2.5) is such that we can rearrange the order of the leaf level DPs to achieve a decoupled design matrix as shown in Equation (2.6). This method is known as system-wide rearrangement of the DPs and FRs and can be used to decouple an apparently couple system (Melvin & Suh, 2002). In several complex systems, a coupled design matrix at the highest level may be decoupled by system-wide rearrangement of the DPs and FRs.

$$\begin{Bmatrix} \text{FR}_{\text{ex}} 11 \\ \text{FR}_{\text{ex}} 22 \\ \text{FR}_{\text{ex}} 21 \\ \text{FR}_{\text{ex}} 12 \end{Bmatrix} = \begin{bmatrix} X & O & O & O \\ X & X & O & O \\ X & O & X & O \\ X & X & X & X \end{bmatrix} \begin{Bmatrix} \text{DP}_{\text{ex}} 11 \\ \text{DP}_{\text{ex}} 22 \\ \text{DP}_{\text{ex}} 21 \\ \text{DP}_{\text{ex}} 12 \end{Bmatrix} \quad (2.6)$$

In this example, we observed that it is difficult to create a design which would eliminate the coupling between FR 4 and FR 5 at the highest level. But it is possible to have a decoupled system after decomposition and system-wide rearrangement. To illustrate this, FR 42 and FR 5 are decomposed together and the corresponding design matrix presented in Equation (2.7).

$$\begin{Bmatrix} \text{FR} 51 \\ \text{FR} 52 \\ \text{FR} 421 \\ \text{FR} 422 \\ \text{FR} 423 \\ \text{FR} 53 \end{Bmatrix} = \begin{bmatrix} X & X_1 & X_3 & O & O & O \\ X & X & O & O & O & O \\ X & O & X & O & O & O \\ X & O & X & X & O & O \\ X & O & X & O & X & O \\ X & X_2 & X_4 & O & O & X \end{bmatrix} \begin{Bmatrix} \text{DP} 51 \\ \text{DP} 52 \\ \text{DP} 421 \\ \text{DP} 422 \\ \text{DP} 423 \\ \text{DP} 53 \end{Bmatrix} \quad (2.7)$$

2.2.1 Existing designs: Identification of coupling

The elements X_1 , X_2 , and X_3 in the design matrix in Equation (2.7), indicate the coupling. X_1 indicates that suspension travel causes the wheel alignment parameters to change and this causes undesired turning torque changes, as indicated by X_2 . The extent to which the wheel alignment parameters change and hence the magnitude of the unwanted turning torques change depends on the spring stiffness. This interaction is indicated by the elements X_3 and X_4 . Note that X_2 being non-zero does not make the design matrix coupled. But DP 52: Suspension travel is a dynamic design parameter and it affects FR 53 (Adjust desired torque). Hence, to satisfy FR 53, we would require real-time adjustment of DP 53 (Wheel angle). To avoid this, we need a design that is uncoupled with respect to the dynamic design parameter DP 52 ($X_1=0$, $X_2=0$).

These elements can be made zero and the coupling can be removed by making the wheel alignment parameters independent of suspension travel. The next sub-section examines the changes in wheel alignment parameters that result from suspension travel in the existing designs, lists the problems caused by this coupling and explores the possibility of removing this coupling by making the WAP independent of suspension travel.

2.2.2 Existing suspension systems: Four-bar linkages

All existing front-wheel independent suspension systems are variations of the four-bar mechanism. For instance, the parallel arm suspension, the short long arm (SLA) suspension and the MacPherson strut suspension can be kinematically represented as shown in Figure 2-2.

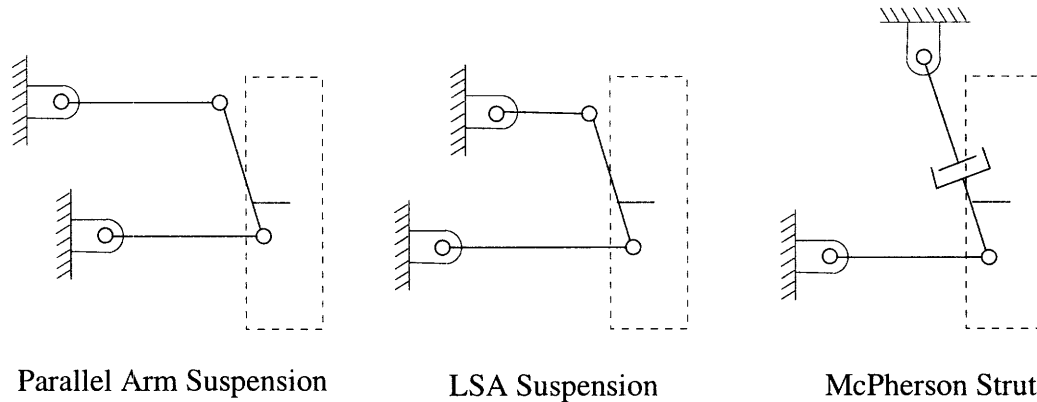


Figure 2-2 : Kinematic representation of independent suspensions

The FRs that DP 51: Suspension Kinematics (Four-bar linkage) is expected to satisfy are given in the form of FR/DP decomposition in Table 2.5 and are indicate in Figure 2-3. Δy indicates the lateral motion of the tire-patch (commonly known as “track changes”) caused by suspension travel. $\Delta\phi$ indicates the changes in the inclination of the steering axis as seen in the front view. We will only look into the following three important FRs for simplifying the analysis in this chapter: FR 511: Provide relative Z-motion, FR 512: Avoid track changes ($\Delta y=0$) and FR 513: Avoid camber and caster changes ($\Delta\phi =0$). Here Δy indicates tire scrub and $\Delta\phi$ indicates camber change. The other FRs are uncoupled and can be easily satisfied independently.

Table 2.5 : FR/DP decomposition of FR 51 (Maintain wheel alignment)

	Functional Requirements	Design Parameters
51	Maintain wheel alignment	Suspension kinematics
511	Permit relative Z-motion	Single degree of freedom system
512	Avoid track changes ($\Delta y=0$)	Effective swing axle radius
513	Avoid camber and caster changes ($\Delta\phi =0$)	Equal motion of steering axis joints

Analysis of the parallel arm suspension shows that it is capable of providing relative Z motion by change of angle θ as shown in Figure 2-4 and can maintain $\Delta\phi=0$ as both joints of the steering axis have equal vertical motion during suspension travel. But the parallel-arm suspension is incapable of satisfying FR 512: $\Delta y=0$ during suspension travel. This causes excessive tire-scrub due to suspension travel as illustrated in Figure 2-4. This sideways motion of the tire causes unnecessary tire-wear. It also causes the tire slip angle to change without any toe and results in destabilizing lateral forces.

In the SLA suspension, we can achieve $\Delta y=0$ (no tire scrub) through assignment of appropriate values to the link lengths, but this doesn't allow $\Delta\phi=0$ during suspension travel. This causes camber change and caster change due to suspension travel (Bastow, 1987). A compromise solution for Δy and $\Delta\phi$ can be obtained through optimization of the link lengths and joint positions, but we cannot satisfy all three FRs simultaneously using a four bar linkage. Both Δy and $\Delta\phi$ can be reduced by increasing the link lengths, but this is limited by the constraints of cost, packaging and unsprung weight of the vehicle

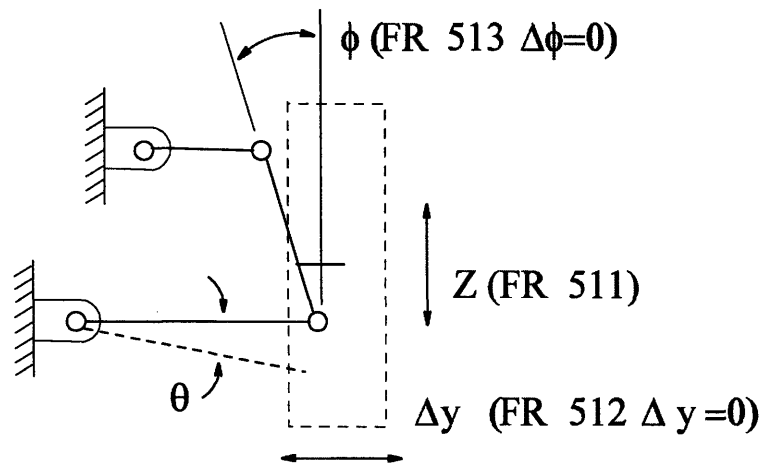


Figure 2-3 : Representation of the FRs of the suspension system

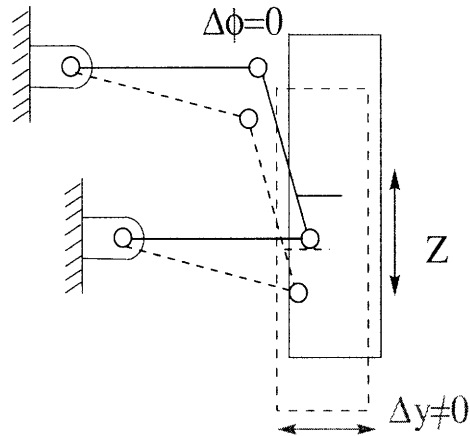


Figure 2-4 : Kinematic representation of parallel-arm suspension showing tire-scrub

The MacPherson strut suspension, also a four-bar linkage with one prismatic joint, is incapable of satisfying the three FRs simultaneously as well. It exhibits tire-scrub as well as WAP changes due to suspension travel.

This implies that in the existing designs, suspension travel affects the WAP. This makes the system coupled as indicated by the elements X_1 , X_2 and X_3 in Equation (2.7). This coupling leads to several problems. The changes in camber angle and toe due to excess suspension travel under overload causes unnecessary tire-wear. This could be a serious issue in trucks as the WAP could change significantly from unloaded to fully loaded condition. Under offset load, different suspension travel for the wheels could cause camber spread, caster spread or toe spread leading to directional instability or *Drift/pull* of the vehicle. Toe change due to suspension travel causes *Bump Steer* due to road undulations. Toe change due to suspension travel is also a possible source for the *Nibble* problem, in which the high frequency road noises are transmitted back to the steering wheel.

2.2.3 Manifestation of coupling in existing systems

Very often in coupled designs, when one DP affects two or more FRs, these FRs require the DP to have different values. This leads to a trade-off between the conflicting FRs and the designer has to resort to optimization of the DPs to achieve the best compromise solution. The coupling in the automobile suspension and steering system is manifested by the following trade-offs to achieve compromise solutions:

1. Compromise between $\Delta\phi=0$ and $\Delta y=0$ through optimization of link lengths.
2. Compromise between comfort and handling through optimization of spring stiffness K .
Handling requires a stiff suspension, whereas comfortable ride requires a soft suspension.

Since the existing designs cannot make the wheel alignment parameters independent of suspension travel, optimization of the spring stiffness has been the approach of the industry to get a compromise solution for FRs of comfort and handling. The axiomatic design approach points out the coupling between the FRs and indicates the need for developing a new uncoupled solution so that the compromise can be eliminated. Axiomatic design theory suggests the need for a new design that can satisfy both $\Delta\phi=0$ and $\Delta y=0$ simultaneously. Such a design would make the wheel alignment parameters independent of not only the suspension travel, but also of spring stiffness. Hence the control of the vehicle will improve. This will lead to improved handling. Spring stiffness can be designed only from comfort considerations and this will also improve passenger comfort.

2.3 Proposed new design

This section discusses the new suspension and steering system proposed to remove the identified coupling.

2.3.1 Proposed design of a suspension system

Analysis in the previous section indicated that the four-bar linkage is incapable of satisfying all three FRs (provide suspension travel, maintain $\Delta\phi=0$ and maintain $\Delta y=0$) simultaneously. This leads to coupling at a higher level. The DM indicates that the coupling can be removed by a change of DP 51: Suspension kinematics (Four-bar mechanism). A decision was made to change to DP 51: Suspension kinematics (Single degree of freedom system). Stating this as the DP presents several single degree of freedom systems as options for the hardware of the suspension kinematics, namely- a single revolute or prismatic joint, six-bar linkage and so on, apart from the four-bar linkage.

A prismatic joint is used in two wheeler suspensions, but there are issues involved in incorporating it in an automobile suspension. Revolute joint is used in the swing-axle suspension and it is capable of meeting only one FR out of the three FRs simultaneously. In a

swing-axle suspension, both camber and track changes during suspension travel (neither $\Delta y=0$, nor $\Delta\phi=0$).

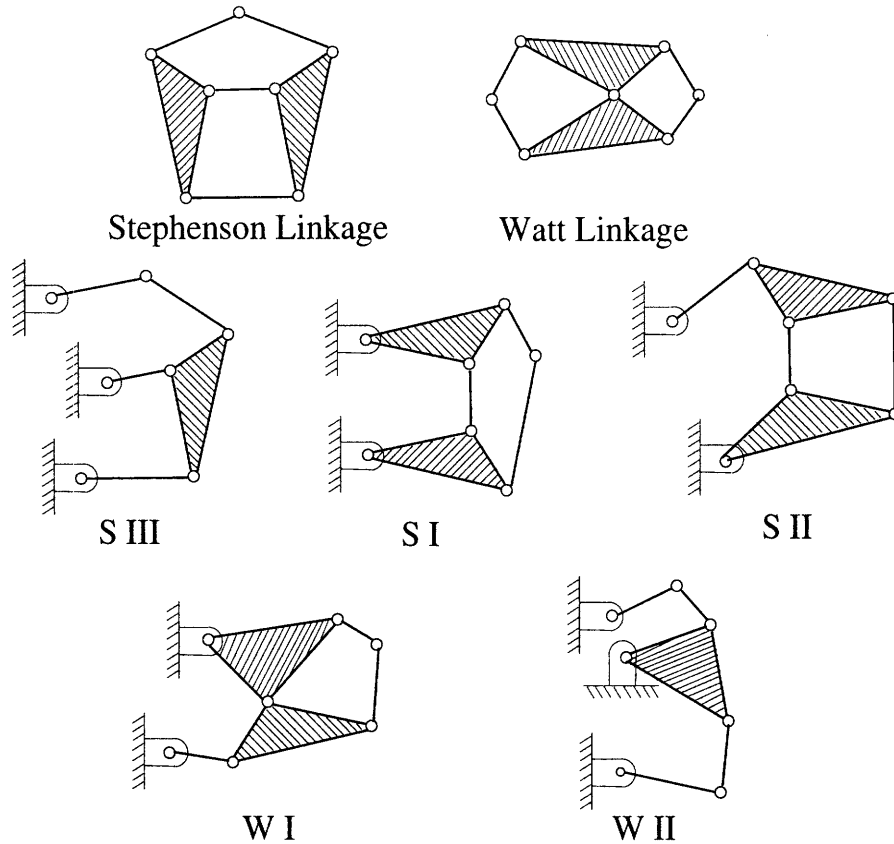


Figure 2-5 : Different possible six-bar mechanisms

The five possible inversions of a six-bar linkage using all revolute joints are shown in Figure 2-5. Investigation revealed that the Stephenson chains and the Watt-II chain are incapable of satisfying the three FRs simultaneously. This is illustrated with the example of the Stephenson-I chain as shown in Figure 2-6, where AB is the steering axis. In this linkage joint B moves in an arc with C as the center during suspension travel. There is no path that joint A can follow such that we can have relative Z-motion and at the same time maintain $\Delta y=0$ and $\Delta\phi=0$. Hence we proceed with the dimensional synthesis of the Watt-I linkage to see if it can satisfy the three FRs simultaneously. Maclaurin (2003) has presented a survey of six-bar linkage suspensions in which other chains were used for satisfying different FRs such as improved packaging and better camber control over full range of suspension travel.

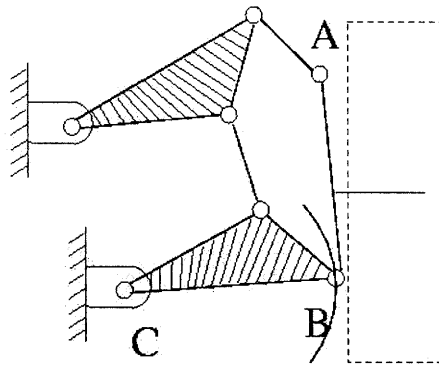


Figure 2-6 : Stephenson-I chain cannot satisfy the FRs

2.3.2 Dimensional synthesis of Watt-I linkage for the suspension

In this section, we present the dimensional synthesis of the six-bar suspension system. Complex number representation is very convenient to model linkage members and their motions, and is very commonly used in kinematic analysis and synthesis (Sandor & Erdman, 1989). A great majority of planar linkages can be thought of as combinations of vector pairs called *dyads*. For instance the four-bar linkage in Figure 2-7 can be perceived of as two dyads: the left side of the linkage represented as a vector pair W and Z , and the right side represented by the dyad W^* and Z^* . The path point P of the coupler moves along a path from position P_1 to P_j defined in an arbitrary complex coordinate system by R_1 and R_j .

Suppose we specify two positions for an unknown dyad by prescribing the values of R_1 , R_j , α_j , and β_j . To find the unknown starting position vectors of the dyad W and Z , a loop-closure equation may be derived by summing the vectors clockwise around the loop containing $W \exp\{i\alpha_j\}$, $Z \exp\{i\beta_j\}$, W and Z :

$$W(e^{i\alpha_j} - 1) + Z(e^{i\beta_j} - 1) = \delta_j \quad (2.8)$$

where $\delta_j = R_j - R_1$ is the displacement vector along the prescribed trajectory from P_1 to P_j . This equation is called the standard-form equation and is simply the vector sum around the loop containing the first and the j^{th} positions of the dyad forming the left side of the four-bar linkage. This synthesis technique is well developed for synthesis of four-bar mechanisms for different tasks: Path generation, motion generation and function generation (Sandor & Erdman, 1989). It involves expressing the desired motions and angular displacements of the input, output or coupler links (depending on the application) in the standard-form equation and solving these

equations to get the desired link lengths. This enables us to get an analytical solution to the synthesis problem. The next section discusses the application of this technique for the synthesis of the suspension system from the Watt-I linkage

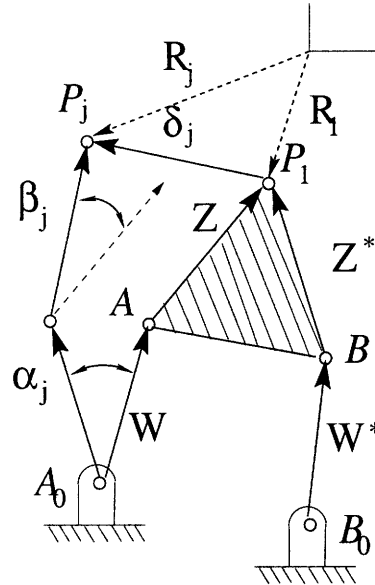


Figure 2-7 : Notation for the dyad

2.3.3 Application to suspension design

The FRs and the constraints that DP 51: Suspension kinematics has to satisfy are shown in Table 2.6. Figure 2-8 shows the application of the dyad technique for the synthesis of the suspension system using the six-bar Watt-I linkage. Here δ_j indicates the displacement of the steering axis joints A and B. Since δ_j are same for A and B, δ_j is also the displacement of the steering axis as a whole. Z_1 through Z_6 are vectors which characterize the link lengths and the existing state of the mechanism. The angular rotations of the links 1 to 4 are given by α_i , β_i , γ_i , and θ_i respectively as shown in Figure 2-8.

$$\begin{Bmatrix} \text{FR 511} \\ \text{FR 512} \\ \text{FR 513} \\ \text{FR 514} \end{Bmatrix} = \begin{bmatrix} X & O & O & O \\ O & X & O & O \\ O & O & X & O \\ X & O & O & X \end{bmatrix} \begin{Bmatrix} \text{DP 511} \\ \text{DP 512} \\ \text{DP 513} \\ \text{DP 514} \end{Bmatrix} \quad (2.9)$$

Table 2.6 : FR/DP decomposition of FR 51 (Maintain wheel alignment)

	Functional Requirements	Design Parameters
51	Maintain wheel alignment	Suspension kinematics
511	Permit relative Z-motion	Single degree of freedom system
512	Avoid track changes ($\Delta y=0$)	$\text{Im}(\delta_j)=0$
513	Avoid camber and caster changes ($\Delta\phi=0$)	Equal motion of steering axis joints
514	Hardening characteristics	α_i

The conditions imposed to meet the FRs are incorporated in the synthesis technique. The six-bar Watt-I linkage is a single degree of freedom system and we can attain relative Z-motion (FR 511). To avoid camber and caster changes (FR 513), we specify that the motion of the two steering axis joints A and B be the same (All δ_j are the same for both joints as shown in Figure 2-8). To avoid tire-wear (FR 512), we specify the imaginary parts of all δ_j to be zero. This ensures the wheel moves straight up and down, and not sideways, ensuring $\Delta y=0$. FR 514 can be easily met by specifying α_i .

Figure 2-8 shows four prescribed positions of the two joints of the steering axis. We formulate the standard-form equations for the three dyads for the three desired displacements δ_1 , δ_2 and δ_3 . This gives us the 9 equations given below. Each of these 9 complex equations actually consists of two equations- one equating the real parts and the other equating the imaginary parts of the complex equation. Note that, since Z_2 and Z_4 are a part of the same rigid body, they undergo the same angular displacements β_i . This is also the case for Z_3 and Z_5 , which have equal angular displacements γ_i .

For the first dyad (Z_1 and Z_2)

$$\begin{aligned}
 \delta_1 &= Z_1(e^{i\alpha_1} - 1) + Z_2(e^{i\beta_1} - 1) \\
 \delta_2 &= Z_1(e^{i\alpha_2} - 1) + Z_2(e^{i\beta_2} - 1) \\
 \delta_3 &= Z_1(e^{i\alpha_3} - 1) + Z_2(e^{i\beta_3} - 1)
 \end{aligned} \tag{2.10}$$

For the second dyad (Z_3 and Z_4)

$$\begin{aligned}
 \delta_1 &= Z_3(e^{i\gamma_1} - 1) + Z_4(e^{i\beta_1} - 1) \\
 \delta_2 &= Z_3(e^{i\gamma_2} - 1) + Z_4(e^{i\beta_2} - 1) \\
 \delta_3 &= Z_3(e^{i\gamma_3} - 1) + Z_4(e^{i\beta_3} - 1)
 \end{aligned} \tag{2.11}$$

For the third dyad (Z_5 and Z_6)

$$\begin{aligned}\delta_1 &= Z_5(e^{i\gamma_1} - 1) + Z_6(e^{i\theta_1} - 1) \\ \delta_2 &= Z_5(e^{i\gamma_2} - 1) + Z_6(e^{i\theta_2} - 1) \\ \delta_3 &= Z_5(e^{i\gamma_3} - 1) + Z_6(e^{i\theta_3} - 1)\end{aligned}\tag{2.12}$$

The values of δ_1 , δ_2 and δ_3 depend on the desired suspension travel (FR 511). We can specify α_1 , α_2 , and α_3 based on the desired hardening characteristics. $\delta_3/\alpha_3 > \delta_2/\alpha_2$ will give a hardening suspension (FR 514). The first set of equations has 6 equations and 7 unknowns, Z_1 , Z_2 , β_1 , β_2 and β_3 . Z_1 and Z_2 are planar vectors and hence constitute four unknowns. We can fix one unknown and solve for the other six. This gives us Z_1 and Z_2 .

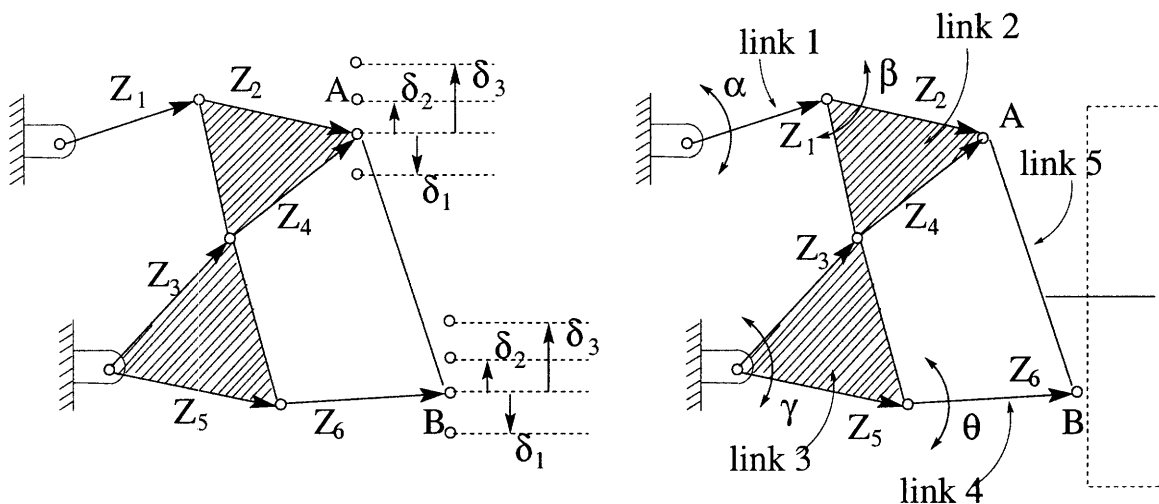


Figure 2-8 : Dimensional synthesis for the six-bar Watt-I linkage

The second set of equations has β_1 , β_2 and β_3 specified from the previous equation. This again is a set of 6 equations with 7 unknowns. We can fix one unknown and solve for the other six to get Z_3 and Z_4 . Similarly, we can solve for Z_5 and Z_6 from the third set of equations. The other link lengths can be obtained from vector additions of the known vectors Z_1 through Z_6 .

2.3.4 Proposed design of steering system

Existing steering system

A top view schematic of typical existing steering system is shown in Figure 2-9. Rotation of the steering wheel causes rotation of the Pitman arm through the steering column and the steering

gear. This motion of the Pitman arm is transmitted through the tie rod to the steering knuckle which is rigidly connected to the vehicle wheel. This linkage transmits the motion of the steering wheel to the vehicle wheel. The joints on both ends of the tie-rod are ball and socket joints to allow the suspension travel (in this case in and out of the plane of the paper).

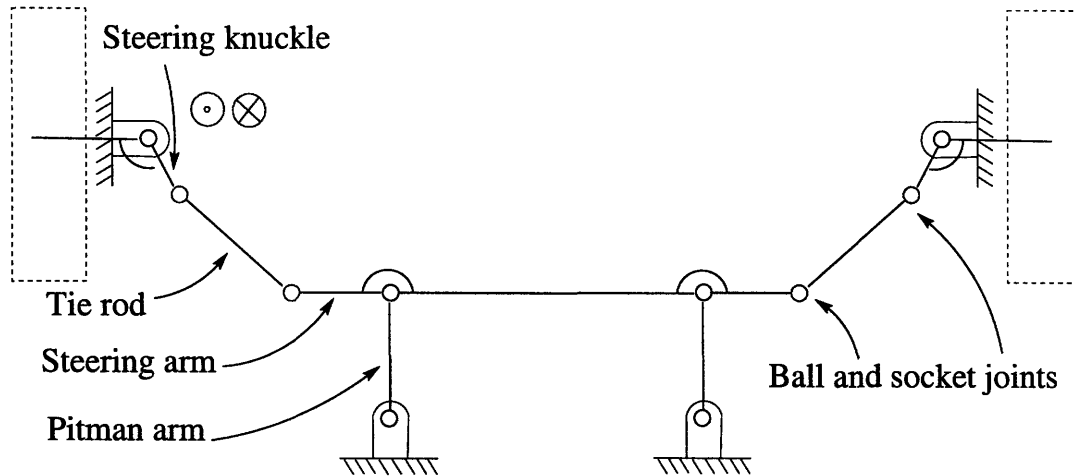


Figure 2-9 : Top view schematic of existing steering system

Need for a new steering system

As discussed in a previous section, toe-changes due to suspension travel in existing suspension systems causes tire-wear, directional instability, bump steer and nibble. During suspension travel, there is a mismatch between the unconstrained curves followed by the tie-rod outer point and the steering knuckle inner point as shows by the two curves in Figure 2-10. Toe change during suspension travel occurs because these the two points are forced together by the ball joint constraint. This phenomenon is commonly known as Bump Steer. Also suspension travel changes the effective tie-rod length according to the relation $L=L_1\cos\phi$. The steering mechanism link lengths are designed for, amongst other features, toe-out on turns. Thus the toe-out on turns characteristics of the linkage will change under overload load causing unnecessary tire-wear

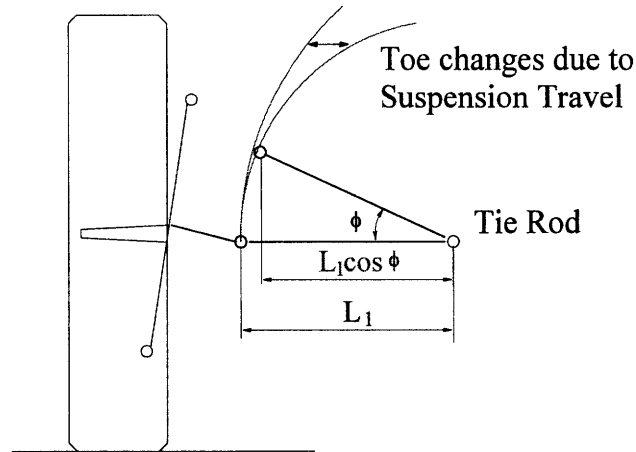


Figure 2-10 : Suspension travel causes toe-change and change in turning characteristics

Also, the existing steering system is incompatible with the new six-bar suspension system as it shows excessive toe-sensitivity due to the vertical suspension travel. This toe-sensitivity is highlighted in Figure 2-11

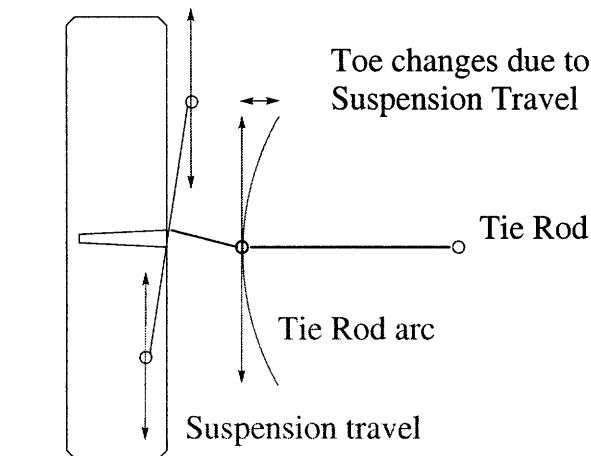


Figure 2-11 : Existing steering system is incompatible with the proposed suspension systems due to excessive toe-sensitivity

Design of a new steering system

To solve these problems, we have proposed a new steering system as shown in Figure 2-12. The proposed modification has a tie rod with a revolute joint at the inner tie rod end and a cylindrical joint at the outer tie rod end, instead of the ball and socket joints at both tie rod ends. In the new six-bar suspension system, the steering knuckle moves exactly vertically (in the Z-direction). It does not have any horizontal motion or any angle changes. This allows the use a cylindrical joint in place of ball and socket joints.

This system has a drawback that it does not allow the camber to change. We desire a camber roll on turns for suitable turning characteristics (Reimpell et al.,1996). Hence we need to modify this steering system to allow camber roll on turns.

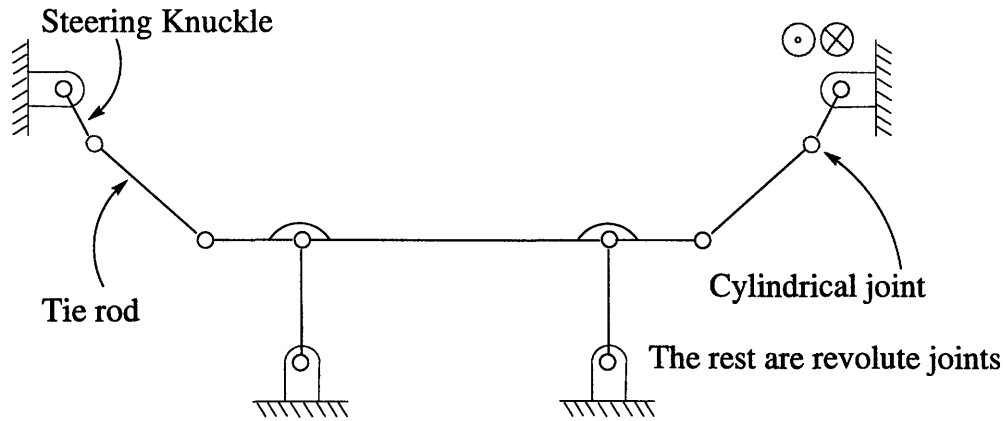


Figure 2-12 : Top view schematic of the proposed steering system

Modifications to allow camber change

To allow camber changes, a universal joint is introduced between the outer tie-rod end and the cylindrical joint as shown in Figure 2-13. Thus the steering system does not restrict camber changes and hence allows for camber roll on turns possible. Note that although the steering system does not restrict the camber changes, the suspension system does.

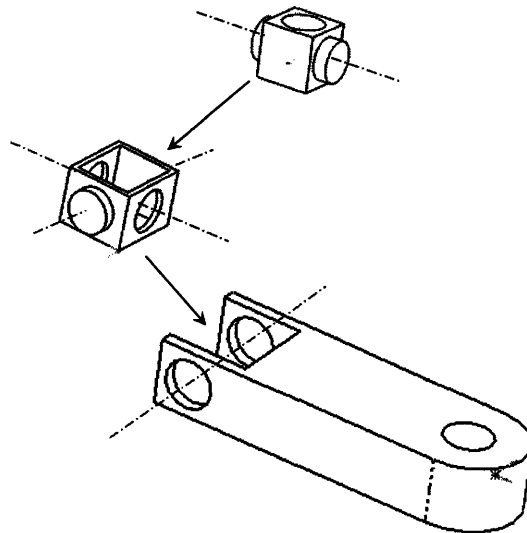


Figure 2-13 : Modifications of the tie-rod for camber roll on turns

2.4 Evaluation of the proposed design

2.4.1 Advantages

Wheel Alignment Parameters: Independent of suspension travel

To evaluate the advantages of the proposed design over the existing design, we compare the design matrices for the existing and proposed suspension and steering systems. The design matrices are shown in Equation (2.5) and Equation (2.13). The elements X_1 , X_2 and X_3 in Equation (2.5) indicate the coupling in the existing design. The design matrix for the proposed design is a lower triangular matrix and hence satisfies the Independence axiom. Moreover, the design is uncoupled with respect to the dynamic DPs, namely DP 52: Suspension travel and DP 53: Wheel angle, i.e. these DPs do not affect any other FR.

A careful look at the DM for the existing systems indicates that we must fix DP 52 before DP 422 and DP 423. But this is a contradiction since DP 422 is static in most cases and DP 423 is static in all cases, whereas DP 52 is dynamic.

$$\begin{Bmatrix} \text{FR 51} \\ \text{FR 421} \\ \text{FR 422} \\ \text{FR 423} \\ \text{FR 52} \\ \text{FR 53} \end{Bmatrix} = \begin{bmatrix} X & 0 & 0 & 0 & 0 & 0 \\ X & X & 0 & 0 & 0 & 0 \\ X & X & X & 0 & 0 & 0 \\ X & X & 0 & X & 0 & 0 \\ X & 0 & 0 & 0 & X & 0 \\ X & 0 & 0 & 0 & 0 & X \end{bmatrix} \begin{Bmatrix} \text{DP 51} \\ \text{DP 421} \\ \text{DP 422} \\ \text{DP 423} \\ \text{DP 52} \\ \text{DP 53} \end{Bmatrix} \quad (2.13)$$

Both the DMs show that DP 422: Damping coefficient does not affect any FR other than FR 422. Axiomatic design theory indicates that DP 422 can be used as a dynamic DP. Indeed, this is used in variable damping suspension systems and slow-active suspension systems. This is another example of application of axiomatic design theory to facilitate the rapid identification of such novel ideas through the FR/DP decomposition and the DM.

In the proposed system, WAP are independent of suspension travel and hence there are no unwanted turning torque changes ($X_1=0$, $X_2=0$). This leads to better handling. Since the WAP are independent of suspension, the problems of directional instability and tire-wear due to overload, offset load or road undulations are also eliminated. Since $X_3=0$ and $X_4=0$ in the proposed design, spring stiffness does not affect WAP or turning torque. Hence spring stiffness can be designed based only on comfort considerations and independent of handling consideration.

Hardening characteristics

It is desirable for the suspension to be responsive to the bumps for small displacements, so that we get a smooth ride. But we also want to limit the relative displacements between the wheel and the frame to some reasonable value. This can be achieved if we have a suspension that hardens as the deflection increases.

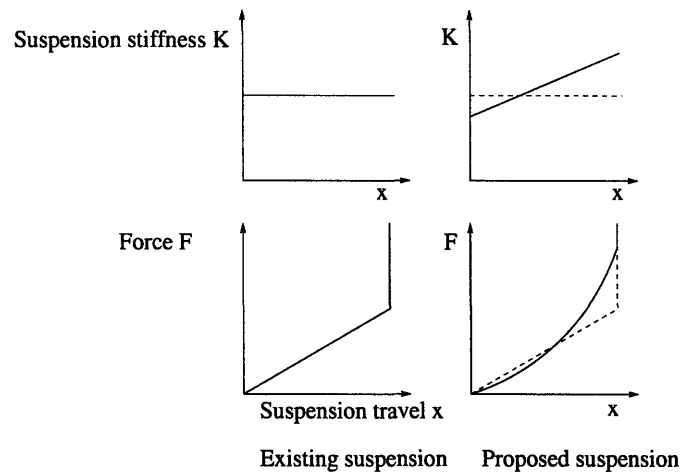


Figure 2-14 : Hardening characteristics in proposed six-bar suspension system

In existing suspension systems, the spring compression or extension is directly proportional to suspension travel, giving a linear relation between force and suspension travel as shown in Figure 2-14. The force increases suddenly when the control arm hits the jounce bumper.

In the proposed six-bar Watt-I linkage, suitable design can achieve a non-linear relation between the suspension travel and spring compression giving rise to a progressive effective spring rate and a hardening suspension as shown in Figure 2-14.

2.4.2 Limitations

The six-bar Watt-I linkage has the disadvantages of more number of links and joints. These will lead to higher cost and higher unsprung weight, and may also lead to reduced reliability. Packaging constraints are also an issue for incorporating this suspension in a car.

Unfavorable camber changes due to body roll and possible solutions

The proposed suspension maintains $\Delta\phi=0$, but ϕ is measured with respect to the vehicle frame, whereas camber is measured with respect to ground. If the vehicle frame tilts with respect to the ground (exhibits roll), we will have an equal and opposite camber on both wheels, with magnitude equal to the vehicle roll. This leads to a positive camber on the outer wheels, which is unfavorable on turns.

One solution to avoid this problem could be to eliminate body-roll. This can be done by *active roll-stabilization* (ARS). Several existing vehicles have this ARS feature. Incorporating ARS will further improve handling and comfort levels.

2.5 Summary

In this chapter, we have presented an axiomatic design approach to remove the coupling in the vehicle suspension and steering systems. FR/DP decomposition of the existing suspension and steering system is presented and coupling is identified. A new suspension system has been proposed which removes the coupling by making the wheel alignment parameters independent of suspension travel and hence delivers a better performance in terms of comfort, handling and reduced tire-wear. An analytical technique for the kinematic synthesis of the suspension system using a six-bar Watt-I mechanism is presented. A new steering system conformal to the new suspension system has been proposed. FR/DP decomposition of the vehicle system is also presented. This decomposition indicates other couplings and DP redundancies in the vehicle system and provides a framework for design of novel vehicles.

Several drawbacks of this system have been discussed, including higher unsprung weight, higher cost, and possibly lower reliability. But the most important drawback is the unfavorable camber on turns, which cannot be eliminated in this system (or in other existing suspension systems) with a SDOF suspension kinematics. This indicates that changing SDOF suspension kinematics may have limited benefit in eliminating the trade-off between the conflicting requirements of comfort and handling. Having explored this approach of changing the suspension kinematics to uncouple the conflicting requirements of comfort and handling, we will attempt to redesign the suspension dynamics. We will try to uncouple the conflicting requirements of comfort (which requires a soft suspension) and handling (which requires a stiff suspension) by separating the DP: Stiffness in the temporal domain. This can be done by designing a suspension with time-varying stiffness, such that the vehicle has low stiffness when

comfort is of primary importance, and has high stiffness when handling is of primary importance.

Chapter 3

Customizable Automotive Suspension System

The design of existing suspension systems typically involves a compromise solution for the conflicting requirements of comfort and handling. For instance, cars need a soft suspension for better comfort, whereas a stiff suspension leads to better handling. Cars need high ground clearance on rough terrain, whereas a low center of gravity (CG) height is desired for swift cornering and dynamic stability at high speeds. It is advantageous to have low damping for low force transmission to vehicle frame, whereas high damping is desired for fast decay of oscillations. To avoid these trade-offs, we have proposed a novel design for a customizable automotive suspension system with independent control of stiffness, damping and ride-height. This system is capable of providing the desired performance depending on user preference, road conditions, vehicle speed and maneuvering inputs. A suspension prototype has been built to demonstrate the concept. In this chapter, the development of the concept using axiomatic design theory, design and fabrication of the prototype and design and implementation of the control system for the suspension system is discussed.

The mechanical design of the proposed system is decoupled with respect to the functional requirements (FRs) of stiffness and ride-height; moreover ride-height is affected by the load on the vehicle (noise factor). A feedback control system for the customizable suspension was designed and implemented to uncouple the system and to make it robust to the noise factor. With this example, feedback control is proposed as a strategy for converting coupled or decoupled designs to uncoupled designs and for achieving robustness to noise factors.

Application of the proposed system to improved vehicle dynamics places certain requirements on the desired bandwidth of stiffness change and on the structure of the design matrix. These requirements are also highlighted in this chapter.

3.1 Introduction

Active vehicle suspensions have attracted a large number of researchers in the past few decades and comprehensive surveys on related research can be found in the papers by Elbeheiry et al (1995), Hedrick and Wormely (1975), Sharp and Crolla (1987), Karnopp (1995), and Hrovat (1997), among others. These review papers classify various suspension systems discussed in the literature as passive, active, semi-active, slow-active, self-leveling and adaptive systems. In passive systems, the vehicle chassis is supported by only springs and dampers. Active systems (fully active or high frequency active) replace, in part or full, the springs and dampers of passive systems by actuators which act as force producers according to some control law, using feedback from the vehicle. The actuator control bandwidth extends beyond the wheel hop frequency, which is typically 8-10 Hz. Semi-active suspension systems are considered to be derived from active systems, with the actuator replaced by controllable damper (whose force-velocity relation can be modulated at relatively high frequencies) with a spring in parallel. These employ feedback control to track the force demand signal which is similar to a corresponding active system, except that in circumstances where the active system would supply work, the force demanded of the damper is zero. Slow-active systems (low frequency active) use actuator bandwidths in the range of body resonant frequencies in bounce, pitch and roll, and the frequency range of interest as far as responses to steering control are concerned, but lower than the wheel hop frequency.

Actuators may be of one of the two basic types. They can be flexible like a spring when they become inactive in a control sense beyond the bandwidth, in which case they can support the body weight or act in parallel with the spring. Or they can be rigid when inactive in which case they must be mounted in series with the spring. Pneumatic actuators belong to the first category, whereas hydraulic, electric motor or irreversible lead screw actuators belong to the second category and are typically modeled as a displacement producer rather than a force producer. Preview systems involve acquisition and use of information of the road profile ahead of the vehicle wheels for actuator control purpose. Adaptive suspension systems are essentially passive

systems in which the parameters of the system can be changed in response to some information. Dynamic vibration absorbers have been used in passive as well as active (Hrovat, 1997; Hrovat, 1990) suspension systems to get improved performance. In addition, an introduction to the subject of suspension kinematics, suspension systems and vehicle dynamics in general is presented in a number of books (Bastow, 1990; Wong, 1993; Gillespie, 1994).

The applicability of fully active suspensions is limited because the size, weight, power requirements and cost increase prohibitively with the bandwidth of the actuators. Semi-active suspensions have only dissipative elements and slow-active suspensions are band-limited; and hence are limited in their capabilities. This work will look at adaptive suspension systems, which are essentially passive systems in which the parameters of the system can be changed in response to some information. Karnopp and Margolis (1984) have discussed the effects of parameter variation on frequency response and proposed that suspensions with adaptive stiffness and damping coefficient have potential in improvement of ride comfort and handling. Damping control, typically achieved through orifice control, is an established technology in existing vehicles (Crosby & Karnopp, 1973; Karnopp, 1983). Several road vehicles with pneumatic springs are capable of achieving self-leveling and variable ride-height (Esmailzadeh, 1979; Chance, 1984). Although advantages of variable stiffness have been illustrated in literature (Karnopp & Margolis, 1984), no system with independent control of stiffness has been proposed so far. In this chapter, we propose a design for a novel customizable automotive suspension with independent control of stiffness, damping and ride-height, which is capable of providing the desired performance depending on user preference, road conditions and maneuvering inputs. This can be classified as an adaptive suspension with variable ride-height and the novelty of this work is that this is the only system with independent control of stiffness and ride-height.

Moreover, this chapter proposes the use of feedback control to uncouple a decoupled system and to achieve robustness to noise factors. Earlier research has investigated system-wide rearrangement of leaf-level FR/DP elements as a collective set, in order to decouple a design that is coupled at a higher level to achieve a non-iterative design process, has been investigated (Melvin & Suh, 2002). Use of mathematical transforms to achieve uncoupling and robustness has also been proposed (Deo & Suh, 2004). Suh (2001) has discussed reduction of the sensitivity to noise factors, and Melvin and Deo (2002) have discussed the introduction of robustness FRs as strategies for achieving robustness in the axiomatic design framework.

3.2 Motivation for customizable suspension

3.2.1 Need for variable stiffness: Effect of stiffness on suspension performance

To understand the trade-off between comfort and handling caused by stiffness, we have defined high-frequency road noise isolation as parametric measures of comfort, and low-frequency wheel alignment parameter changes as parametric measures of handling. In this section, we will study the effect of stiffness on these parametric measures.

The orientation of the wheel and wheel axis with respect to the vehicle and the road are described by the wheel alignment parameters such as camber, caster, toe, steering axis inclination etc. Suspension travel causes the wheel alignment parameters to change. This creates lateral forces on the vehicle and may cause directional instability (Gillespie, 1992). The nature of the tire-road interactions is such that the vehicle is relatively insensitive to the high-frequency wheel alignment parameter changes. Hence low-frequency wheel alignment parameter change is a good parametric measure for directional stability or handling. A stiff suspension reduces suspension travel and the ensuing wheel alignment parameter changes, thereby reducing the destabilizing lateral forces and directional instability.

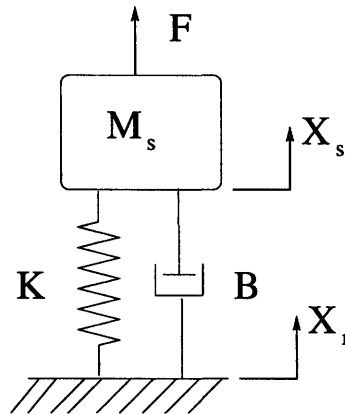


Figure 3-1: Quarter-car single DOF model

A simple quarter-car single degree of freedom (SDOF) model, as shown in Figure 3-1, is used to study the response of the sprung mass x_s to the road disturbance x_r and the force F acting on the sprung mass.

$$M\ddot{x}_s = B(\dot{x}_r - \dot{x}_s) + K(x_r - x_s) + F \quad (3.1)$$

where M , B and K are the suspension parameters mass, damping coefficient and stiffness respectively. The vertical force F , included in this formulation, could be the weight of the passengers or cargo (to study the static deflection of the vehicle) or the inertial forces acting on the vehicle caused by acceleration, braking or cornering. (For instance F could be the force transferred from the right wheel to left when the car is turning right). The two transfer functions of interest, relating road disturbance x_r and force F to the chassis displacement x_s , are compared for soft and stiff suspensions (while maintaining the same damping coefficient ζ by changing B with K) to understand how soft suspensions provide better comfort, while stiff suspensions provide better handling.

The road noise isolation transfer function given by Equation (3.2) shows the effect of road disturbance x_r on the chassis displacement x_s and hence is indicative of comfort. The Bode plot in Figure 3-2 for this transfer function for two different values of stiffness shows the same performance at low frequency, but a soft suspension provides better comfort due to better high-frequency road noise isolation.

$$\frac{X_s}{X_r} = \frac{Bs + K}{Ms^2 + Bs + K} \quad (3.2)$$

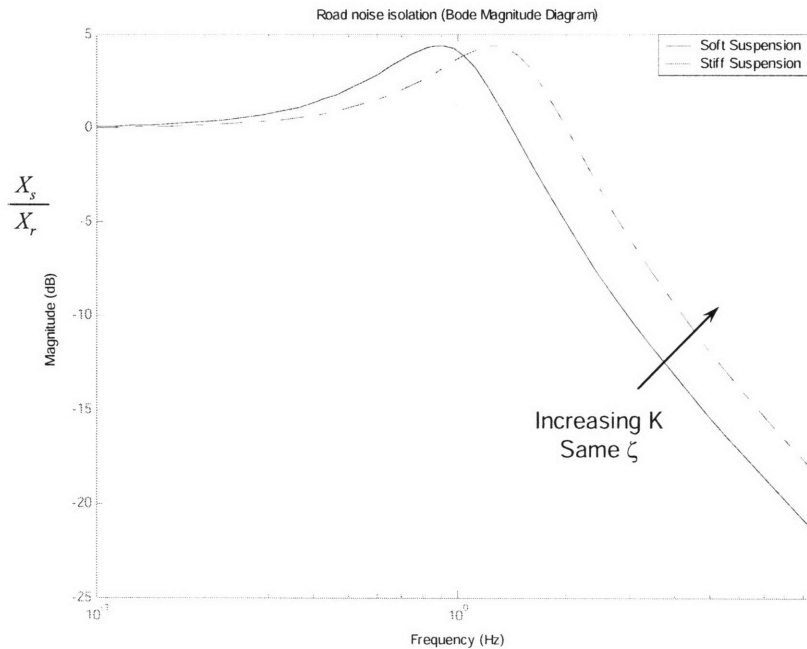


Figure 3-2: Bode plot showing road-noise isolation (comfort) for soft and stiff suspensions

The second transfer function, given by Equation (3.3), shows the effect of the force F on the chassis displacement x_s and hence is indicative of wheel alignment parameter changes or handling. The Bode plot in Figure 3-3 for this transfer function for two different values of stiffness shows the same response at high frequencies, but a stiff suspension provides better handling as it reduces the low-frequency wheel alignment parameter changes caused by force F (i.e. due to overload, cornering, acceleration or braking).

$$\frac{X_s}{F} = \frac{1}{Ms^2 + Bs + K} \tag{3.3}$$

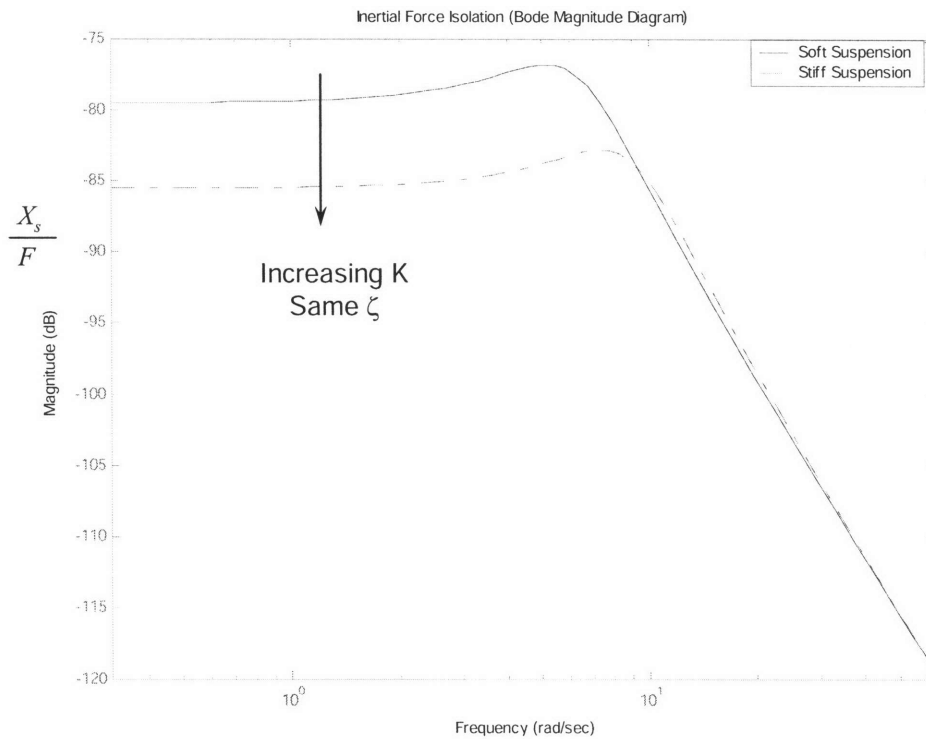


Figure 3-3: Bode plot showing suspension response to inertial forces (handling) for soft and stiff suspension

The analysis above shows that a stiff suspension leads to a better handling because of reduced low-frequency wheel alignment parameter changes and a soft suspension leads to better comfort due to better high-frequency road noise isolation. Hence, with a customizable suspension with user-control of stiffness, the user can get the desired performance (for example comfort mode or performance mode) by changing the stiffness.

This formulation is different from the formulation in existing active and passive suspension optimization literature, in which road random excitations are taken as disturbance inputs; and suspension velocity, suspension deflection, and tire deflection are included in the quadratic cost

function as proxies for comfort, suspension work-space and vehicle attitude, and road handling respectively for application of LQG/H2 optimization techniques. Inertial forces due to maneuvering inputs are never included as they cannot be expressed as a filtered white noise. Tire-deflection due to road noise is used as a proxy for handling, and the comfort-handling trade-off is addressed by changing the weighting in the cost function. Assigning of weights is arbitrary and is typically tuned to get the desirable results. Hrovat (1997) actually refers to the weighing parameter as a “tuning knob”, which is incorrect as tuning knobs should be associated with DPs, and not FRs. The application of these techniques in highlighting the handling-comfort trade-off are questionable, especially in a low-order system such as a quarter-car 2-DOF model, as we end up optimizing the weights instead of the suspension parameters K and B . Exclusion of inertial forces due to maneuvering inputs is not a reasonable assumption as that is the most important parameter that needs to be considered for handling.

Another motivation for variable stiffness is that the optimum stiffness changes with vehicle speed. Road noise is characterized by a certain power spectral density in terms of spatial frequency ν (Robson, 1975; Sharp, 1987). If the vehicle is driven at constant speed V , the temporal excitation frequency ω is related to the spatial frequency ν by $\omega=2\pi V\nu$. The power spectral density in terms of temporal frequency keeps changing with the speed of the vehicle and hence the optimum suspension parameters keep changing with speed. Several researchers have approached the problem of optimizing the suspension parameters to minimize the cost function that includes the requirements of ride comfort, road handling, vehicle attitude, and suspension workspace. Li and Kuo (2000) employ evolutionary algorithms to optimize a passive quarter-car suspension. Optimal/suboptimal suspension parameters as a function of vehicle speed to minimize the cost function have been presented for a quarter-car suspension by Coirriga et.al (1996) using a Simplex search method; for a half-car model by Lin and Zhang (1989) by minimizing the variance of the control force difference between the passive suspension and the LQG active suspension with full-state feedback; and for a full car model by Elbeheiry et.al (1996), and Zuo and Nayfeh (2004) by using decentralized LQG/H2 optimization (Results in Figure 3-4). A suspension with adaptive suspension parameters (damping and stiffness) provides the capability to get an optimum ride over the entire speed range by changing the suspension parameters as a function of speed according to a suitable algorithm. Adaptive suspension

parameters can also be changed based on maneuvering inputs such as steering, braking, or throttle changes.

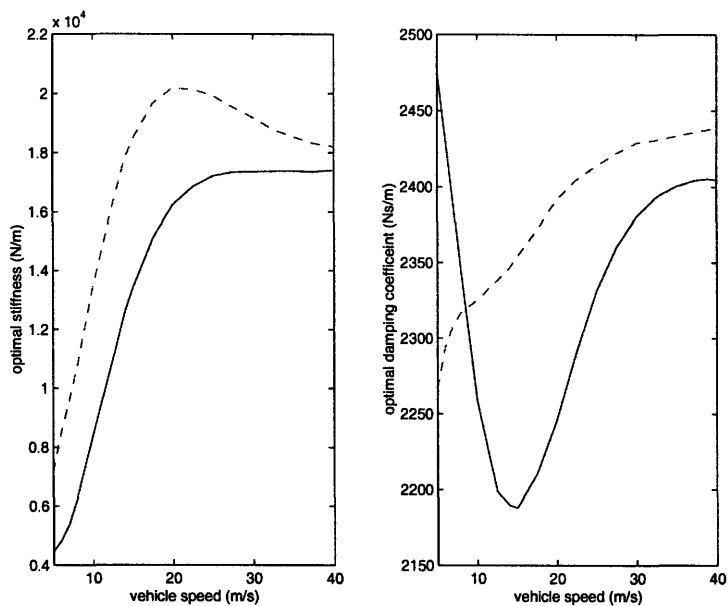


Figure 3-4: Optimal stiffness and damping (front and rear) as a function of vehicle speed (Zuo 2004)

3.2.2 Need for variable ride-height

Cars need high ground clearance on rough terrain and greater height for better vision; whereas a low center of gravity (CG) height is desired for swift cornering, dynamic stability at high speeds. A suspension capable of ride-height control can avoid this trade-off as the ride-height can be changed on the fly based on user input or automatically based on vehicle speed and maneuvering inputs.

Soft suspension is necessary for good high-frequency road-noise isolation (comfort). We cannot use an excessively soft suspension, because of the disadvantages of excessive unfavorable suspension travel redistribution between jounce and rebound under overload, excessive wheel attitude changes (leading to directional instability) and excessive vehicle attitude changes (leading to passenger discomfort and excess headlight beam swaying). Low frequency ride-height compensation can satisfy handling requirements such as low-frequency body and wheel attitude control, and also fix the unfavorable suspension travel redistribution. This allows the use of lower stiffness (as compared to a passive suspension) for better comfort without compromising on handling. This is an example of uncoupling the conflicting requirements of comfort and handling.

3.2.3 Prior art on variable stiffness and ride-height

Variable stiffness can be achieved through the use of a non-linear spring such as an air spring, the stiffness of which depends on the equilibrium pressure and volume of the working fluid. We can use the amount of air in the air spring as a DP to achieve variable stiffness. But this DP affects ride height as well, as shown in Equation (3.4). This leads to coupling as the number of FRs exceeds the number of DPs (Suh, 2001) and we cannot satisfy the two FRs of stiffness and ride-height independently. In practice, the DP: Amount of air is varied to get the desired ride-height, and the user has to live with the stiffness that results from it. To overcome this drawback, we have proposed a novel design for a customizable automotive suspension system with independent control of stiffness and ride-height, which is described below.

$$\left\{ \begin{array}{l} \text{FR1: Control Stiffness} \\ \text{FR2: Control Ride Height} \end{array} \right\} = \begin{bmatrix} X \\ X \end{bmatrix} \{ \text{DP: Amount of air} \} \quad (3.4)$$

3.3 Proposed design for customizable suspension

3.3.1 Concept development

The highest level functional requirements and constraints for a customizable automotive suspension are stated as follows:

Parent FR: Provide a customizable automotive suspension

FR1: Control stiffness

FR2: Control ride-height

FR3: Control damping

Constraint 1: Proposed customizable suspension design must be compatible with existing suspension kinematics.

Constraint 2: Since the size, weight, power requirements and cost of an actuator increase prohibitively with the bandwidth, the bandwidth of the actuators has to be lower than the wheel-hop frequency (8-10 Hz).

Suspension kinematics are designed for desired vehicle dynamics performance, which is often characterized by performance indices such as camber curve, caster curve, anti-pitch, anti-dive, understeer gradient etc. The vehicle dynamics performance is very sensitive to changes in

suspension kinematics. Hence it is accepted as a highest level constraint that the proposed modifications, that introduce customization, should not require any change in the existing suspension kinematics. In this chapter, we will design the customizable suspension for the SLA (short long arm) suspension architecture, which is the most widely used architecture for front-wheel independent suspensions. SLA suspension system can be kinematically represented as shown in Figure 3-5. This figure shows the front-view of the SLA suspension architecture with the spring and the wheel (shown in dotted line). The proposed modifications to achieve variable stiffness, variable ride-height and variable damping are shown in Figure 3-6 and are discussed below.

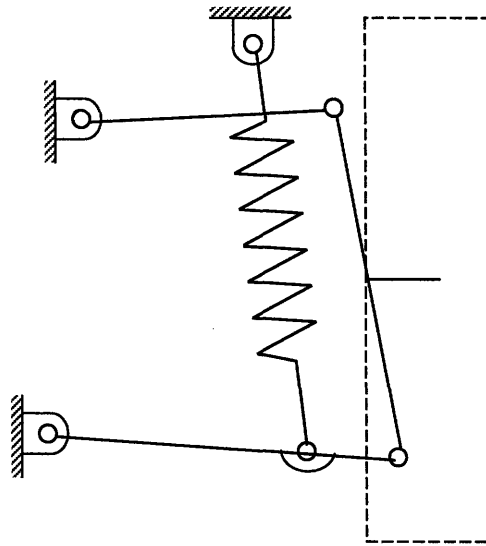


Figure 3-5: Kinematic representation of existing independent SLA suspension

FR1 Control stiffness: Variable stiffness can be achieved by making the lower spring pivot movable along the LCA (lower control arm). Change in the lower spring pivot position alters the effective stiffness seen at the wheel K_w by changing the relation between the wheel travel and spring deflection. The lower spring pivot can be driven by a linear stage, consisting of a stepper motor, a lead screw and a linear bearing as shown in Figure 3-6. The effective stiffness seen at the wheel K_w is related to the spring stiffness K_s and the lower spring pivot position DP1: l_s as given by Equation (3.5).

$$K_w = K_s \left(\frac{l_s}{L} \right)^2 \tag{3.5}$$

FR2 Control Ride-height: Variable ride-height can be achieved by making the upper spring pivot movable with respect to the vehicle frame in the vertical direction. There are several ways in which this can be done; a hydraulic actuator or a servo-motor is the most likely choice for actuating the motion of the upper pivot. Figure 3-6 shows one possible mechanism in which ride-height can be changed by moving the upper spring pivot by a motor driven cam. Movement of the upper pivot (lift of the cam) is used as DP2: U as depicted in the design matrix in Equation (3.6).

FR3 Control Damping: Variable damping is achieved by DP3: Orifice control, which is an established technology in existing vehicles. The damper (not shown in the figure for clarity) is connected between the vehicle frame and LCA, in parallel with the spring. Since FR3 is not affected by any other DP and DP3 doesn't affect any other FR, we will neglect this FR/DP pair in the subsequent analysis for simplicity. Damping control can also be achieved by employing electro or magneto-rheological fluids instead of simple orifice control (Pinkos et. al., 1994; Sturk et. al., 1995).

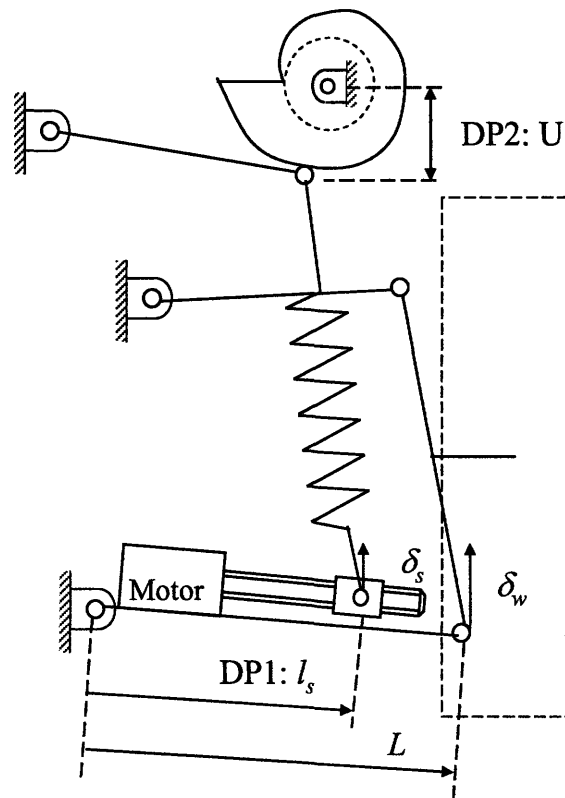


Figure 3-6: Proposed modification to achieve independent control of stiffness, damping and ride-height

The design matrix in Equation (3.6) shows that the design is decoupled with respect to the FRs of stiffness and handling.

$$\begin{Bmatrix} \text{FR1: Control Stiffness} \\ \text{FR2: Control Ride-height} \\ \text{FR3: Control Damping} \end{Bmatrix} = \begin{bmatrix} \text{X} & \text{O} & \text{O} \\ \text{X} & \text{X} & \text{O} \\ \text{O} & \text{O} & \text{X} \end{bmatrix} \begin{Bmatrix} \text{DP1: Pivot position } l_s \\ \text{DP2: Cam position U} \\ \text{DP3: Orifice control} \end{Bmatrix} \quad (3.6)$$

3.3.2 Prototype design and development

A 1:1 scale half-car 2-DOF model prototype was designed and built to demonstrate the capabilities of variable stiffness, variable ride-height, and wheel and vehicle attitude control. The suspension kinematics, with SLA architecture, were adopted from an existing vehicle and as per constraint 1, the modifications in the prototype did not change the kinematics.

Several arrangements of linear/rotary bearings and various choices of actuators were considered. For the prototype, we used the kinematics depicted in Figure 3-6. For changing stiffness, the prototype employs a linear stage on the LCA (lower control arm). The lower spring pivot is pivoted to a carriage supported on a linear bearing. A stepper motor driven acme lead screw is used to move the carriage to avoid back-drivability.

The upper pivot is moved by a cam, driven by a stepper motor through a planetary gearhead and a bearing. The upper spring pivot is constrained by the top-arm to follow an arc with the length of the top-arm as the radius. Since the length of the top-arm is significantly greater than the length of travel of the upper pivot, the motion of the upper pivot is very close to a straight line. This arrangement achieves an almost linear motion of the upper pivot without the use of expensive and bulky linear bearings. (A servo motor or a hydraulic actuator is the most likely to be used for ride-height change in an actual system instead of the stepper motor which was used in the prototype for low cost). A roller cam-follower is used to reduce friction and this reduced the required torque by 33%.

The upper and lower spring seats in existing conventional suspension systems are fixed to the chassis and the LCA respectively. The spring seats for the proposed customizable suspension need to have an additional degree to allow for the lower spring pivot motion. The lower spring seat has to be pivoted to the carriage on the linear drive, and the upper spring seat has to be pivoted to the top arm as shown in Figure 3-6. A picture of the actual prototype is shown in

Figure 3-6. Two encoders provide feedback for ride-height control. The first encoder measures the rotation of the motor that drives the cam. The second encoder is mounted to the upper control arm (UCA) to measure the suspension deflection or ride-height.

Controls execution was done using the NI-Motion module in National Instruments™-LabVIEW software. NI PCI-7344 4-axis controller board was used for controlling the four stepper motors for control of stiffness and ride-height for the right and left suspensions of the half-car prototype.

The prototype is capable of ride-height changes up to 5 in. The range of stiffness change can be quantified by the range of natural frequencies attainable by the stiffness change, The prototype demonstrated a change in natural frequencies in the range 1-1.5 Hz which is significantly greater than the range of natural frequencies encountered in passenger cars (Natural frequencies for Luxury cars are around 1.1 Hz and sports/performance cars are around 1.3-1.5 Hz). We conclude this section with the remark that the proposed design provides independent control and the desired range of stiffness and ride-height.

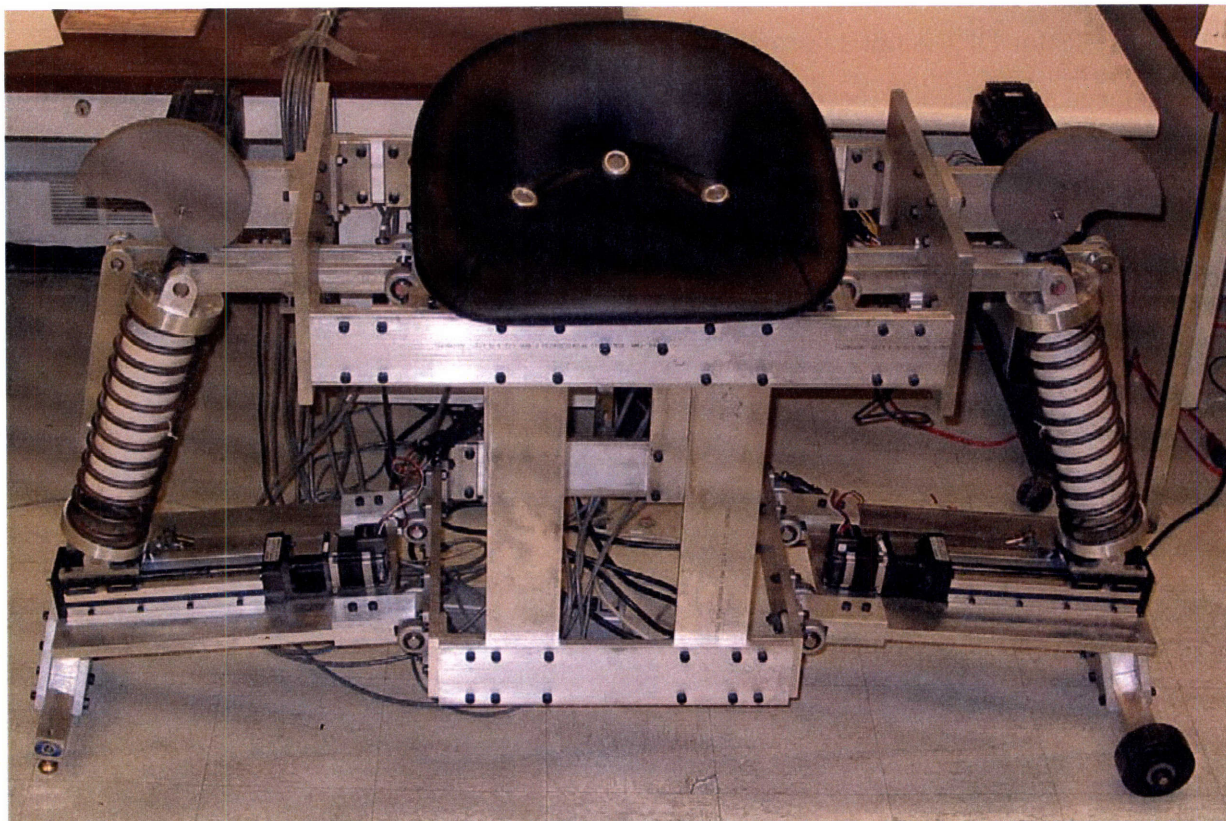


Figure 3-7: Photograph of customizable suspension prototype (front view)

3.4 Control system design

3.4.1 Stiffness control

FR1: Control Stiffness is not affected by any noise factor; hence we can use open loop control of stiffness. Equation (3.7) is used to calculate the required position of the lower pivot (DP1: l_s) from the desired value of FR1: Stiffness K_w , and the controller directs the stepper motor to position the lower spring pivot as required. The desired value of FR1: Stiffness could be input by the user depending on the desired ride (say comfort mode or sporty mode). Alternatively, depending on speed of the vehicle, the road conditions and maneuvering inputs, the stiffness could be automatically set to the optimum value according to a suitable algorithm. More details on stiffness scheduling will be discussed later in this thesis.

3.4.2 Ride-height control

FR2: Ride-height depends not only on the cam position U (DP2), but also on stiffness (hence on DP1), and load on the vehicle (noise factor, which will be denoted subsequently as DP_{nf}). Note that the noise factor DP_{nf} is not a normal design parameter that the user can set to satisfy the FR. It is introduced in the design equation to indicate effect of the noise factor (DP_{nf}) on the FRs (Melvin 2003). To study the effect of the DPs on FR2: Ride-height, the system is modeled as a quarter-car single degree of freedom model as shown in Figure 3-7. The actuator (motor driven cam in this case) is modeled as a low bandwidth displacement provider. The actuator provides displacement U (DP2) in series with the spring. The response of the sprung mass x_s to the road disturbance x_r , the actuator input U , and the force F acting on the sprung mass is given by the equation of motion:

$$M\ddot{x}_s + B\dot{x}_s + K_w x_s = B\dot{x}_r + K_w x_r + K_w U + F \quad (3.7)$$

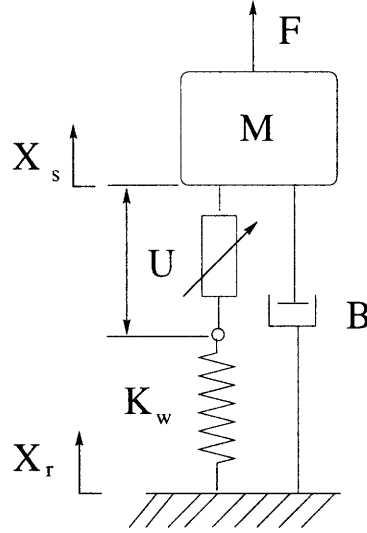


Figure 3-8: Modeling of the system as a quarter car single DOF model for feedback control of ride-height
 From Equation (3.7), we get the following three transfer functions of interest as shown in Equation (3.8), relating road disturbance x_r , actuator input U and force F to the chassis displacement x_s .

$$X_s = \left(\frac{Bs + K_w}{Ms^2 + Bs + K_w} \right) \cdot X_r + \left(\frac{K_w}{Ms^2 + Bs + K_w} \right) \cdot U + \left(\frac{1}{Ms^2 + Bs + K_w} \right) \cdot F \quad (3.8)$$

From these transfer functions, we can construct the block diagram indicating the effect of road disturbance x_r , actuator input U and force F on the chassis displacement x_s , as shown in Figure 3-9 and the design matrix as given by Equation (3.9).

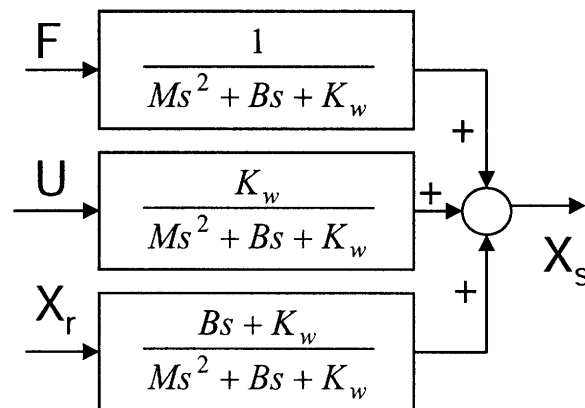


Figure 3-9: Block diagram representation of the proposed system

$$\left\{ \begin{array}{l} \text{FR1: Control Stiffness} \\ \text{FR2: Control Ride-height} \end{array} \right\} = \begin{bmatrix} \text{O} & \text{A} & \text{O} \\ \text{D} & \text{C} & \text{B} \end{bmatrix} \left\{ \begin{array}{l} \text{DP}_{\text{nf}}: \text{Load } F \\ \text{DP1: Pivot position } l_s \\ \text{DP2: Cam position } U \end{array} \right\} \quad (3.9)$$

The design matrix in Equation (3.9) shows that this is a decoupled system (due to off-diagonal term C) and FR2: Ride-height is affected by noise factor DP_{nf}: Load on the vehicle (as shown by term D). As a result, any change in DP1: Stiffness setting or DP_{nf}: Load necessitates a change in DP2 by the user to maintain ride-height at the desired value. To achieve insensitivity to stiffness change and load change, a feedback control system for ride-height was designed as depicted in Figure 3-10. Since the system is decoupled and we set the DPs in an appropriate order (set stiffness followed by ride-height), we can treat ride-height control as a single-input single-output (SISO) system. This enables the use of classical control techniques, where DP2: U is treated as an input to the plant and K_w and F are treated as noise factors.

The feedback control system consists of a minor loop and a major loop. The minor loop is a motor position control loop, which comprises of the actuator dynamics (modeled as a servo-motor and cam in this case) and the PID controller of the motor, with unity feedback. The minor loop (actuator) accepts the desired value for DP2: U_{des} as input and provides a displacement U in series with the spring. The major loop is the ride-height control loop, which comprises of the plant, the minor loop (actuator) and the controller block. In the major loop, the actual ride-height $(X_s - X_r)_{actual}$ is measured and compared with the desired ride-height $(X_s - X_r)_{desired}$. An encoder connected to the suspension UCA (upper control arm) gives a measurement for $(X_s - X_r)_{actual}$. The controller determines the desired value for DP2: U_{des} according to a control law based on the difference between the actual and desired ride-height values. The controller in the customizable suspension prototype is a PI controller in series with a low pass filter, which are described below.

The plant and the actuator are type-0 systems. A PI controller is used to make it a type-1 system and ensure zero steady state error for a step input.

Suspension motion has two components; the first component is a low frequency component caused by the static load or other low frequency inertial forces acting on the vehicle, and the second component is a high frequency component caused by high frequency road noise. According to the control strategy, we intend to isolate the high frequency road noise passively

and use the actuator and control loop to counter the suspension deflection due to low frequency load changes and inertial forces. To filter out the high frequency component of the actual ride-height change: $(X_s - X_r)_{actual}$ caused due to road-noise, we use a 2nd order low-pass filter with cut-off frequency a . The cut-off frequency a is designed such that the actuator signal U_{des} is not affected by the high-frequency road noise.

After the introduction of the feedback control loop, the resultant system accepts ride-height command $(X_s - X_r)_{desired}$ as an input from the user and sets FR2: Ride-height to that value. Hence we use the ride-height command $(X_s - X_r)_{desired}$ as DP_{user2}. The design matrix of the resultant system, given by Equation (3.10), shows that introduction of the feedback control system converts the decoupled system to an uncoupled system. Note that we have used different DPs in Equation (3.9) and Equation (3.10). In Equation (3.9), cam position U is used as DP2, whereas in Equation (3.10), ride-height command $(X_s - X_r)_{desired}$ is used as DP_{user2}. DP_{user2} is an operational design parameter that the user sets to satisfy the FR and in this example, DP2 is used as an intermediate DP (Deo & Suh, 2004). The advantage of this formulation is that, with minimal hardware change, the physically decoupled system (Equation (3.9)) has been converted to a system (Equation (3.10)) that the user sees as uncoupled during the operation of the system! Also Equation (3.10) shows that ride-height is independent of the load on the vehicle and hence this transform has also achieved robustness to a noise factor. Also the imaginary complexity is eliminated as the system appears uncoupled to the user during operation.

$$\left\{ \begin{array}{l} \text{FR1:Control Stiffness} \\ \text{FR2:Control Ride-height} \end{array} \right\} = \begin{bmatrix} \text{O} & \text{A} & \text{O} \\ \text{O} & \text{O} & 1 \end{bmatrix} \left\{ \begin{array}{l} \text{DP}_{\text{nf}}: \text{Load } F \\ \text{DP}_{\text{user1}}: \text{Pivot position } l_s \\ \text{DP}_{\text{user2}}: \text{Desired Ride-height } (X_s - X_r)_{desired} \end{array} \right\} \quad (3.10)$$

This example illustrates the utility of axiomatic design theory as a tool for innovation. The existing suspensions with air springs have less number of DPs than FRs as illustrated in Equation (3.4), and hence it is impossible to satisfy the two FRs independently. By following axiomatic design principles, we were able to achieve a novel decoupled design as illustrated in Equation (3.9). This design requires compensation for ride-height whenever stiffness or load on the vehicle changes. By designing a feedback control system, we have converted the decoupled design to an uncoupled design and also achieved robustness to noise factor load as shown in Equation (3.10).

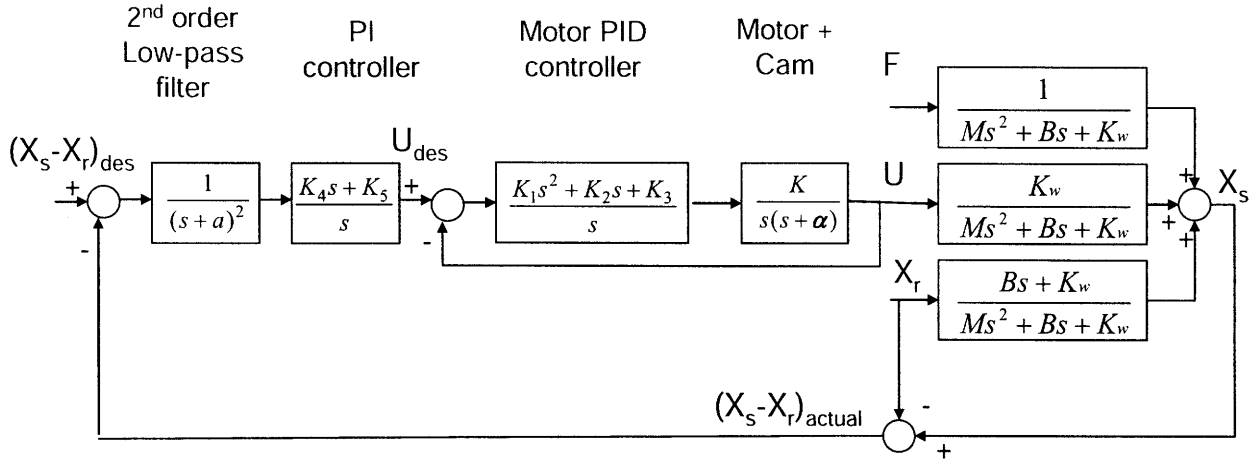


Figure 3-10: Ride-height feedback control

3.5 Limitations: Motivation for instantaneous stiffness change

The proposed design is capable of achieving independent control of stiffness, damping and ride-height, but it has the following drawbacks:

Use of a linear stage on the lower control arm to achieve the stiffness change presents cost and robustness issues, especially because the linear stage may have to operate in a harsh environment.

Linear stages capable of supporting the weight of the car will be bulky and the increased unsprung mass leads to deteriorated dynamic performance.

This system is not capable of rapid stiffness change. This is because moving the lower spring pivot involves energy input to the motor. Rapid stiffness change will require large power input and high-torque producing motor, which will add to the unsprung mass. Application of a variable stiffness suspension system to improved vehicle dynamics is discussed in Chapter 5. It is observed that rapid stiffness change capability is highly desirable as it can significantly improve the vehicle dynamics by responding to vehicle speed, maneuvering inputs, and changes in road conditions.

The design matrix in Equation (3.6) shows that stiffness change affects ride-height change. Although this change in ride-height can be compensated for by changing DP2: U , the ride-height compensation requires power input and involves a time-delay. Thus the decoupled design matrix structure shown in Equation (3.11) is another reason why instantaneous/rapid stiffness change is not possible.

$$\left\{ \begin{array}{l} \text{FR1: Control Stiffness} \\ \text{FR2: Control Ride-height} \end{array} \right\} = \begin{bmatrix} X & O \\ X & X \end{bmatrix} \left\{ \begin{array}{l} \text{DP1} \\ \text{DP2} \end{array} \right\} \text{ (Existing Design)} \quad (3.11)$$

It is desirable to come up with an uncoupled design as shown in Equation (3.12). If it is not possible to come up with an uncoupled design, a decoupled design in the design matrix structure as shown in Equation (3.13) is preferred over the existing design matrix structure as shown in Equation (3.11).

$$\left\{ \begin{array}{l} \text{FR1: Control Stiffness} \\ \text{FR2: Control Ride-height} \end{array} \right\} = \begin{bmatrix} X & O \\ O & X \end{bmatrix} \left\{ \begin{array}{l} \text{DP1A} \\ \text{DP2A} \end{array} \right\} \text{ (Ideal Design)} \quad (3.12)$$

$$\left\{ \begin{array}{l} \text{FR1: Control Stiffness} \\ \text{FR2: Control Ride-height} \end{array} \right\} = \begin{bmatrix} X & X \\ O & X \end{bmatrix} \left\{ \begin{array}{l} \text{DP1 B} \\ \text{DP2 B} \end{array} \right\} \text{ (Preferred over Existing Design)} \quad (3.13)$$

To eliminate these drawbacks, we have investigated the possibility of coming up with a design capable of instantaneous stiffness change with no ride-height change as indicated by Equation (3.12) or Equation (3.13). We have looked into the design of pneumatic and hydro-pneumatic springs to achieve independent control of stiffness and ride-height, and preferably an instantaneous change in stiffness. This is described in greater detail in Chapter 4.

3.6 Summary

Advantages of a customizable suspension have long been known, but no system with independent control of stiffness and ride-height has so far been proposed. In this chapter, a novel suspension system with independent control of stiffness, damping and ride-height is proposed. The use of axiomatic design theory in the concept development and design and fabrication of the prototype is discussed. This example illustrates the use of axiomatic design theory as a tool for innovation.

A method is proposed to uncouple a decoupled or coupled design and also to achieve robustness to noise factors, by superimposing it with a feedback control system. The mechanical design of the customizable suspension prototype is decoupled with respect to the FRs of ride-height and stiffness; moreover ride-height is affected by load (noise factor). Through the design and implementation of a feedback control system, insensitivity to stiffness change and load change is demonstrated.

Motivation for instantaneous stiffness change capability is provided and it is noted that of the two decoupled designs possible, one design matrix structure is preferable over the other.

Chapter 4:

Design, Modeling and Fabrication of a Customizable Pneumatic Suspension System

In the previous chapter we proposed an electromechanical suspension system capable of independent control of stiffness, damping and ride-height. The electromechanical system was designed for slow stiffness change to satisfy the constraint of low power requirement. But the application of a variable stiffness suspension to improved vehicle dynamics requires the stiffness change to be instantaneous and without any resulting change in ride-height due to stiffness change. This is not possible for the electromechanical system proposed in the previous chapter. In this chapter, we investigate the possibility of using pneumatic and hydro-pneumatic suspension systems to create a customizable automotive suspension with independent control of stiffness, damping and ride-height. Ideally this suspension system would be capable of instantaneous stiffness change, with limited or no power input and no effect on ride-height change as described in the design matrix in Equation (3.13). We begin with preliminary modeling of pneumatic springs and attempt to identify suitable DPs to achieve independent control of stiffness and ride-height. Based on this modeling and the FR-DP decomposition, we propose several designs to achieve these FRs and discuss their advantages and disadvantages. One of the proposed designs employs auxiliary volumes connected to the air-spring volume through On-Off valves for changing the stiffness of the system. This system is capable of instantaneous stiffness change with no power input, and no ride-height change resulting from stiffness change. Moreover this design is robust, light-weight and low-cost, which makes it applicable to generic vibration isolation systems with conflicting or time-varying stiffness requirements. A detailed model of this design has been developed and the variable stiffness

suspension system has been incorporated in a car. In this chapter, modeling, design, fabrication and testing of this system is discussed. Based on this modeling and test results, the performance limitations and practical applicability of this design is outlined.

4.1 Basic cylinder and piston air-spring:

An air-spring is essentially a volume of gas enclosed in cylinder with a movable piston connected to the load as shown in Figure 4-1. Neglecting the sliding friction, the load supported by this air-spring is given by Equation (4.1).

$$F = (P - P_a) A_p \tag{4.1}$$

where A_p is the area of the plate, P is the absolute pressure of air in the air-spring and P_a is the atmospheric pressure. The air-spring is a non-linear spring and its stiffness depends on the load, deflection as well as the frequency of oscillations. The frequency dependence is characterized by adiabatic stiffness, isothermal stiffness and polytropic stiffness as discussed next.

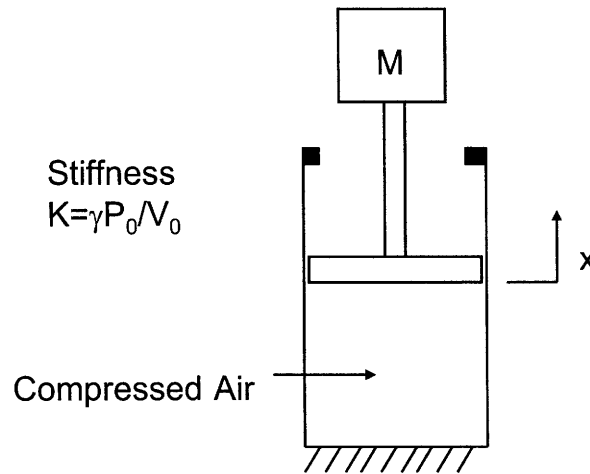


Figure 4-1 Basic Piston and Cylinder type Air Spring

4.1.1 Adiabatic stiffness

For rapid oscillations, there is negligible heat-transfer between the air and the atmosphere during the compression and expansion. The stiffness of an air spring for rapid oscillations (frequency > 2Hz) can be derived by assuming adiabatic compression and expansion of air at pressure P and temperature T , contained in a variable volume V . The adiabatic compression and expansion of air is governed by Equation (4.2), where P_0 , T_0 , and V_0 are the equilibrium values of pressure, temperature and volume respectively and $\gamma = C_p / C_v =$ Heat Capacity Ratio of air.

$$PV^\gamma = P_0V_0^\gamma \quad (4.2)$$

The spring constant is proportional to the rate of change of pressure with volume and is given by Equation (4.3). Here we use the fact that $dF=dP.A_p$ and $A_p.dx=dV$.

$$K = -\frac{dF}{dx} = A_p^2 \frac{dP}{dV} = \gamma A_p^2 \frac{P_0V_0^\gamma}{V^{\gamma+1}} \quad (4.3)$$

The air-springs are non-linear as manifest by the term $V^{\gamma+1}$ in Equation (4.3). It hardens on compression and softens on extension. For small deflections around the operating point (volume V_0), the nominal adiabatic stiffness K_{ad} is given by:

$$K_{ad} = -\left. \frac{dF}{dx} \right|_{V=V_0} = \gamma \frac{P_0 A^2}{V_0} \quad (4.4)$$

4.1.2 Isothermal stiffness

The modeling of compression and expansion of air in the air spring as adiabatic compression and expansion is a reasonable assumption for high frequency oscillations. But for low frequency oscillations, the compression and expansion processes are slow enough to allow complete heat-transfer (thermal equalization). Isothermal compression and expansion as described by Equation (4.5) is a more reasonable model for this process.

$$PV = P_0V_0 \quad (4.5)$$

The non-linearity of the air-spring can be seen from the stiffness relation in Equation (4.6). The nominal isothermal stiffness K_{iso} is smaller by a factor γ than the nominal adiabatic stiffness K_{ad} .

$$K = -\frac{dF}{dx} = A^2 \frac{dP}{dV} = A^2 \frac{P_0V_0}{V^2} \quad (4.6)$$

$$K_{iso} = -\left. \frac{dF}{dx} \right|_{V=V_0} = \frac{P_0 A^2}{V_0} \quad (4.7)$$

4.1.3 Polytropic stiffness

In the frequency range where the process cannot be modeled as either isothermal or adiabatic, the polytropic spring rate is used with κ instead of γ , where κ is a number between 1 and γ .

$$K_{poly} = -\left. \frac{dF}{dx} \right|_{V=V_0} = \kappa \frac{P_0 A^2}{V_0} \quad (4.8)$$

A more accurate model that describes the change from isothermal stiffness at low frequencies to adiabatic stiffness at higher frequencies has been determined experimentally (Kornhauser & Smith, 1993; Kornhauser, 1994). In the intermediate frequency range, the air-spring provides damping as the pressure change leads the volume change. The proposed model and the corresponding frequency response are shown in Figure 4-2.

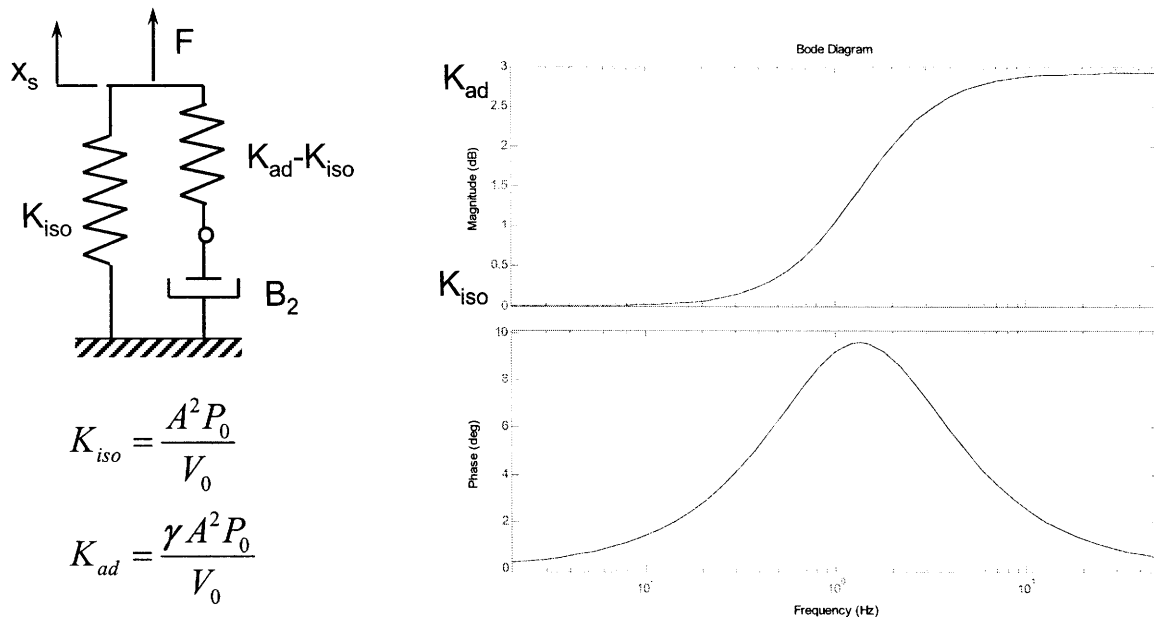


Figure 4-2 : Model to illustrate frequency-dependant stiffness of the air spring

The frequency range in which the spring stiffness changes from isothermal stiffness to adiabatic stiffness depends on the heat transfer coefficient, and can be changed by suitable design of the cylinder wall material and thickness. Moreover, the adiabatic stiffness can be reduced by introducing a heat sink, such as fine polyester fibers, in the air spring (Anderson, 1967; SAE, 1996). This is because the γ for the polyester fiber and air combination is lower than the γ for air. In the subsequent sections we will use adiabatic stiffness K_{ad} , as we are more interested in the high frequency behavior of the air-spring in road-noise isolation.

4.2 Proposed modifications to achieve independent control of stiffness and ride-height

Based on this preliminary model, several different strategies using hydro-pneumatic suspension systems are proposed in this section, along with their modeling, implementation, advantages and disadvantages.

From Equation (4.3), we can see that nominal air-spring stiffness depends on the area of the piston, the operating pressure P_0 , the operating volume V_0 and the heat-capacity ratio γ . These are all potential Design Parameters (DPs) to vary stiffness K , and we will look at the possibility of using or modifying these to achieve independent control of stiffness and ride-height. For a piston and cylinder type air-spring, the area of the piston is fixed at the manufacturing stage, and the operating pressure P_0 depends on the load on the air-spring and hence cannot be controlled by the designer when the spring is in operation. The parameters that the designer can control are the operating volume V_0 and the heat-capacity ratio γ . We will investigate using these parameters as DPs for satisfying the two FRs according to the decoupled design matrix as shown in Equation (3.13).

In certain existing adaptive suspensions, air springs are employed to achieve variable stiffness and variable ride-height by pumping in additional air into (or out of) the air springs (Esmailzadeh, 1979, Chance, 1984). But this leads to coupling as the *DP: Amount of air* affects both *FR1: Control stiffness* and *FR2: Control ride-height*.

$$\left\{ \begin{array}{l} \text{FR1: Control Stiffness} \\ \text{FR2: Control Ride Height} \end{array} \right\} = \begin{bmatrix} \text{X} \\ \text{X} \end{bmatrix} \{ \text{DP: Amount of air } V_1 \} \quad (4.9)$$

Coupling due to insufficient number of DPs is a common mistake made by designers and Suh (2001) has proposed decoupling of such a coupled system by addition of new DPs to make the number of FRs and DPs equal (Theorem 2). We introduce additional DPs in this design through the following proposed modification.

- **Strategy 1:** The first strategy uses a pneumatic spring in which the operating fluid is a mixture of two gases with different specific heat ratios. The total amount of the two gases is used to control the ride-height, whereas their relative proportion (molar fraction) is used to change the effective heat-capacity ratio γ_{eff} , to control the stiffness as described by the design equation (4.10).

$$\left\{ \begin{array}{l} \text{FR1: Control Stiffness} \\ \text{FR2: Control Ride Height} \end{array} \right\} = \begin{bmatrix} X & O \\ X & X \end{bmatrix} \left\{ \begin{array}{l} \text{DP1: Effective heat-capacity ratio } \gamma_{eff} \\ \text{DP2: Total amount of gas } V_o \end{array} \right\} \quad (4.10)$$

The relation of the effective heat-capacity ratio γ_{eff} as a function of the molar fractions of the two gases is presented in Equation (4.11), where x_1 is the molar fraction of the gas 1 with molar heat capacity $C_{Vm,1}$.

$$\gamma_{effective} = \left(\frac{C_{Vm,effective} + R_m}{C_{Vm,effective}} \right) = \left(\frac{x_1 C_{Vm,1} + (1-x_1) C_{Vm,2} + R_m}{x_1 C_{Vm,1} + (1-x_1) C_{Vm,2}} \right) \quad (4.11)$$

The natural choices of gas for the operating fluid are air and CO₂, as they can be obtained from the atmosphere and engine exhaust respectively. But use of air and CO₂ restricts the achievable range of stiffness to $K_{max}/K_{min} = \gamma_{max}/\gamma_{min} = 1.47/1.33 = 1.12$. Moreover CO₂ obtained from the exhaust contains nitrogen (diatomic) and this reduces the range further. This range can be increased to $K_{max}/K_{min} = \gamma_{max}/\gamma_{min} = 1.66/1.33 = 1.25$ if we can use a monoatomic gas such as He, Ar, Ne or Xe and a polyatomic gas such as CO₂, but this requires storage of two gases at high pressure, and frequent refilling as they are mixed together and leaked when γ_{eff} has to be changed. This added cost may not outweigh the potential benefit. Moreover changing stiffness involves pumping gas into the air-spring, which requires energy input and is not instantaneous.

- **Strategy 2:** To overcome the problem of frequent refilling, the second strategy uses a pneumatic spring separated into two chambers by flexible membrane as shown in Figure 4-3, and each chamber is filled with a gas of different specific heat ratio. The total amount of the two gases is used to control the ride-height, whereas their relative proportion (ratio of individual equilibrium volumes V_{01} and V_{02} at ride-height) is used to change the effective heat-capacity ratio γ_{eff} , to control the stiffness. This overcomes the problems of refilling, but the problems of storage, limited range of stiffness change, and power input and time required for stiffness change are still present. Also stiffness change requires energy input and time. The relation of the effective heat-capacity ratio γ_{eff} as a function of the individual volumes V_{01} and V_{02} of the two gases is presented in Equation (4.12).

$$\gamma_{eff} = \left(\frac{\gamma_1 \gamma_2 (V_{01} + V_{02})}{\gamma_1 V_{02} + \gamma_2 V_{01}} \right) \quad V_0 = (V_{01} + V_{02}) \quad (4.12)$$

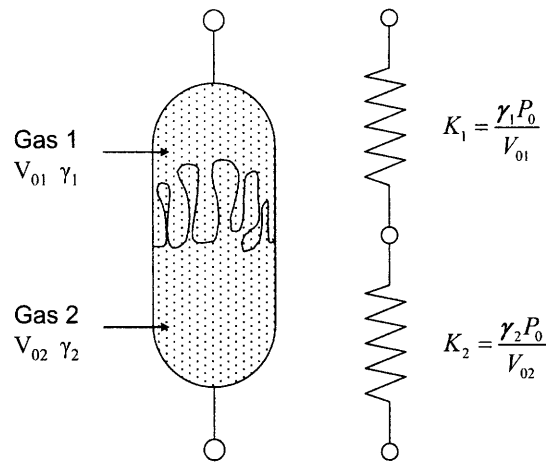


Figure 4-3 : Pneumatic spring separated into two chambers by flexible membrane and filled with two gases of different heat capacity ratios γ

- **Strategy 3:** The third strategy uses a pneumatic spring in series with a low frequency hydraulic actuator as indicated in Figure 4-4. The amount of working fluid (air) in the air-spring is used to control the stiffness; and the hydraulic actuator displacement is used to control the ride-height. This leads to a decoupled design matrix as given by the Equation (4.13).

$$\left\{ \begin{array}{l} \text{FR1: Control Stiffness} \\ \text{FR2 : Control Ride-height} \end{array} \right\} = \begin{bmatrix} X & O \\ X & X \end{bmatrix} \left\{ \begin{array}{l} \text{DP1: Total amount of gas } V_0 \\ \text{DP2 : Actuator displacement input } U \end{array} \right\} \quad (4.13)$$

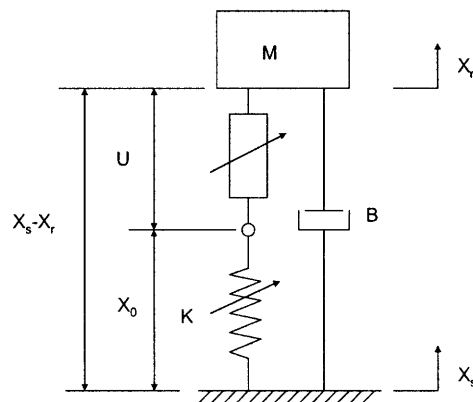


Figure 4-4 : Schematic of a hydro-pneumatic spring with a hydraulic actuator and pneumatic spring in series
This system requires one pneumatic circuit, including a compressor, for the air control and another hydraulic circuit, including a pump, for the hydraulic fluid control.

Moreover, stiffness change requires power input and affects ride-height, and as a result cannot be instantaneous.

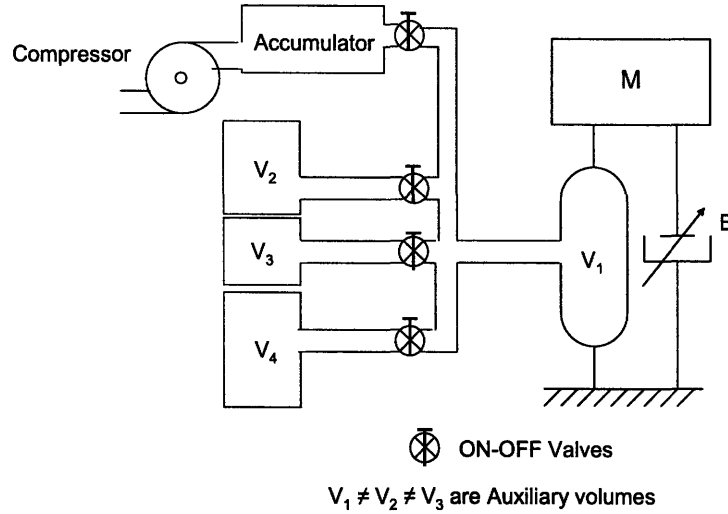


Figure 4-5 : Proposed design with auxiliary volumes connected to air spring through On-Off Valves

- **Strategy 4:** In the final proposed modification, we connect the air spring volume V_1 to additional (multiple) auxiliary volumes, shown by V_2 , V_3 and V_4 in the figure, through On-Off valves. When all three valves are closed, the effective volume is V_1 and the system has maximum stiffness, as given by Equation (4.14).

$$K_{\max} = \gamma A^2 \frac{P_0}{V_1} \quad (4.14)$$

When all three valves are open and all three auxiliary volumes are in communication with the air-spring volume, the effective volume is $(V_1 + V_2 + V_3 + V_4)$ and the effective stiffness is minimum, as given by Equation (4.15).

$$K_{\min} = \gamma A^2 \frac{P_0}{(V_1 + V_2 + V_3 + V_4)} \quad (4.15)$$

By adequately choosing non-equal volumes $V_2 \neq V_3 \neq V_4$, we can get $2^3=8$ stiffness settings between the minimum K_{\min} and maximum K_{\max} , by having different combinations of valves open and closed. In general, by adequately choosing N different volumes, $V_2 \neq V_3 \neq \dots \neq V_{N+1}$, we can get 2^N different stiffness settings. Note that all the volumes are at the same static pressure. As a result there is no change in pressure or ride-height, when

the valves are opened or closed to adjust the stiffness. Secondly, opening and closing of valves is effortless (involves no pumping effort) and instantaneous (time required is small as compared to the characteristic time-constant of the system). Ride-height control is achieved by using a compressor to pump in more air into the air-spring. Damping control is achieved through orifice control (Crosby & Karnopp, 1973; Karnopp, 1983) or by employing magneto-rheological fluid (Pinkos et al., 1994; Sturk et al., 1995) in the damper that is in parallel with the air-spring arrangement.

The decoupled design matrix is given in Equation (4.16).

$$\left\{ \begin{array}{l} \text{FR1: Control Stiffness} \\ \text{FR2: Control Ride Height} \\ \text{FR3: Control Damping} \end{array} \right\} = \begin{bmatrix} X & X & O \\ O & X & O \\ O & O & X \end{bmatrix} \left\{ \begin{array}{l} \text{DP1: Valve control } \left(\sum V_i \right) \\ \text{DP2: Compressor control } (V_1) \\ \text{DP3: Orifice control} \end{array} \right\} \quad (4.16)$$

Patent literature search revealed similar designs employing single auxiliary volume (Imani, 1993) and also multiple volumes (Svartz & White, 2005; Buma, 1988) connected to the air-spring through On-Off valves. The advantage of using multiple volumes over a single volume is obvious in terms of the number of stiffness settings possible. The prior art uses equal volumes for the auxiliary volumes and as a result they achieve N+1 stiffness settings for N auxiliary volumes. Our proposal to employ unequal volumes $V_2 \neq V_3 \neq \dots \neq V_{N+1}$, allows us to get 2^N different stiffness settings using N auxiliary volumes. This can help us reduce the number of volumes required and the associated hardware, which is critical considering the packaging constraints in automotive suspensions.

4.2.1 Advantages of the proposed design (Strategy 4)

- Instantaneous stiffness change through simple On-Off control of valves.
- No power input required for stiffness change (Valve opening and closing is considered effortless as the power requirement for that is orders of magnitude lower than pumping air into an air-spring).
- Change in stiffness causes no dimension-change of the isolator (no ride-height change). This dimension-invariance is especially important for vibration isolation, as any dimension change could act as a source of vibrations.

- Independent control of stiffness and ride-height is possible. The design matrix is decoupled with the stiffness change not affecting ride-height, which is the desired case as discussed in Equation (3.13).
- Additional hardware required is simple, inexpensive and reliable. It is possible to conveniently modify existing isolation systems to include these features.

Because of these advantages, we chose to implement this design in an actual automotive suspension system. In the subsequent sections, we discuss the implementation of this design, the detailed modeling required for accurate description of the system and the testing of the implemented design.

4.2.2 Other potential applications

The proposed vibration isolator can be used in generic vibration isolation stages with conflicting stiffness requirements or time-varying stiffness requirements. An example of conflicting and time-varying stiffness requirements is a precision motion stage for semiconductor metrology in which a stiff isolation system is required to isolate from the inertial forces during the rapid motion of the stage and a soft isolation system is desired for isolation from fab ground vibrations during the optical measurements. An example of time-varying stiffness requirements could be for isolation in prosthetic limbs, where the required stiffness changes with gait, walking style and speed, terrain and other factors.

Example application 1: Vibration isolation for precision motion stages

Consider a simplified planar representation of a precision motion stage (such as the ones typically used in semiconductor manufacturing and metrology) as shown in Figure 4-6. In this stage, the cradle of mass M is supported by the isolation system consisting of springs (with stiffness K_1 and K_2 as shown) and dampers (not shown in figure). The moving mass m carries the semiconductor wafer during its operation. There are typically two steps

1. *Move step*: The wafer is moved from one point to another
2. *Operate step*: This could be measure, expose, or process depending on the application.

For higher productivity, it is desirable to move the mass m as fast as possible during the *Move* step. This introduces significant inertial forces on the cradle, which act as a source of vibration

for the cradle. It is desirable to have high stiffness values for K_1 and K_2 to limit the vibration due to these inertial forces caused by rapid motion of the stage mass m .

During the *Operate* step, it is essential to minimize the vibration of the cradle and the stage due to fab-ground vibrations, and this requires low stiffness values for K_1 and K_2 .

The proposed system can be very conveniently applied to such applications with conflicting and time-varying stiffness requirements. The stiffness can be adjusted by adequate valve opening or closing, to have high stiffness during the *Move* step and low stiffness during the *Operate* step. Notice that all the three mentioned advantages of the proposed system, namely instantaneous stiffness change with no power input and no dimension change are critical for this application. The dimension-invariance is important because any dimension change in the isolator can act as a source of vibration for the cradle.

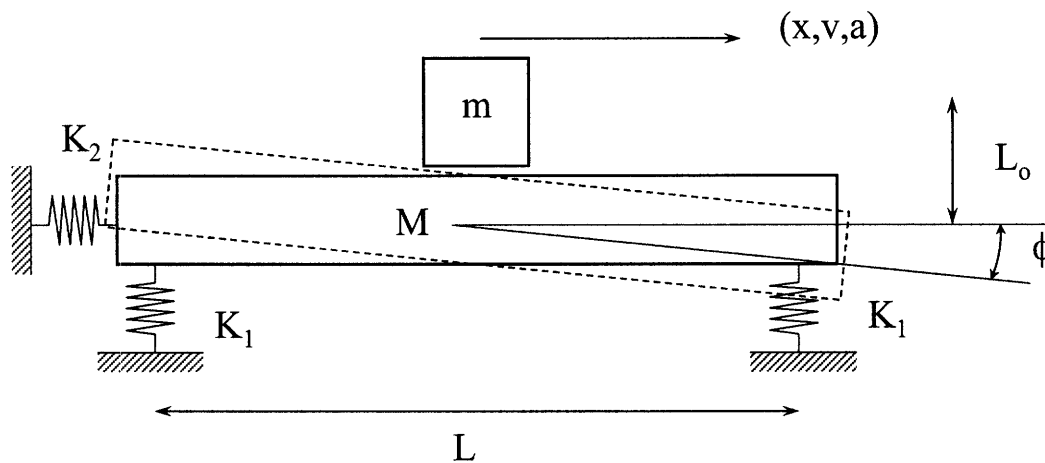


Figure 4-6 : Simplified planar representation of a precision motion stage consisting of cradle M , moving mass m , and a passive isolation stage consisting of springs (K_1 and K_2) and dampers (not shown).

Example application 2: Variable-stiffness prosthetic limbs

Shock absorbers are required for lower-limb prostheses to attenuate forces associated with walking and high-impact activities such as running and descending curbs and stairs. It is desirable to be able to adjust the stiffness of the vibration isolators depending on several factors including user preference, running speed (McMohan & Cheng, 1990), gait and pattern of walking (McMohan, 1985), surface conditions etc (Ferris et. al., 1998; Ferris & Farley, 1997; McMohan & Greene, 1979). Human and animal limbs exhibit variable stiffness depending on these factors. Current methods of achieving variable stiffness in prosthetic limbs use high

bandwidth actuators and are not acceptable in terms of weight, cost, energy requirements and control requirements. The proposed system can be conveniently applied to the design of prosthetic limbs, to achieve variable stiffness, in a convenient, reliable, energy-efficient, cost-effective, low-weight manner.

4.3 Reinforced flexible member springs construction

Cylinder and piston type air-springs are not in popular use because of the following disadvantages:

1. Sliding friction between the piston and cylinder surfaces cause significant hysteresis and lead to a higher and unpredictable effective stiffness, and jitter during operation
2. Significant leakage can occur past the piston and rod seals. The piston-cylinder arrangement is coupled with respect to the two functional requirements; FR_A : Provide sealing and FR_B : Eliminate friction.
3. The piston and rod guide present wear problems.

To overcome these problems, reinforced flexible member springs are used. The use of a reinforced flexible member in conjunction with rigid structures overcomes many of the deficiencies encountered with basic cylinder and piston springs. However, careful design is required to prevent high local stresses and severe fluctuations in stresses that could lead to reduced life. The flexible member carries only a portion of the developed spring force, with the remainder being transmitted to the rigid supporting members through the gas column.

The two main types of Reinforced flexible member springs are:

- Convoluted / Bellows Type
- Rolling Lobe Type / Reversible Sleeve Type

4.3.1 Convoluted/Bellows type air-spring

Convoluted/Bellows type pneumatic springs are commercially available in one, two or three convolutions. They are capable of providing natural frequencies in the range of 1-5 Hz. The two most common styles are crimped design and the sleeve design. The crimped design employs metal end retainers that are permanently attached by mechanically crimping the retainer around the built-in bead wire of the flexible member, as shown in Figure 4-7.

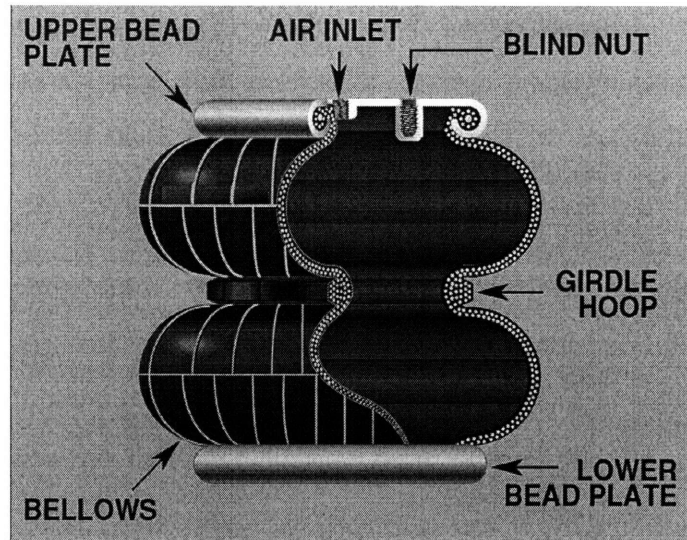


Figure 4-7 : Convoluted air-spring with crimped bead plates (Firestone 2005)

In certain bellows applications, bolted bead rings are used in place of permanently crimped on retainers (Figure 4-8). The upper and lower bead attachments are fixed with multiple bolts and an air-tight seal is achieved when all bolts are securely fastened through the bead ring into the mounting plate.

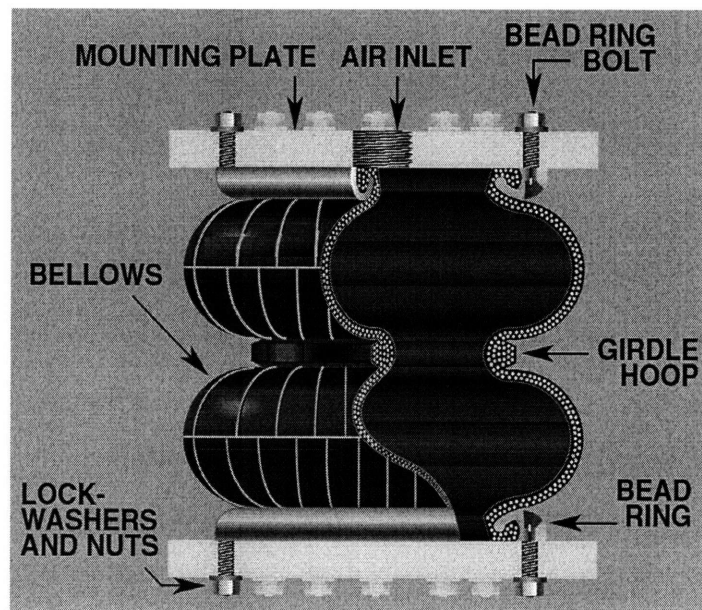


Figure 4-8 : Convoluted air-spring with bead rings (Firestone 2005)

Sleeve type convoluted pneumatic springs offer similar performance characteristics to the crimped design, but the flexible member is constructed without internally molded-in bead wires. The end retainers are commonly attached to the flexible member with an outer swage ring, and

the flexible member is compressed between the end retainer and swage ring by mechanically reducing the diameter of the swage ring.

4.3.2 Rolling lobe or reversible sleeve type air-spring

Rolling lobe pneumatic springs incorporate a piston which allows the flexible member to roll along the piston's surface as the force changes. The two most common types of rolling lobes are the built-in bead, as shown in Figure 4-9 and the beadless sleeve. Bolted bead rings are also available in this case. The upper bead attachments are affixed with multiple bolts and an air-tight seal is achieved when all bolts are securely fastened through the bead ring into the upper mounting plate.

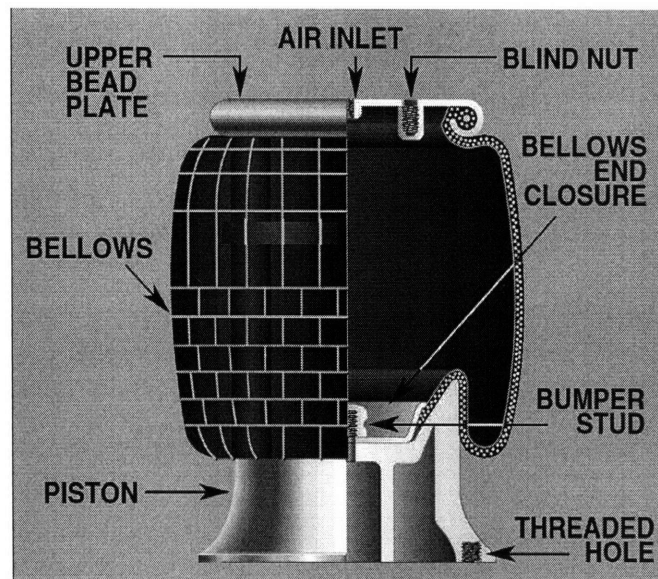


Figure 4-9 : Reversible Sleeve Air Spring with crimped bead plates (Firestone 2005)

Beadless sleeve

The beadless sleeve rolling lobe spring is constructed without internally molded-in beads. The end retainers are commonly attached to the flexible member with either inner or outer swage rings or a combination of both. The flexible member is compressed between the end retainer and the swage ring.

4.3.3 Modified stiffness due to the effect of air-spring membrane

The use of reinforced flexible membrane changes the stiffness relation from the one for a basic cylinder and piston type air spring. The flexible member carries a portion of the developed spring force, with the remainder being transmitted to the rigid supporting members through the gas

column. The force carried by the flexible member depends on air-spring geometry, type of air-spring (namely single convoluted, double convoluted, triple convoluted or reversed bellows), and the construction, stiffness and dimensions of the membrane. This force is difficult to compute analytically, but can be estimated conveniently by defining the effective area A_{eff} and using the following formulation.

The load supported by an air-spring is given as

$$F = (P - P_a) A_{eff} \quad (4.17)$$

where A_{eff} is an imaginary area over which the pressure is assumed to act and is defined as

$$A_{eff} = \frac{F}{(P - P_a)} \quad (4.18)$$

A_{eff} is a function of the spring deflection and the pressure, but is relatively insensitive to pressure and is approximated as a function of spring deflection only.

$$A_{eff} = A_{eff}(P, x) \approx A_{eff}(x) \quad (4.19)$$

Differentiating Equation (4.17) with respect to spring extension x , we can find the different contributions to air-spring stiffness as follows

$$\frac{dF}{dx} = (P - P_a) \frac{dA_{eff}}{dx} + \frac{dP}{dV} \frac{dV}{dx} A_{eff} \quad (4.20)$$

$$K = -\frac{dF}{dx} = K_A + K_T \quad (4.21)$$

where K_A is the first component of stiffness due to changing effective area as a function of spring deflection as defined by the relation

$$K_A = -(P - P_a) \frac{dA_{eff}}{dx} \quad (4.22)$$

and K_T is the thermodynamic component of stiffness as defined by the relation

$$K_T = -\frac{dP}{dV} \frac{dV}{dx} A_{eff} \quad (4.23)$$

K_A : The stiffness component due to changing effective area (or *area change stiffness*) depends on the air-spring geometry (type of air-spring, namely single convoluted, double convoluted, triple convoluted or reversed bellows; and also the construction, stiffness and dimensions of the membrane). Quaglia and Guala (2003), Frydrych et. al. (2004) and Prasil et. al. (2005) have proposed an analytical model for determination of effective area change as a function of spring deflection for a bellow spring by making some simplifying assumptions. The effective area is difficult to compute analytically, but can be estimated conveniently by conducting the following experiment. Air is leaked out of the air spring while it is supporting a constant load and the pressure P is plotted as a function of displacement x (or alternately lower control arm deflection θ) as shown in Figure 4-11. This graph is from the test conducted on the air spring incorporated in the customizable suspension prototype.

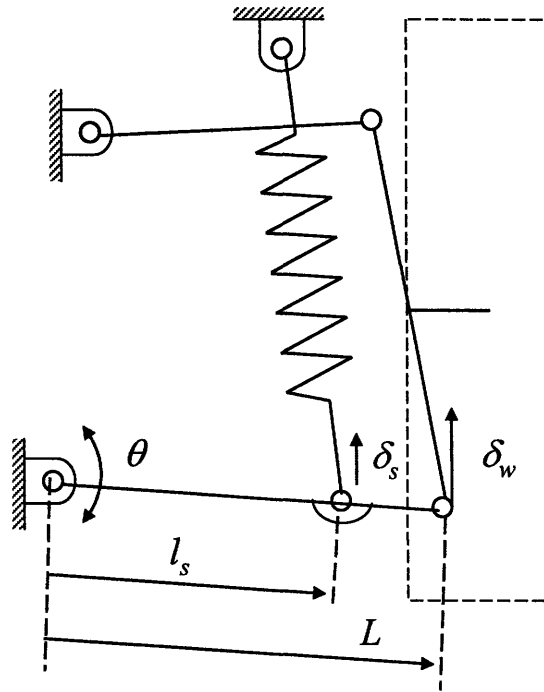


Figure 4-10 : Short Long Arm Suspension Geometry

The wheel deflection δ_w and spring deflection δ_s are related to the suspension lower control arm angular deflection θ , by the relations below.

$$\begin{aligned} \delta_s &= l_s \theta \\ \delta_w &= L \theta \end{aligned} \tag{4.24}$$

where l_s and L are the distances of the spring lower pivot and the steering axis pivot on the suspension lower control arm respectively from the inner pivot of the lower control arm where it is connected to the chassis. Moreover the relation between the force acting on the wheel and the force acting on the spring is given by Equation (4.25).

$$F_w = F_s \left(\frac{l_s}{L} \right) \quad (4.25)$$

A_{eff} can be computed from this graph by using the relation in Equation (4.24) and Equation (4.25) and the definition of A_{eff} (Equation (4.18)). The graph of effective area as a function of spring deflection for the front suspension is shown in Figure 4-12 and for the rear suspension is shown in Figure 4-13. Figure 4-12 shows that $dA_{eff}(x)/dx$ changes as a function of position for and is lowest at zero-deflection. This position corresponds to a static gauge pressure of $P_0 - P_a = 80\text{psi}$ to support the load of the car.

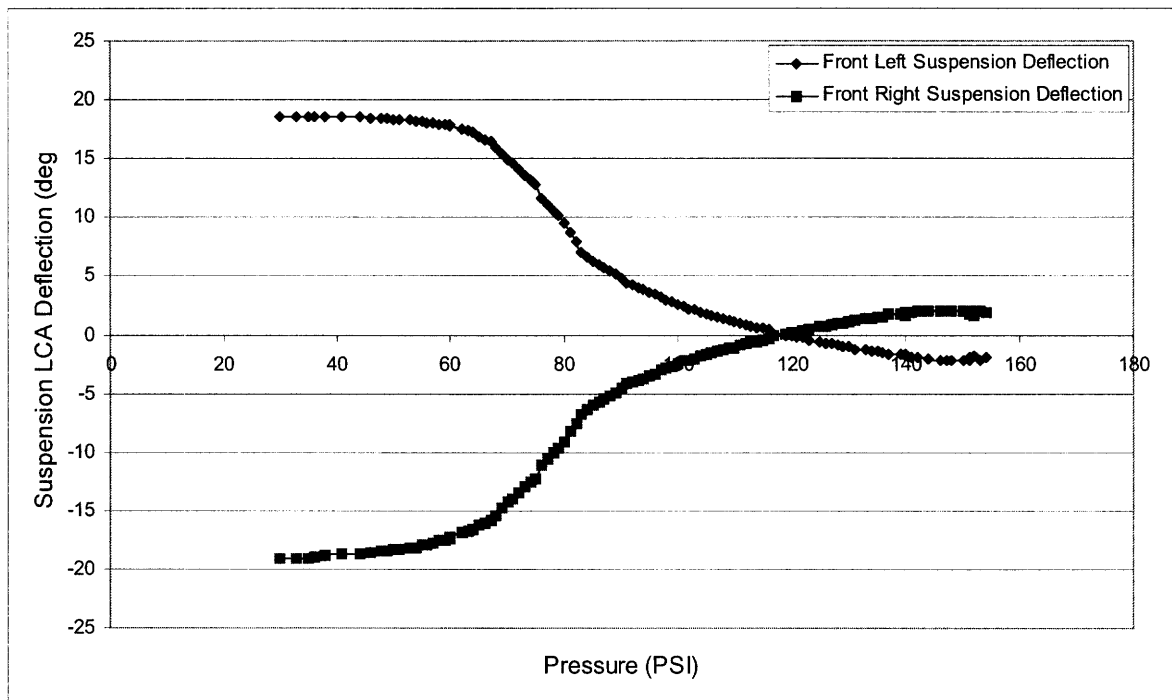


Figure 4-11 : Suspension Lower Control Arm deflection as a function of air spring pressure for constant load

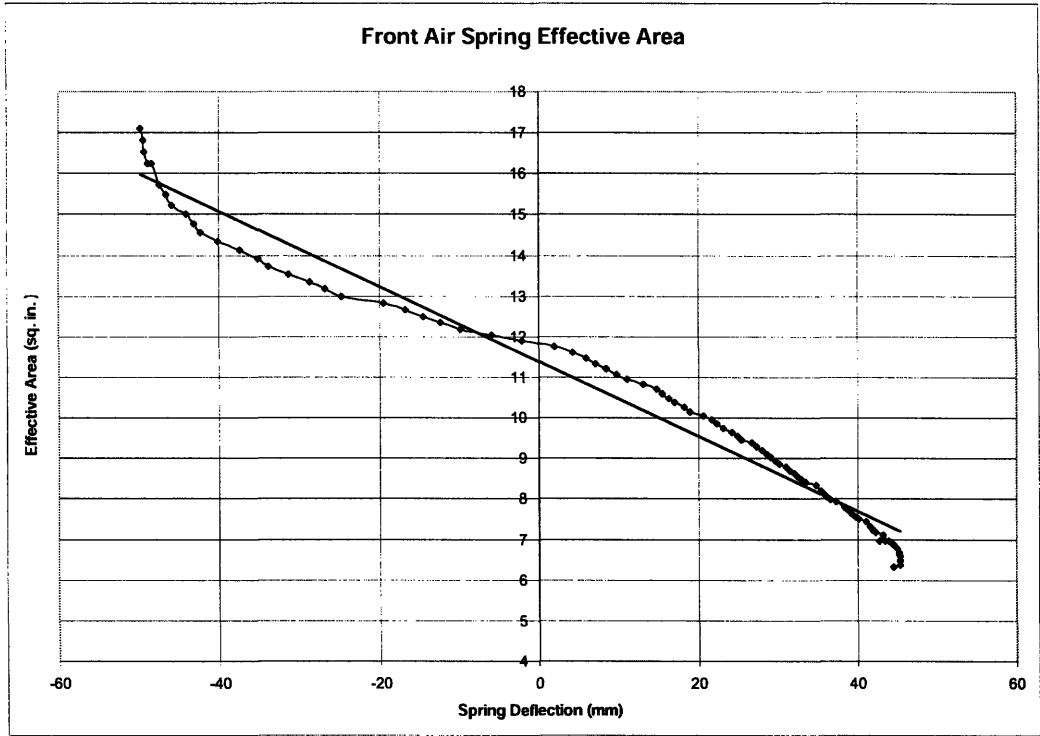


Figure 4-12 Effective Area for the front air-spring as a function of suspension deflection

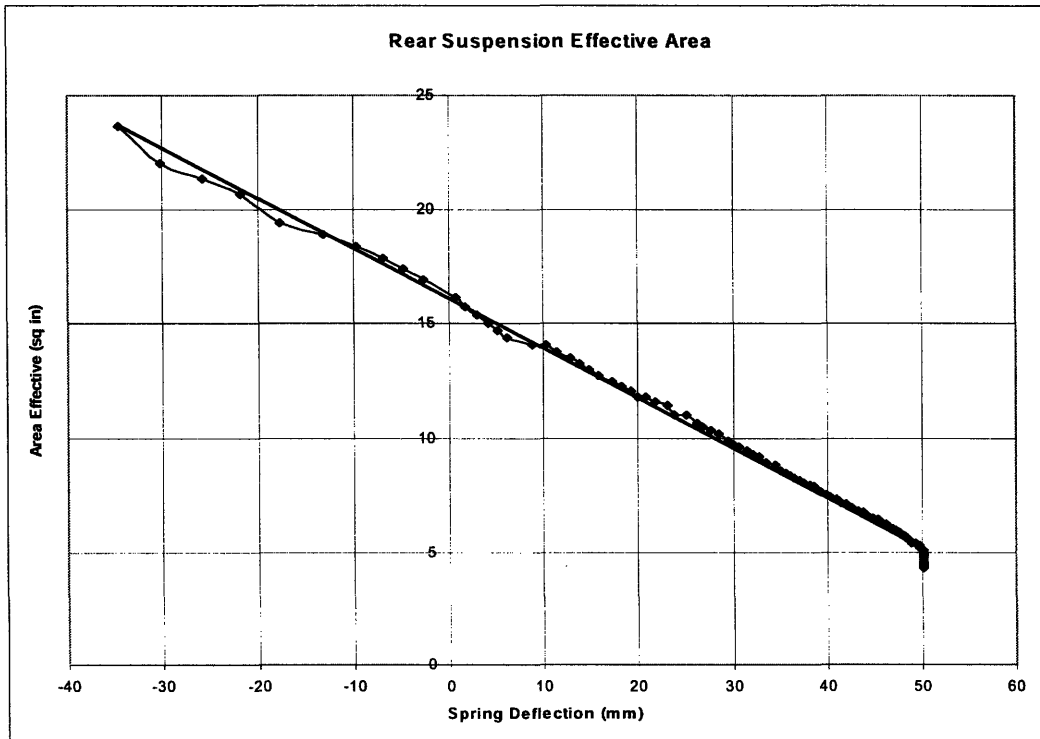


Figure 4-13 Effective Area for the rear air-spring as a function of suspension deflection

K_T : The thermodynamic component of stiffness (or *thermodynamic stiffness*) comes from compression and expansion of air enclosed in the air-chamber. For the first term on the right hand side of Equation (4.23), we will assume adiabatic expansion and compression of air and the nominal value around the operating point (volume V_0) is given by Equation (4.26).

$$\frac{dP}{dV} = -\gamma \frac{P_0}{V_0} \quad (4.26)$$

The second term $A_V = dV/dx$ is either provided by the manufacturer or can be determined experimentally. In the literature, it is usually assumed to be A_{eff} . The theoretical justification for this assumption can be found in the fact that the air spring effective area A_{eff} is relatively independent of the pressure and is a strong function of the ride-height. With this assumption, the air-spring behaves as a transformer in the bond-graph terminology. From the definitions of the two areas in Equation (4.18) and Equation (4.27), we can see that A_{eff} is the ratio of the efforts in the two domains and A_V is the ratio of the flows in the two domains and hence the two areas are equal.

$$A_V = \frac{\Delta dV}{dx} \quad (4.27)$$

$$A_V \approx A_{eff} \quad (4.28)$$

Thus the thermodynamic stiffness is given by:

$$K_T = \gamma \frac{P_0}{V_0} A_{eff}^2 \quad (4.29)$$

By suitable design of the air-spring, we can get a variety of profiles for the effective area $A_{eff}(x)$ and its rate of change with displacement $dA_{eff}(x)/dx$. This way, the area change stiffness K_A can be altered during the design phase of the air-spring. Contoured pistons can be used on rolling lobe type air springs to control the load-deflection characteristics by varying the effective area as illustrated in Figure 4-14 (SAE, 1996). Secondly since $dA_{eff}(x)/dx$ is a function of spring displacement x , stiffness K_A can be altered during operation by changing the spring deflection (or ride-height). This strategy has been employed in certain after-market suspension modifications (Tener, 2004). But this leads to coupling as both ride-height and stiffness have to be changed

simultaneously. Moreover stiffness change causes the ride-height to change, requires power input and is not instantaneous.

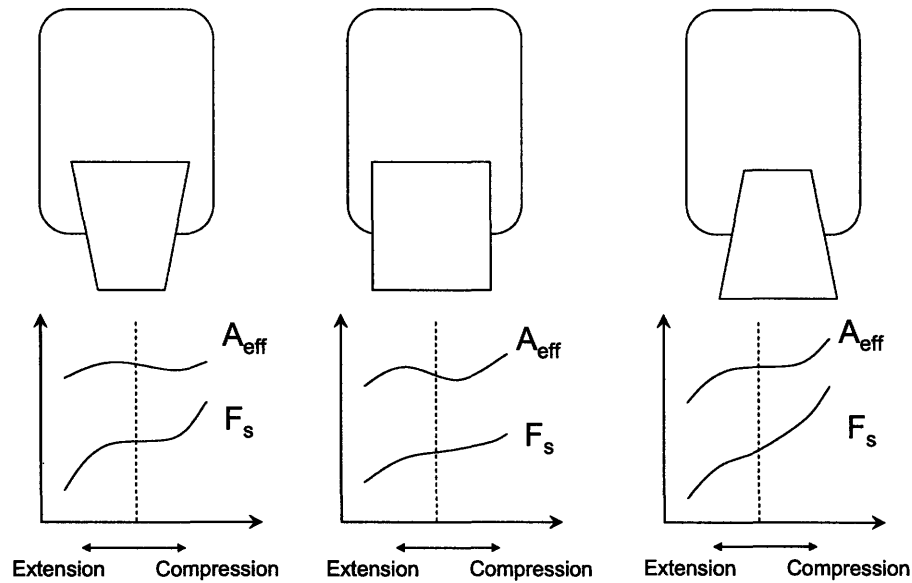


Figure 4-14 Use of contoured pistons on reversible sleeve air springs to control effective area

The second component of the stiffness K_T can be altered during the operation of the air-spring by changing the effective volume of the air spring, by opening and closing of valves connecting the air-spring volume to auxiliary volumes as shown in Figure 4-5.

4.4 Detailed Thermodynamic Model to determine the Frequency Response of an Air-Spring with auxiliary volumes

Consider the set-up in Figure 4-5 with only one auxiliary volume (instead of three) connected to the main volume through an On-Off valve. This can be schematically represented as shown in Figure 4-15. When the valve is closed, $B_2 = \infty$ resulting in stiffness $K = K_A + K_{high}$; and when the valve is open, $B_2 = 0$ resulting in stiffness $K = K_A + K_{low}$, where $K_{low} = K_1 K_2 / (K_1 + K_2)$ and $K_{high} = K_1$. B denotes the adjustable damper in parallel with the air spring.

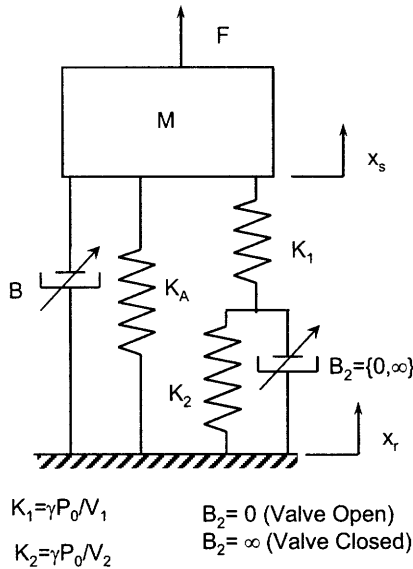


Figure 4-15 Schematic representation of the design intent (On-Off valve-control to vary stiffness)

Note that the model above assumes no pressure drop across the valve or inertial or viscous forces acting on the gas in the tubing when the valve is open. This assumption may be reasonable at low frequencies, but we need a better model to study the behavior of this suspension system at higher frequencies. In this section, thermodynamic modeling of an air spring with auxiliary volumes is presented.

1. Our original choice of DPs was solenoid valves for rapid opening and closing, and to mount the auxiliary volumes close to the air-springs to minimize the transport delay. The solenoid valves provide significant flow resistance and the pressure drop across them is likely to be significantly greater than the inertial and viscous forces on the air in the short pipes. In sub-section 4.4.1, the flow resistance of the valve is modeled. This flow resistance introduces damping in the suspension system, and as a result the suspension has low stiffness at low frequency and high stiffness at high frequency. Simulation of the linearized model of the air spring is used to determine the effect of this damping on the road-noise isolation.
2. In the actual prototype we used automated ball valves instead of solenoid valves. Packaging constraints required us to mount the auxiliary volumes at a distance from the air-springs. The ball valves offer a very small resistance to flow, and as a result, the inertial and viscous forces on the air in the pipe are dominant. In sub-section 4.4.4, inertia of air in the pipe is modeled and it is shown that the suspension has low stiffness at low

frequency and high stiffness at high frequency. Simulation of the linearized model is used to determine the effect of the inertia of air in the pipe on the road-noise isolation for the quarter car SDOF model and the quarter car 2-DOF model.

4.4.1 Thermodynamic modeling to estimate damping due to the valve flow resistance

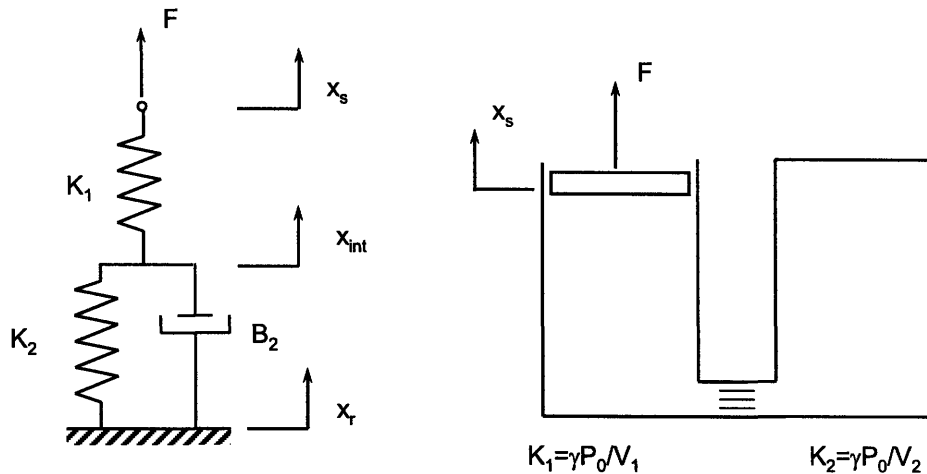


Figure 4-16 Piston and cylinder air-spring with one auxiliary volume and valve resistance

The system is characterized by the pressure, volume, mass and temperature (P_1, V_1, m_1, T_1) for CV1 (Control Volume 1), and the pressure, volume, mass and temperature (P_2, V_2, m_2, T_2) for CV2. We have made an assumption that all the gas in CV1 is in the same state, and all the gas in CV2 is in the same state. It is reasonable to assume that the properties are not a function of position within the chamber for modeling the air-spring, as the corner frequency for the suspension system is orders of magnitude lower than the frequency at which pressure waves propagate within the chamber to equalize the pressure at different points in the chamber. The damping in the system is due the pressure drop (“effort”) across the valve which is proportional to the square of the flow through the valve. There is another source of irreversibility in the system, namely the mixing of air at the outlet of the valve as it flows from one chamber to another. This irreversibility is captured in Equation (4.36) and Equation (4.40), which assume isenthalpic flow across the valve. Oda and Nishimura (1969), and Quaglia and Sorli (2001) have proposed and simulated the model shown in Figure 4-16, but they include only the first source of dissipation and neglect the second source of dissipation. They also neglect the heat-transfer from the air in the system to the surroundings. If the damping introduced by the valve resistance affects the spring behavior in the frequency domain of interest there has to be significant heat

generation, which makes their assumption unreasonable. Bachrach and Rivin (1983) have removed the damper in the system, and used the damping in the pipe as the primary source of damping. Even in this case they have neglected the irreversibility and heat transfer.

For the simulation, we apply a sinusoidal forcing of magnitude ΔV and frequency ω to the volume V_1 as depicted in Equation (4.30) and study the pressure variation as a function of the magnitude and the forcing frequency, i.e., $\Delta P_1 = f(\Delta V, \omega)$.

There are 8 variables and we need a relation of the form $\Delta P_1 = f(\Delta V, \omega)$. The required equations are given by Equations (4.30)-(4.34), (4.37), (4.39) and (4.41).

The following equations describe the system.

$$V_1 = V_0 + \Delta V \sin(\omega t) \quad (4.30)$$

$$V_2 = \text{constant} \quad (4.31)$$

Mass conservation

$$\begin{aligned} m_1 + m_2 &= m \\ \dot{m}_1 + \dot{m}_2 &= 0 \end{aligned} \quad (4.32)$$

Constitutive relation for gas in CV1 in algebraic and differential form

$$\begin{aligned} P_1 &= \frac{m_1 R T_1}{V_1} \\ \frac{\dot{P}_1}{P_1} + \frac{\dot{V}_1}{V_1} &= \frac{\dot{m}_1}{m_1} + \frac{\dot{T}_1}{T_1} \end{aligned} \quad (4.33)$$

Constitutive relation for gas in CV2 in algebraic and differential form

$$\begin{aligned} P_2 &= \frac{m_2 R T_2}{V_2} \\ \frac{\dot{P}_2}{P_2} &= \frac{\dot{m}_2}{m_2} + \frac{\dot{T}_2}{T_2} \end{aligned} \quad (4.34)$$

First Law for CV 1 is given as:

$$\frac{dE_{CV1}}{dt} = \dot{Q}_{H1} - \dot{W}_1 + \dot{m}_1 C_P T_{int1} \quad (4.35)$$

$$\dot{m}_1 C_V T_1 + \dot{m}_1 C_V \dot{T}_1 = h_1 A_1 (T_a - T_1) - P_1 \dot{V}_1 + \dot{m}_1 C_P T_{int1}$$

The state of the gas leaving the CV is the same as the state of the gas in the CV ($T_{int1} = T_1$ for flow from CV1 to CV2). But the state of the gas entering the CV is different from the state of the gas in the CV. The nature of the gas entering the CV depends on the valve characteristics. If we assume that the valve is well insulated, we can assume the flow across the valve to be an isenthalpic process. Hence we get:

$$T_{int1} = \begin{cases} T_1 & \text{for flow from CV1 to CV2} \\ T_2 & \text{for flow from CV2 to CV1} \end{cases} \quad (4.36)$$

From Equation (4.34) and Equation (4.35), we get

$$C_V \left(\frac{\dot{m}_1}{m_1} + \frac{\dot{T}_1}{T_1} \right) + R \frac{\dot{V}_1}{V_1} = C_P \left(\frac{T_{int1}}{T_1} \right) \frac{\dot{m}_1}{m_1} + \frac{h_1 A_1 (T_a - T_1)}{m_1 T_1} \quad (4.37)$$

$$C_V \frac{\dot{P}_1}{P_1} + C_P \frac{\dot{V}_1}{V_1} = C_P \frac{\dot{m}_1}{m_1} \left(\frac{T_{int1}}{T_1} \right) + \frac{h_1 A_1 (T_a - T_1)}{m_1 T_1}$$

First Law for CV2 is given by:

$$\frac{dE_{CV2}}{dt} = \dot{Q}_{H2} - \dot{W}_2 + \dot{m}_2 C_P T_{int2} \quad (4.38)$$

$$\dot{m}_2 C_V T_2 + \dot{m}_2 C_V \dot{T}_2 = h_2 A_2 (T_a - T_2) + \dot{m}_2 C_P T_{int2}$$

Considering isenthalpic flow across the valve:

$$C_V \left(\frac{\dot{m}_2}{m_2} + \frac{\dot{T}_2}{T_2} \right) = C_P \left(\frac{T_{int2}}{T_2} \right) \frac{\dot{m}_2}{m_2} + \frac{h_2 A_2 (T_a - T_2)}{m_2 T_2} \quad (4.39)$$

$$C_V \frac{\dot{P}_2}{P_2} = C_P \frac{\dot{m}_2}{m_2} \left(\frac{T_{int2}}{T_2} \right) + \frac{h_2 A_2 (T_a - T_2)}{m_2 T_2}$$

where

$$T_{int2} = \begin{cases} T_1 & \text{for flow from CV1 to CV2} \\ T_2 & \text{for flow from CV2 to CV1} \end{cases} \quad (4.40)$$

The mass/volume flow rate is related to the pressure drop across the valve. In this simulation, we use the relation in Equation (4.41) where C_{valve} is the valve flow coefficient. (Commonly known as C_V , but we have used C_{valve} so as not to confuse it with specific heat at constant volume C_V)

$$\dot{m}_1 = -\dot{m}_2 = f(P_1 - P_2)$$

$$q = C_{valve} \sqrt{\frac{P_1 - P_2}{SG}}$$

$$\dot{m}_1 = \rho q \tag{4.41}$$

Equations (4.30)-(4.34), (4.36), (4.37), (4.40) and (4.41) present the complete set of equations that describe the behavior of this spring. This is a set of non-linear differential equations and it not possible to obtain an analytical solution for the purpose of determining the effect of the DPs on FRs. We simulated these non-linear equations in Matlab and the relations of the form $\Delta P_1 = f(\Delta V_1, \omega)$ are obtained as shown in Figure 4-17.

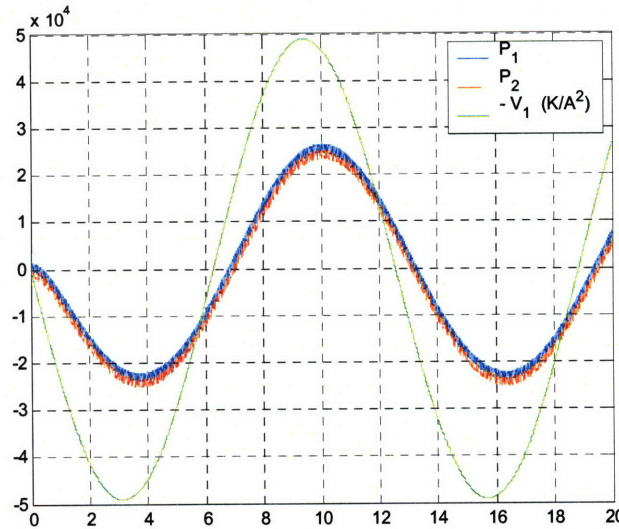


Figure 4-17: Results of the simulation (for $\omega=1$ rad/sec) showing pressure variation in the two chambers and the weighted volume variation.

The following observations can be made from the simulation results:

1. At low frequencies, the pressure variation ΔP_1 is in phase with the volume variation $(-\Delta V_1)$ which means that the system behaves as a pure spring at low frequencies. Moreover the ratio $A^2 \Delta P_1 / \Delta V_1$ is equal to the low stiffness $K_{low} = \gamma A^2 P_0 / (V_1 + V_2)$. The

pressure variation ΔP_2 is the same as ΔP_1 which means the two volumes are in communication.

2. In the mid-frequency range, the pressure variation ΔP_1 leads in phase with respect to the volume variation ($-\Delta V_1$). This means that the system exhibits dissipation in the mid-frequency range. Moreover the ratio $A^2 \Delta P_1 / \Delta V_1$ increases from the low stiffness $K_{low} = \gamma A^2 P_0 / (V_1 + V_2)$ to the high stiffness $K_{high} = \gamma A^2 P_0 / V_1$ as the frequency ω increases. The pressure variation ΔP_2 has smaller magnitude than ΔP_1 and lags in phase.
3. At high frequencies, again the pressure variation ΔP_1 is in phase with the volume variation ($-\Delta V_1$) which means that the system behaves as a pure spring at high frequencies. Moreover the ratio $A^2 \Delta P_1 / \Delta V_1$ is equal to the high stiffness $K_{high} = \gamma A^2 P_0 / V_1$. The pressure variation ΔP_2 is very small in comparison with ΔP_1 which means that flow across the valve chokes for higher frequencies and the auxiliary volume becomes ineffective at higher frequencies, as manifested by high stiffness at higher frequencies.
4. The flow resistance is non-linear. As a result, the frequency range where the transition from low stiffness to high stiffness occurs depends on the magnitude of the ΔV in addition to the valve flow-coefficient C_{valve} .
5. These trends can be captured in the following linearized model shown in Figure 4-18 which can be used for setting the valve DPs.

This qualitative force-deflection behavior of the air spring with auxiliary volumes can be represented as lead compensator element, employing a spring in series with a parallel arrangement of spring and damper as shown in Figure 4-18. The complex stiffness of this element is given by Equation (4.42) and the Bode plot shows that such element has low stiffness at low frequency and high stiffness at high frequency, with the two corner frequencies being $\omega_{c1} = K_2 / B_2$ and $\omega_{c2} = (K_1 + K_2) / B_2$. The corner frequencies ω_{c1} and ω_{c2} can be altered by changing B_2 or the flow-resistance of the valve.

$$K_{comp} = \frac{K_1 (K_2 + B_2 s)}{K_1 + K_2 + B_2 s} \quad (4.42)$$

The weakness of this formulations is that the damping introduced by the valve resistance cannot be expressed as an analytical function of the valve flow-coefficient C_{Valve} . This is because the irreversibility in the system caused by the isenthalpic flow across the valve cannot be modeled accurately. Moreover the valve flow-coefficient C_{Valve} is typically presented for steady-state flow across the valve and the flow in our case is unsteady. But the qualitative behavior can be captured from the modeling above and it is recommended that the corner frequencies ω_{c1} and ω_{c2} be determined experimentally. It should also be noted that since the pressure is proportional to square of the flow, damping coefficient B_2 will depend on the amplitude of the oscillations, leading to lower corner frequencies for larger amplitude oscillations. Determination of equivalent viscous damping from square-law damping will be illustrated in subsection 4.4.4.3.

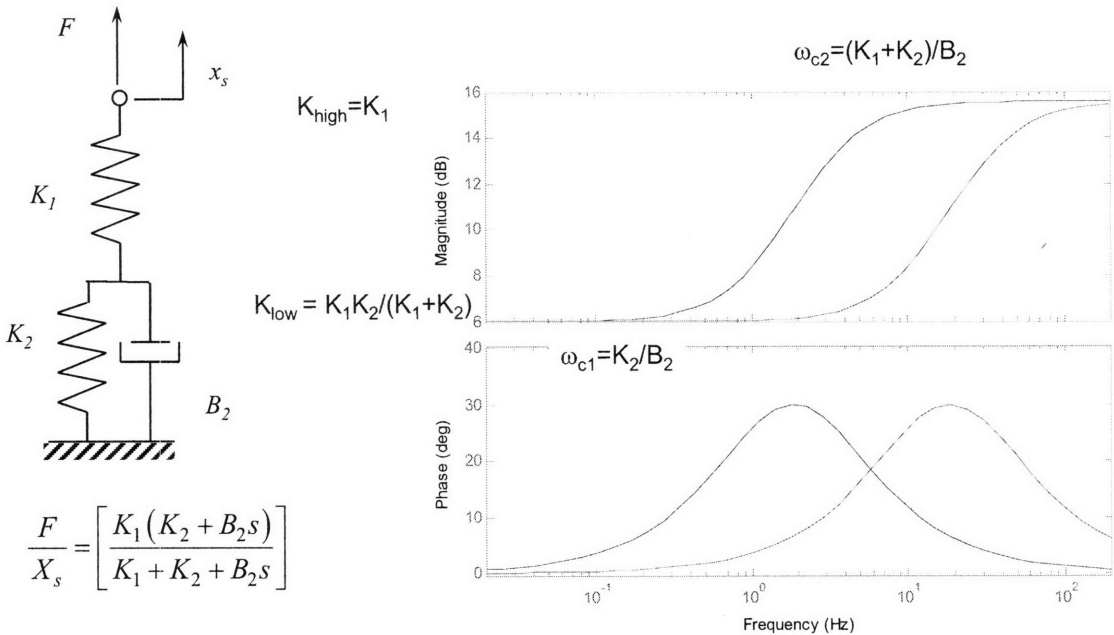


Figure 4-18 : Frequency dependent stiffness behavior of an air spring with auxiliary volume due to valve damping

4.4.2 Effect of valve damping on road noise isolation

The original design intent was to get a low stiffness at all frequencies, but flow resistance due to the valve causes frequency dependant stiffness behavior as shown in Figure 4-18. We evaluated the effect of this frequency dependant stiffness on comfort, which is characterized by the road noise isolation transfer function x_s/x_r . We have used the linearized model of the air-spring with an auxiliary volume and evaluated the deviation of its performance from the performance of a soft and stiff suspension as shown in Figure 4-19.

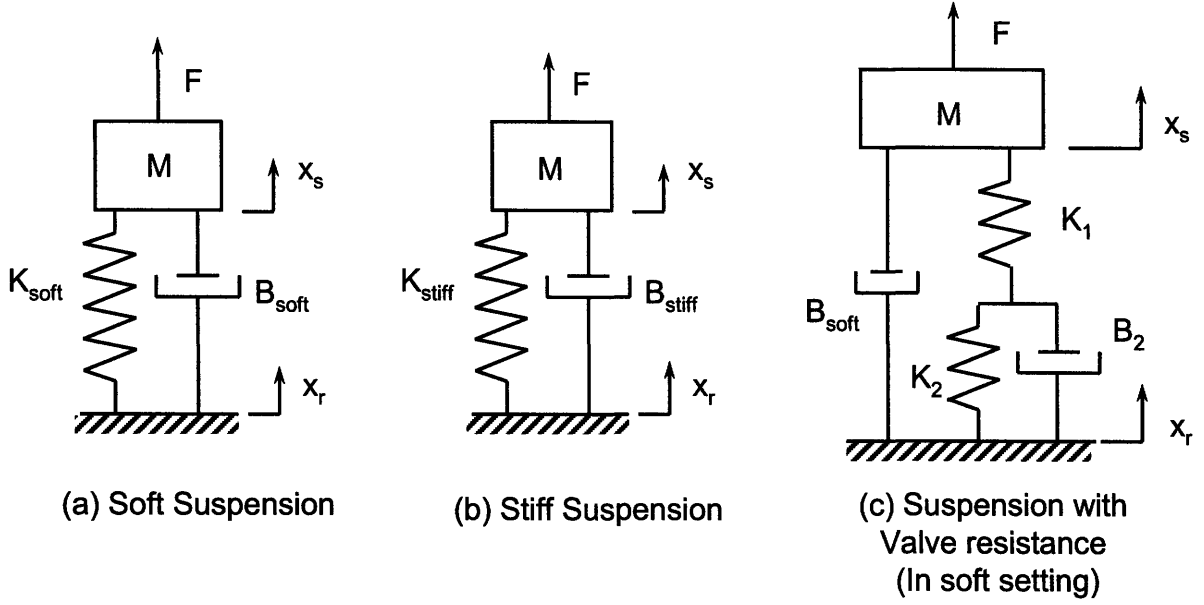


Figure 4-19 : Comparison of SDOF quarter car model road noise isolation for a soft suspension, stiff suspension and an air-spring with auxiliary volumes and valve resistance

For this simulation, we have used $K_{stiff}=2K_{soft}$ and $B_{stiff} = \sqrt{2}B_{soft}$ to maintain ζ constant. For the air spring with auxiliary volume, we have assumed equal volumes and $K_1=K_2=K_{stiff}$ such that this suspension has low stiffness $K_{low}=K_{soft}$ at low frequencies and high stiffness $K_{high}=K_{stiff}$ at high frequencies. The road noise isolation transfer function for the soft and stiff suspensions, as shown in Figure 4-19, are given by Equation (4.43) and Equation (4.44) respectively.

$$\frac{x_s}{x_r} = \frac{B_{soft}s + K_{soft}}{Ms^2 + B_{soft}s + K_{soft}} \quad (4.43)$$

$$\frac{x_s}{x_r} = \frac{B_{stiff}s + K_{stiff}}{Ms^2 + B_{stiff}s + K_{stiff}} \quad (4.44)$$

The asymptotic behavior of these transfer functions at high frequency is given by Equation (4.45) and Equation (4.46). The asymptotic behavior explicitly depends on B and M , but not on K . Since $B = 2\zeta\sqrt{KM}$ and ζ has to be close to 0.4 to avoid excessive magnification at resonance, the asymptotic behavior does depend on K (although not explicitly).

$$\left| \frac{x_s}{x_r} \right| \rightarrow \frac{B_{soft}}{Ms} = \frac{2\zeta\sqrt{K_{soft}M}}{Ms} = \frac{2\zeta\omega_{n1}}{s} \quad (4.45)$$

$$\left| \frac{x_s}{x_r} \right| \rightarrow \frac{B_{high}}{Ms} = \frac{2\zeta \sqrt{K_{high}M}}{Ms} = \frac{2\zeta \omega_{n2}}{s} \quad (4.46)$$

The road noise isolation transfer function for this case is given by Equation (4.47).

$$\frac{x_s}{x_r} = \frac{B_{soft}s + K_{comp}}{Ms^2 + B_{soft}s + K_{comp}} \quad (4.47)$$

where K_{comp} is the complex stiffness given by Equation (4.42).

The transfer function then becomes:

$$\frac{x_s}{x_r} = \frac{B_{soft}s(K_1 + K_2 + B_2s) + K_1(K_2 + B_2s)}{(Ms^2 + B_{soft}s)(K_1 + K_2 + B_2s) + K_1(K_2 + B_2s)} \quad (4.48)$$

Figures 4-20 through 4-24 indicate the Bode plots for the transfer function x_s/x_r for the soft suspension, stiff suspension (with same ζ) and the air-spring with auxiliary volume for different values of B_2 . The ratio of the lower corner frequency of the lead compensator to the natural frequency of the system i.e. $(K_2/B_2)/\omega_n$ can be used as a non-dimensional parameter to quantify the damping introduced by the valve. Notice that the air spring with auxiliary volume has the same asymptotic behavior at high frequencies irrespective of the valve flow resistance. This is because we have used low damping B_{soft} in parallel with the air-spring system.

Figure 4-20 shows that if the flow-resistance due to the valve is too high ($K_2/B_2=0.1\omega_n$), then the auxiliary volume does not reduce the stiffness in the frequency region of interest and the lead compensator introduces significant damping in the system in the frequency region of interest. As a result road noise isolation is worse than not only the soft suspension, but also the stiff suspension. As the damping reduces ($K_2/B_2=\omega_n$), we still observe a deterioration in the comfort as compared to the soft suspension, but it does better than the stiff suspension at higher frequencies. Further improvement in isolation is observed for further reduction in damping introduced by the valve ($K_2/B_2=10\omega_n$). Notice that the maximum amplification at resonant frequency is actually reduced as the lead compensator introduces damping near the resonant frequency, but not at higher frequencies. For $K_2/B_2=100\omega_n$, the stiffness change from K_{low} to K_{high} occurs at a very high frequency and there is no deviation from the road noise isolation transfer function. Thus we conclude that the deviation from a soft suspension road noise isolation

transfer function depends on the corner frequency of the lead compensator. The deviation is marginal provided that the corner frequency of the lead compensator is high enough (or in other words, the damping due the valve is low).

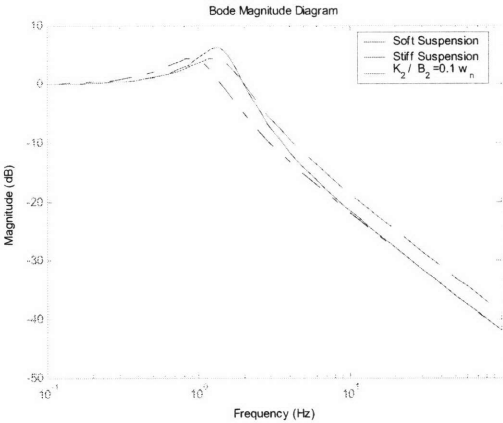


Figure 4-20 : Road noise isolation for high damping $K_2/B_2 = 0.1\omega_n$

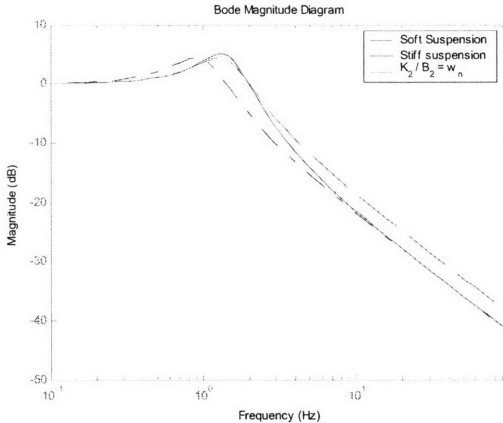


Figure 4-21 : Road noise isolation for moderate damping $K_2/B_2 = \omega_n$

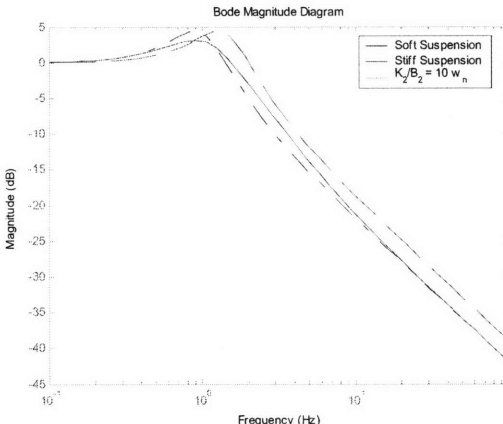


Figure 4-22 : Road noise isolation for low damping $K_2/B_2 = 10\omega_n$

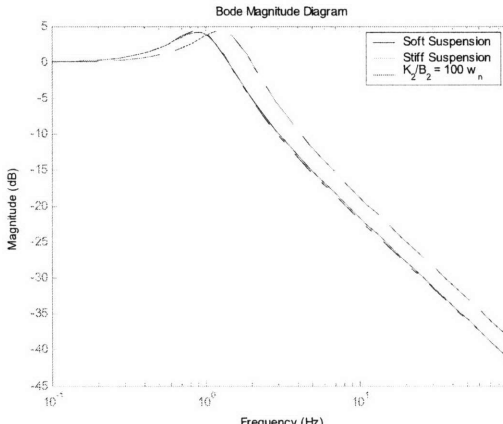


Figure 4-23 : Road noise isolation for very low damping $K_2/B_2 = 100\omega_n$

4.4.3 Implementation issues with the solenoid valve arrangement

The use of solenoid valves presented a challenge, as they are not bi-directional. Two-port two-position solenoid valves (commonly referred to as two-way solenoid valves) have an upstream port and a downstream port. The construction of the solenoid valves is such that there is a preferred flow direction from upstream port to downstream port when the valve is open. The

flow coefficient C_{valve} for flow in the non-preferred direction is around one tenth of the C_{valve} for the flow in the preferred direction. This poses a problem as the high flow resistance in the non-preferred flow direction reduces the frequency at which the stiffness increase occurs.

Potential solutions and associated problems

Use of two valves in parallel

This problem can be overcome by employing two valves in parallel instead of one as shown in Figure 4-24. This way we could get 110% of the flow in either direction, no matter which port has higher pressure or which direction the flow occurs. But this arrangement is not possible, as direct-acting solenoid valves use the pressure difference across the ports to achieve perfect sealing. When the downstream port has a higher pressure than the upstream port, this pressure difference opens the valve. So the arrangement of two valves in parallel will have at least one valve open at all times.

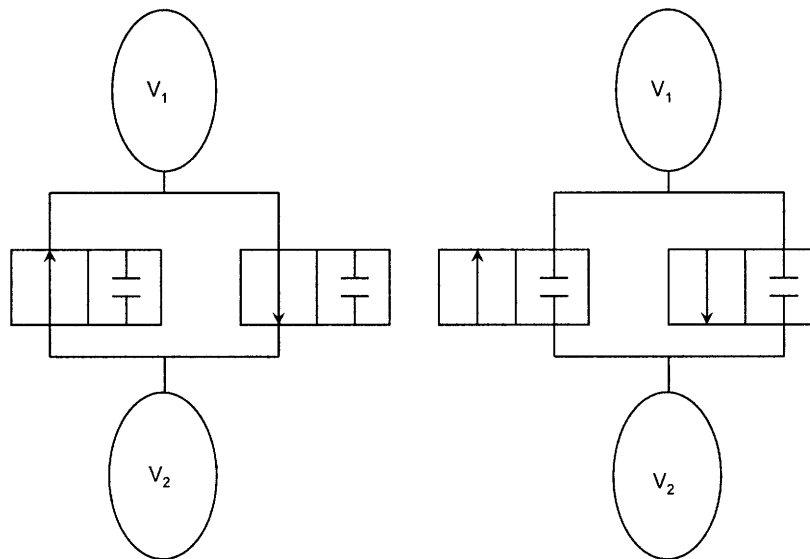


Figure 4-24 : Arrangement of two 2-way valves to connect air-spring to the auxiliary volumes (a) Open position and (b) Closed position

Use of two three-port two-position valves in parallel

The problem of higher downstream pressure opening the solenoid valve can be overcome by using a parallel arrangement of two three-port two-position valves (commonly known as three-way valves). In this arrangement, the two ports of each valve are connected to the two

volume and one is port sealed as shown in Figure 4-25. In the open position, the valve on the left has preferred flow direction from volume V_2 to V_1 and the valve on the right has preferred flow direction from volume V_1 to V_2 . In the closed position, the volumes are disconnected from one another.

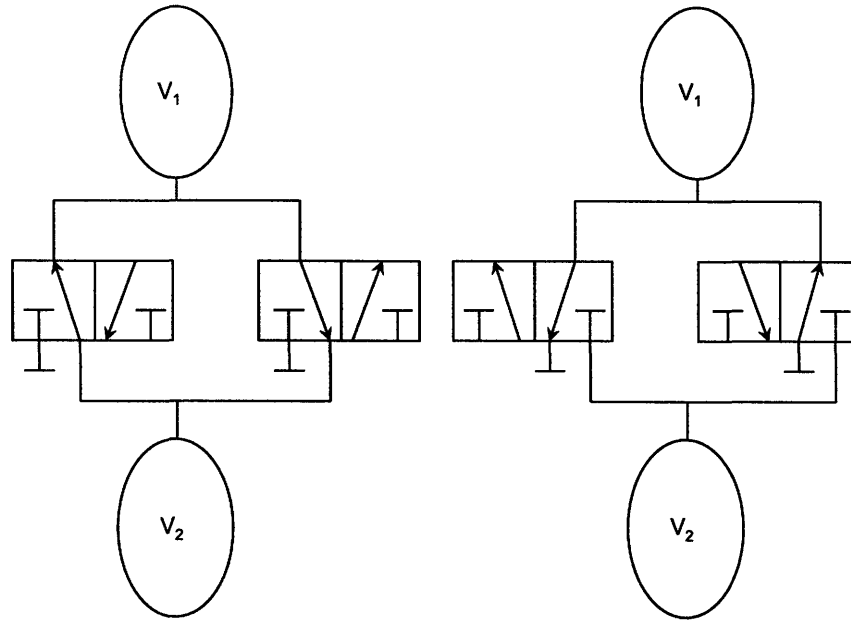


Figure 4-25: Arrangement of two 3-way valves to connect air-spring to auxiliary volumes (a) Open position and (b) Closed position

This arrangement posed packaging constraints in the car which arise due to the following reasons:

1. The three-port two-position solenoid valves are bulkier than the two-port solenoid valves.
2. Two valves are needed instead of one.
3. This arrangement needs additional union-tees, where the tubing to the air-spring or the auxiliary volumes needs to split to connect to the two valves. Air-brake tubing, used to connect the air-springs to the auxiliary volumes, has a minimum bend radius of 3 in. and this makes insertion of union tees especially space-consuming.

Moreover, power needs to be supplied to a Normally Closed (NC) solenoid valve to keep it open or alternately to a Normally Open (NO) solenoid valve to keep it closed.

The additional tubing and tube-connection introduce resistance to the flow due to expansion losses, contraction losses, bending losses due to the tube-connections and also increase the inertia forces and friction losses due to longer tubing.

Use of automated ball valves

In the actual prototype, automated ball valves have been used for the following reasons:

1. They provide for better packaging.
2. They eliminate the need for additional tubing and tube-connections that are required for the arrangement of two three-port two-position solenoid valves.
3. They provide excellent sealing when closed and low resistance to the flow when open.
4. They do not consume power except when they are required to open or close.

Imani (1993) has proposed an even better solution, which is to use a single valve block with multiple orifices, which requires only one actuator per air-spring and allows for better packaging. If adequately designed, it only consumes power during valve operation.

4.4.4 Modeling of effective inertia in the tubing

As the ball valves used in the system have a larger diameter than the tube ID, the pressure drop across the valve is insignificant. Packaging constraints in an existing car made it necessary to mount the auxiliary volumes at a distance from the air-springs, and a schematic representation of this setup is shown in Figure 4-27. This introduces significant inertia in the tubing which is modeled in this section.

Air springs with auxiliary volumes are very often employed on train and heavy vehicle (truck and bus) suspensions to achieve the desired low natural frequency. Experimental investigations of air spring with auxiliary volumes have been performed for train suspensions air springs by Berg (2000) and for bus suspension air-springs by Toyofuku et.al. (1999). In these experiments, the frequency response is measured for small oscillations, equivalent spring-mass-damper systems are proposed. The model parameters are adjusted to fit the experimentally observed frequency response data. Berg has proposed experimental determination of these model parameters for different operating pressures, ride-height etc. Toyofuku et.al. (1999) and Presthus (2002) have presented derivation of air-spring model parameters, but their formulation is

incorrect. Presthus considers volume changes of the auxiliary volume that is assumed rigid. Toyofuku considers isothermal spring rate without any consideration for the heat transfer across the walls of the air-spring or the auxiliary volumes. In this section, we formulate a thermodynamic model of the system, show its equivalence to a spring mass damper system and provide estimates for the model parameters.

4.4.4.1 Incompressible flow assumption in pipe

In this model, we make the assumption that the flow in the pipe is incompressible. The justification for this assumption is presented below.

1. The velocity of air in the tube is significantly lower than the velocity of sound in air, leading to a low Mach number regime. As a result the flow in the pipe can be treated as incompressible and we can use Navier-Stokes equation.
2. The volume of the air in the pipe is two orders of magnitude smaller than the volume of air in the air-spring or the auxiliary volumes ($V_{pipe} \ll V_1, V_2$). As a result, the compliance of the air in the pipe can be neglected (or lumped into the compliance of the auxiliary volume) and the flow of air in the pipe can be considered as an incompressible flow.

$$\text{Air Spring Volume } (V_1) \approx 125 \text{ in}^3$$

$$\text{Auxiliary Volume } (V_2) = 172 \text{ in}^3$$

$$\text{Auxiliary Volume } (V_3) = 283 \text{ in}^3$$

$$\text{Volume of 1m pipe} = 2.80 \text{ in}^3$$

3. It is also important to consider the frequency at which there will be acoustic resonance in the tubing and to ensure that the resonant frequency is significantly higher than the frequency range of interest. Due to packaging constraints, the auxiliary volumes in the front are farther from the corresponding air-springs as compared to the rear. The lengths of the tubing are of the order of 1m in both front and rear. Speed of sound in air at room temperature is about 340m/s ($C_{air}^2 = \gamma RT$). The tube behaves as an open-open pipe and for this case, the wavelength of the first harmonic will be around $\lambda = 2L \approx 2\text{m}$. Hence the fundamental frequency of the first harmonic for $L=1\text{m}$ is $C_{air}/\lambda = f_0 \approx 170\text{Hz}$ and for $L=2$ is $f_0 \approx 85\text{Hz}$. The elevated pressure in the air spring does not change this frequency, as the

speed of sound in air is independent of pressure. The frequencies of the subsequent harmonics will be a multiple of the fundamental frequency f_0 . This frequency is significantly greater than the suspension bounce frequency ($\sim 1\text{Hz}-1.5\text{Hz}$) as well as the wheel-hop frequency ($\sim 10\text{Hz}$). The compressible flow assumption introduces dynamics in the system in the range of 5-10 Hz, which is in the frequency range of interest.

4.4.4.2 Thermodynamic equations for air-spring and auxiliary volume

The system is characterized by the pressure, volume, mass and temperature of air (P_1, V_1, m_1, T_1) for CV1 (Control Volume 1); pressure, volume, mass and temperature (P_2, V_2, m_2, T_2) for CV2 (Control Volume 2); and the pressure, temperature and density ($P(z), \rho(z), T(z)$) of air in the tube which is a function of the position z along the length of the pipe. We will make an assumption that all the gas in CV1 is in the same state, and all the gas in CV2 is in the same state. It is reasonable to assume that the properties are not a function of position within the chamber for modeling the air-spring, as the natural frequency of the suspension system is orders of magnitude lower than the frequency at which pressure waves propagate within the chamber to equalize the pressure at different points in the chamber. This frequency is of order of magnitude of the $L_{sp}/C_{air} \sim 350\text{Hz}$, where L_{sp} is the length of the air spring or the auxiliary volume and C_{air} is the speed of sound in air.

Air-spring equations

Mass conservation

$$m_1 + m_2 + m_{pipe} = m \quad (4.49)$$

Since the mass of air in the pipe is three orders of magnitude smaller than the mass of air in the air-spring or the auxiliary volumes, the change in mass of air in the pipe can be neglected.

$$\dot{m}_{pipe} \approx 0 \quad (4.50)$$

This gives us a simplified relation

$$\dot{m}_1 + \dot{m}_2 = 0 \quad (4.51)$$

Constitutive relation for gas in CV1 is given as:

$$P_1 = \frac{m_1 R T_1}{V_1} \quad (4.52)$$

This relation can be expressed in the differential form as

$$\frac{\dot{P}_1}{P_1} + \frac{\dot{V}_1}{V_1} = \frac{\dot{m}_1}{m_1} + \frac{\dot{T}_1}{T_1} \quad (4.53)$$

Constitutive relation for gas in CV2 in algebraic and differential form

$$P_2 = \frac{m_2 R T_2}{V_2} \quad (4.54)$$

$$\frac{\dot{P}_2}{P_2} = \frac{\dot{m}_2}{m_2} + \frac{\dot{T}_2}{T_2} \quad (4.55)$$

First Law for CV 1

$$\frac{dE_{CV1}}{dt} = \dot{Q}_{H1} - \dot{W}_1 + \dot{m}_1 C_P T_1 \quad (4.56)$$

Assuming no heat transfer across the air-spring walls for fast oscillations and substituting $E_{CV1} = m_1 C_V T_1$ for the internal energy of the gas and $\dot{W} = P_1 \dot{V}_1$ for the shaft work, we get:

$$\dot{m}_1 C_V T_1 + m_1 C_V \dot{T}_1 = -P_1 \dot{V}_1 + \dot{m}_1 C_P T_1 \quad (4.57)$$

$$C_V \left(\frac{\dot{T}_1}{T_1} + \frac{\dot{m}_1}{m_1} \right) + R \frac{\dot{V}_1}{V_1} = C_P \frac{\dot{m}_1}{m_1} \quad (4.58)$$

First Law for CV2:

$$\frac{dE_{CV2}}{dt} = \dot{Q}_{H2} - \dot{W}_2 + \dot{m}_2 C_P T_2 \quad (4.59)$$

We assume no heat transfer across the auxiliary volume walls for fast oscillations. As there is no volume change in auxiliary volume, the shaft work is also zero.

$$\dot{m}_2 C_V T_2 + m_2 C_V \dot{T}_2 = \dot{m}_2 C_P T_2 \quad (4.60)$$

$$C_V \left(\frac{\dot{m}_2}{m_2} + \frac{\dot{T}_2}{T_2} \right) = C_P \frac{\dot{m}_2}{m_2} \quad (4.61)$$

From Equation (4.53) and Equation (4.58), we get

$$C_V \frac{\dot{P}_1}{P_1} = -C_P \frac{\dot{V}_1}{V_1} + C_P \frac{\dot{m}_1}{m_1} \quad (4.62)$$

which can be linearized about the operating point ($P_1=P_0$, $V_1=V_{10}$, $m_1=m_{10}$) as

$$\dot{P}_1 = -\gamma \frac{P_{10}}{V_{10}} \dot{V}_1 + \gamma \frac{P_{10}}{m_{10}} \dot{m}_1 \quad (4.63)$$

Substituting $\dot{m}_1 = -\rho_0 Q_{12}$; $-\dot{V}_1 = Q_1$ and $Q_2 = Q_1 - Q_{12}$, we get

$$\dot{P}_1 = \gamma \frac{P_{10}}{V_{10}} Q_1 - \gamma \frac{P_{10} \rho_0}{m_{10}} Q_{12} \quad (4.64)$$

$$\dot{P}_1 = \gamma \frac{P_0}{V_{10}} (Q_1 - Q_{12}) = \gamma \frac{P_0}{V_{10}} Q_2 \quad (4.65)$$

Q_{12} is the volumetric flow rate from volume V_1 to V_2 .

Q_1 is the total rate of change of the air spring volume.

Q_2 is the contribution to the rate of change of air-spring volume due to compliance of air in the air-spring.

Q_1 , Q_2 and Q_{12} are illustrated in the bond graph notation in Figure 4-26. The incompressible flow assumption lets us use the bond graph formulation (Karnopp, Margolis & Rosenberg, 1990).

From Equation (4.55) and Equation (4.61), we get

$$\dot{P}_2 = \gamma \frac{P_2}{m_2} \dot{m}_2 \quad (4.66)$$

Using the relation $\dot{m}_2 = -\dot{m}_1 = \rho_0 Q_{12}$, this equation can be linearized about the operating point ($P_2=P_0$, $m_2=m_{20}$) to get the compliance of the auxiliary volume.

$$\dot{P}_2 = \gamma \frac{P_0 \rho_0}{m_{20}} Q_{12} = \gamma \frac{P_0}{V_{20}} Q_{12} \quad (4.67)$$

4.4.4.3 Pipe flow equations

The assumption of incompressible flow in the tube allows us to use the Navier-Stokes equation. The Navier-Stokes equation in the cylindrical coordinates is given by Equation (4.68).

$$\rho \left(\frac{\partial v_z}{\partial t} + v_r \frac{\partial v_z}{\partial r} + v_\theta \frac{\partial v_z}{\partial \theta} + v_z \frac{\partial v_z}{\partial z} \right) = -\frac{\partial P}{\partial z} + \mu \left[\frac{1}{r} \frac{\partial}{\partial r} \left(r \frac{\partial v_z}{\partial r} \right) + \frac{1}{r^2} \frac{\partial^2 v_z}{\partial \theta^2} + \frac{\partial^2 v_z}{\partial z^2} \right] + \rho g_z \quad (4.68)$$

By symmetry, we can eliminate the partial derivatives with respect to θ . We can neglect the radial component of velocity and the gravity forces on air. Due to the incompressible flow assumption, the flow rate and velocity remains the same along the length of the tube. As a result, the first derivative and second derivative of the air velocity with respect to length along the tube can also be neglected.

$$\rho \frac{\partial v_z}{\partial t} = -\frac{\partial P}{\partial z} + \mu \frac{1}{r} \frac{\partial}{\partial r} \left(r \frac{\partial v_z}{\partial r} \right) \quad (4.69)$$

The first term on the left hand side of Equation (4.69) reflects the inertia of the air in the pipe.

The order of magnitude of the two terms in the Navier-Stokes' equation can be estimated as follows.

$$f_{inertial} = \rho \frac{\partial v_z}{\partial t} \propto \rho \frac{U}{T} \quad (4.70)$$

$$f_{viscous} = \mu \frac{1}{r} \frac{\partial}{\partial r} \left(r \frac{\partial v_z}{\partial r} \right) \propto \mu \frac{U}{r_{pipe}^2} \quad (4.71)$$

Here U is the velocity of the air in the tube averaged over the cross-sectional area of the tube and T can be estimated as the forcing period in seconds or inverse of the forcing frequency. The ratio of the two terms gives:

$$\frac{f_{inertial}}{f_{viscous}} = \frac{\rho \frac{U}{T}}{\mu \frac{U}{r_{pipe}^2}} = \frac{\rho r_{pipe}^2}{\mu T} = \frac{(1.2 \times 5) \times (0.5 \times 0.01)^2}{1.8 \times 10^{-5} \times T} \approx \frac{8}{T} \quad (4.72)$$

This shows that both terms are significant. To estimate the viscous forces, we introduce wall shear τ_w which is assumed to be correlated by a local Darcy friction factor f_D as given by Equation (4.74).

$$\rho \frac{\partial U}{\partial t} = -\frac{\partial P}{\partial z} - 2 \frac{\tau_w}{r_{pipe}} \quad (4.73)$$

$$\tau_w = \frac{1}{8} f_D \rho U^2 \quad (4.74)$$

Integrating along the length of the tube, we get

$$\rho L \frac{\partial U}{\partial t} = -(P_2 - P_1) - \frac{1}{4} \frac{f_D L \rho U^2}{r_{pipe}} \quad (4.75)$$

In this formulation, we have effectively lumped all the compliance of the air into the air spring and the auxiliary volumes and all the inertia of the air into the tube. Both of these are reasonable assumptions. The lumping of compliance into the air-spring and the auxiliary volume can be justified by the fact that the volume of air in the pipe is two orders of magnitude smaller than the volume of air in the air-spring or the auxiliary volumes, and the fact that the compliance of a gas varies linearly with its volume. Although the mass of air in the air spring is three orders of magnitude smaller than the mass of air in the air-spring, the lumping of all the inertia into the tube can be justified by looking at the velocity ratios in the tube and the air-spring, which goes inversely as the area ratio of the tube to the effective area of the air-spring.

$$\frac{v_{pipe}}{v_{spring}} \approx \left(\frac{A_{effective}}{A_{pipe}} \right) \approx \left(\frac{d_{eff}}{d_{pipe}} \right)^2 \approx 64 \quad (4.76)$$

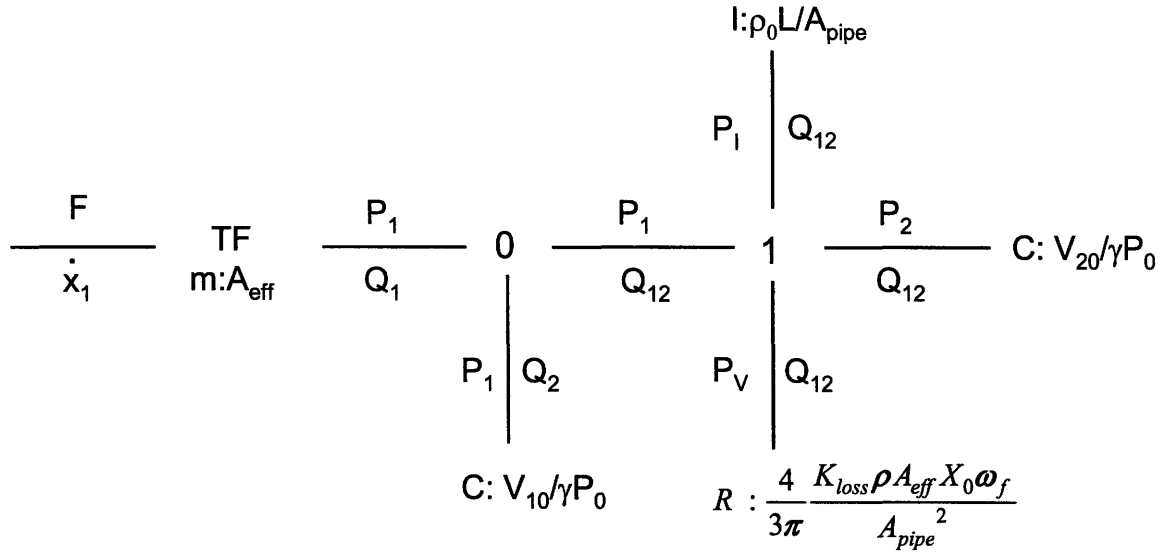


Figure 4-26 Bond Graph representation of the air spring with auxiliary volume with inertia of air in pipe
The force and velocity of the top plate are related to the pressure and rate of change of volume in the air spring by the effective area as follows.

$$F = P_1 A_{eff} \quad (4.77)$$

$$A_{eff} \dot{x}_1 = Q_1 \quad (4.78)$$

From Equation (4.65) and Equation (4.67), we get the constitutive relations for the contribution due to the air spring compliance and constitutive relation for the auxiliary volume compliance.

$$P_1 = \left(\frac{\gamma P_0}{V_{10}} \right) \int Q_2 dt \quad (4.79)$$

$$P_2 = \left(\frac{\gamma P_0}{V_{20}} \right) \int Q_{12} dt \quad (4.80)$$

Equation (4.75) can be rearranged in the form

$$P_1 = P_2 + P_I + P_V \quad (4.81)$$

P_I is the pressure drop due to the inertial forces and is given by:

$$P_I = \rho L \frac{dU}{dt} = \frac{\rho L}{A_{pipe}} \frac{dQ_{12}}{dt} \quad (4.82)$$

U is the velocity of the air in the tube averaged over the cross-sectional area of the tube and it is related to the volumetric flow-rate by the relation $Q_{12} = A_{pipe}U$.

P_V is the pressure drop due to viscous forces and is given by the following equation.

$$P_V = \frac{1}{4} \frac{f_D L}{r_{pipe}} \rho U^2 = \frac{1}{4} \frac{f_D L \rho Q_{12}^2}{r_{pipe} A_{pipe}^2} \quad (4.83)$$

If we include the expansion losses, contraction losses and bending losses for the tube connections and T-junctions used to connect the air spring to the pipe friction loss, the complete relation for the pressure drop becomes:

$$P_V = \frac{1}{2} \left(\frac{f_D L}{2r_{pipe}} + k_{exp} + k_{con} + k_{bend} \right) \frac{\rho Q_{12}^2}{A_{pipe}^2} = \frac{K_{loss} \rho}{2 A_{pipe}^2} Q_{12}^2 \quad (4.84)$$

where k_{exp} , k_{con} , and k_{bend} are loss coefficients due to expansion, contraction and bending respective and K_{loss} is the sum of the sum of the four loss coefficients.

Putting together the Equations (4.79)-(4.84), we get

$$P_1 = \left(\frac{\gamma P_0}{V_{10}} \right) \int Q_2 dt = \left(\frac{\gamma P_0}{V_{20}} \right) \int Q_{12} dt + \frac{\rho L}{A_{pipe}} \frac{dQ_{12}}{dt} + \frac{K_{loss} \rho}{2 A_{pipe}^2} Q_{12}^2 \quad (4.85)$$

We define two new variables x_2 , and x_{12} as follows

$$\begin{aligned} \int Q_2 dt &= A_{eff} x_2 \\ \int Q_{12} dt &= A_{eff} x_{12} \end{aligned} \quad (4.86)$$

With these new variables, Equation (4.85) becomes

$$F = P_1 A_{eff} = \left(\frac{\gamma P_0}{V_{10}} \right) A_{eff}^2 x_2 = \left(\frac{\gamma P_0}{V_{20}} \right) A_{eff}^2 x_{12} + \frac{\rho L}{A_{pipe}} A_{eff}^2 \dot{x}_{12} + \frac{K_{loss} \rho A_{eff}^3}{2 A_{pipe}^2} \dot{x}_{12}^2 \quad (4.87)$$

Since $Q_1 = Q_2 + Q_{12}$, we get $x_1 = x_2 + x_{12}$.

From Equation (4.87), we see that the system follows square law damping (characterized by B_{SL}), which we would like to approximate by effective viscous damping B_V as shown in Equation (4.88).

$$F_B = \frac{K_{loss} \rho A_{eff}^3}{2 A_{pipe}^2} \dot{x}_{12}^2 = B_{SL} \dot{x}_{12}^2 \approx B_V \dot{x}_{12} \quad (4.88)$$

Linearization about the operating point $\dot{x}_{12} = 0$ leads to effective damping $B_{eff} = 0$. To linearize this relation in a meaningful way, we calculate the effective viscous damping B_V by equating the energy dissipated by the square-law damping in one cycle of forced vibration to that due to viscous damping as illustrated by Timoshenko et.al. (1990). Let U_V be the energy dissipated by viscous damping in one cycle of forced vibration of amplitude X_0 and forcing frequency ω_f . U_V can be calculated as:

$$U_V = \int_0^T F_B \dot{x} dt = \int_0^T B_V \dot{x}^2 dt \quad (4.89)$$

$$U_V = B_V \int_0^T X_0^2 \omega_f^2 \sin^2(\omega_f t) dt \quad (4.90)$$

$$U_V = \pi B_V X_0^2 \omega_f \quad (4.91)$$

Let U_{SL} be the energy dissipated by viscous damping in one cycle of forced vibration of amplitude X_0 and forcing frequency ω_f . U_{SL} can be calculated as:

$$U_{SL} = 4 \int_0^{T/4} F_B \dot{x} dt = 4 \int_0^{T/4} B_{SL} \dot{x}^3 dt \quad (4.92)$$

Notice that the integration is performed over a quarter cycle and multiplied by 4 as the damping force is always opposite to the velocity and the quantity being integrated is always negative, but the integral of $\sin^3 x$ over the complete cycle will result in zero.

$$U_{SL} = 4 B_{SL} X_0^3 \omega_f^3 \int_0^{T/4} \sin^3(\omega_f t) dt \quad (4.93)$$

$$U_{SL} = \frac{8}{3} B_{SL} X_0^3 \omega_f^2 \quad (4.94)$$

Equating U_V and U_{SL} , we get

$$B_V = \frac{8}{3\pi} B_{SL} X_0 \omega_f \quad (4.95)$$

Substituting the value of B_{SL} from Equation (4.88), we get:

$$B_V = \frac{4}{3\pi} \frac{K_{loss} \rho A_{eff}^3 X_0 \omega_f}{A_{pipe}^2} \quad (4.96)$$

Due to the square-law damping, the effective damping increases with the amplitude of the oscillations. This trend is captured accurately by the term $X_0 \omega_f$ in our effective viscous damping calculation in Equation (4.96). From this equation, we see that the only unknown term is K_{loss} , which can be evaluated for steady flow using Moody's chart for the friction loss and the relevant graphs for bending, expansion and contraction losses (White, 1999). Experimental analysis is recommended for finding the correction factor for unsteady flow. Substituting the equivalent viscous damping into Equation (4.87), we get:

$$F = \left(\frac{\gamma P_0}{V_{10}} \right) A_{eff}^2 x_2 = \left(\frac{\gamma P_0}{V_{20}} \right) A_{eff}^2 x_{12} + \frac{\rho L}{A_{pipe}} A_{eff}^2 \ddot{x}_{12} + \frac{4}{3\pi} \frac{K_{loss} \rho A_{eff}^3 X_0 \omega_f}{A_{pipe}^2} \dot{x}_{12} \quad (4.97)$$

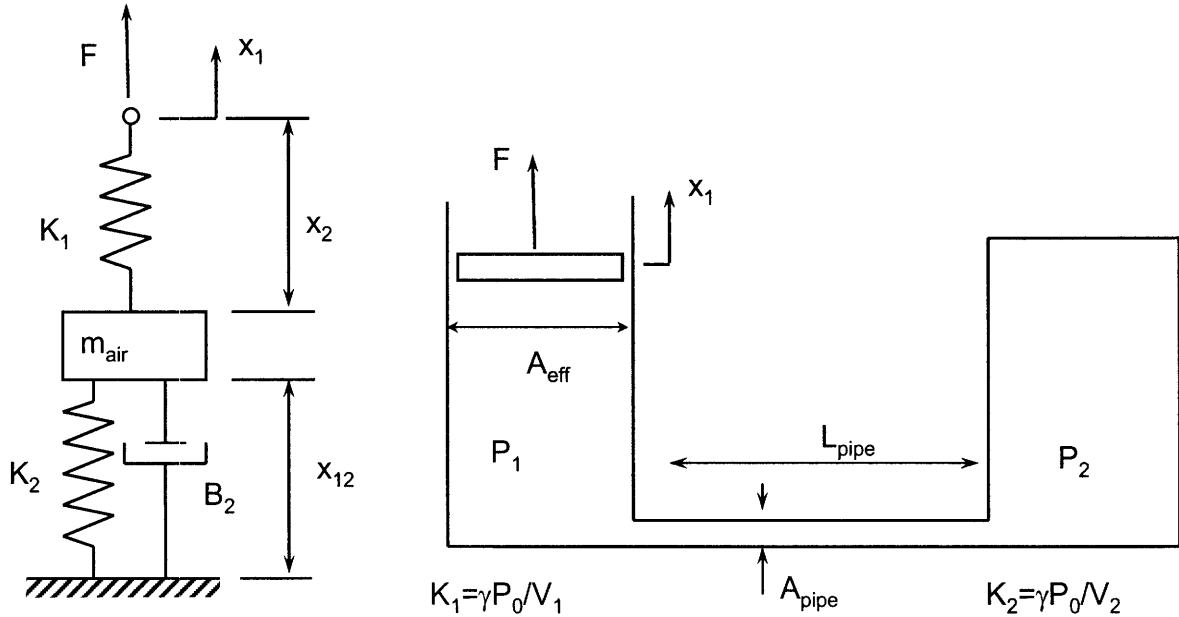


Figure 4-27 : Mass of air in the connecting tube introduces effective inertia in the system indicated by m_{air} . Consider the spring-mass-damper system depicted in Figure 4-27. The force-deflection relation for the spring K_1 and the equation of motion for the mass m_{air} are given by

$$F = K_1 x_2 = m_{air} \ddot{x}_{12} + B_2 \dot{x}_{12} + K_2 x_{12} \quad (4.98)$$

Combining the relation above with geometric compatibility $x_1 = x_2 + x_{12}$, we get:

$$x_1 = \frac{F}{K_1} \left(\frac{ms^2 + B_2s + K_1 + K_2}{ms^2 + B_2s + K_2} \right) \quad (4.99)$$

The complex stiffness of this system can be represented by the relation

$$K_{complex} = K_1 \left(\frac{m_{air}s^2 + B_2s + K_2}{m_{air}s^2 + B_2s + K_1 + K_2} \right) \quad (4.100)$$

$$K_{complex} = K_1 \left(\frac{s^2 + 2\zeta_2\omega_{corner1}s + \omega_{corner1}^2}{s^2 + 2\zeta'_2\omega_{corner2}s + \omega_{corner2}^2} \right) \quad (4.101)$$

where $\omega_{corner1}$, $\omega_{corner2}$, ζ_2 and ζ'_2 are defined from the equivalence of the two relations above.

4.4.4.4 Estimates of the effective parameters in the model

Equation (4.97) and Equation (4.98) have the exact same form and by comparing the two equations, the effective parameters for the equivalent mechanical system can be obtained as shown below.

$$K_1 = \left(\frac{\gamma P_0}{V_{10}} \right) A_{eff}^2 \quad (4.102)$$

$$K_2 = \left(\frac{\gamma P_0}{V_{20}} \right) A_{eff}^2 \quad (4.103)$$

$$m_{air} = \frac{\rho L}{A_{pipe}} A_{eff}^2 \quad (4.104)$$

$$B_2 = \frac{4}{3\pi} \frac{K_{loss} \rho A_{eff}^3 X_0 \omega_f}{A_{pipe}^2} \quad (4.105)$$

The lower and higher corner frequencies for the system are given by Equation (4.106) and Equation (4.107).

$$\omega_{corner1} = \sqrt{\frac{K_2}{m_{air}}} = \sqrt{\frac{\gamma RT_0 A_{pipe}}{V_2 L}} \quad (4.106)$$

For our system, with $d_{pipe}=3/8$ in, Auxiliary Volume $V_2 = 283$ in³ and $L_{pipe}=1$ m, we have $\omega_{corner1}=6.84$ Hz; and for $L_{pipe}=2$ m, we have $\omega_{corner1}=4.84$ Hz. Hence we see that the stiffness change occurs in the frequency range of interest.

$$\omega_{corner2} = \sqrt{\frac{K_1 + K_2}{m_{air}}} = \sqrt{\frac{\gamma RT_0 A_{pipe}}{L} \left(\frac{1}{V_{10}} + \frac{1}{V_2} \right)} \quad (4.107)$$

From Equation (4.101),

$$2\zeta_2 \omega_{corner1} = \frac{B_2}{m_{air}} = \frac{4}{3\pi} \frac{K_{loss} A_{eff} X_0 \omega_f}{L A_{pipe}} \quad (4.108)$$

$$\zeta_2 = \frac{2}{3\pi} \frac{K_{loss} X_0}{L} \left(\frac{A_{eff}}{A_{pipe}} \right) \left(\frac{\omega_f}{\omega_{corner1}} \right) \quad (4.109)$$

Since we are interested in the damping behavior around the corner frequency $\omega_{corner1}$, we can approximate the damping ratio ζ_2 , by Equation (4.110), by using the forcing frequency $\omega_f \approx \omega_{corner1}$. This analysis shows that the damping ratio is proportional to the amplitude of the oscillations. This expression can be used for the simulations in the next section.

$$\zeta_2 \approx \frac{2}{3\pi} \frac{K_{loss}}{L} \left(\frac{A_{eff}}{A_{pipe}} \right) X_0 \quad (4.110)$$

4.4.4.5 Simulation of air-spring with complex stiffness model

Bode plot of the complex stiffness in Figure 4-28, shows that the system exhibits a low stiffness $(K_1 K_2)/(K_1 + K_2)$ at low frequencies. Beyond the corner frequency $\omega_{corner1}$, the effective stiffness starts rising and the system behaves like a spring and a damper. The phase angle in the Bode plot indicates the damping introduced in this frequency range. Beyond the upper corner frequency $\omega_{corner2}$, the system behaves as a spring of higher stiffness K_1 . Beyond $\omega_{corner2}$, the inertia in the tube prevents any flow between the two chambers and this renders the auxiliary volume ineffective. For this simulation, we have used $K_1=K_2$, $\omega_{corner1}=5$ Hz and $\zeta_2=0.5$.

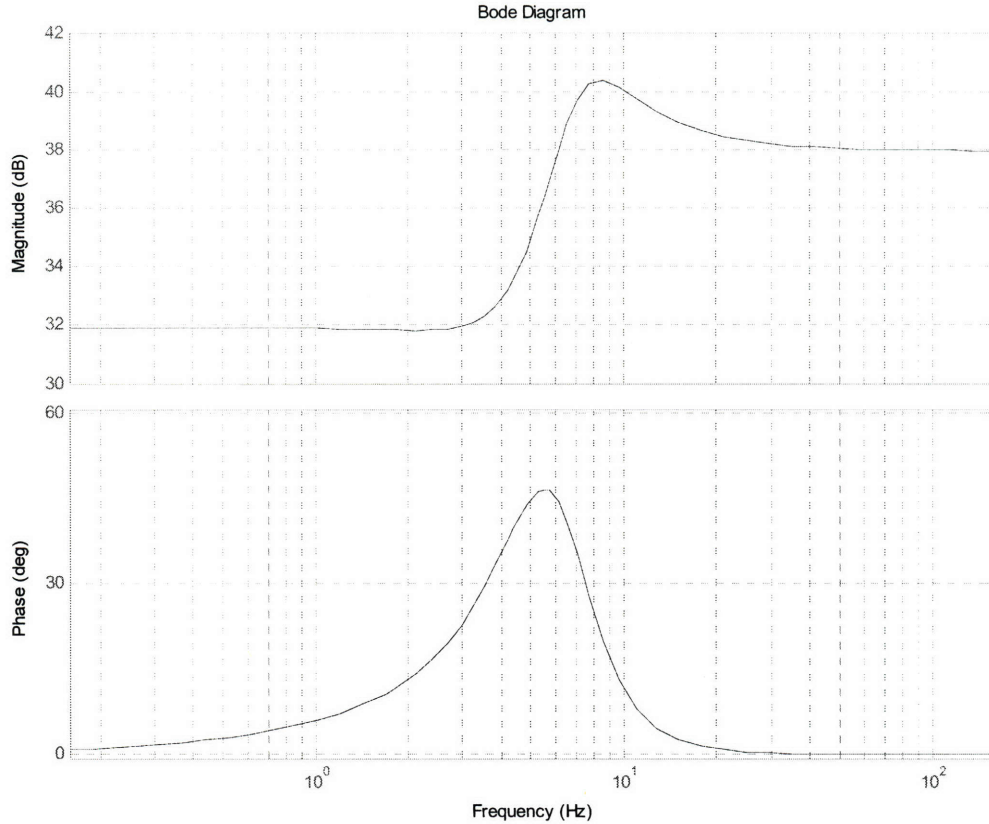


Figure 4-28: Bode plot showing the complex stiffness of an air spring with lower corner frequency of 5 Hz
 The complex stiffness of this system depends only on $\omega_{corner1}$, $\omega_{corner2}$ and ζ_2 . From the relations for $\omega_{corner1}$ and $\omega_{corner2}$, we can see that their dependence on various parameters such as L , A_{pipe} , V_{10} and V_2 can be evaluated without any difficulty. An interesting fact to note is that although the stiffness K_1 and K_2 , as well as the effective inertia m_{air} depend on pressure in the air spring and on the effective area A_{eff} of the air spring, their ratios (or the corner frequencies $\omega_{corner1}$ and $\omega_{corner2}$) are independent of the pressure in the air spring or the effective area A_{eff} of the air spring. This lets us calculate the corner frequencies just once and use the same value even when the operating pressure changes or when the effective area changes with the deflection of the air spring.

For the evaluation of ζ_2 , we need to quantify K_{loss} , which is straightforward for steady flow (White, 1999). We recommend experimental determination of a correction factor for unsteady flow. Due to the square-law damping, the effective damping increases with the amplitude of the oscillations. This trend is captured accurately by the term X_0 in damping calculation. In case the

damping is inadequate, we can make design changes, such as increasing the roughness of the tubing or inserting an orifice in the tubing etc., to introduce additional damping in the system.

To study the sensitivity of the complex stiffness of the system to the damping coefficient ζ_2 , the frequency response of the system is simulated for different values of the damping coefficient ζ_2 . The Bode plot for the complex stiffness, in Figure 4-29, shows that the system is relatively insensitive to the parameter ζ_2 .

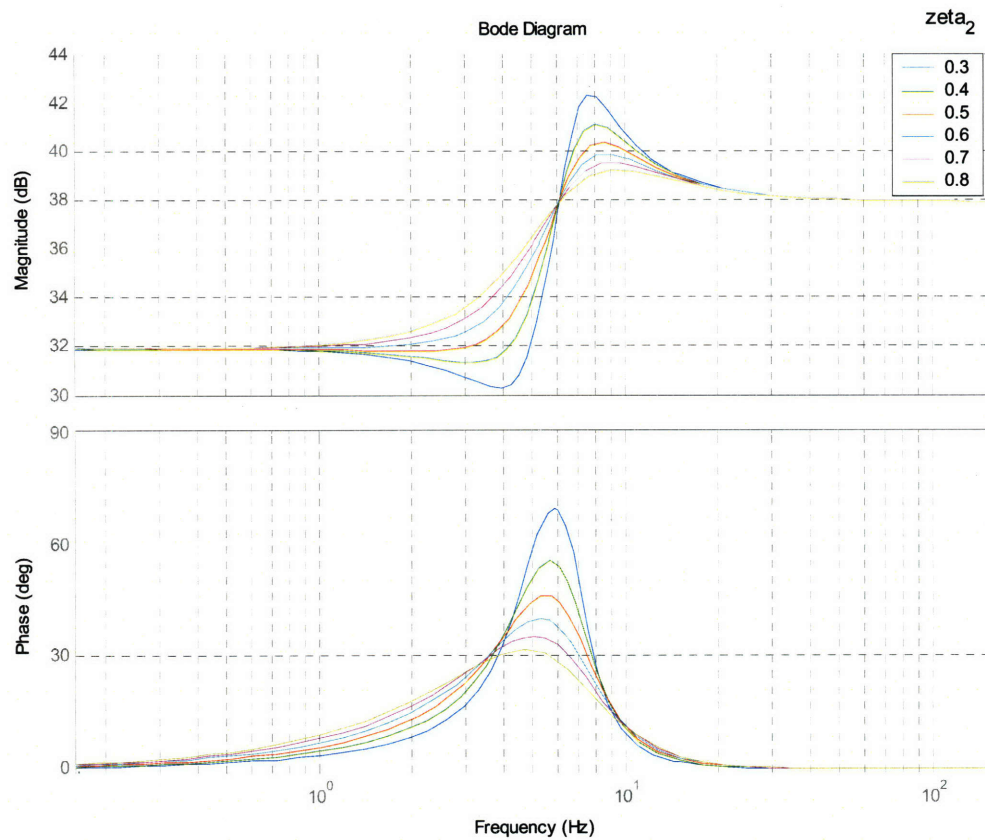


Figure 4-29 : Complex stiffness of the air spring for different values of the parameter ζ_2

4.4.4.6 Comparison with experimental results

To verify our derivation, we compare our predicted complex stiffness to the experimentally observed frequency response reported by Berg (1999). The parameters of interest in this paper are $L_{pipe} = 2.2$ m; $r_{pipe} = 20\text{mm} = 0.02$ m; $V_{10} = 35$ litres = 0.035 m³; and $V_2 = 100$ litres = 0.1 m³.

From this calculation,

$$\omega_{corner1} = \sqrt{\frac{\gamma RT_0 A_{pipe}}{V_2 L}} = \sqrt{\frac{1.4 \times 287 \times 300 \times \pi \times 0.02^2}{0.1 \times 2.2}} = 4.17 \text{ Hz} \quad (4.111)$$

$$\omega_{corner2} = \sqrt{\frac{\gamma RT_0 A_{pipe}}{L} \left(\frac{1}{V_{10}} + \frac{1}{V_2} \right)} = \sqrt{\frac{1.4 \times 287 \times 300 \times \pi \times 0.02^2}{2.2} \left(\frac{1}{0.035} + \frac{1}{0.1} \right)} = 8.19 \text{ Hz} \quad (4.112)$$

Both the values agree well with the graphs below, validating our assumption of almost compressible flow in the tubing.

The system has non-linear damping as was seen in our formulation and hence depends on the amplitude of oscillations as can be seen from the different frequency responses for different amplitudes in graph (a) of Figure 4-30. Secondly additional damping can be introduced in the system by inserting an orifice in the tubing, as seen from graph (b) in Figure 4-30.

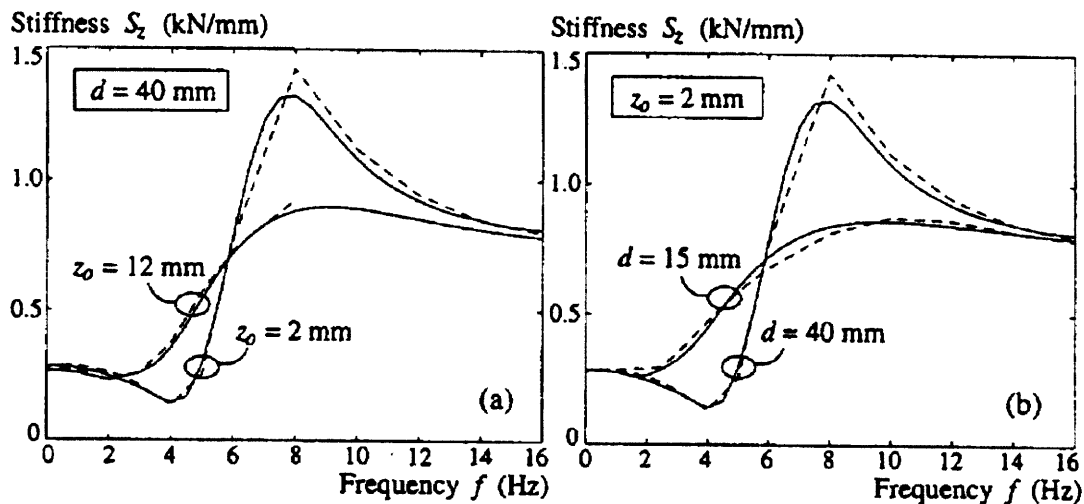


Fig. 7. Vertical stiffness vs. frequency. $P = 80 \text{ kN}$. Calculation (solid line) and measurement (dashed line). (a) Without orifice damping: amplitudes 2 and 12 mm, (b) Amplitude 2 mm: without/with orifice damping. Model data: $K_{sz} = 0.250 \text{ kN/mm}$, $F_{fz,max} = 0.5 \text{ kN}$, $z_2 = 10 \text{ mm}$, $K_{vz} = 0.420 \text{ kN/mm}$, $C_{z\beta} = 0.000065/0.000400 \text{ kN(s/mm)}^\beta$ (no orifice / orifice diameter $d = 15 \text{ mm}$), $\beta = 1.8$ and $M = 215 \text{ kg}$.

Figure 4-30 : Experimentally observed frequency response of an air spring with auxiliary volume (Berg 1999)

4.4.5 Effect of inertia in pipe on road noise isolation for a quarter-car SDOF model

Simulation was done to determine the effect of the inertia of air in the pipe on the road noise isolation performance for a quarter car SDOF model. We have compared the road noise isolation transfer function x_s/x_r for a soft suspension, a stiff suspension and an air-spring with an auxiliary

volume in the soft setting (as shown in Figure 4-31). For this simulation, we have used $K_{stiff}=2K_{soft}$ and $B_{stiff} = \sqrt{2}B_{soft}$ to maintain ζ constant. For the air spring with auxiliary volume, we have assumed equal volumes, and $K_1=K_2=K_{stiff}$ such that this suspension has low stiffness of $K_{low}=K_{soft}$ at low frequencies, and a high stiffness of $K_{high}=K_{stiff}$ at high frequencies. The effective mass of air m_{air} is such that the corner frequency is $\omega_{corner1}=5\text{Hz}$, and B_2 is such that $\zeta_2 = B_2 / 2\sqrt{K_2 m_{air}} = 0.5$. The three road noise isolation transfer function for the soft suspension, stiff suspensions and an air-spring with an auxiliary volume in the soft setting are given by Equation (4.113), Equation (4.114), and Equation (4.115) respectively.

$$\frac{x_s}{x_r} = \frac{B_{soft}s + K_{soft}}{Ms^2 + B_{soft}s + K_{soft}} \quad (4.113)$$

$$\frac{x_s}{x_r} = \frac{B_{stiff}s + K_{stiff}}{Ms^2 + B_{stiff}s + K_{stiff}} \quad (4.114)$$

$$\frac{x_s}{x_r} = \frac{B_{soft}s + K_{complex}}{Ms^2 + B_{soft}s + K_{complex}} \quad (4.115)$$

where $K_{complex}$ complex stiffness given by Equation (4.101).

From the Bode plot in Figure 4-32, the difference between the road noise isolation transfer functions, for the soft suspension and the air-spring with auxiliary volume, is marginal. Thus the inertia of air in the pipe has a negligible effect on the road noise isolation for a quarter car SDOF model. The same simulation was carried out for different values of $\omega_{corner1}$ and ζ_2 and the results were insensitive to both the parameters as long as $\omega_{corner1} > 2\text{Hz}$, which is true for our construction. We conclude that although the stiffness changes from K_{low} at low frequencies to K_{high} at high frequencies, this does not affect the road-noise isolation as the high frequency asymptotic behavior depends on the damping coefficient and not the stiffness. Moreover the damping added due to the pipe inertia and the friction losses is not significant, as indicated by the phase plot in Figure 4-29.

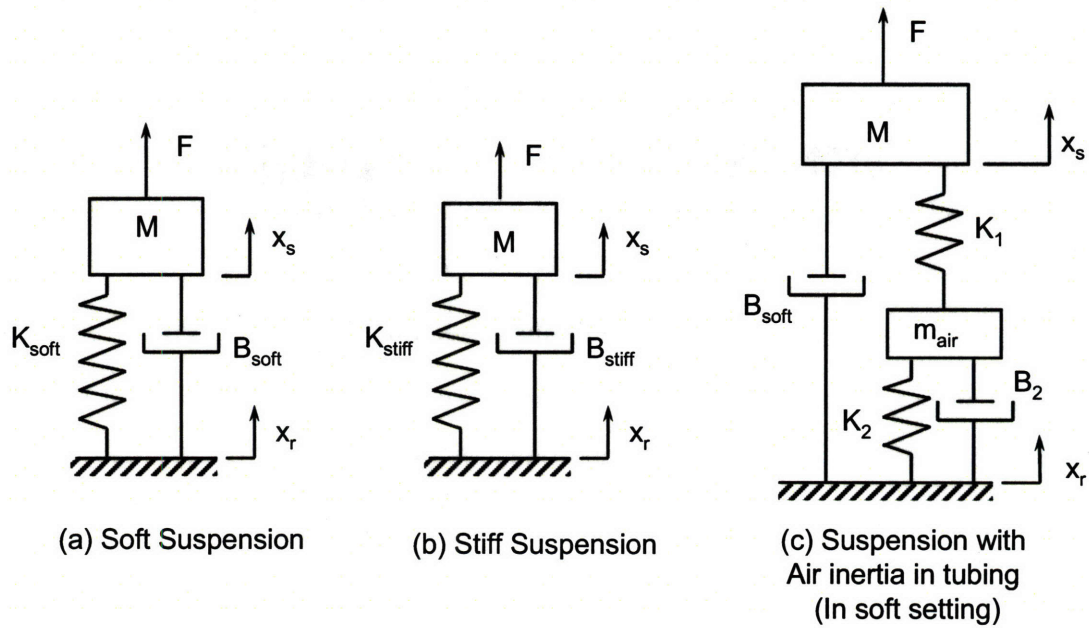


Figure 4-31 : Comparison of SDOF quarter car model road noise isolation for a soft suspension, stiff suspension and an air-spring with auxiliary volumes

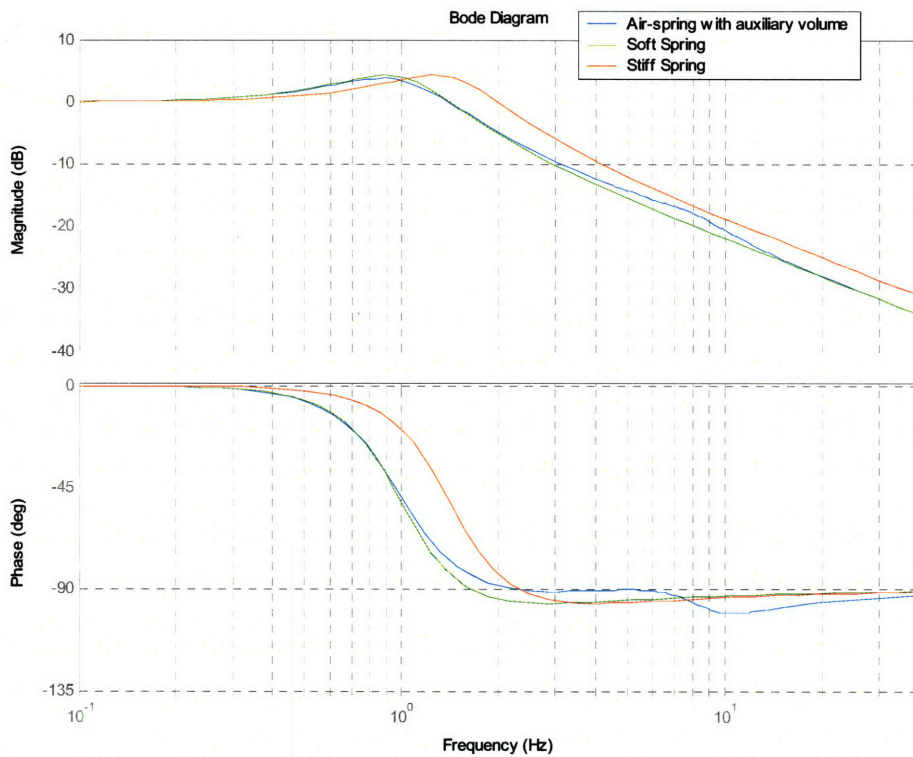


Figure 4-32 : Bode plot showing comparison of a SDOF quarter car model road noise isolation transfer functions for a soft suspension, stiff suspension and an air-spring with auxiliary volumes

4.4.6 Effect of inertia in pipe on road noise isolation for a quarter-car 2DOF model

From the Bode plot in Figure 4-32, we see that the deviation of the air-spring suspension with auxiliary volume from the soft suspension, although small, occurs near the wheel hop frequency. As a result it is important to determine the effect of the inertia of air in the pipe on the road noise isolation for a quarter car 2-DOF model. We have compared the road noise isolation transfer function x_s/x_r for a soft suspension, a stiff suspension and an air-spring with an auxiliary volume in the soft setting (as shown in Figure 4-33). The parameters for this simulation are the same as the previous case, with the addition of two more parameters: $m_{us}=M/10$ and $K_t=10K_{soft}$. The three road noise isolation transfer function for the soft suspension, stiff suspensions and an air-spring with an auxiliary volume in the soft setting are given by Equation (4.116), Equation (4.117) and Equation (4.118) respectively.

$$\frac{x_s}{x_r} = \frac{K_t (B_{soft}s + K_{soft})}{(Ms^2 + B_{soft}s + K_{soft})(m_{us}s^2 + B_{soft}s + K_t + K_{soft}) - (B_{soft}s + K_{soft})^2} \quad (4.116)$$

$$\frac{x_s}{x_r} = \frac{K_t (B_{stiff}s + K_{stiff})}{(Ms^2 + B_{stiff}s + K_{stiff})(m_{us}s^2 + B_{stiff}s + K_t + K_{stiff}) - (B_{stiff}s + K_{stiff})^2} \quad (4.117)$$

$$\frac{x_s}{x_r} = \frac{K_t (B_{soft}s + K_{complex})}{(Ms^2 + B_{soft}s + K_{complex})(m_{us}s^2 + B_{soft}s + K_t + K_{complex}) - (B_{soft}s + K_{complex})^2} \quad (4.118)$$

From the Bode plot in Figure 4-34, we can see that the inertia of air in the pipe has a negligible effect on the road noise isolation for a quarter car 2-DOF model. The same simulation was carried out for different values of $\omega_{corner1}$ and ζ_2 and the results were insensitive to both the parameters. We conclude that although the stiffness changes from K_{low} at low frequencies to K_{high} at high frequencies, this does not affect the road-noise isolation for the quarter-car 2-DOF model.

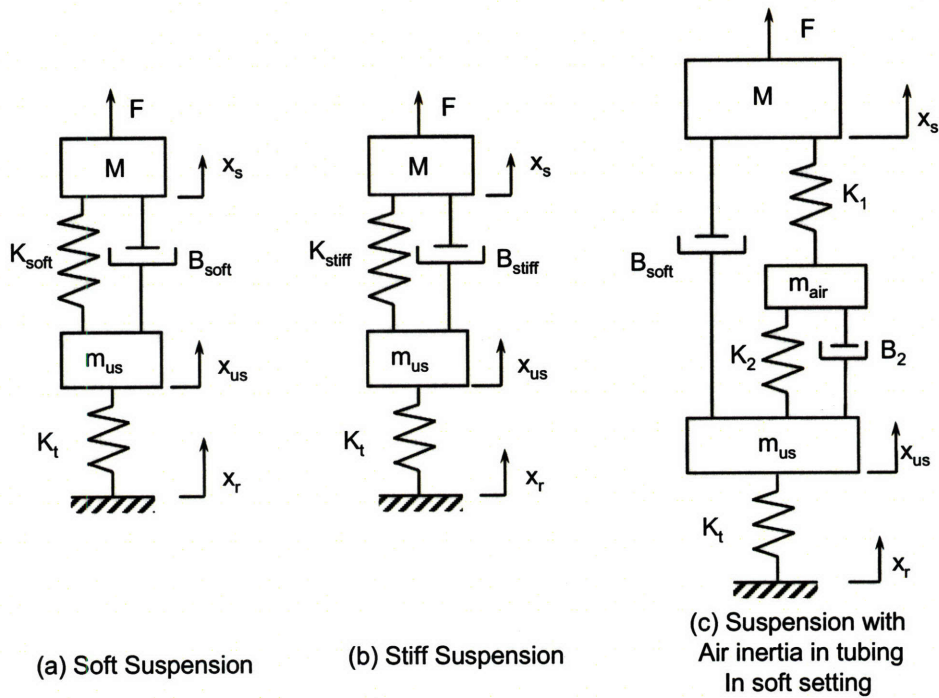


Figure 4-33 : Comparison of 2-DOF quarter car model road noise isolation for a soft suspension, stiff suspension and an air-spring with auxiliary volumes

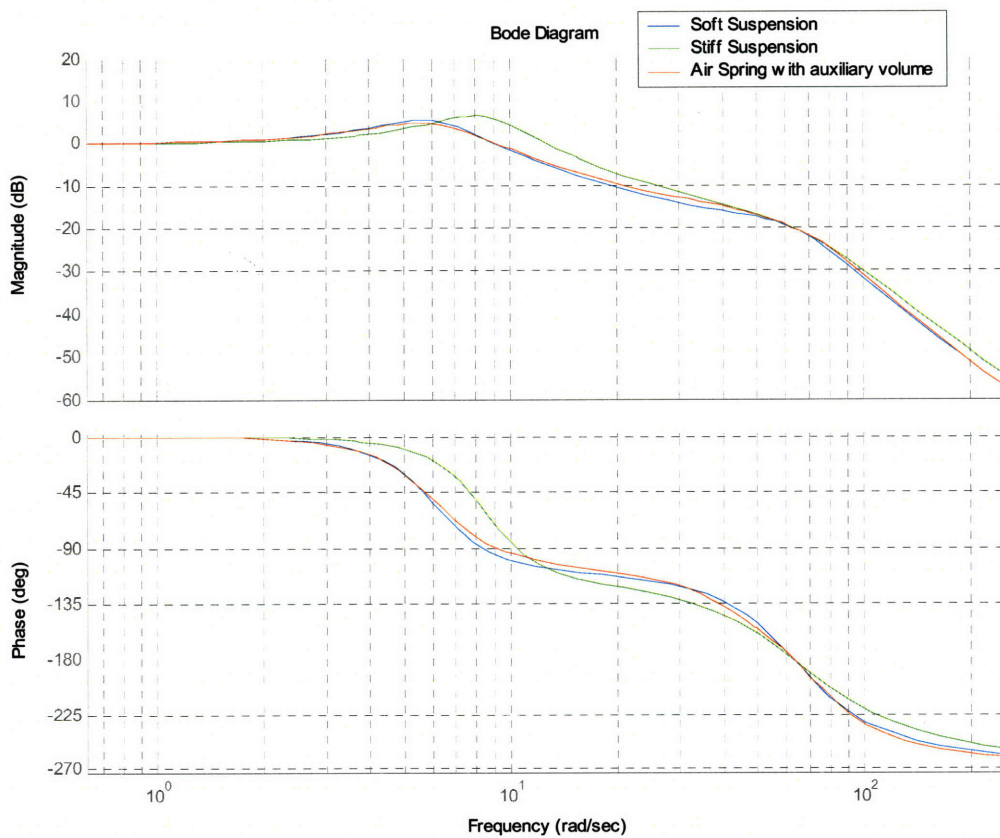


Figure 4-34 : Bode plot showing comparison of 2-DOF quarter car road noise isolation transfer functions for a soft suspension, stiff suspension and an air-spring with auxiliary volumes

4.5 Suspension Prototype

4.5.1 Fabrication/Implementation

We have implemented this customizable pneumatic suspension system, with air springs connected to auxiliary volumes through valves, on a used 1999 Honda Civic. The schematic is shown in Figure 4-5. A compressor (VIAIR 380C) is used to pump air into the air into a 5 gallon air tank (accumulator). The compressor is capable of maximum pressure of 200psi. Pressure sensor switch is used to measure the pressure in the air tank (accumulator) for compressor on/off control to maintain the pressure in the air tank in the range 145-175psi. The pressure switch turns the compressor on when the pressure falls below 145psi and turns it off when it reaches 175psi. The coil springs were replaced with air-springs on the front and rear suspension. Figure 4-35 and Figure 4-36 show the front air spring in the extended and compressed position. The air springs used have maximum inflation pressure of 100psi and blow-off pressure of 175psi (Air Lift Company part number 75440 for front suspension; part number 75540 for rear suspension). Two auxiliary volumes per air-spring are used. Off the shelf medical cylinders, rated to 1800psi, with standard outside diameter of 4.38in and lengths of 16.2in and 25.2in (and volumes 172 in³ and 283 in³) were used. This OD was chosen to enable the replacement of existing cylinders and convenient packaging of new cylinders, as the medical cylinders are available in different lengths for this OD. Moreover the largest available lengths for this OD were selected, so as to facilitate convenient replacement of these with shorter cylinders of the same OD, if the need arose. Air brake pneumatic nylon tubing (SAE J844 Type B) with 0.5in OD and 0.375in ID is used for connecting the air springs to the auxiliary volumes and the accumulator. Holes had to be drilled into structural elements to gain access to the air springs with the air brake lines for connection to the auxiliary volumes and the compressor and accumulator as shown in Figure 4-37. Certain areas around the air springs had to be cut and polished to ensure that it does not rub against or puncture the air-bag. For instance, the flanges on the front suspension upper control arm had to be trimmed and polished (Figure 4-36). As mentioned in a previous section, automated ball valves (A-TControls Series 22, 0.5in ID, electrically actuated ball valve) were used instead of solenoid valves to connect the auxiliary volumes to the air-springs. Four solenoid valves were used for controlling the flow from the accumulator to the individual air-springs to increase the ride-height. Four more were used for controlling the flow out of the air-spring to the atmosphere to reduce the ride-height.

4.5.2 Sensors and data acquisition

Quadrature Incremental encoders are used to measure suspension deflection and steering wheel rotation. Heavy-duty industrial encoders (US Digital part number HD-25-2500) are used on the rear suspension lower control arm to withstand rugged exterior environment. These are capable of 2500 pulses per revolution or resolution 10000 counts per revolution. Due to packaging constraints, these industrial encoders could not be mounted on the front lower control arm. Medium-duty encoders (Metronix part number H40-8-3600) are mounted on the front lower control arm (LCA), as shown in Figure 4-37. These are capable of 3600 pulses per revolution or resolution 14400 counts per revolution. Another rotary encoder (US Digital part number HD-25-1000) is mounted on the steering column to measure the steering wheel rotation. Mounting in the restricted space was challenging and special mounts had to be fabricated to mount them to the suspension control arms. The mounting on the steering column was especially challenging as the shaft is connected to the steering linkage on one end and the steering wheel on the other; and there is no access to the steering column to slide a gear on to it. This problem was overcome by drilling a hole in the spur gear to the exact OD of the steering column, cutting a spur gear into half, threading one half and making a clearance hole in the other and then joining them together with two screws and washers to compensate for the material lost while cutting with a band-saw. To measure the lateral and longitudinal acceleration, a 3-axis $\pm 3g$ accelerometer (Dimension Engineering DE-ACCM3D) was mounted on the longitudinal axis of the car close to the CG.

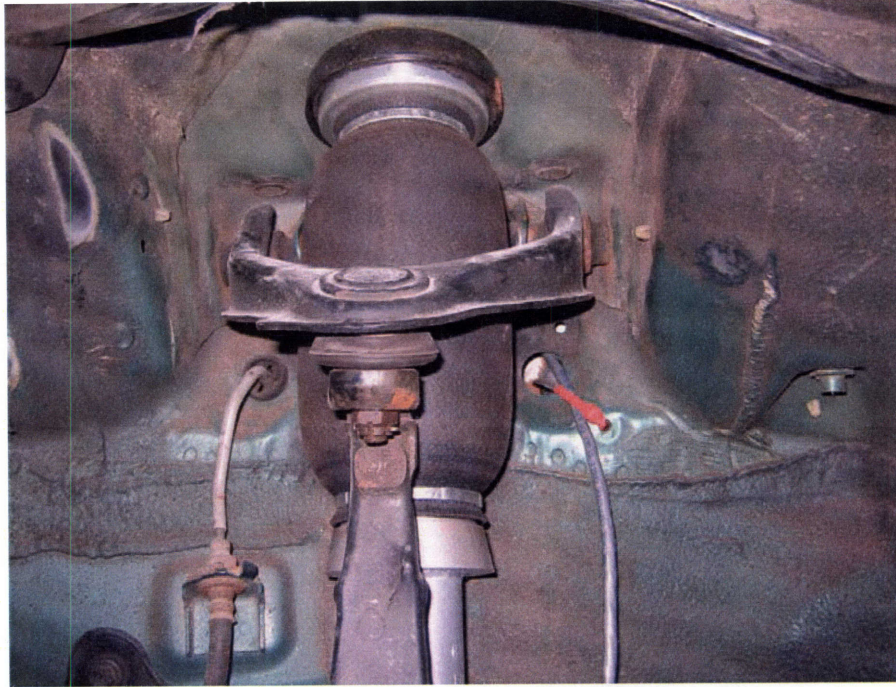


Figure 4-35 : Front air-spring in the extended position

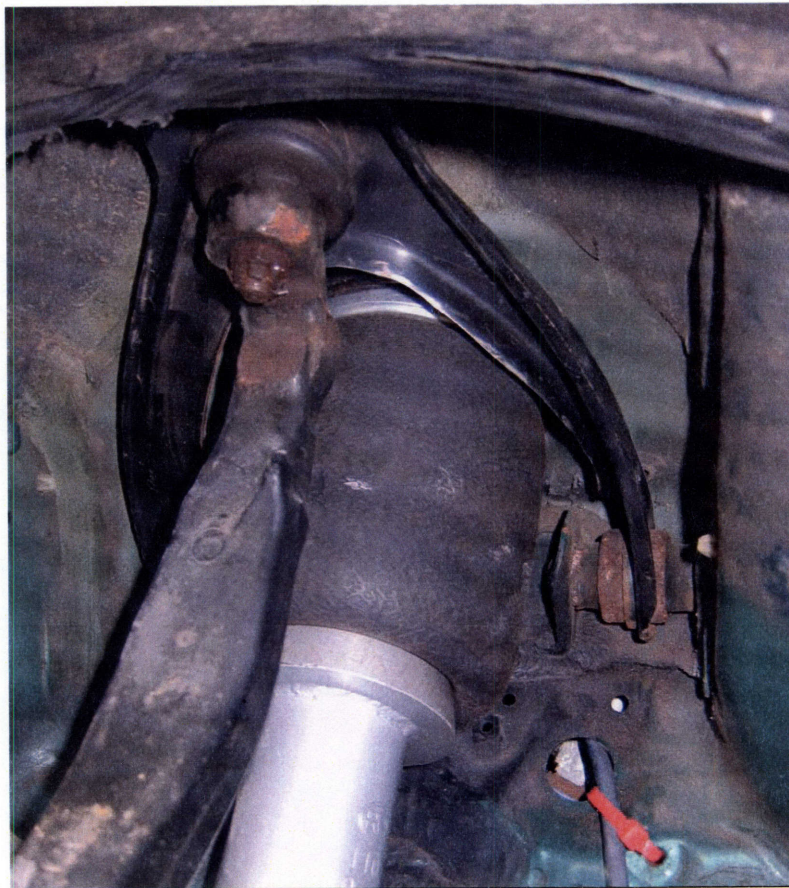


Figure 4-36 : Front air spring in the compressed position. The flange of the upper control arm is trimmed and polished for clearance

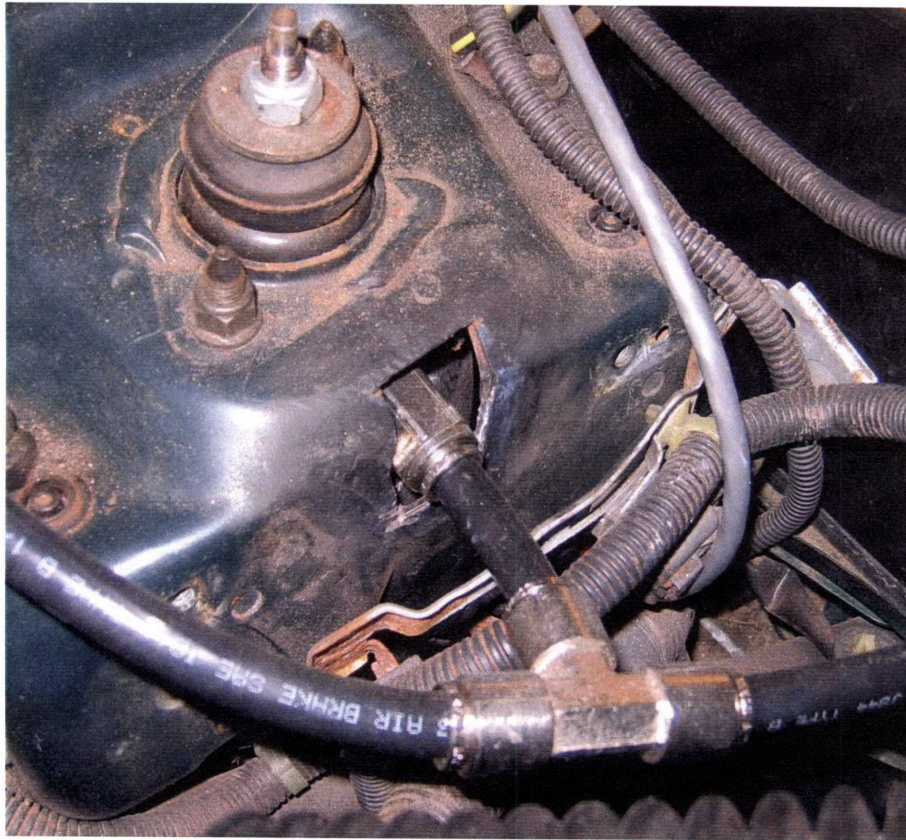


Figure 4-37 : Holes cut in the structural members, air-brake tubing and air-line fittings

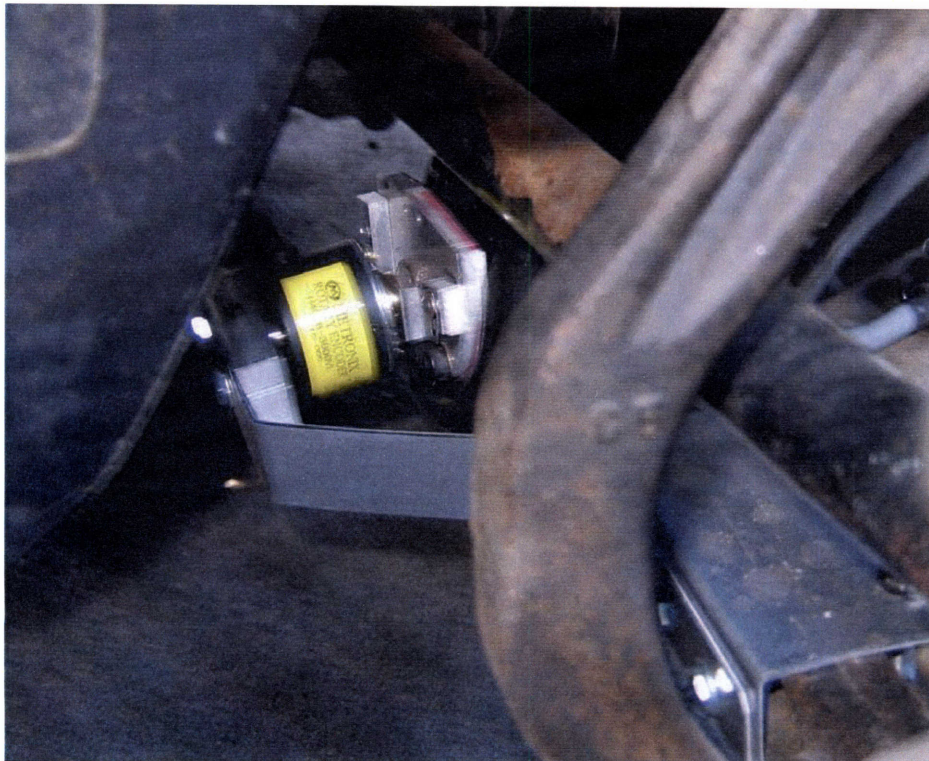
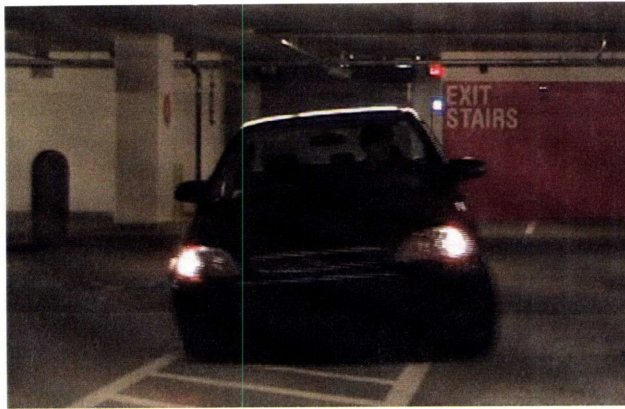


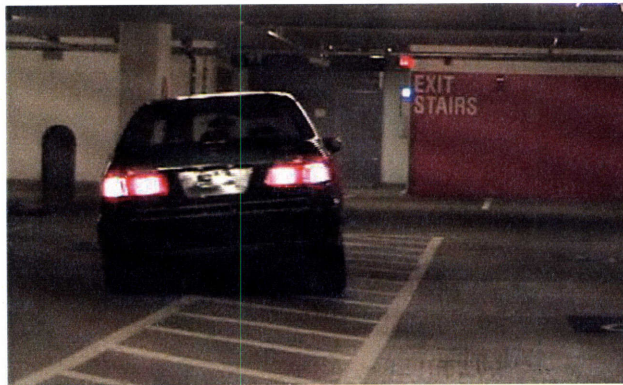
Figure 4-38 : Front encoder mounting



Soft Setting (Front View)



Stiff Setting (Front View)



Soft setting (Rear View)



Stiff Setting (Rear View)

Figure 4-39 : Demonstration of stiffness reduction by addition of auxiliary volumes: Excessive roll in the soft setting for the same speed ($V=15\text{mph}$) and same radius of turn

Table 4.1 : Suspension kinematics and spring mounting data (See Figure 4-10)

	Front Suspension Geometry	Rear Suspension Geometry
L	385 mm (15.15in)	425 mm (16.73in)
l_s	270 mm (10.63in)	318 mm (12.5in)
Maximum wheel travel	160 mm	130 mm
Maximum angular travel	$2\sin^{-1}(0.5 \times 160/385) = 23^\circ$	$2\sin^{-1}(0.5 \times 130/425) = 17.5^\circ$
Maximum spring deflection	112 mm	97 mm

4.6 Experiments

The experiment to determine the effective area profile $A_{eff}(x)$ for the front and rear suspensions has been described earlier. In the next experiment to determine roll behavior and steady-state cornering, the car was driven in a circle of radius 84ft at constant speed. The speed was increased in steps of 2.5mph, starting with 10mph up to the maximum speed considered safe by the driver. The maximum speed varied for the different stiffness cases from 22.5mph to 27.5mph. The variables measured were the suspension deflections at the four wheels, steering wheel angle, vehicle speed, and accelerations in the car-reference frame. The minimum recommended radius of turn for this procedure is about 100ft (SAE, 1981; ISO, 2004), but the parking lot we used allowed only a radius of 84ft. An attempt was made to maintain the speed constant and to maintain the car along the circular path of radius 84ft. This was difficult as the parking lot was crowned and the speed changed at the sloped surfaces and steering angle adjustments had to be made to maintain the car along the circular path. It was difficult to maintain speed constant at low speed and trajectory following was difficult at high speeds. Moreover the parking lot surface was quite rough. Due to these reason the data is quite noisy. A sample data collected is shown in Figure 4-40, where the measured parameters are shown as a function of time. The speed of the car is shown at the bottom of each data set.

The following settings were tested:

1. All valves open (All volumes connected to the air-springs)
2. Valves to big volumes open; Valves to small volumes closed
3. Valves to small volumes open; Valves to big volumes closed
4. All valves closed (None of the volumes connected to the air-springs)
5. Valves to front volumes open; Valves to front volumes closed
6. Valves to rear volumes open; Valves to front volumes closed

The problem of noisy data was overcome by collecting data for two or more rotations of the circular curve and by averaging this data over time. In this section we will present the front and rear suspension deflection trends in compression and extension. The front suspension deflection trends can be explained by the stiffness model discussed earlier ($K=K_A+K_T$). The

rear suspension deflection trends, however exhibit counter-intuitive behavior, which is explained by proposing a non-linear model for the spring.

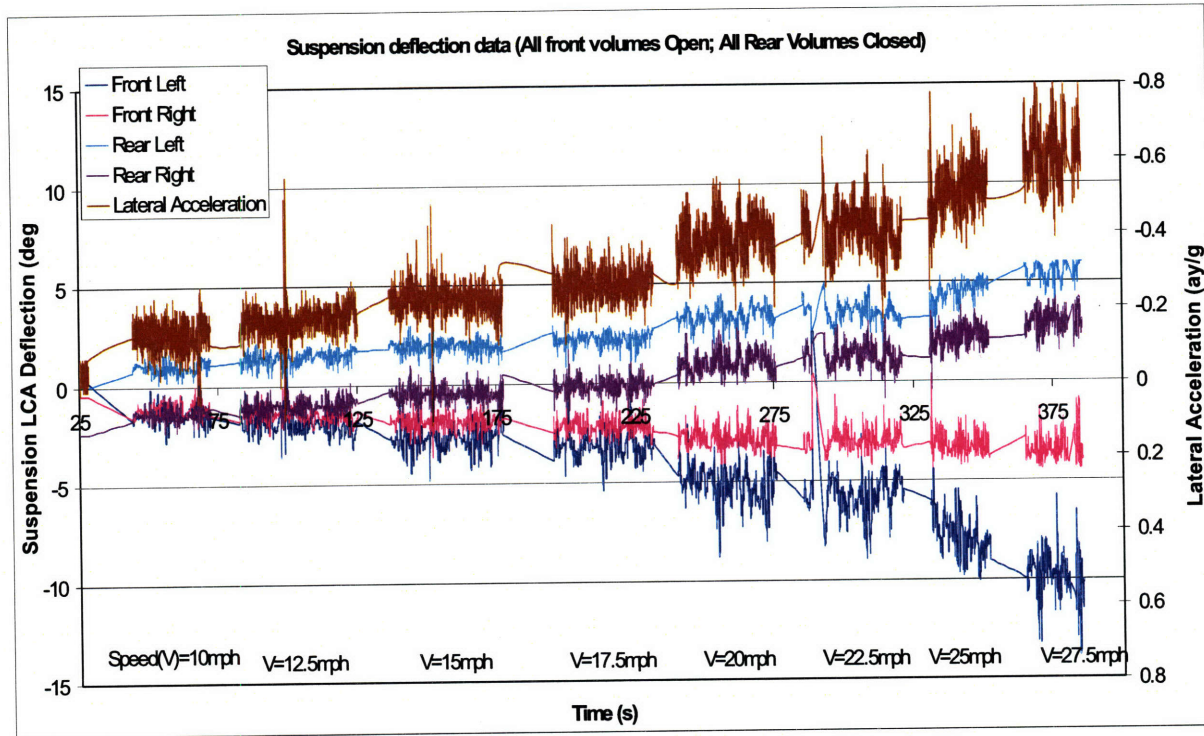


Figure 4-40 Suspension data measurements for steady state cornering where speed is increased in increments on 2.5mph as indicated below the data sets

4.6.1 Determination of lateral acceleration from body-mounted accelerometers

In the experimental set-up, the accelerometers are mounted on the car body which undergoes roll θ under these test conditions. Consider two reference frames YZ and yz with the origin at the CG of the car, such that yz moves with the roll of the car, whereas YZ does not. Since YZ does not roll with the car, Z is always aligned with gravity and Y is parallel to the ground. The accelerometers are mounted on the car and as a result move with the yz frame. The acceleration in the YZ frame is given by the Equation (4.119).

$$a_y = \frac{MV^2}{R} \tag{4.119}$$

$$a_z = -g$$

These are related to the measure acceleration a_y and a_z by the relation in Equation (4.120).

$$\begin{Bmatrix} a_y \\ a_z \end{Bmatrix} = \begin{bmatrix} \cos \theta & \sin \theta \\ -\sin \theta & \cos \theta \end{bmatrix} \begin{Bmatrix} a_Y \\ a_Z \end{Bmatrix} \quad (4.120)$$

This from the two readings a_y and a_z , we can determine both lateral acceleration a_Y as well as the body roll θ .

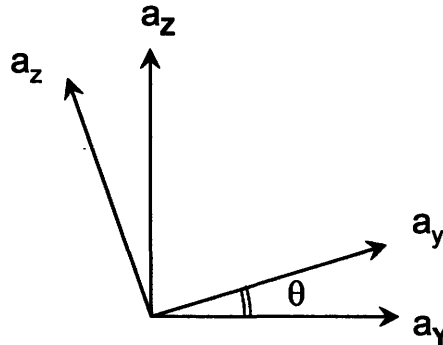


Figure 4-41 Determination of lateral acceleration and roll from accelerometer readings

4.6.2 Front suspension deflection trends

The front suspension stiffness values for gauge pressure of 90psi are shown in Table 4.2. The observed front suspension deflection as a function of lateral acceleration for the four different stiffness settings is shown in Figure 4-42 for extension and Figure 4-43 for compression. Due to the difficulty in maintaining a constant speed and radius of curvature on a crowned road and the noisy suspension deflection data caused by the road roughness, the error margin in these data points is significantly large. But the trend of decreasing stiffness with increasing effective volume is evident from the two graphs.

Table 4.2 Stiffness calculations for the front suspension ($P_0 - P_a = 90\text{psi}$)

V_0 (in ³)	$K_A = -(P_0 - P_a) \frac{dA_{eff}}{dx}$	$K_T = \gamma \frac{P_0}{V_0} A_{eff}^2$	$\frac{dF}{dx} = -(K_A + K_T)$
107	37532 N/m	28137 N/m	-65669 N/m
279	37532 N/m	10791 N/m	-48323 N/m
390	37532 N/m	7720 N/m	-45251 N/m
562	37532 N/m	5357 N/m	-42889 N/m

The calculated stiffness values from Table 4.2 indicate that the stiffness due to area change K_A (37.5 kN/m) is greater than the thermodynamic stiffness K_T (28.1 kN/m) in the stiffest setting. Since we can only reduce stiffness K_T , the achievable range of stiffness is limited (42-65 kN/m), with $K_{max}/K_{min}=1.5$. This ratio can be improved if K_A is smaller than K_T . From the graph of effective area profile for the front air-spring in Figure 4-12, we see that $dA_{eff}(x)/dx$ is lower than average at a gauge pressure of 80psi. The calculated stiffness components at this operating pressure are shown in Table 4.3. In this case, the area change stiffness K_A (17.8 kN/m) is much smaller than the thermodynamic stiffness K_T (32.19 kN/m) and at this “sweet spot” we get a larger stiffness variation in terms of the ratio $K_{max}/K_{min}=2.1$. This “sweet spot” can be exploited by the designer to achieve a larger stiffness ratio K_{max}/K_{min} , but this leads to coupling as our design intent is to achieve independent control stiffness and ride-height. Notice that although we get a larger stiffness ratio K_{max}/K_{min} , this comes at the cost of lowering the two stiffness values K_{max} and K_{min} . This is not acceptable and during testing, the car bottomed out at very low lateral accelerations due to reduced ride-height and lower stiffness.

Table 4.3 Stiffness calculations for the front suspension ($P_0 - P_a = 80$ psi)

V_0 (in ³)	$K_A = -(P_0 - P_a) \frac{dA_{eff}}{dx}$	$K_T = \gamma \frac{P_0}{V_0} A_{eff}^2$	$\frac{dF}{dx} = -(K_A + K_T)$
107	17793 N/m	32190 N/m	-49983 N/m
279	17793 N/m	12345 N/m	-30138 N/m
390	17793 N/m	8832 N/m	-26625 N/m
562	17793 N/m	6129 N/m	-23922 N/m

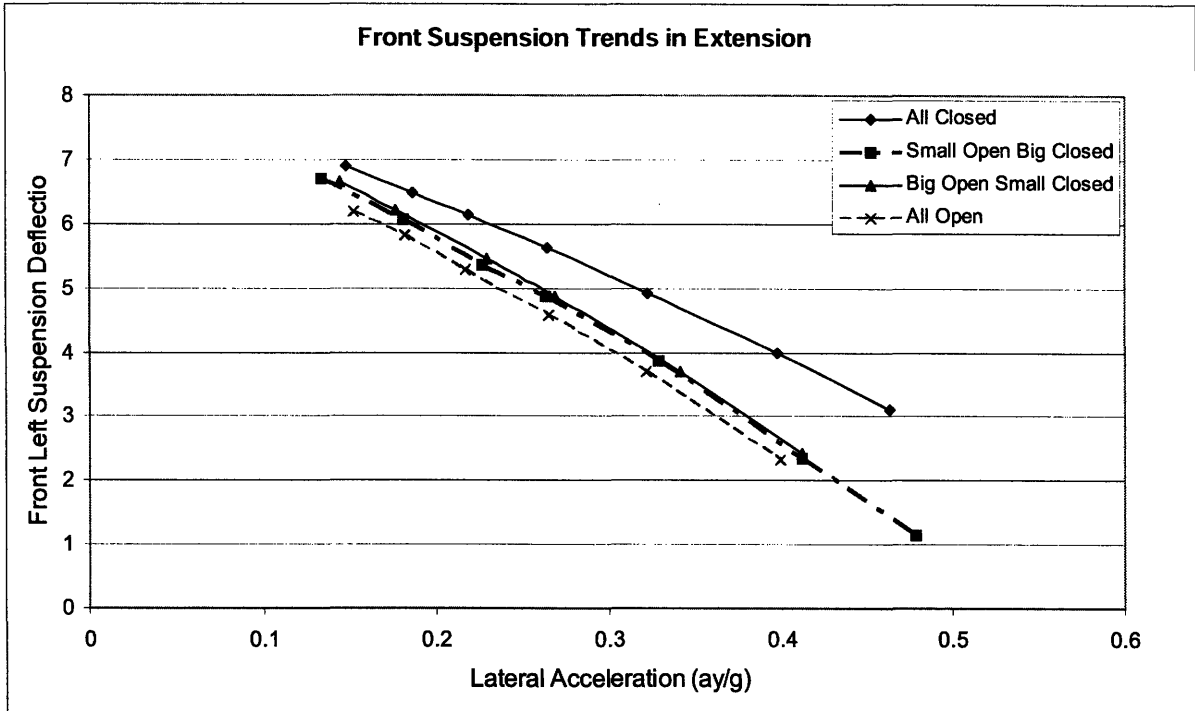


Figure 4-42 Front Suspension Trends in Extension ($P_0 - P_a = 90\text{psi}$)

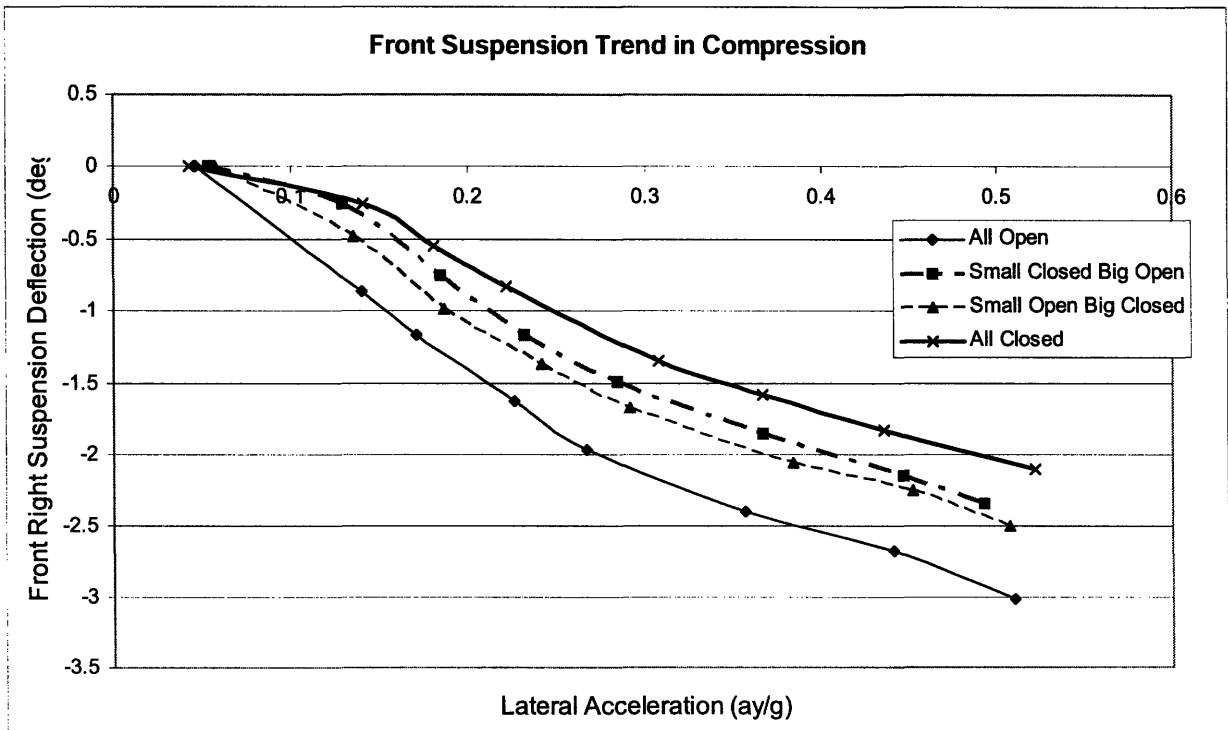


Figure 4-43 Front Suspension Trends in Compression ($P_0 - P_a = 90\text{psi}$)

4.6.3 Rear suspension deflection trends

The rear suspension stiffness values for gauge pressure of 90psi are shown in Table 4.4. It can be seen from the stiffness values, that the area change stiffness K_A (73.9 kN/m) is more than 6 times the thermodynamic stiffness K_T (11.36 kN/m) in the stiffest setting. As a result, the achievable range of stiffness is very limited (76.3-85.3 kN/m) with the ratio $K_{max}/K_{min} = 1.11$. With such a small stiffness ratio, we expect to see no change in stiffness due to the noise in the system. The rear air-spring effective area profile in Figure 4-13 shows that $dA_{eff}(x)/dx$ is almost constant for the rear air-spring and there is no “sweet spot” like the front air-spring had at 80psi. From the equation for K_A , we observe that $K_A \propto (P_0 - P_a)$ for constant $dA_{eff}(x)/dx$, and hence reduces with lower operating pressure. Whereas, from the equation for K_T , we see that $K_T \propto A_{eff}$ (as the weight of the car is fixed and $P_0 A_{eff} \approx Mg$) and A_{eff} increases with decreasing operating pressures. Thus we can increase the relative contribution of K_T to the total stiffness by operating at a lower static pressure.

Table 4.4 Stiffness calculations for the rear suspension ($P_0 - P_a = 90\text{psi}$)

V_0 (in ³)	$K_A = -(P_0 - P_a) \frac{dA_{eff}}{dx}$	$K_T = \gamma \frac{P_0}{V_0} A_{eff}^2$	$\frac{dF}{dx} = -(K_A + K_T)$
122	73903 N/m	11366 N/m	-85269 N/m
294	73903 N/m	4717 N/m	-78620 N/m
405	73903 N/m	3424 N/m	-77327 N/m
577	73903 N/m	2403 N/m	-76306 N/m

The rear suspension stiffness values for gauge pressure of 70psi are shown in Table 4.5. At this setting, the achievable range of stiffness (60-72 kN/m) is marginally greater than the previous case and the stiffness ratio marginally improves to $K_{max}/K_{min} = 1.2$. The experiment was carried out with the rear air-spring static gauge pressure at 70psi. The observed rear suspension deflection as a function of lateral acceleration for the four different stiffness settings is shown in Figure 4-44 for extension and Figure 4-45 for compression. The data for suspension deflection in extension in Figure 4-44 shows practically no change in stiffness, whereas the data for suspension deflection in compression in Figure 4-45 shows a disproportionately large stiffness

change. This departure of the observed behavior from the linear stiffness calculations is due to the large deflections. To explain this we look at the second derivative of the air-spring values force-deflection relation.

Table 4.5 Stiffness calculations for the rear suspension ($P_0 - P_a = 70\text{psi}$)

$V_0 \text{ (in}^3\text{)}$	$K_A = -(P_0 - P_a) \frac{dA_{eff}}{dx}$	$K_T = \gamma \frac{P_0}{V_0} A_{eff}^2$	$\frac{dF}{dx} = -(K_A + K_T)$
122	57480 N/m	15200 N/m	-72680 N/m
294	57480 N/m	6308 N/m	-63788 N/m
405	57480 N/m	4579 N/m	-62059 N/m
577	57480 N/m	3213 N/m	-60694 N/m

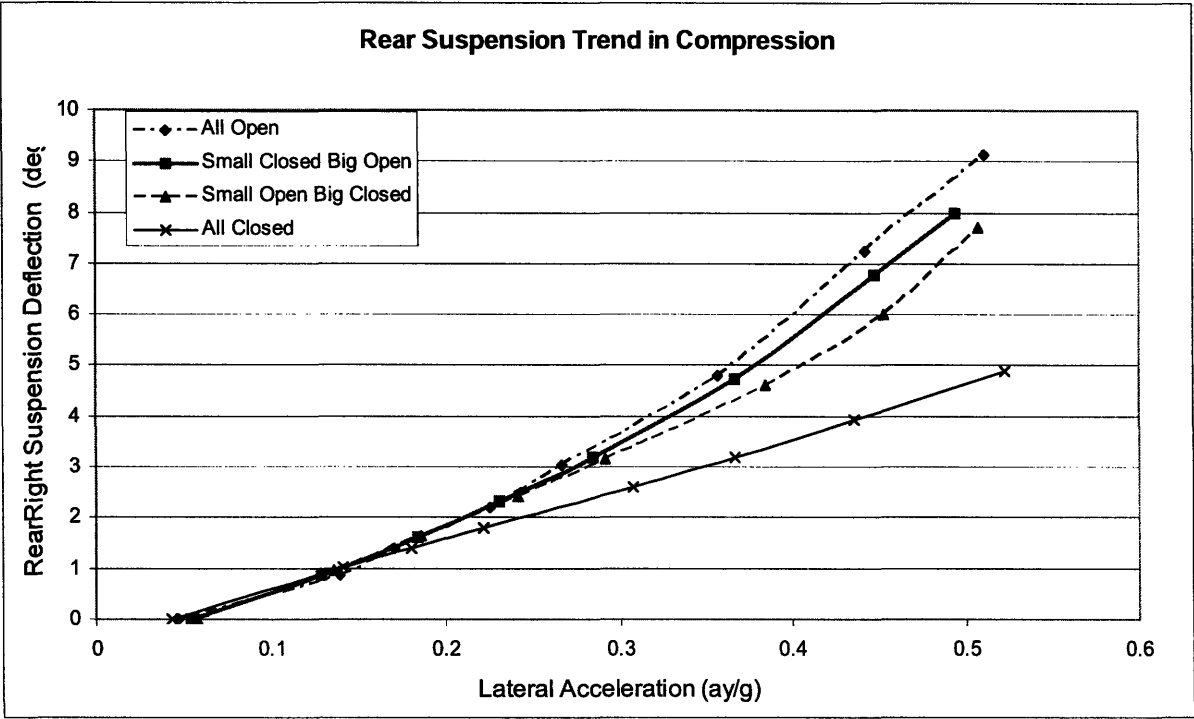


Figure 4-44 Rear Suspension Trends in Compression ($P_0 - P_a = 70\text{psi}$)

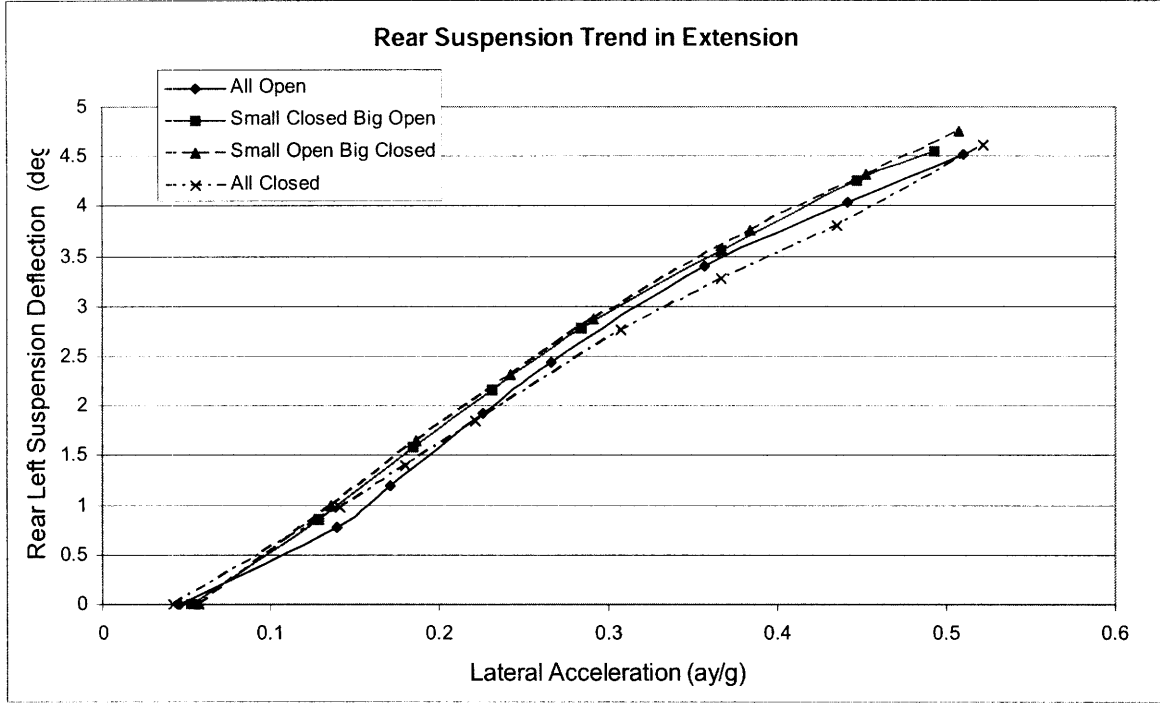


Figure 4-45 Rear Suspension Trends in Extension ($P_0 - P_a = 70\text{psi}$)

4.6.4 Nonlinear force-deflection analysis for the air-spring

In this section, we will derive the non-linear force-deflection relations for the air-spring, to explain the observed counter-intuitive behavior shown in Figure 4-44 and Figure 4-45. The adiabatic compression and expansions process can be expressed as:

$$P = P_0 V_0^\gamma (V_0 + A_{eff} x)^{-\gamma} \quad (4.121)$$

The first and second derivatives of pressure in the air-spring with respect to spring extension x are given below in Equation (4.123) and Equation (4.124) respectively.

$$\frac{dP}{dx} = -\gamma P_0 V_0^\gamma (V_0 + A_{eff} x)^{-\gamma-1} \left(A_{eff} + x \frac{dA_{eff}}{dx} \right) \quad (4.123)$$

$$\frac{d^2 P}{dx^2} = \gamma(\gamma+1) \frac{P_0 V_0^\gamma}{(V_0 + A_{eff} x)^{\gamma+2}} \left(A_{eff} + x \frac{dA_{eff}}{dx} \right)^2 - \gamma \frac{P_0 V_0^\gamma}{(V_0 + A_{eff} x)^{\gamma+1}} \left(2 \frac{dA_{eff}}{dx} + x \frac{d^2 A_{eff}}{dx^2} \right) \quad (4.124)$$

The values of these derivatives around the operating point ($x=0$) are:

$$\left. \frac{dP}{dx} \right|_{x=0} = -\gamma \frac{P_0}{V_0} A_{eff} \quad (4.125)$$

$$\left. \frac{d^2 P}{dx^2} \right|_{x=0} = \gamma(\gamma+1) \frac{P_0}{V_0^2} A_{eff}^2 - 2\gamma \frac{P_0}{V_0} \frac{dA_{eff}}{dx} \quad (4.126)$$

The first and second derivatives of the force are given below.

$$\frac{dF}{dx} = (P - P_a) \frac{dA_{eff}}{dx} + \frac{dP}{dx} A_{eff} \quad (4.127)$$

$$\frac{d^2 F}{dx^2} = (P - P_a) \frac{d^2 A_{eff}}{dx^2} + 2 \frac{dP}{dx} \frac{dA_{eff}}{dx} + \frac{d^2 P}{dx^2} A_{eff} \quad (4.128)$$

The values of these derivatives about the operating point ($x=0$) can be found using the relations in Equation (4.125) and Equation (4.126) are given as:

$$\left. \frac{dF}{dx} \right|_{x=0} = (P - P_a) \frac{dA_{eff}}{dx} - \gamma \frac{P_0}{V_0} A_{eff}^2 \quad (4.129)$$

$$\left. \frac{d^2 F}{dx^2} \right|_{x=0} = (P - P_a) \frac{d^2 A_{eff}}{dx^2} - 4\gamma \frac{P_0}{V_0} A_{eff} \frac{dA_{eff}}{dx} + \gamma(\gamma+1) \frac{P_0}{V_0^2} A_{eff}^3 \quad (4.130)$$

Air-spring force as a function of air-spring extension is given by Equation (4.131), and we compare it with the linear approximation in Equation (4.132). The calculations for the slope and curvature for the rear air-spring are shown in Table 4.6, and the linear and non-linear force-deflection curves are plotted in Figures 4-46 and 4-47.

Table 4.6 Air-spring force-deflection slope and curvature data ($P_0 - P_a = 70$ psi)

$V_0(\text{in}^3)$	$K_A = -(P_0 - P_a) \frac{dA_{eff}}{dx}$	$K_T = \gamma \frac{P_0}{V_0} A_{eff}^2$	$\frac{dF}{dx} = -(K_A + K_T)$	$\frac{d^2 F}{dx^2}$
122	57480 N/m	15200 N/m	-72680 N/m	$12.99 * 10^5 \text{ N/m}^2$
294	57480 N/m	6308 N/m	-63788 N/m	$5.12 * 10^5 \text{ N/m}^2$
405	57480 N/m	4579 N/m	-62059 N/m	$3.68 * 10^5 \text{ N/m}^2$
577	57480 N/m	3214 N/m	-60694 N/m	$2.56 * 10^5 \text{ N/m}^2$

$$F = \left(\frac{dF}{dx} \right) \delta x + \frac{1}{2} \left(\frac{d^2 F}{dx^2} \right) (\delta x)^2 \quad (4.131)$$

$$F_{linear} = \left(\frac{dF}{dx} \right) \delta x \tag{4.132}$$

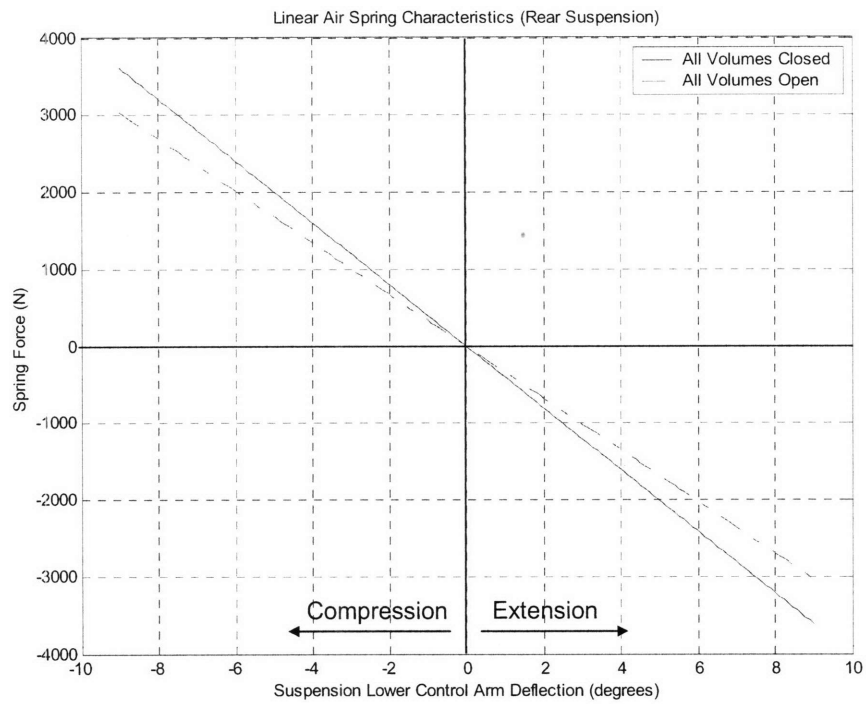


Figure 4-46 Linear air-spring force deflection characteristics ($P_0 - P_a = 70\text{psi}$)

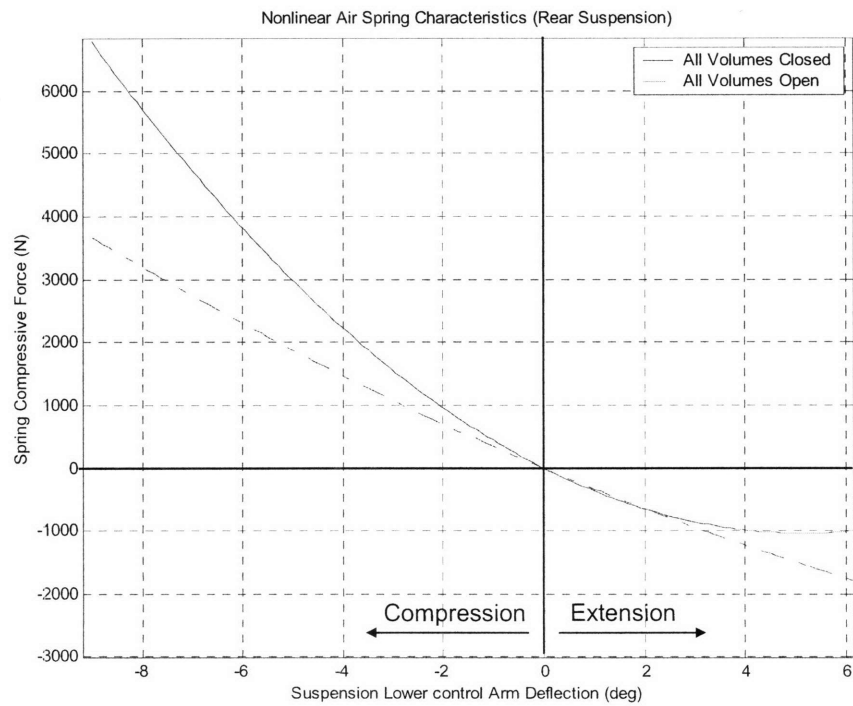


Figure 4-47 Nonlinear air-spring force-deflection characteristics ($P_0 - P_a = 70\text{psi}$)

Observations from the linear and nonlinear air-spring characteristics:

1. From Figure 4-46, we observe a very small difference in stiffness for the two stiffness settings ($K_{min}/K_{max}=1.2$), which does not explain the observed data in Figure 4-44 and Figure 4-45, namely no stiffness change in extension and disproportionately large stiffness change in compression
2. The second derivative of the force-deflection relation in the case with all volumes closed is significantly larger than the case with all volumes open. As a result this suspension exhibits significantly greater hardening on compression with all volumes closed as can be seen from the nonlinear data for spring compression in Figure 4-47. The force-deflection curve in Figure 4-47 matches very closely with the lateral acceleration-deflection curve in Figure 4-44 and this explains the disproportionately large observed stiffness change.
3. The extension data in Figure 4-47, shows that the force-deflection curve is coincident for the two settings for low displacements. This explains the observed data in Figure 4-45.
4. The extension data in Figure 4-47, at larger spring deflections shows counter-intuitive behavior. The setting with higher effective volume is actually stiffer than the setting with lower effective volume. This means that we have to modify our original strategy due to this non-linear behavior.

Original strategy based on linear stiffness predictions: Increase effective volume to reduce stiffness.

Modified strategy based on nonlinear stiffness predictions: Increase effective volume to reduce stiffness when spring is compression. Decrease effective volume to reduce stiffness when spring is extension.

4.6.5 Cross-coupling between the two stiffness components

From Figure 4-13, the $d^2V_{eff}/dx^2=0$ for the rear air-spring. Rewriting Equation (4.130) as Equation (4.133), we can see the contribution of the other two terms to the curvature of the force-deflection relation.

$$\left. \frac{d^2 F}{dx^2} \right|_{x=0} = \gamma \frac{P_0}{V_0} A_{eff} \left(4 \frac{dA_{eff}}{dx} + (\gamma + 1) \frac{A_{eff}^2}{V_0} \right) \quad (4.133)$$

In this example, as the area change stiffness dominates over the thermodynamic stiffness, we have the following inequality and this leads to the approximation in Equation (4.135).

$$4 \frac{dA_{eff}}{dx} \gg (\gamma + 1) \frac{A_{eff}^2}{V_0} \quad (4.134)$$

$$\left. \frac{d^2 F}{dx^2} \right|_{x=0} \approx 4\gamma \frac{P_0}{V_0} A_{eff} \frac{dA_{eff}}{dx} \quad (4.135)$$

In the linear stiffness predictions, we had assumed that the stiffness is due to two springs in parallel as shown in Figure 4-49, and the spring K_T is a non-linear spring as indicated in Equation (4.3). From this analysis, we see that the non-linearity is predominantly due to cross-coupling between the two springs- K_A and K_T . The change of pressure with deflection dP/dx is due to the nonlinearity in the adiabatic compression and expansion of air, but it is amplified by the change of effective area with deflection dA_{eff}/dx . Simulation of the thermodynamic stiffness for different operating volumes is shown in Figure 4-48. This shows that although the non-linear air-springs soften on extension, the spring with greater volume is still softer than the spring with lower volume. From this analysis, we see that the counter-intuitive behavior observed in Figure 4-47, wherein the spring with greater volume is stiffer than the spring with lower volume, is due to the cross-coupling between the two stiffness components K_A and K_T .

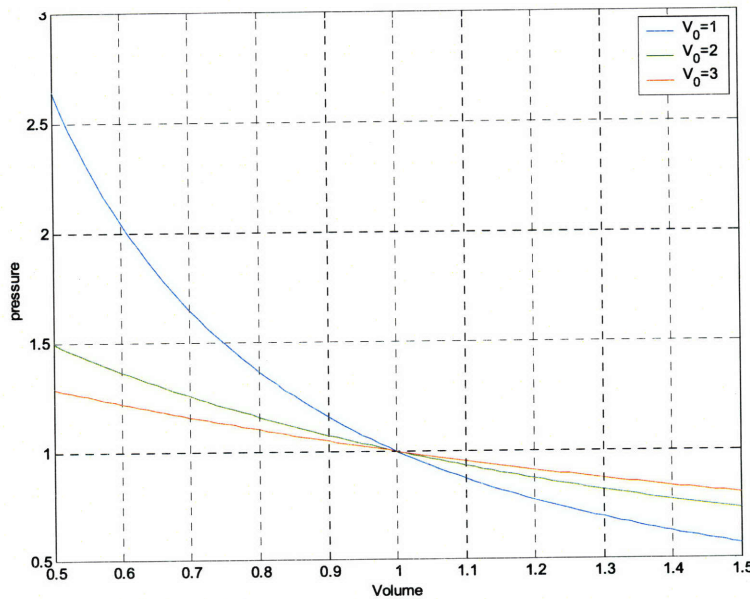


Figure 4-48 : Nonlinear stiffness of a constant area air-spring

4.7 Limitations

In this section we will discuss the performance limitations of the proposed system and comment on the practical applicability of this system to achieve the FRs mentioned in Equation (4.16).

4.7.1 Limited stiffness change and packaging issues

From the linear stiffness relation, we saw that the stiffness of an air spring is the sum of two stiffness components K_A and K_T . With the proposed design, we can only reduce the thermodynamic component. For the air-springs used, $K_A > K_T$, and as a result the range of stiffness that can be achieved is very small.

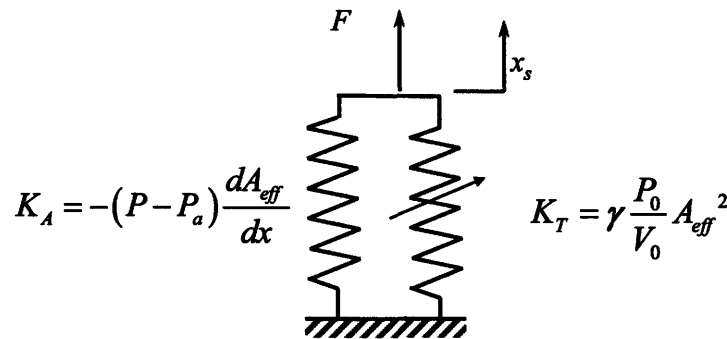


Figure 4-49 : Linear approximation of two springs in parallel

This problem can be overcome by designing the air-spring such that $dA_{eff}/dx = 0$ or small in magnitude. This approach has two drawbacks.

1. This approach works only in reversible sleeve air-spring (not in bellows-type air-spring) and only over a limited range of spring deflections. The existence such a “sweet spot” was demonstrated for the front air-spring (at $P_0 - P_a = 80$ psi). This is not acceptable in our design, as we want independent control of stiffness and ride-height as indicated by Equation (4.16).
2. Secondly, even if it were possible to reduce the contribution of K_A or dA_{eff}/dx , say through the use of a cylinder and piston type air spring or otherwise, this would lead to very low stiffness values. This was also demonstrated for the front air-spring (at $P_0 - P_a = 80$ psi). As a result reduction in K_A has to be accompanied by increase in K_T to maintain the overall desired stiffness K .

3. Increasing the thermodynamic stiffness K_T requires very low air-spring volume. This presents serious packaging constraints and limits the maximum suspension deflections as seen from the following equations.

The pressure P_0 required to support the static load is given by the relation

$$Mg = (P_0 - P_a) A_{eff} \quad (4.136)$$

From the linear analysis, the nominal stiffness is given by:

$$K_0 = -\frac{dF}{dx} = (P_0 - P_a) \left(-\frac{dA_{eff}}{dx} \right) + \gamma \frac{P_0}{V_0} A_{eff}^2 \quad (4.137)$$

The natural frequency of the resulting system for small oscillations about the operating point can be estimated as shown below, where $V_0 = A_{avg} l_0 = \epsilon A_{eff} l_0$.

$$\omega_n^2 = \frac{K_0}{M} = \frac{g}{A_{eff}} \left(-\frac{dA_{eff}}{dx} \right) + \gamma \frac{\left(g + \frac{P_a A_{eff}}{M} \right)}{\epsilon l_0} \quad (4.138)$$

For packaging issues, we desire A_{eff} to be as small as possible, and that requires the static pressure P_0 to be significantly greater than P_a . As a result we get inequality $Mg \gg P_a A_{eff}$, and we will neglect the smaller term in the subsequent analysis.

$$\omega_n^2 = \frac{g}{A_{eff}} \frac{dA_{eff}}{dx} + \gamma \frac{g A_{eff}}{A_{avg} l_0} \quad (4.139)$$

To achieve a greater range of stiffness by connecting/disconnecting auxiliary volumes, we need to reduce the contribution of area change stiffness K_A , preferably to zero, which implies:

$$\omega_n^2 = \gamma \frac{g A_{eff}}{A_{avg} l_0} = \frac{\gamma g}{\epsilon l_0} \quad (4.140)$$

Since $dA_{eff}/dx < 0$ and $dV/dx = A_{eff}$, we get the inequality $\epsilon \geq 1$, where the equality $\epsilon = 1$ holds for $dA_{eff}/dx = 0$. Using this we get the following relation between the length of the air column in the air-spring and the natural frequency ν (in Hz) of the air-spring alone.

$$l_0 = \frac{g}{4\pi^2\nu^2} = \frac{0.25}{\nu^2} \quad (4.141)$$

From this equation, for a natural frequency $\nu = 1.5\text{Hz}$ which is probably the lowest acceptable value for the natural frequency of the system in the stiff setting, we get $l_0 = 10\text{cm}$. This distance is really small for nominal length of the air column, considering the fact we need suspension travel of this order. This nominal length of the air column would be even more unacceptable when we soften the air-spring by adding auxiliary volumes. For $\nu = 2\text{Hz}$, we get $l_0 = 5.6\text{cm}$.

If we choose to split the total stiffness contribution into two fractions f_T due to K_T and $(1-f_T)$ due to K_A , and follow the same exercise as above, we get:

$$f_T \omega_n^2 = \frac{\gamma g}{\varepsilon l_0} \quad (4.142)$$

where $f_T = \frac{K_T}{K_A + K_T}$.

From Equation (4.142), for $f_T = 0.75$ (75-25 distribution between K_T and K_A); we get $l_0 < 13.33\text{cm}$ for $\nu = 1.5\text{Hz}$ in the stiff setting; and we get $l_0 < 7.46\text{cm}$ for $\nu = 2\text{Hz}$.

From Equation (4.142), for $f_T = 0.50$ (50-50 distribution between K_T and K_A); we get $l_0 < 20\text{cm}$ for $\nu = 1.5\text{Hz}$ in the stiff setting; and for $\nu = 2\text{Hz}$, we get $l_0 = 11.2\text{cm}$.

The factor ε could be reduced by inserting buffers to reduce the internal air-spring volume and this would allow us to get a larger l_0 . Further research is needed to determine the feasibility of this idea.

4.7.2 Time and power input requirements for stiffness change

When we had claimed that this suspension system is capable of instantaneous stiffness change, we meant that the time required to open and close the valves is significantly lower than the characteristic time constant of the system. This is true for direct-acting solenoid valves, which have opening and closing times of about 30 to 40 milliseconds. The FRs of the opening and closing time for the valves and the power requirement are coupled for off-the-shelf valves. An intelligent valve design is required for uncoupling these FRs. Typical values for the performance comparison of off-the-shelf valves is given in Table 4.7.

Table 4.7 Specifications of interest for certain types of valves

Type of Valve	Opening/Closing Time	Opening/Closing Power	Holding Power
Solenoid Valve (2-way Bidirectional)	30-40 milliseconds	6-30 W	6-30 W (depending on valve construction and C_{Valve})
Automated Ball Valve with electric motor	5 seconds (for operation using a 12V car battery)	2W	0
Automated Ball Valve with pneumatic pilot valve	~0.3 seconds	2W (Pressurized air is used)	0

4.7.3 Ride-height change due to unequal pressures in chambers

We had discussed that the air-spring as well as the auxiliary volumes have the same static pressure, and as a result the pressure in the air spring does not change due to opening and closing of the valves, i.e., stiffness change does not cause any ride-height change. But it is possible that the pressures in the air-spring and the auxiliary volume could be different- either because the air-spring pressure may have leaked greater than auxiliary volume pressure during inactivity, or because we may have closed the valve at a time when the pressures are unequal leading to change in static pressures in both the air-spring as well as the auxiliary volume. In this case, opening of the valve will lead to ride-height change which can be estimated from the formulation below.

Consider air of mass m_1 is occupying a volume V_1 in the air-spring at static pressure P_1 and temperature T_0 , and air of mass m_2 is occupying a volume V_2 in the auxiliary volume at static pressure P_2 and temperature T_0 , where $P_1 \neq P_2$. These variables are related to each other by the Ideal Gas law as indicated in Equation (4.143).

$$\begin{aligned} P_1 V_1 &= m_1 R T_0 \\ P_2 V_2 &= m_2 R T_0 \end{aligned} \tag{4.143}$$

The pressure in the air spring is related to the supported load by the relation in Equation (4.144), where l_0 is the operating length of the air-spring in this position and $A_{eff}(l_0)$ refers to the effective area at operating length l_0 .

$$P_1 = \frac{Mg}{A_{eff}(l_0)} \tag{4.144}$$

On opening the valve, the final pressure in the two volumes become P_f and the air spring undergoes an extension x and volume increase ΔV_1 which are related by $\Delta V_1 \approx A_{eff}(l_0)x$. The Ideal Gas Law after opening the valve is given by Equation (4.145).

$$P_f = \frac{(m_1 + m_2)RT_0}{(V_{10} + \Delta V_1 + V_2)} \quad (4.145)$$

The pressure in the air spring is related to the supported load by the relation in Equation (4.146), where (l_0+x) is the operating length of the air-spring in this position and $A_{eff}(l_0+x)$ refers to the effective area at operating length (l_0+x) .

$$P_f = \frac{Mg}{A_{eff}(l_0 + x)} \quad (4.146)$$

Notice that the effective area reduces as the air-spring extends and increases as the air-spring compresses.

$$\frac{Mg}{A_{eff}(l_0 + x)} = \frac{P_1V_{10} + P_2V_2}{(V_{10} + A_{eff}(l_0)x + V_2)} \quad (4.147)$$

$$\frac{Mg}{A_{eff}(l_0 + x)} = \frac{MgV_{10} + A_{eff}(l_0)P_2V_2}{A_{eff}(l_0)(V_{10} + A_{eff}(l_0)x + V_2)} \quad (4.148)$$

Combining the equations above and rearranging, we get the following equation which can be solved for the extension x , if the effective area as a function of spring extension $A_{eff}(l_0 + x)$ is known.

$$x = \left(\frac{V_{10}}{A_{eff}(l_0)} + \frac{P_2V_2}{Mg} \right) \frac{A_{eff}(l_0 + x)}{A_{eff}(l_0)} - \left(\frac{V_{10} + V_2}{A_{eff}(l_0)} \right) \quad (4.149)$$

4.7.4 Modified stiffness control strategy

Original strategy based on linear stiffness predictions was to increase effective volume to reduce stiffness. But from the nonlinear force-displacement curve in Figure 4-47, we see that at larger spring deflections in extension, the setting with higher effective volume is actually stiffer than the setting with lower effective volume. This means that we have to modify our original strategy due to this non-linear behavior.

Modified strategy based on asymmetric nonlinear stiffness predictions could be:

1. Increase effective volume to reduce stiffness when spring is compression.
2. Decrease effective volume to reduce stiffness when spring is extension.

Further modeling and testing is required to study the effect of this asymmetric stiffness behavior on the suspension performance. Further work is needed to come up with a modified strategy that accounts for and possibly exploits this non-linearity.

4.8 Summary

In this chapter, we have investigated the possibility of using pneumatic and hydro-pneumatic suspension systems to come up with a customizable automotive suspension with independent control of stiffness, damping and ride-height; preferably with instantaneous (or rapid) stiffness change, and limited or no power input and no effect of stiffness change on ride-height change. Based on preliminary modeling of pneumatic springs, we have proposed several designs to achieve these FRs. One of the proposed designs employs unequal auxiliary volumes connected to the air-spring volume through On-Off valves for changing the stiffness of the system. The preliminary modeling of this system suggested the potential of instantaneous stiffness change with no power input, and no ride-height change due to stiffness change. This design is robust, light-weight and low-cost, which makes it applicable to generic vibration isolation systems with time-varying or conflicting stiffness requirements.

A customizable pneumatic suspension system with independent control of stiffness and ride-height has been designed and incorporated in a car and it demonstrates the concept well. A data acquisition system has been designed and incorporated in the car for the testing of the pneumatic suspension system. Detailed modeling, design, fabrication and testing of this system has been discussed.

A detailed model of this design has been developed and the analysis suggested certain potential limitations to the performance of this design:

1. The stiffness of an air spring can be considered to be the sum of two components- area change stiffness K_A and thermodynamic stiffness K_T . With our proposed design, we can only reduce the thermodynamic stiffness K_T . This may restrict the achievable range of stiffness if K_A is greater than K_T , which was the case in the prototype design.

2. Two possible solutions for this problem are discussed. Reduction of area change stiffness K_A is possible only in limited operating range and is not acceptable as it makes the functional requirements FR1: Control Stiffness and FR2: Control Ride-height coupled. Moreover it leads to a very low overall stiffness, and hence has to be accompanied by increase of thermodynamic stiffness K_T . The associated packaging and suspension travel issues are discussed.
3. Due to packaging requirements, the auxiliary volumes had to be mounted at a distance from the air-spring. This introduces significant effective air inertia in the pipe. Moreover there are losses due to flow across valves and pipes. This makes the auxiliary volumes ineffective at high frequencies. A detailed thermodynamic model to incorporate the effect of air inertia and the pipe losses on the frequency response of the air-spring with auxiliary volumes is developed and it is shown that the air-spring with auxiliary volumes exhibits a low stiffness at low frequencies and high stiffness at high frequencies. This model matches well with the experiments for small displacements. This linearized model is used to study the effect of this frequency dependant stiffness behavior on the road-noise isolation performance of the system, and it is verified that this behavior has a negligible effect on the road-noise isolation performance.
4. On the rear air-spring, area change stiffness K_A dominates the thermodynamic stiffness K_T , and the linear stiffness analysis predicts very small stiffness variation. But the observed variation in stiffness was quite significant. To explain this, equations for the slope and curvature of the air-spring force-deflection curves are derived. This non-linear analysis explains the observed behavior accurately. Moreover this analysis reveals a counter-intuitive stiffness behavior for the air-spring in extension. The air-spring with higher effective volume is actually stiffer than the air-spring with lower effective volume beyond a certain deflection. This means that our original strategy of increasing effective volume to reduce stiffness needs to be modified. Further study of this asymmetric stiffness behavior is needed to account for, and possible exploit this non-linear behavior.

The use of off-the-shelf valves is not satisfactory for this system, as we need fast opening and closing times, with low power input during actuation and no power input for holding in either state. Future work involves design of an innovative valve system to solve this problem.

4.9 List of abbreviations and car parameters

P_0 = Nominal Pressure of air in the air-spring

V_0 = Nominal Volume of the air-spring

T_0 = Nominal Temperature of the air-spring

T_a = Ambient atmospheric temperature

A_p = Area of plate

A_{eff} =Air spring effective area

$A_V = dV/dx$ for the air-spring

$A_{avg}=V/l_0$

$\varepsilon = A_{avg} / A_{eff}$

κ = Polytropic stiffness constant

P_a = Atmospheric pressure

z = Distance along the length of the tubing

l_0 = Length of air column

ζ = Damping Coefficient

ζ_2 = Damping Coefficient for air-spring with auxiliary volume with inertia of air in pipe

C_P = Specific Heat Capacity of air at constant pressure

C_V = Specific Heat Capacity of air at constant volume

R =Specific gas constant for air

C_{Pm} = Molar Specific Heat Capacity of air at constant pressure

C_{Vm} = Molar Specific Heat Capacity of air at constant volume

R_m =Molar gas constant

C_{Valve} = Valve flow coefficient

ρ = Density of air

q = Flow-rate of air through valve

γ = Heat Capacity Ratio of air.

CV1, CV2 = Control Volume 1, Control Volume 2

P_1 = Pressure of air in CV1

V_1 = Volume of CV1

m_1 = Mass of air in CV1

T_1 = Temperature of air in CV1

P_2 = Pressure of air in CV2

V_2 = Volume of CV2

m_2 = Mass of air in CV2

m = Total mass of air in the system

m_{pipe} = mass of air in the pipe

T_2 = Temperature of air in CV2

h_1 = Heat transfer coefficient for CV1

h_2 = Heat transfer coefficient for CV2

A_1 = Area exposed for heat transfer for CV1

A_2 = Area exposed for heat transfer for CV2

T_{int1} = Temperature of air flowing into or out of CV1

T_{int2} = Temperature of air flowing into or out of CV2

K_1 = Stiffness contribution due to compliance of air in chamber 1

K_2 = Stiffness contribution due to compliance of air in chamber 2

B_2 = Damping introduced due to valve resistance

B = Damping constant of the main damper in the suspension system

K_{ad} = Adiabatic Stiffness

K_{iso} = Isothermal Stiffness

K_{poly} = Polytropic Stiffness

K_{comp} = Complex stiffness for air spring with auxiliary volume with valve flow resistance

$K_{complex}$ = Complex stiffness for air spring with auxiliary volume with inertia of air in pipe

K_{low} = Lower Stiffness of air spring with one auxiliary volume observed at low frequency

K_{high} = Higher Stiffness of air spring with one auxiliary volume observed at high frequency

r_{pipe} = Radius of the pipe

Q_1 = Total rate of change of the air spring volume

Q_2 = Contribution to the rate of change of air-spring volume due to compliance of air in the air-spring

Q_{12} = Volumetric flow rate from volume V_1 to V_2

Q_{H2} = Heat added to CV1

Q_{H1} = Heat added to CV2

X_0 = Amplitude of oscillations

ω_f = Forcing frequency

U_V = Energy dissipated by viscous damping in one cycle of forced vibration

U_{SL} = Energy dissipated by square-law damping in one cycle of forced vibration

B_V = Equivalent Viscous Damping Constant

B_{SL} = Square Law Damping Constant

θ = body roll

Car Parameters

Weight of Car 2387 lbs

Mass of Car 1083 kg

Weight on Front Wheels = $0.58 \times 2387 = 1384$ lb (692lbs/wheel)

Front Mass of Car = 627kg (315 kg/wheel)

Weight on Rear Wheels = 0.42 X 2387 = 1002 lb (501 lbs/wheel)

Rear Mass of Car = 454kg (227 kg/wheel)

Wheelbase = 1.45 m (57in)

Track = 2.6 m (103 in)

Front Air Spring Volume (V_{F1}) = 107 in³

Dimensions (Radius = 2.38in; Length = 6in @ 90psi)

Rear Air Spring Volume (V_{F2}) = 125 in³

Dimensions (Radius = 2.38in; Length = 7in @ 90psi)

Auxiliary Volume (V_2) = 172 in³

Auxiliary Volume (V_3) = 283 in³

Auxiliary Volume Dimensions: Outside Diameter = 4.38 in; Lengths = 16.2 in and 25.2 in

$F_{w,front}$ = Load on front wheel = 0.5 X 0.58 X 2500 lb = 725lb

$F_{s,front}$ = Load on front spring = (385/270) X 725 lb = 1033 lb

$F_{w,rear}$ = Load on rear wheel = 0.5 X 0.42 X 2500 lb = 525lb

$F_{s,rear}$ = Load on rear spring = (425/318) X 525 lb = 701 lb

Chapter 5

Application to Improved Vehicle Dynamics

In this chapter, the application of variable stiffness and variable ride-height suspension systems to achieve improved vehicle dynamics is discussed. Numerous applications of variable stiffness are possible as stiffness affects almost every aspect of ride and handling. User control of stiffness and ride-height is demonstrated to achieve customization and to avoid the trade-offs that arise from the conflicting requirements of comfort and handling. Optimum suspension performance over the entire speed range can be achieved by varying the adaptive suspension parameters as a function of speed. Strategies to minimize wheel and vehicle attitude changes due to maneuvering inputs using the proposed system are discussed. The implication of the time required for the stiffness change for the proposed strategies to be effective is discussed.

The application of variable stiffness to achieve real-time alteration of pitch and bounce motion centers, and real time alteration of anti-pitch and anti-dive characteristics is discussed. Moreover the possibility of ensuring stability through real-time alteration of understeer-oversteer characteristics is explored and demonstrated experimentally on the pneumatic customizable suspension system. The suspension geometries (kinematics) and stiffness settings required for achieving the desired vehicle dynamic characteristics (such as anti-pitch/anti-dive characteristics, understeer-oversteer characteristics or pitch and bounce motion center locations) are well known. But the geometries required for the different characteristics are very often contradictory and this leads to a trade-off solution for the suspension kinematics. The capability to alter these characteristics on the fly lets enables us to eliminate the design coupling involved.

Experimental evaluation of the proposed applications is discussed for the two prototypes, wherever applicable.

5.1 User customization of comfort and handling

5.1.1 Stiffness customization

The capability to control the stiffness (or natural frequency) of the suspension on the fly, allows the user to select the desired ride and handling of the car. This also eliminates the trade-off perpetually faced by the suspension designer as well as the marketing team, in deciding on the suspension stiffness. The trade-off between comfort and handling was described in Chapter 3, where high-frequency road noise isolation and low-frequency wheel alignment parameter changes were defined as parametric measures of comfort and handling respectively and the effect of stiffness on these parameters was studied in the Bode plots shown in Figure 5-1 and Figure 5-2.

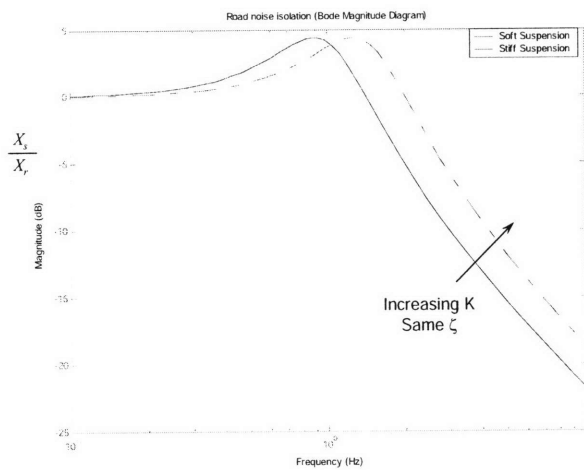


Figure 5-1 Road noise isolation for soft and stiff suspension systems

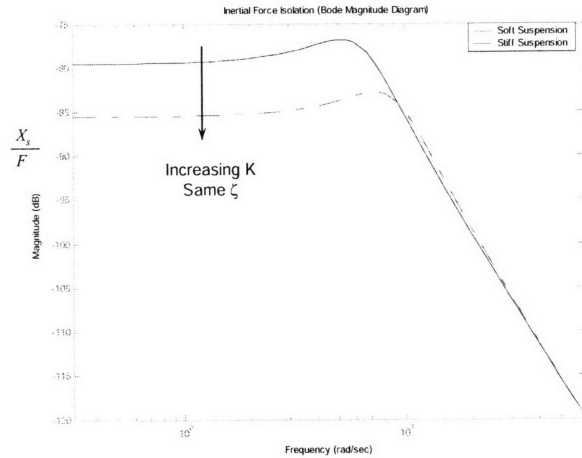


Figure 5-2 WAP changes due to inertial forces caused by maneuvering inputs for soft and stiff suspensions

The electromechanical suspension prototype is capable of a natural frequency range of 1-1.6Hz, which is the desired range for systems capable of slow stiffness change. The natural frequency for luxury cars is around 1.1Hz and the natural frequency for sports cars is around 1.3-1.6Hz, as any increase over this natural frequency involves significant sacrifices in comfort for handling benefits. For systems, that are capable of rapid stiffness change, it may be beneficial to use a larger range of natural frequency, as the deterioration in ride for handling benefits may be acceptable for short periods of time, such as hard braking, acceleration or cornering.

Experiments were also conducted on the pneumatic suspension system for comfort evaluation. In this experiment, wooden planks were placed at a regular interval and the car was driven over the planks at constant speed. But the results were inconclusive because of lack of characterized proving ground surface, limited length of the testing space available, and the inability to maintain the same speed over the planks placed over the limited length.

Implementation: This customization feature will probably be implemented in passenger cars, by providing a stiffness setting on the control panel. This could offer stiffness changes in a continuous fashion within a given stiffness range, or could have discrete settings, such as comfort, intermediate or sport modes. This application is envisaged as a setting a driver makes before driving and hence does not require the stiffness change or the ride-height change to be rapid.

5.1.2 Ride-height customization

Cars need high ground clearance on rough terrain and greater height for better vision; whereas a low center of gravity (CG) height is desired for swift cornering, dynamic stability at high speeds and reduced drag. A suspension capable of ride-height control can avoid this trade-off as the ride-height can be changed on the fly based on user input or automatically based on vehicle speed and maneuvering inputs. The proposed system has independent ride-height control for front and rear wheels and can thereby control the pitch attitude to modify aerodynamic lift. The proposed system offers dual benefit of providing flexibility to the suspension designer and providing customization to the user to select the desired ride-height.

The electro-mechanical suspension prototype is capable of 5in ride-height travel, whereas the pneumatic suspension incorporated in the Honda Civic is capable of the maximum possible ride-height change, i.e., it can alter the static height from the lower bump stop to the upper bump-stop, which is about 6.25in for the front suspension and 5in for the rear suspension. Ride-height control for the pneumatic system is discussed in more detail in the next chapter.

5.1.3 Low-frequency attitude control: Ride-height change to uncouple comfort and handling

Soft suspension is necessary for good high frequency road noise isolation (comfort). We cannot use an excessively soft suspension, because of the disadvantages of excessive unfavorable suspension travel redistribution between jounce and rebound under overload, excessive wheel attitude changes (leading to directional instability) and excessive vehicle attitude changes

(leading to passenger discomfort and excess headlight beam swaying). Ride height control can take care of handling requirements such as low-frequency body and wheel attitude control, and also fix the unfavorable suspension travel redistribution. This allows the use of lower stiffness (as compared to a passive suspension) for better comfort without compromising on handling. This is an example of uncoupling the conflicting requirements of comfort and handling.

5.1.4 Optimum performance over the entire speed range

The optimum stiffness of an automotive suspension system changes with vehicle speed. Road noise is characterized by a certain power spectral density in terms of spatial frequency ν (Robson 1975, Sharp 1987). If the vehicle is driven at constant speed V , the temporal excitation frequency ω is related to the spatial frequency ν by $\omega=2\pi V\nu$. The power spectral density in terms of temporal frequency keeps changing with the speed of the vehicle and hence the optimum suspension parameters keep changing with speed. Several researchers have approached the problem of optimizing the suspension parameters to minimize the cost function that includes the requirements of ride comfort, road handling, vehicle attitude, and suspension workspace. Li and Kuo (2000) employ evolutionary algorithms to optimize a passive quarter-car suspension. Optimal/suboptimal suspension parameters as a function of vehicle speed to minimize the cost function have been presented for a quarter-car suspension by Coirriga et.al (1996) using a Simplex search method; for a half-car model by Lin and Zhang (1989) by minimizing the variance of the control force difference between the passive suspension and the LQG active suspension with full-state feedback; and for a full car model by Elbeheiry et.al (1996), and Zuo and Nayfeh (2004) using decentralized LQG/H2 optimization. A suspension with adaptive suspension parameters (damping and stiffness) provides the capability to get an optimum ride over the entire speed range by changing the suspension parameters as a function of speed according to a suitable algorithm. Current suspension parameters are optimized for a certain average speed and the performance drops on either side of the design speed. This trade-off can be eliminated by changing the suspension parameters as a function of speed according to a suitable algorithm or heuristic. One such stiffness scheduling algorithm was presented in a graphical form in Figure 3-4.

5.2 Handling: Response to maneuvering inputs

As discussed before, handling is characterized by wheel alignment parameter changes caused by inertial forces due to maneuvering inputs. Typical approach for a fully active suspension system would be to measure the inertial force (directly by accelerometers or indirectly through brake pressure sensor, velocity sensor and steering angle sensor) and to compensate for it using feed-forward control as shown in Figure 5-3. This strategy is not included in typical LQG/H2 optimization for active suspensions or decentralized H2 optimization for passive suspensions. This could be included in the LQG formulation to account for the comfort-handling trade-off, but there are problems involved with modeling the inertial forces due to maneuvering inputs as stochastic disturbance input.

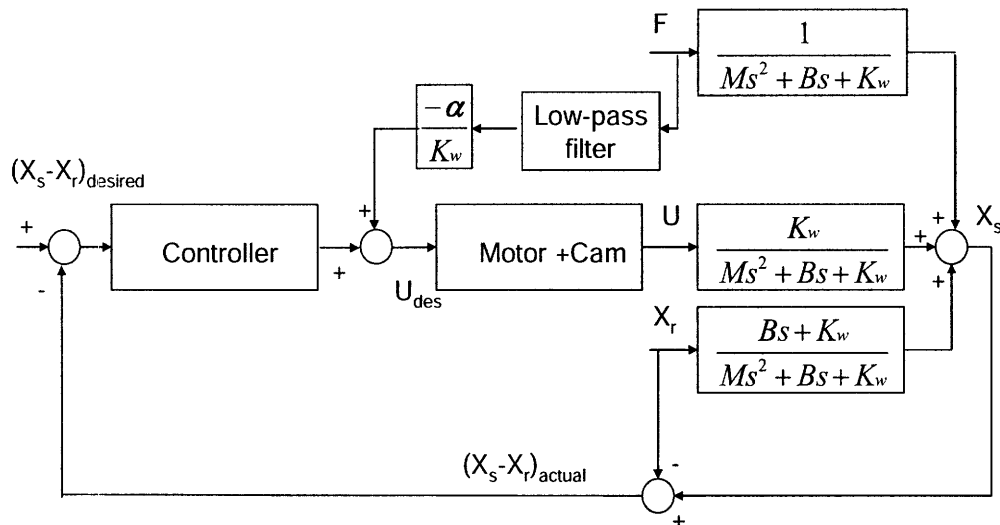


Figure 5-3: Feed-forward control for attitude control

5.2.1 Instantaneous stiffness change on hard braking, acceleration or cornering to limit wheel attitude changes

The previous approach requires high bandwidth and high-force producing actuators, which tend to be bulky, expensive and power-consuming. With the variable stiffness suspension system, a very simple and effective strategy can be employed to reduce wheel alignment parameter changes caused by inertial forces due to maneuvering inputs. This can be done by sensing the lateral or longitudinal acceleration and hardening the suspension when the acceleration exceeds a threshold. The stiffness range can be split into 2^N settings if we are using N unequal auxiliary volumes. Stiffness can be gradually increased based on the pre-determined threshold levels or based on another heuristic algorithm. This strategy can only reduce roll or squat and dive by

increasing stiffness; it cannot eliminate it completely as is possible with completely active suspension systems. Hence it requires the stiffness change to be rapid. As a rule of thumb, the switching time should be an order or magnitude smaller than the characteristic time constant of the mode that is to be restricted. For instance the roll resonant frequencies of passenger cars are in the range 1.5-2 Hz and the characteristic time is of the order of 0.5-0.66 seconds. The pitch and bounce frequencies are of the order of 1.3 Hz with the characteristic times of around 0.77 seconds. In the case of roll caused during cornering, it may be advantageous to measure maneuvering inputs (steering angle position, brake fluid pressure and vehicle speed) over lateral acceleration, as the lateral dynamics (vehicle moment of inertia about the vertical axis and the first moment of the vehicle cornering stiffness) of the vehicle introduce a delay of about 0.2 seconds between the steer angle and the yaw velocity.

Experimental results for the electro-mechanical suspension system indicate a natural frequency range of 1-1.5 Hz. This can provide significant stiffness increase and significant reduction in wheel alignment parameters caused by inertial forces due to maneuvering inputs. But this system is not capable of instantaneous stiffness change and the stiffness change requires significant energy input. Hence this system can be used effectively when the stiffness is changed occasionally and slowly; it is not capable of changing stiffness on the fly to reduce the attitude changes caused by lateral and longitudinal accelerations.

For the pneumatic suspension, experimental investigation for suspension deflection or roll caused due to lateral acceleration has been discussed extensively in Chapter 5 and the results show that this system can drastically reduce the wheel alignment parameter changes caused by inertial forces due to maneuvering inputs in the stiff setting. This system also has the potential of rapid stiffness change through the use of solenoid valves (opening and closing time of 40 μ sec). This opening and closing time satisfies the condition of one tenth of the characteristic time for the different attitude change modes and hence can be used for stiffening on hard braking or acceleration or for stiffening in a corner.

This "Increase stiffness on sensing acceleration/inertial force" is the most trivial application of the proposed system. Other applications such as real-time alteration of anti-pitch and anti-dive characteristics, real-time alteration of understeer-oversteer characteristics, and real-time alteration of pitch and bounce motion centers are discussed subsequently.

5.3 Alteration of anti-dive and anti-pitch characteristics

The weight transfer from the front wheel to the rear wheel, during acceleration, causes compression in the rear suspension, known as “squat”, and rebound in the front suspension, known as “lift”, which together produce vehicle pitch. The weight transfer, during braking, causes compression in the front suspension, known as “dive”, and rebound in the rear suspension, known as “rise”, which together produce vehicle pitch. Suspension geometries and stiffness can be designed to counteract the effect of the weight transfer and minimize squat, dive and pitch. These are referred to as anti-squat, anti-dive or anti-pitch geometries. In this section, the derivation of these geometries is outlined and their dependence on front and rear stiffness is highlighted. For the purpose of this analysis, any suspension system can be analyzed as a trailing arm suspension with the trailing arm pivot point at the instantaneous center A as shown in the Figure 5-4.

The load on the front wheels and the rear wheels changes during acceleration due to longitudinal weight-transfer is given by:

$$W_r = W \left(\frac{b}{L} + \frac{a_x h}{g L} \right) \quad (5.1)$$

$$W_f = W \left(\frac{c}{L} - \frac{a_x h}{g L} \right)$$

where W is the weight of the car, and W_f and W_r is load on the front and rear wheels respectively. L is the wheelbase, a and b are distance of the CG from the front and rear wheel respectively, and a_x is the longitudinal acceleration.

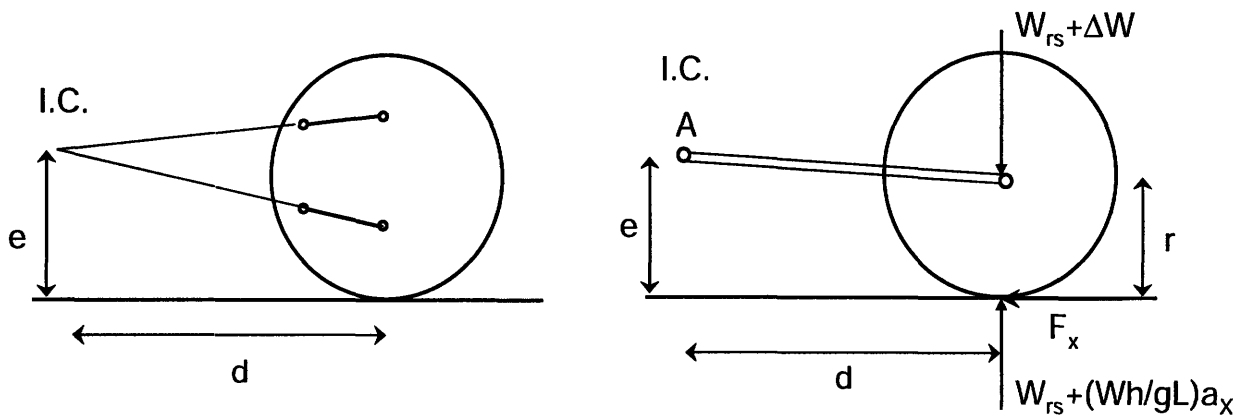


Figure 5-4 Forces acting on a rear drive axle during acceleration

Consider the forces acting on a rear solid-drive axle during acceleration as shown in Figure 5-4. The load on the rear wheel is the sum of the static load on the car and the dynamic component arising from longitudinal load transfer during acceleration a_x .

Force balance and moment balance about the instantaneous center A gives the relation in Equation (5.2) for the rear suspension deflection δ_r . The rebound deflection of the front suspension due to the load-transfer is given by Equation (5.3).

$$\Delta W_r = \frac{W}{g} \frac{h}{L} a_x - \frac{W}{g} \frac{e}{d} a_x = K_r \delta_r \quad (5.2)$$

$$\Delta W_f = -\frac{W}{g} \frac{h}{L} a_x = K_f \delta_f \quad (5.3)$$

The pitch angle of the vehicle θ_p , during acceleration is the difference of the suspension deflections divided by the wheelbase.

$$\theta_p = \frac{\delta_f - \delta_r}{L} = \frac{W}{g} \frac{a_x}{L} \left(\frac{1}{K_r} \frac{h}{L} - \frac{1}{K_r} \frac{e}{d} + \frac{1}{K_f} \frac{h}{L} \right) \quad (5.4)$$

From this equation, we can see that zero pitch angle is achieved when the following condition is satisfied:

$$\frac{e}{d} = \frac{h}{L} + \frac{h}{L} \left(\frac{K_r}{K_f} \right) \quad (5.5)$$

The first term of the right hand side of this equation corresponds to the condition by which anti-squat is achieved on the rear suspension. That is, if $e/d=h/L$, the rear suspension will not deflect during acceleration. The degree to which this is achieved is described as percent anti-squat. For example, if $e/d=0.5h/L$, the suspension is said to be 50% anti-squat. Since h/L is around 0.2 for most passenger cars, full anti-squat generally requires an effective trailing arm length of about five times the elevation of “ e ”. The anti-squat equation $e/d=h/L$ defines a locus of points extending from the tire-contact point on the ground to the height of the CG over the front axle. Locating the trailing arm pivot at any point on this line will provide 100% anti-squat. Satisfying Equation (5.5), with the inclusion of the second term implies that the rear suspension will lift to compensate for rebound of the front suspension, thereby keeping the vehicle level (Gillespie, 1992).

Normally some degree of squat and pitch is expected during vehicle acceleration, so full compensation is unusual. For other suspension configurations, the anti-pitch, anti-squat (for rear drive) and anti-lift (for front drive) geometries are given in Table 5.1.

Table 5.1: Anti-pitch anti-squat and anti-lift geometries for different suspensions

Type of suspension	Anti-squat / Anti-lift relation	Anti-pitch relation
Rear Solid Drive Axle	$\frac{e}{d} = \frac{h}{L}$ (Anti-squat)	$\frac{e}{d} = \frac{h}{L} + \frac{h}{L} \left(\frac{K_r}{K_f} \right)$
Independent Rear Drive	$\frac{e-r}{d} = \frac{h}{L}$ (Anti-squat)	$\frac{e-r}{d} = \frac{h}{L} + \frac{h}{L} \left(\frac{K_r}{K_f} \right)$
Front Solid Drive Axle	$\frac{e}{d} = -\frac{h}{L}$ (Anti-lift)	$\frac{e}{d} = -\frac{h}{L} - \frac{h}{L} \left(\frac{K_f}{K_r} \right)$
Independent Front Drive	$\frac{e-r}{d} = -\frac{h}{L}$ (Anti-lift)	$\frac{e-r}{d} = -\frac{h}{L} - \frac{h}{L} \left(\frac{K_r}{K_f} \right)$

In a similar fashion anti-dive geometry to counter hard-braking is derived (Gillespie, 1992) as:

$$\frac{e_{front}}{d_{front}} = -\frac{h}{\xi L} \quad (5.6)$$

$$\frac{e_{rear}}{d_{rear}} = \frac{h}{(1-\xi)L} \quad (5.7)$$

where ξ is the fraction of the brake force developed on the front axle.

From the relation in Table 5.1 and Equation (5.6) and Equation (5.7), we can see that the requirements are conflicting with each other and also with the other requirements (Gillespie, 1992; Dixon, 1996) such as:

1. Anti-squat performance requires a short trailing arm, due to which the rear axle may experience “power-hop” during acceleration.
2. The goals for anti-squat may conflict with those for braking or handling. In this case, placing the pivot center above the wheel center can produce roll-oversteer.
3. Full anti-dive causes excessive caster changes and increases the steering effect.
4. In rear suspension, high pivot location to meet the anti-dive geometry, causes oversteer.

Using the proposed pneumatic suspension system, can eliminate these coupling in the following two ways.

1. Instantaneous stiffness increase, through valve closing, during braking or acceleration can provide squat control or dive control and thereby relieve some of the need to design in these geometries. Such removal of coupling will make the job of suspension designer easier.
2. The dependence on front and rear stiffness (K_f and K_r) is manifest in this relation. The proposed system allows us to independently vary the front and rear stiffness and this enables us to alter the anti-pitch relations on the fly, without any change in the suspension kinematics. This is important because it is not possible to meet the anti-pitch geometry prescribed by Equation (5.5), as it this geometry leads to roll-oversteer (Gillespie, 1992). This problem can be overcome, by changing the front and rear stiffness momentarily during acceleration to satisfy the anti-dive/anti-squat relations. The stiffness values can be set to the nominal values dictated by other requirements (such as the desired understeer gradient or the desired location of motion centers) during normal driving conditions.

5.4 Alteration of Understeer-Oversteer behavior

Handling is a very subjective issue and there are differences of opinion regarding the best behavior. For instance, American cars tend to have a higher initial understeer gradient (2-4 deg/g) than European cars (1-3 deg/g), while some European sports cars have neutral steer (-1 to +1 deg/g) (Dixon, 1996). This indicates that the best understeer gradient depends on driver preference and experience and on the predominant nature of roads. Easy customization of understeer-oversteer behavior is a feature that would be appreciated by drivers.

Three types of stability control systems have been proposed and developed for yaw control-Differential Braking, Steer-By-Wire (Ackermann, 1994; Ackermann, 1997) and Active Torque Distribution. Yaw control systems have been commercialized on production vehicles such as BMW DSC3 (Leffler et. al., 1998), Mercedes ESP, Cadillac Stabilitrak system (Jost, 1996), and the Chevrolet C5 Corvette Active Handling System (Hoffman et. al., 1998). In this chapter, we have looked into the possibility of real-time alteration of understeer-oversteer characteristics through front to rear roll stiffness distribution, which can be achieved in our system through simple On-Off valve control. This capability is demonstrated in the steady state cornering test conducted on the suspension prototype.

Steady state cornering of the car and understeer-oversteer behavior is introduced for a simplified bicycle model. The trade-off between understeer and oversteer behavior in terms of efficiency and stability is highlighted. The effect of suspension systems on the cornering behavior is studied to show how understeer and oversteer gradient can be achieved in a simple way on the proposed designs. This can be used to ensure vehicle stability. Experimental results from the customizable suspension system are presented to demonstrate the effectiveness of the proposed strategy.

5.4.1 Cornering behavior of a simplified bicycle model

The simplified two-DOF bicycle model of mass M , weight W , moment of inertia $I_z = Mk^2$, length L , and tire cornering stiffness C_F and C_R moving at speed V is shown in Figure 5-6. Distances of CG from front and rear wheel is a and b respectively. For this model, the vehicle is compressed to a single track. Lateral and longitudinal weight transfer, roll or pitch motion, and chassis compliance effects are neglected and will be considered separately.

Under cornering conditions, the tire develops a lateral force F_y , called the cornering force that is assumed to be a linear function of the slip angle α . The slip angle is the angle between the direction of heading and the direction of travel as shown in Figure 5-5. The proportionality constant is the known as the cornering stiffness C_α .

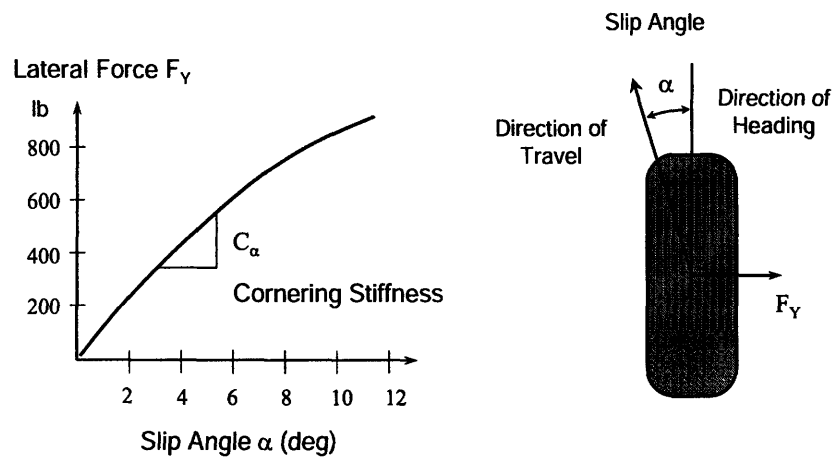


Figure 5-5 Tire cornering force as function of the slip angle

For low speed turning the slip angle and the lateral force are zero. When the front wheel is turned by angle δ , and the vehicle turns about the intersection of the perpendicular bisectors of the two tires with the radius of curvature given by $1/R$ and the steer angle required is $\delta = L/R$ assuming the radius of curvature is much larger than the wheelbase.

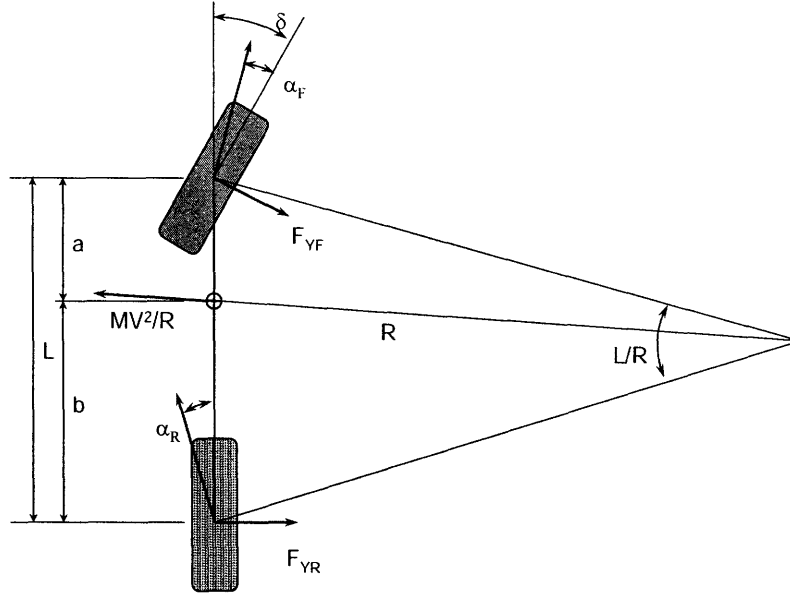


Figure 5-6 : High speed cornering of the bicycle model

During high speed cornering, when the front wheel is turned by an angle δ , the front and rear wheels develop slip and angles α_F and α_R respectively, which are related to the radius of curvature R as given by Equation (5.8).

$$\delta - \alpha_F + \alpha_R = \frac{L}{R} \quad (5.8)$$

These slip angles α_F and α_R create a lateral force F and a moment τ about the centre of mass given by Equation (5.9) and Equation (5.10), which for steady state cornering can be related to the MV^2/R and 0 respectively.

$$F = C_F \alpha_F + C_R \alpha_R = \frac{MV^2}{R} \quad (5.9)$$

$$\tau = aC_F \alpha_F - bC_R \alpha_R = 0 \quad (5.10)$$

Solving these equations, we get Equation (5.11), which shows how the steer angle must be changed with the radius of the turn R or the lateral acceleration a_Y .

$$\delta = \frac{L}{R} + \left(\frac{W_F}{C_F} - \frac{W_R}{C_R} \right) \frac{V^2}{Rg} \quad (5.11)$$

The term in the parenthesis is defined as the understeer gradient and this primarily determines the handling behavior of the car.

$$K_{US} = \left(\frac{W_F}{C_F} - \frac{W_R}{C_R} \right) = \text{Understeer Gradient} \quad (5.12)$$

Three possibilities exist for this analysis:

1. Neutral Steer: $K_{US} = \left(\frac{W_F}{C_F} - \frac{W_R}{C_R} \right) = 0$
2. Understeer: $K_{US} = \left(\frac{W_F}{C_F} - \frac{W_R}{C_R} \right) > 0$
3. Oversteer: $K_{US} = \left(\frac{W_F}{C_F} - \frac{W_R}{C_R} \right) < 0$

The trade-off between Understeer-Oversteer behavior can be seen from Figure 5-7 and Figure 5-8. In Figure 5-7, the steer angle is plotted a function of speed for a constant radius turn.

For an oversteer vehicle ($K_{US} < 0$), we see that at the critical speed given by $V_{crit} = \sqrt{\frac{Lg}{-K_{US}}}$, the

steer angle required to maintain the constant radius curve is zero which implies instability. This unstable plant can be controlled by an expert driver, but regular drivers are uncomfortable in presence of this instability. Hence it is preferred that passenger cars be neutral to oversteer to ensure stability. A factor of safety is needed as the parameters affecting K_{US} are susceptible to significant variation. As a result cars employ more oversteer than required and have more inefficient turning behavior to ensure stability.

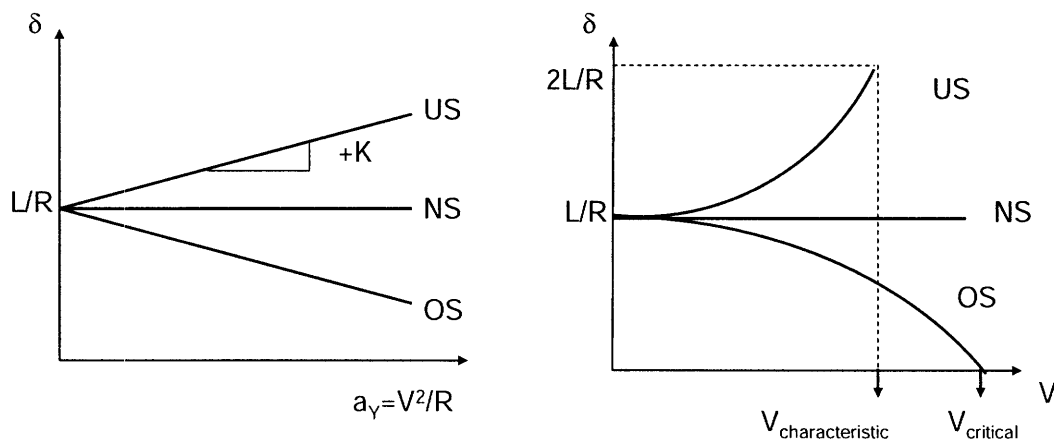


Figure 5-7: Steer angle variation with lateral acceleration or vehicle speed for a constant radius turn

An understeer car has inefficient turning characteristics as the maximum possible front wheel steer angle δ_{max} is limited and this limits the maximum lateral acceleration to a smaller value for

an understeer car than an oversteer car. This can be seen by rewriting Equation (5.11) as Equation (5.13). This is plotted in Figure 5-8 and it shows that great lateral acceleration producing capability for

$$\delta = \frac{V^2}{Rg} \left(\frac{Lg}{V^2} + K_{US} \right) = a_Y \left(\frac{Lg}{V^2} + K_{US} \right) \quad (5.13)$$

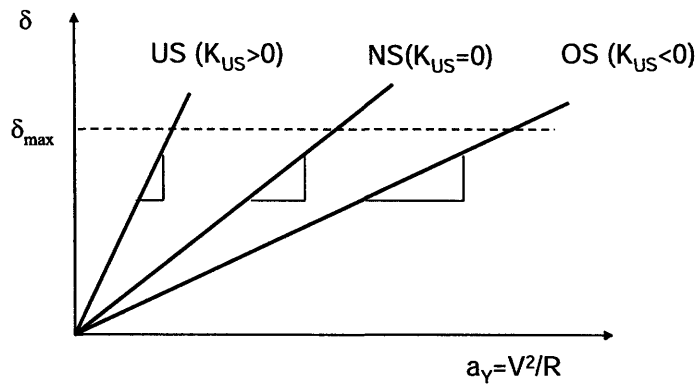


Figure 5-8 Steer angle as a function of lateral acceleration for constant speed curve shows that an understeer car has inefficient turning as compared to an oversteer car

5.4.2 Suspension effects on cornering

It is desirable to be able to change the understeer-oversteer properties depending on the driver and the speed. In the next section we discuss the suspension effects on cornering. Some of the effects that depend on roll stiffness or front/rear roll stiffness distribution are explained below. Since we can control the spring stiffness which determines the roll stiffness of the vehicle independent of the ride-height and independently for the front and rear suspension, the proposed pneumatic suspension can be used to alter the understeer-oversteer behavior on the fly.

Roll Moment Distribution

The cornering stiffness of a pneumatic tire is a concave function of load on the tire as illustrated in Figure 5-9. During cornering, load is transferred in the lateral direction from the inner tire to the outer tire. Due to the concave nature of the tire force-vertical load characteristics, the average lateral force from both tires will reduce. Consequently, the tires will have to assume a greater slip angle to maintain the lateral force necessary for the turn.

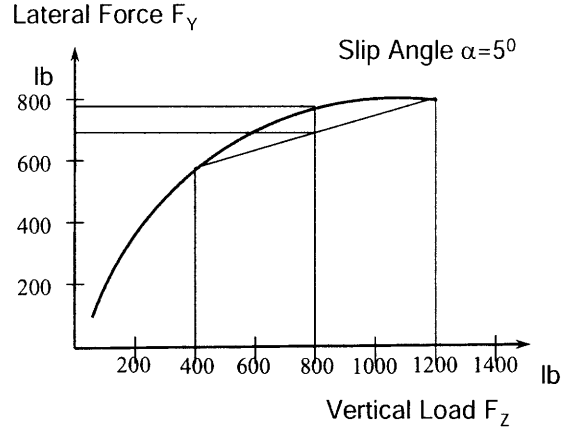


Figure 5-9 : Lateral force variation due to changes in vertical load

The cornering stiffness C_α is a non-linear concave function of the load on the tire and can be approximated by a second order polynomial as shown in Equation (5.14).

$$F_Y = (aF_Z - bF_Z^2) \alpha \quad (5.14)$$

On cornering, the load on the inner wheels increases to $F_{Zi} = F_Z - \Delta F_Z$ and the load on the outer wheels increases to $F_{Zo} = F_Z + \Delta F_Z$ and their cornering stiffness changes. The total force lateral force produced by the two wheels $F_Y = F_{Yi} + F_{Yo}$ is given by:

$$F_Y = (a(F_Z - \Delta F_Z) - b(F_Z - \Delta F_Z)^2 + a(F_Z + \Delta F_Z) - b(F_Z + \Delta F_Z)^2) \alpha \quad (5.15)$$

Using the lateral force produced by the front and rear wheels in the force and moment balance, we get the Equation (5.16) and Equation (5.17) relating the slip angle for the front and rear wheels to the lateral load transfer on the front and rear wheels.

$$\alpha_F = \frac{W_F}{C_F} \left(1 + \frac{2b\Delta F_{ZF}^2}{C_F} \right) a_Y \quad (5.16)$$

$$\alpha_R = \frac{W_R}{C_R} \left(1 + \frac{2b\Delta F_{ZR}^2}{C_R} \right) a_Y \quad (5.17)$$

This changes the relation for the understeer gradient defined in Equation (5.12) as:

$$K_{US} = \left(\frac{W_F}{C_F} - \frac{W_R}{C_R} \right) + \left(\frac{W_F}{C_F} \frac{2b\Delta F_{ZF}^2}{C_F} - \frac{W_R}{C_R} \frac{2b\Delta F_{ZR}^2}{C_R} \right) \quad (5.18)$$

The second term in the relation depends on the load transfer distribution between the on the front tires ΔF_{ZF} and rear tires ΔF_{ZR} , that causes this reduction in lateral force, depends on the ratio of roll stiffness distributed to the front axle $K_{\phi F}$ and the rear $K_{\phi R}$.

$$\Delta F_{ZF} \propto \frac{K_{\phi F}}{K_{\phi F} + K_{\phi R}} \quad (5.19)$$

$$\Delta F_{ZR} \propto \frac{K_{\phi R}}{K_{\phi F} + K_{\phi R}} \quad (5.20)$$

This determines the contribution of this mechanism to understeer-oversteer. Two other mechanisms of understeer-oversteer, due to camber thrust and roll steer, depend on roll stiffness. These make the relation between the steer angle and the lateral acceleration non-linear and the understeer gradient is defined as the slope of the curve at that operating point.

5.4.3 Demonstration of capability to change understeer-oversteer behavior on the fly

Since the proposed customizable suspension system can alter the front and rear roll stiffness independent of each other, this mechanism can be used to change the understeer-oversteer behavior of the car. This was tested on the pneumatic suspension system prototype incorporated on the Honda Civic. This car does not have anti-roll bars and as a result the entire roll stiffness comes from the air-springs.

Four test methods have been suggested to measure the understeer gradient (SAE, 1981; ISO, 2004): constant radius test, constant speed test, constant steer angle and constant throttle, of which only the first two reasonably reflect normal driving conditions. Constant radius test was used and the vehicle speed was increased in steps of 2.5mph. Steering angle is measured using an encoder and lateral acceleration is measured using a car-mounted accelerometer. The road camber on the parking lot and the bump cause the vehicle to move in and out and the resulting steering adjustments required to compensate for that make the steering angle measurements noisy. Maintaining a constant speed is also challenging at low speeds. The minimum radius of turn for this procedure is about 100ft, but the parking lot we used allowed only a radius of 84ft. The resulting data is shown in Figure 5-10, and shows significant change in understeer-oversteer characteristics as described below.

With the front auxiliary volumes closed and rear auxiliary volumes open, greater roll stiffness on front axle leads to greater load transfer (and greater reduction in lateral force) on the front tires and causes the vehicle to understeer. With the front auxiliary volumes open and rear auxiliary volumes closed, greater roll stiffness on the rear axle leads to greater load transfer (and consequently greater reduction in lateral force) on the rear, and causes the vehicle to oversteer.

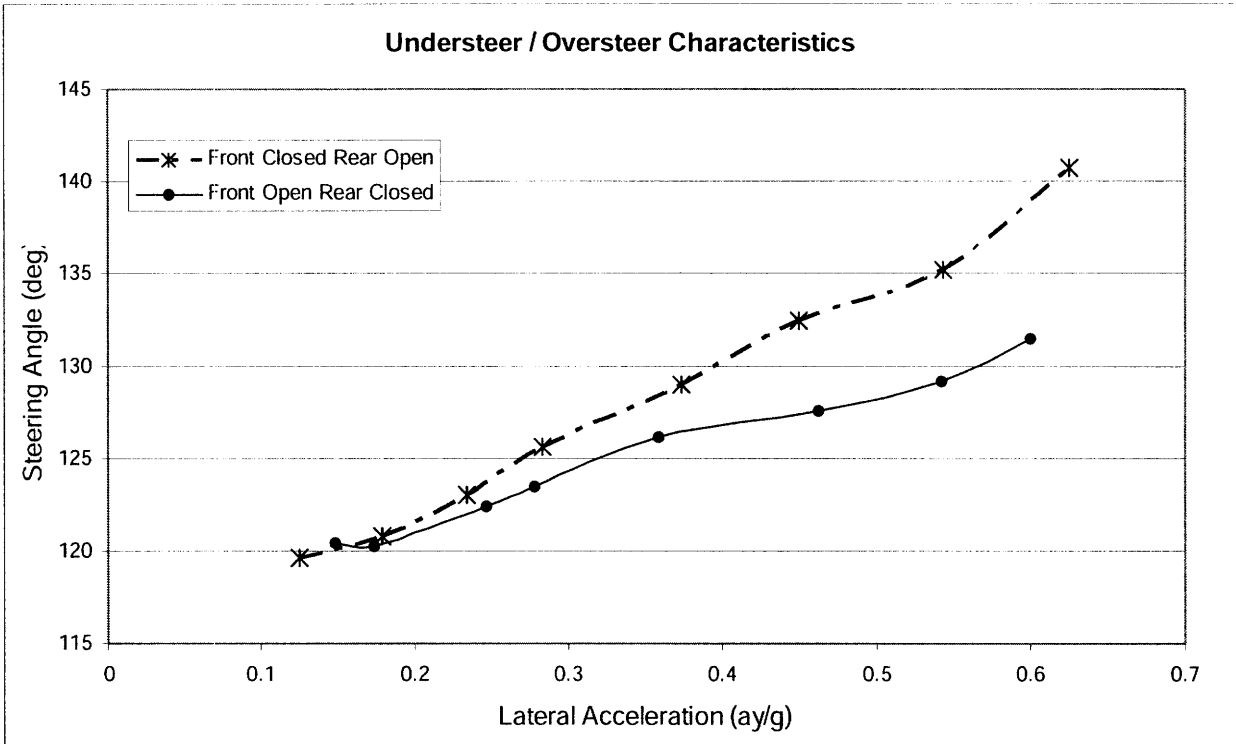


Figure 5-10 : Alteration of Understeer-Oversteer behavior by change the front to rear roll stiffness distribution

5.5 Alteration of pitch and bounce frequencies and the pitch and bounce motion centers

For modeling the bounce and pitch frequencies of a car, we consider the two DOF half-car pitch plane model as shown in Figure 5-11. The differential equations for the bounce and pitch for this simple vehicle model can be given in terms of the mass of the vehicle (M), front and rear ride-rates (K_f and K_r), distance of the front and rear axle to the CG (a and b), pitch moment of inertia (I_y) and radius of gyration (k) as follows.

$$\begin{bmatrix} M & 0 \\ 0 & I_y \end{bmatrix} \begin{Bmatrix} \ddot{x} \\ \ddot{\theta} \end{Bmatrix} + \begin{bmatrix} (K_f + K_r) & (K_r b - K_f a) \\ (K_r b - K_f a) & (K_f a^2 + K_r b^2) \end{bmatrix} \begin{Bmatrix} x \\ \theta \end{Bmatrix} = \begin{Bmatrix} 0 \\ 0 \end{Bmatrix} \quad (5.21)$$

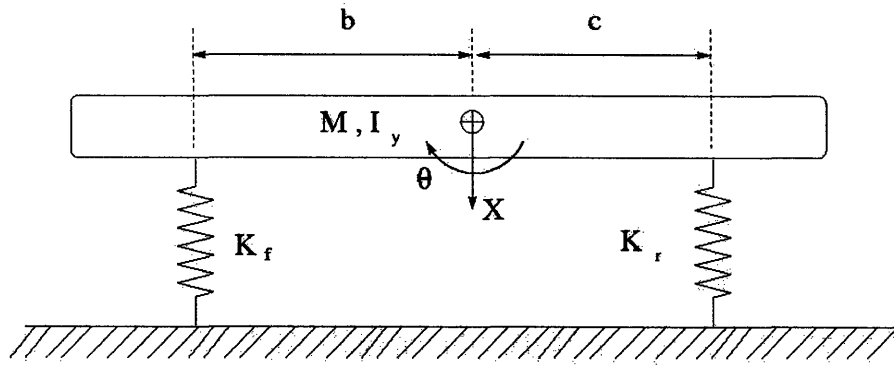


Figure 5-11: Two-DOF half car model to study the bounce and pitch modes of a car

This is an eigenvalue problem and the two eigenvalues give the pitch and bounce frequencies and the eigenvectors indicate the pitch and bounce modes. The eigenvectors determine the predominant modes of oscillations (or in other words the location of the motion centers- pitch center and bounce center). The ratios of the pitch and bounce frequencies and the location of the motion centers are dependent on the relative values of the natural frequencies of the front and rear suspension, which are given by:

$$\omega_f = \sqrt{\frac{K_f g}{W_f}} \quad \text{and} \quad \omega_r = \sqrt{\frac{K_r g}{W_r}} \quad (5.22)$$

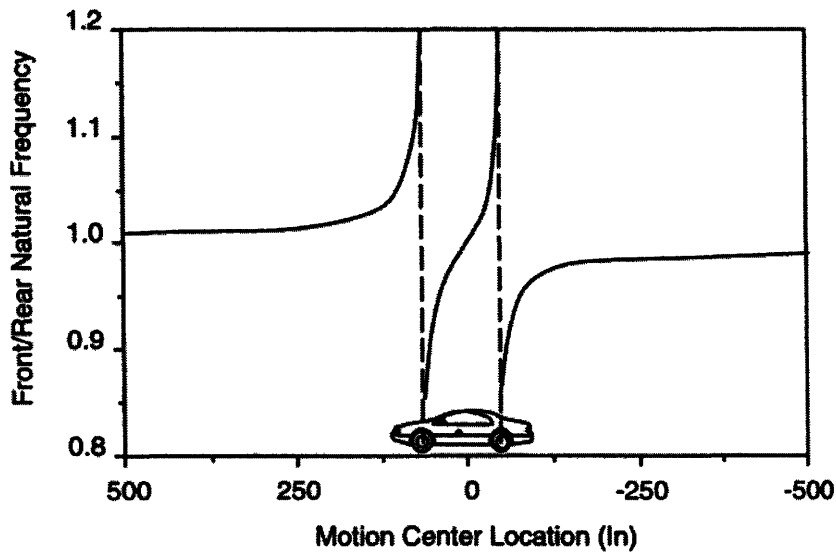


Figure 5-12 Effect of front-rear natural frequency ratio on the position of motion centers (Gillespie 1992)

Figure 5-12 shows the locus of the motion centers as a function of the ratio of the front and rear natural frequencies (Gillespie, 1992). With equal frequencies, one center is at the CG location and the other is at infinity. Equal frequencies result in decoupled or “pure” bounce and pitch

motions. With a higher front frequency, the motion is coupled with the bounce center ahead of the front axle and the pitch center towards the rear axle. A lower front frequency puts the bounce center behind the rear axle and the pitch center forward near the front axle. The latter case (front lower frequency) was recognized by Olley (1983) as the best for achieving “good ride”, and is still followed invariably in the passenger cars.

$$\frac{\omega_f}{\omega_r} = \sqrt{\left(\frac{W_r}{W_f}\right) \cdot \left(\frac{K_f}{K_r}\right)} \quad (5.23)$$

As seen from Equation (5.23), the front and rear natural frequencies depend on the front and rear stiffness as well as the loading on the front and rear wheels. Typically loading increases the load on the rear wheels (W_r) greater than the load on the front wheels (W_f) and as a result, the rear natural frequency reduces. In extreme cases, the condition of lower front frequency may be violated and could result in deteriorated ride. The proposed suspension system allows us to independently vary the front and rear stiffness to compensate for the load distribution and maintain the desired front-rear stiffness distribution (or the desired location of motion centers).

5.6 Summary

User control of stiffness and ride-height is demonstrated to achieve customization and to avoid the trade-offs that arise from the conflicting requirements of comfort and handling. Optimum suspension performance over the entire speed range can be achieved by varying the adaptive suspension parameters as a function of speed. Strategies to minimize wheel and vehicle attitude changes due to maneuvering inputs using the proposed system are discussed, with the most trivial one being “stiffen on hard braking or acceleration” or “stiffen in corners”. Stiffness change bandwidth required for this is discussed, and sensing strategies are recommended. The application of variable stiffness to achieve real-time alteration of pitch and bounce motion centers, and real time alteration of anti-pitch and anti-dive characteristics is discussed. Moreover the possibility of ensuring stability through real-time alteration of understeer-oversteer characteristics is explored and demonstrated on the pneumatic customizable suspension system.

Chapter 6

Ride-Height Control and Stiffness Scheduling for Pneumatic Suspension

The first part of this chapter deals with ride-height control of a pneumatic suspension system. The response of this nonlinear system to valve On-Off control has been modeled and a feedback control law is proposed for ride-height control. It is observed that a feedback control law using only position feedback leads to a limit cycle. A modified state feedback control law using position and pressure feedback is proposed to eliminate the limit cycle, and this leads to convergence to the equilibrium point.

The second part of the chapter deals with stiffness scheduling. In automotive suspension optimization literature, road noise is considered as a disturbance input and sprung mass velocity, suspension deflection and tire-deflection are included in the cost as measures of comfort, road handling, vehicle attitude and suspension workspace. Inertial forces due to maneuvering inputs are never included as they are difficult to model as a stochastic disturbance input. But this is not a reasonable assumption as the inclusion of inertial forces is the most important factor for handling performance optimization. This stiffness scheduling proposed in this chapter is based in the hypothesis that the optimum stiffness depends on the source of disturbance- road noise or inertial forces due to maneuvering inputs. A stiff suspension is required when handling is important in the presence of maneuvering inputs; whereas a soft suspension is required when comfort is desired when road-noise is predominant. In this chapter, an attempt is made to determine the source of disturbance from state measurements exploiting phase relations, and to schedule the stiffness to the optimum value based on the source of disturbance.

6.1 Ride-height control

On-Off valve control for pneumatic actuators for railcar suspension systems have been proposed for the vertical direction using dual airbag actuators by Klinger and Calzado (1977) and for the lateral direction by Cho and Hedrick (1985), but neither reports the existence of a limit cycle. The limit cycle is encountered here as we are using the air-spring for isolation and these papers have used them as actuators. Moreover sliding mode control for an active suspension system, which is in parallel with a passive air suspension, is discussed by Xiao and Kulakowski (2003)

6.1.1 Model for ride-height control

A schematic of the pneumatic suspension system and the ride-height control system is shown in Figure 6-1. It is assumed that the ride-height is changed only when the car is stationary. As a result there are no disturbance inputs, road-noise or load variations, in the system. Compressed air can be pumped into the air-spring through the on-off valve v_1 . The pressure in the air-spring actuator can be reduced by venting it to the atmosphere through the on-off valve v_2 . The system is controlled by On-Off control of these valves.

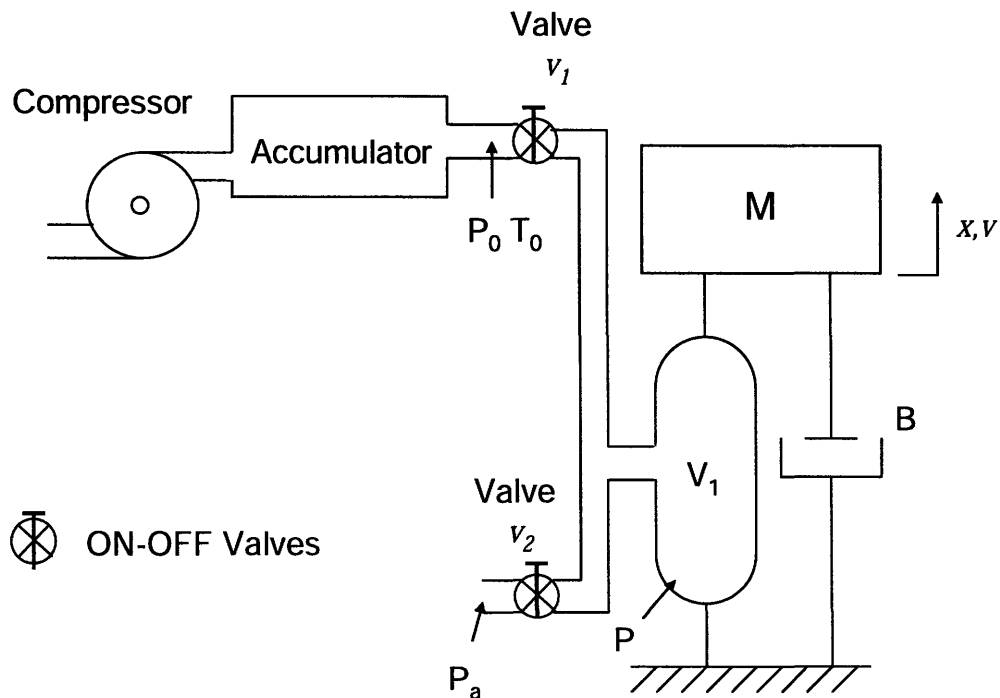


Figure 6-1 : Model for ride-height control of pneumatic suspension system

The equation of motion for the system is:

$$M\ddot{x} + B\dot{x} + Mg + P_a A - PA = 0 \quad (6.1)$$

where M is the mass of the car, B is the damping coefficient, g is the gravitational constant, P is the absolute pressure in the actuator, P_a is the atmospheric pressure and A is the cross-sectional area of a piston and cylinder type air-spring.

Modeling of the air-spring pressurization and depressurization

To model the air-spring pressurization, we begin with the state of the gas in the air-spring as given by Equation (6.2), where the system is characterized by the pressure, volume, mass and temperature (P, V, m, T) of air in the air-spring. The First Law is given by Equation (6.3).

$$\frac{\dot{P}}{P} + \frac{\dot{V}}{V} = \frac{\dot{m}}{m} + \frac{\dot{T}}{T} \quad (6.2)$$

$$C_V \left(\frac{\dot{m}}{m} + \frac{\dot{T}}{T} \right) + R \frac{\dot{V}}{V} = C_P \left(\frac{T_{int}}{T} \right) \frac{\dot{m}}{m} \quad (6.3)$$

Here T_{int} is temperature of the gas entering the air-spring, which can be calculated by assuming isenthalpic flow across the valve v_1 as a function of upstream stagnation pressure P_0 and temperature T_0 , and the specific heat ratio γ , as given by Equation (6.4).

$$T_{int} = T_0 \left(\frac{P}{P_0} \right)^{\frac{\gamma-1}{\gamma}} \quad (6.4)$$

Equation (6.2), Equation (6.3) and Equation (6.4) can be combined to get:

$$\dot{P} = -\gamma \frac{P}{V} \dot{V} + \gamma \frac{RT_0}{V} \left(\frac{P}{P_0} \right)^{\frac{\gamma-1}{\gamma}} \dot{m} \quad (6.5)$$

Modeling of flow from accumulator to air-spring

The flow from the accumulator to the air spring across the valve v_1 is modeled as an isentropic compressible flow. The pressure in the air-spring does not reduce below the threshold required for choked flow. Therefore, the mass flow rate is given by the following equation (White, 1999):

$$\dot{m}_1 = \frac{A_1 P_o}{\sqrt{RT_o}} \sqrt{\frac{2\gamma}{\gamma-1} \left(\frac{P}{P_o}\right)^{\frac{2}{\gamma}} \left[1 - \left(\frac{P}{P_o}\right)^{\frac{\gamma-1}{\gamma}}\right]} \quad (6.6)$$

where A_1 is the cross-sectional area of valve v_1 , and R is the gas constant for air and P_o and T_o are the upstream stagnation pressure and temperature respectively.

Modeling of flow from air-spring to atmosphere

The flow vented from the air-spring to the atmosphere, through valve v_2 , is modeled as a choked flow, since atmospheric pressure is always below the critical pressure for this flow (the critical pressure is about 53% of the actuator pressure for air; the air-spring pressure never falls below 4 atmospheres). The mass flow rate \dot{m}_2 is given by Equation (6.7):

$$\dot{m}_2 = 0.6847 \frac{PA_2}{\sqrt{RT_o}} \quad (6.7)$$

Control Inputs

For the On-Off control of two valves, the control input u for the system has three possible states and is represented as:

1. A control input of $u=1$ corresponds to valve v_1 open and valve v_2 closed ($\dot{m} = \dot{m}_1$)
2. A control input of $u=-1$ corresponds to valve v_1 closed and valve v_2 open. ($\dot{m} = -\dot{m}_2$)
3. A control input of $u=0$ corresponds to both valves closed ($\dot{m} = 0$).

Based on this representation, the Equations (6.5), (6.6), and (6.7) can be combined with the control input u to get:

$$\dot{P} = \gamma \frac{RT_o}{V} \left(\frac{P}{P_o}\right)^{\frac{\gamma-1}{\gamma}} \left[\frac{u(1+u)}{2} \dot{m}_1 + \frac{u(1-u)}{2} \dot{m}_2 \right] - \frac{\gamma P}{V} \dot{V} \quad (6.8)$$

For a piston and cylinder type air-spring, the volume is related to the air-spring deflection by $V = A(x+l_o)$ and $\dot{V} = A\dot{x} = A\dot{v}$, where l_o is the equilibrium length of the air-column at that operating condition.

The state of the system is completely described by the position x , the velocity v , and the air-spring pressure P , and the state evolution equations are given below:

$$\dot{x} = v \quad (6.9)$$

$$\dot{v} = \frac{1}{M}(-Bv + PA - Mg - P_a A) \quad (6.10)$$

$$\dot{P} = -\frac{\gamma P v}{x + l_o} + \frac{\gamma R T_0}{A(x + l_o)} \left(\frac{P}{P_0}\right)^{\frac{\gamma-1}{\gamma}} \left[\frac{u(1+u)}{2} \dot{m}_1 + \frac{u(1-u)}{2} \dot{m}_2 \right] \quad (6.11)$$

6.1.2 Control Law

The object of ride-height control is to determine a control law that will drive the system to the equilibrium point ($x=x_{des}$; $v=0$; $P=P_{eq}=Mg/A-P_a$). As a first iteration, we attempted to use output feedback and the surface $x-x_{des}=0$ was used as a switching surface for the control.

$$u = -\text{sgn}(x - x_{des}) \quad (6.12)$$

The simulation of this control law shows that the system tends to a limit cycle. Figure 6-2 shows the evolution of the system state in time and trajectory in the three-dimensional state space. This simulation was repeated for a number of initial conditions and all the system trajectories converge to the same limit cycle as shown in Figure 6-3. The system exhibits a limit cycle as the energy entering the system when the mass is pumped into the system by the compressor is balanced by the energy dissipated. The energy dissipation occurs via two mechanisms- the viscous damping provided by the damper and the mass of air vented to the atmosphere.

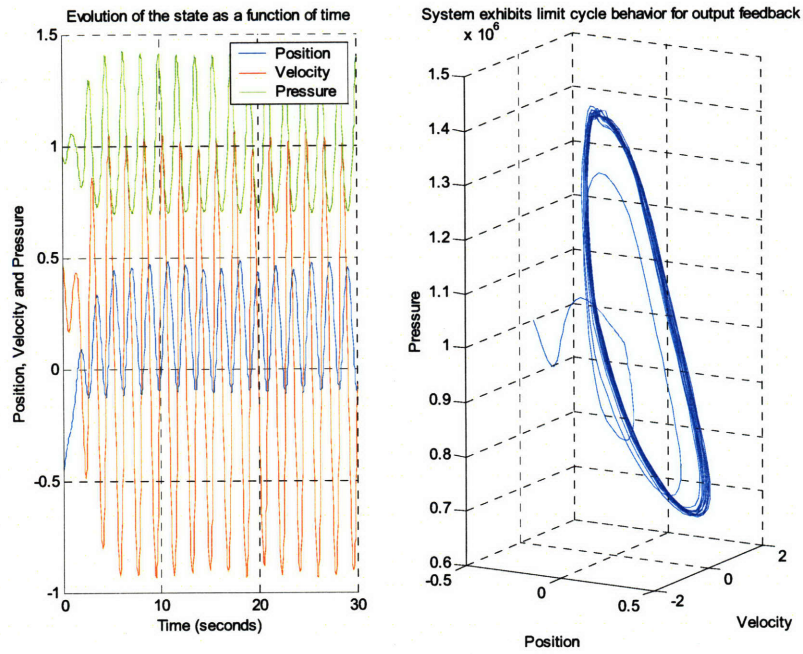


Figure 6-2 Existence of a limit cycle for output feedback $u=-\text{sign}(x)$

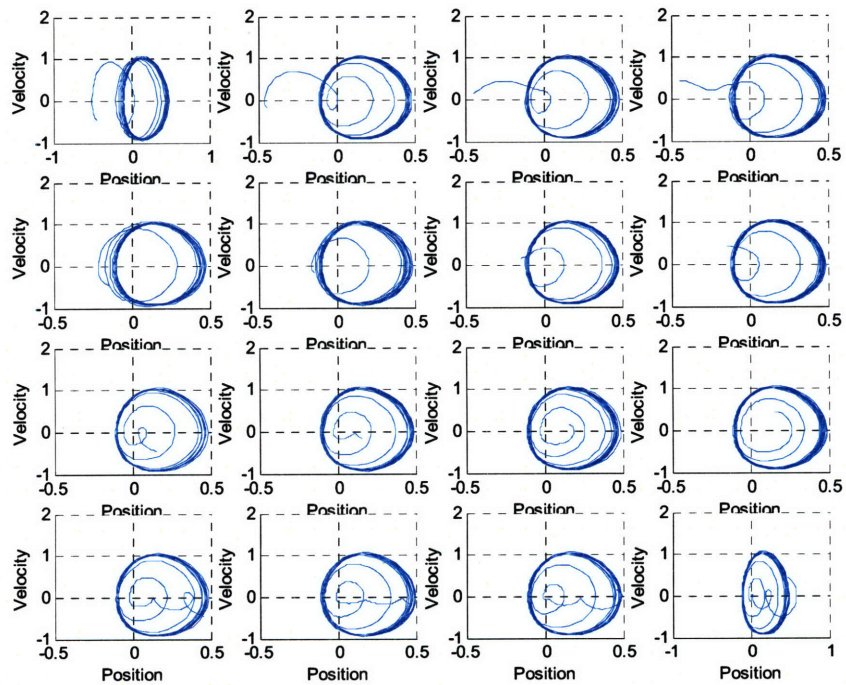


Figure 6-3: Evolution of the system from different initial conditions to the limit cycle.

State feedback to eliminate limit cycle

To eliminate the limit cycle, we define a new switching surface using state-feedback $A \equiv P - P_{eq} + \alpha v + \beta x = 0$. With this switching surface, the control law is as shown in Equation (6.13) and the simulation shows that the system converges to the equilibrium point as shown in Figure 6-4. The same simulation was repeated for several initial conditions and all simulations predicted convergence to the fixed point ($x=x_{des}$; $v=0$; $P = P_{eq} = Mg/A - P_a$).

$$u = -\text{sgn}(P - P_{eq} + \alpha v + \beta x) \quad (6.13)$$

This system also converges to the fixed point without velocity feedback ($\alpha=0$)

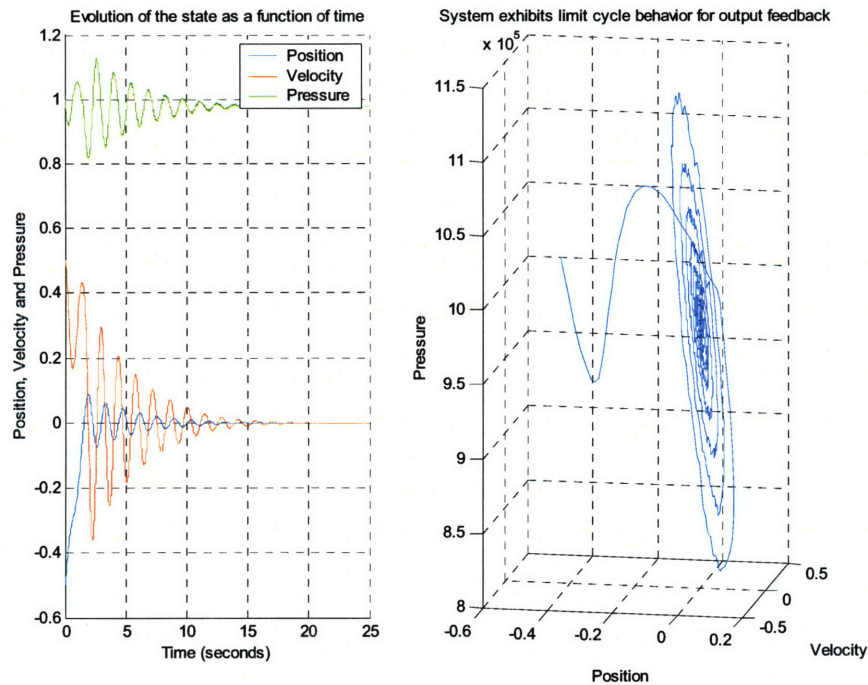


Figure 6-4 : Convergence of the system using the control law $u = -\text{sgn}(P - P_{eq} + \alpha v + \beta x)$

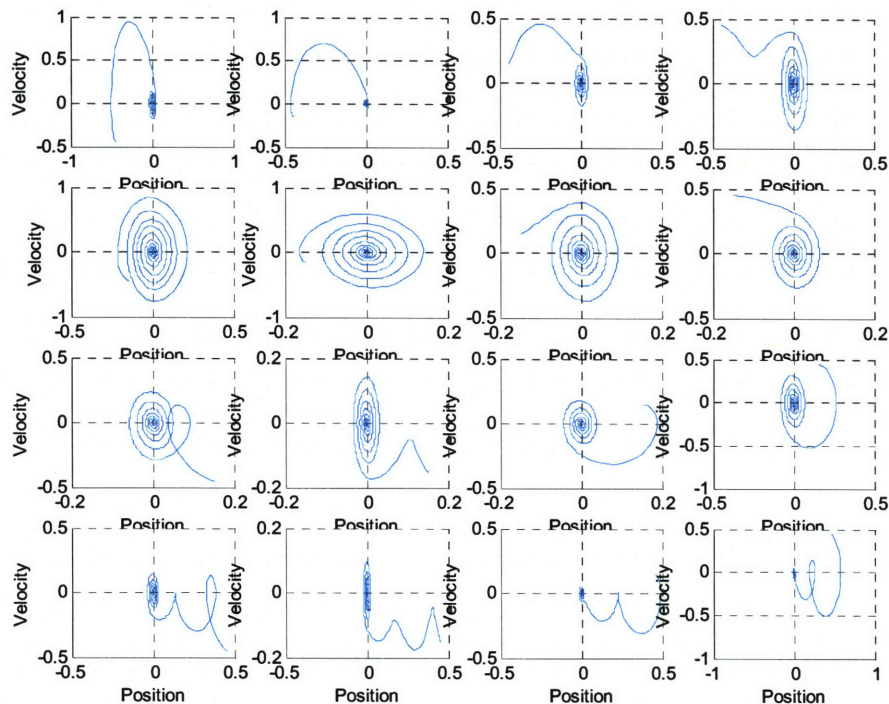


Figure 6-5 The control law $u = -\text{sgn}(P - P_{eq} + \alpha v + \beta x)$ leads to convergence to the fixed point from different initial conditions

6.2 Stiffness Scheduling

6.2.1 Determination of disturbance source from state measurements exploiting phase relations

Several systems have more than one source of disturbance, and optimum isolation from different disturbances requires conflicting isolation parameters (or feedback parameters). For instance, in a vibration-isolation system, ground-vibration isolation requires low stiffness; whereas inertial force isolation requires high stiffness. In this section, an attempt is made to figure out which disturbance is acting and in what proportions using only state-measurements and to adapt the feedback parameters to optimum accordingly. Other strategies for stiffness scheduling discussed in the literature (Coirriga et. al., 1996; Elbeheiry et. al., 1996; Zuo & Nayfeh, 2004) propose optimum stiffness based on road roughness and vehicle speed, and can be easily modified to change with the weighing of the parameters included in the cost function. Another approach discussed in the previous chapter, does scheduling based on sensing of the inertial forces caused by maneuvering inputs by using accelerometers, or by directly measuring vehicle velocity and maneuvering inputs such as steering angle and brake fluid pressure. But this requires the system

to be able to change stiffness instantaneously. The formulation in this chapter assumes that the force F can be modeled as a filtered stochastic disturbance input, with the filter and the amplitude changing gradually in time.

Model

We will use a simple quarter-car 2-degree of freedom model as shown in Figure 6-6. The two disturbance inputs to this system are road noise \dot{x}_r , and inertial forces due to maneuvering inputs F .

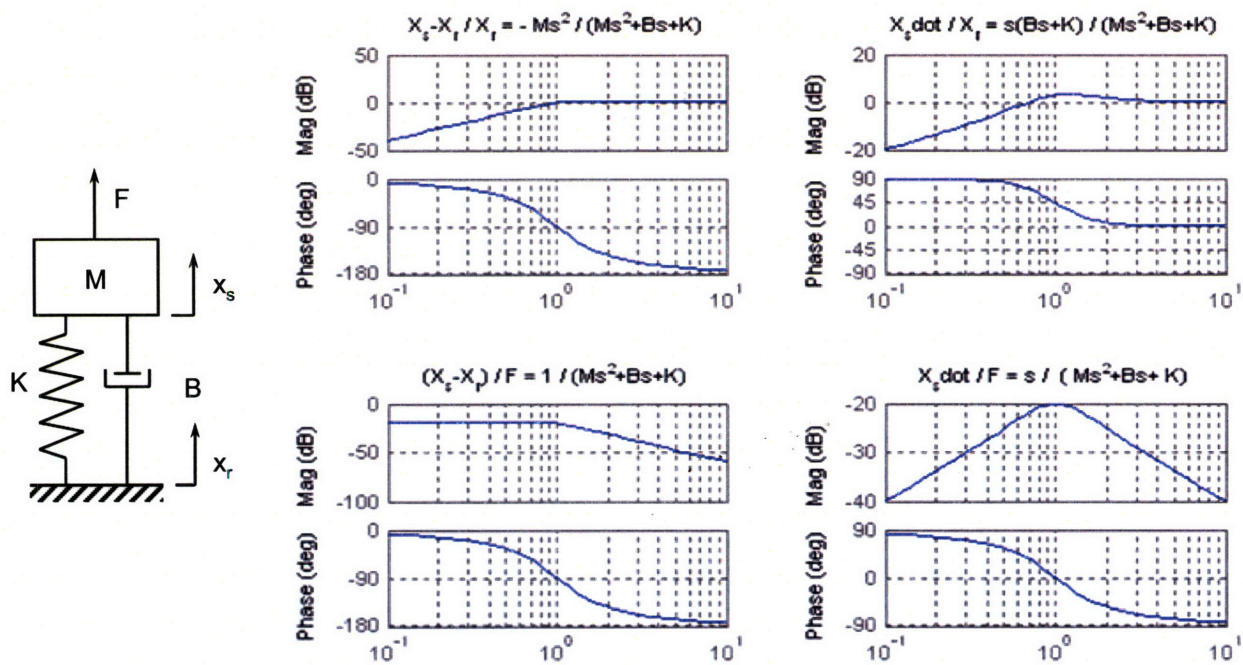


Figure 6-6 Bode plots for spring deflection and chassis velocity as caused by ground vibration and inertial forces

The transfer functions and the Bode plots show that the state \dot{x}_s leads $x_s - x_r$ by greater than 90° when caused by road noise \dot{x}_r ; whereas \dot{x}_s leads $x_s - x_r$ by 90° when caused by inertial force F . This means that the states are orthogonal when only inertial force F is acting. This relative phase difference can be exploited to figure out the source of disturbance and the relative strengths of the disturbances. One way to do that is to evaluate the integral $R(T)$ shown below:

$$R(T) = \int_0^T (x_s - x_r) \dot{x}_s d\tau \quad (6.14)$$

$R(T)$ will stay close to 0 when only F is acting and $R(T)$ will increase at a certain rate when only \dot{x}_r is acting. This gives a potential way to distinguish between the two sources of disturbances F and \dot{x}_r . The spring-mass-damper system is simulated in Simulink as shown in Figure 6-7 and the integral is evaluated for sinusoidal disturbance inputs and white noise disturbance inputs.

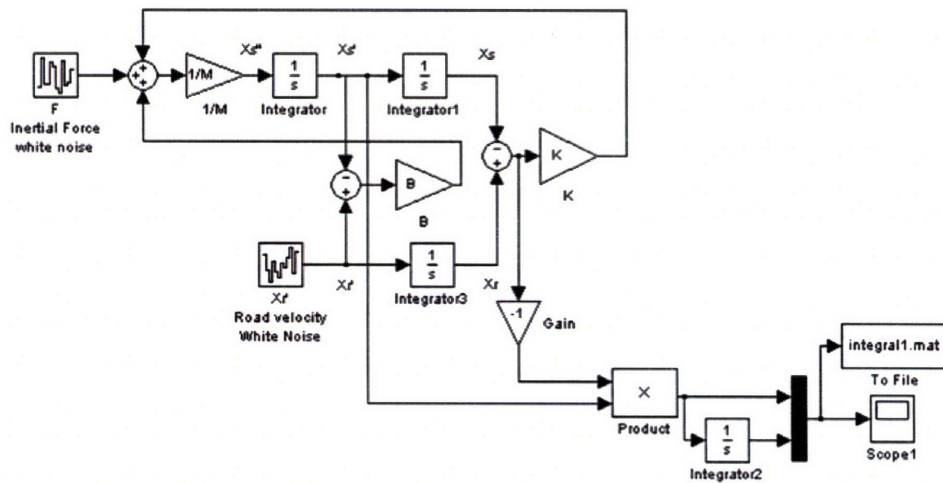


Figure 6-7 Simulink model to calculate the product of the states $P(T)$ and integral $R(T)$

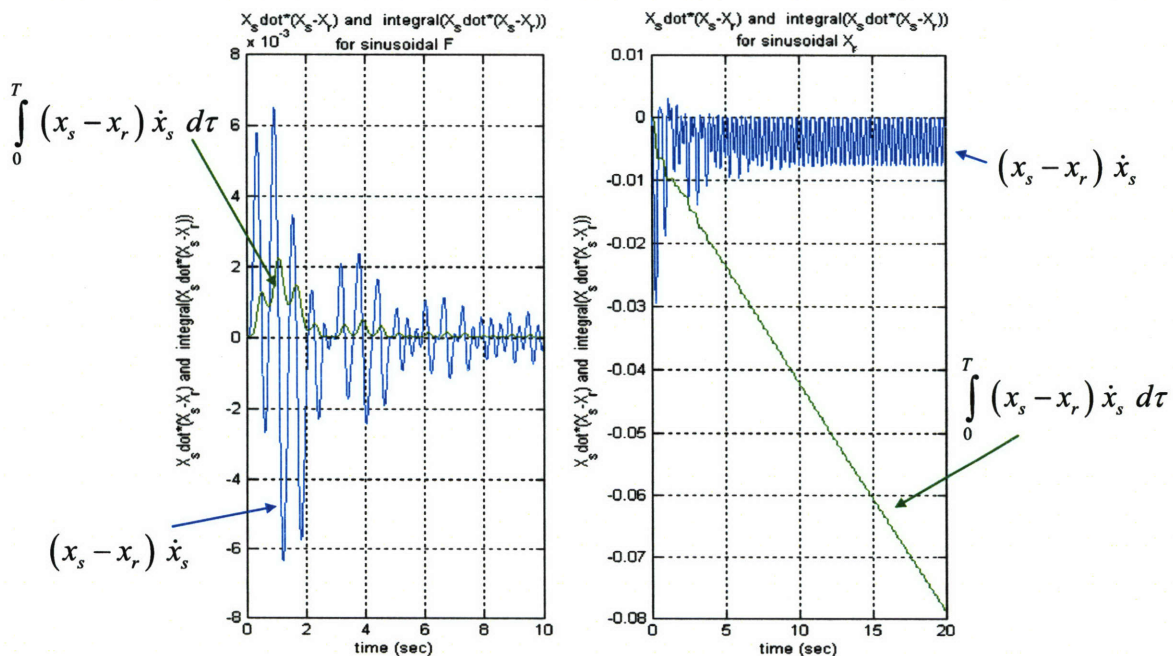


Figure 6-8 : For sinusoidal disturbance input F , $P(T)$ changes sign with time and $R(T)$ stays close to 0; For sinusoidal disturbance input \dot{x}_r , $R(T)$ increases at a steady rate

Figure 6-8 shows the simulation results for sinusoidal disturbance inputs. The graph on the left shows the results of the simulation for sinusoidal disturbance input F . From the blue curve on the graph, we observe that the product of the two states $P(T) = (x_s - x_r) \dot{x}_s$ changes sign for sinusoidal disturbance input F . As a result, the integral $R(T) = \int_0^T (x_s - x_r) \dot{x}_s d\tau$, indicated by the green curve, stays close to 0.

The graph on the right shows results of the simulation for sinusoidal disturbance input \dot{x}_r . From the blue curve on the graph, we observe that the product of the two states $P(T) = (x_s - x_r) \dot{x}_s$ stays negative for sinusoidal disturbance input \dot{x}_r . As a result, the integral $R(T) = \int_0^T (x_s - x_r) \dot{x}_s d\tau$, indicated by the green curve, grows at a steady rate.

The same trend is observed when a white-noise disturbance is applied instead of a sinusoidal disturbance. The results of this simulation for white-noise disturbance inputs F and \dot{x}_r , shown in Figure 6-9, indicate the same trend for $P(T)$ and $R(T)$.

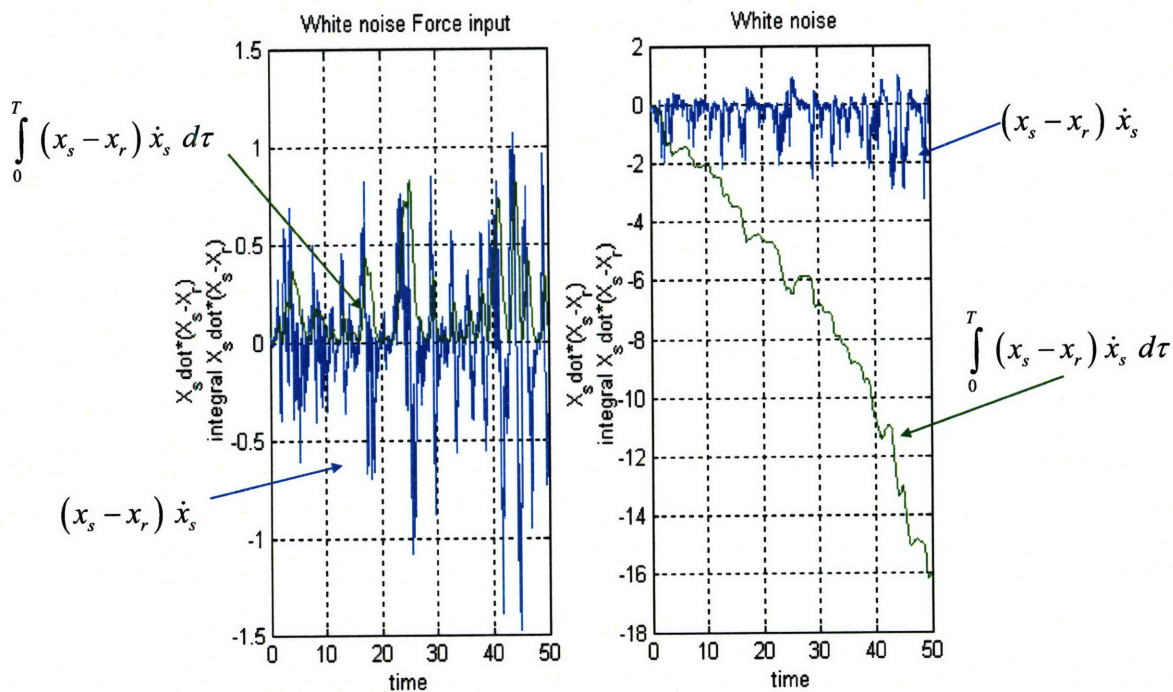


Figure 6-9: For white noise disturbance input F , $P(T)$ changes sign with time and $R(T)$ stays close to 0; For white noise disturbance input \dot{x}_r , $R(T)$ increases at a steady rate

6.2.2 Scaling

Although $R(T)$ provides a potential means to distinguish between the vibrations caused by inertial forces and those caused by road noise, this metric has the following two drawbacks:

1. Growth rate of this integral depends on the type of disturbance as well as the magnitude.
2. Rate is difficult to compute

To eliminate these drawbacks, we scale the integral $R(T)$ by the integral of the product of magnitude of the two states as shown on Equation (6.15). This relation can be modified as shown in Equation (6.16) to include any information about the frequency range or the power spectral density of the road-noise. By including the effective phase lag ϕ_{eff} , we can have the scaling parameter $r(T)$ vary in the range $(-1,0)$. The simulated performance of this metric provides an excellent estimate of the source of the disturbance and their relative power content as illustrated in Figure 6-10.

$$r(T) = \frac{\int_0^T (x_s - x_r) \dot{x}_s d\tau}{\int_0^T |x_s - x_r| \cdot |\dot{x}_s| d\tau} \quad (6.15)$$

$$r(T) = \frac{\int_0^T (x_s - x_r) \dot{x}_s d\tau}{|\cos \phi_{eff}| \int_0^T |x_s - x_r| \cdot |\dot{x}_s| d\tau} = \begin{cases} 0 & \text{when only } F \text{ is acting} \\ (-1,0) & \text{Indicates the proportion of } F \text{ and } \dot{x}_r \\ -1 & \text{when only } \dot{x}_r \text{ is acting} \end{cases} \quad (6.16)$$

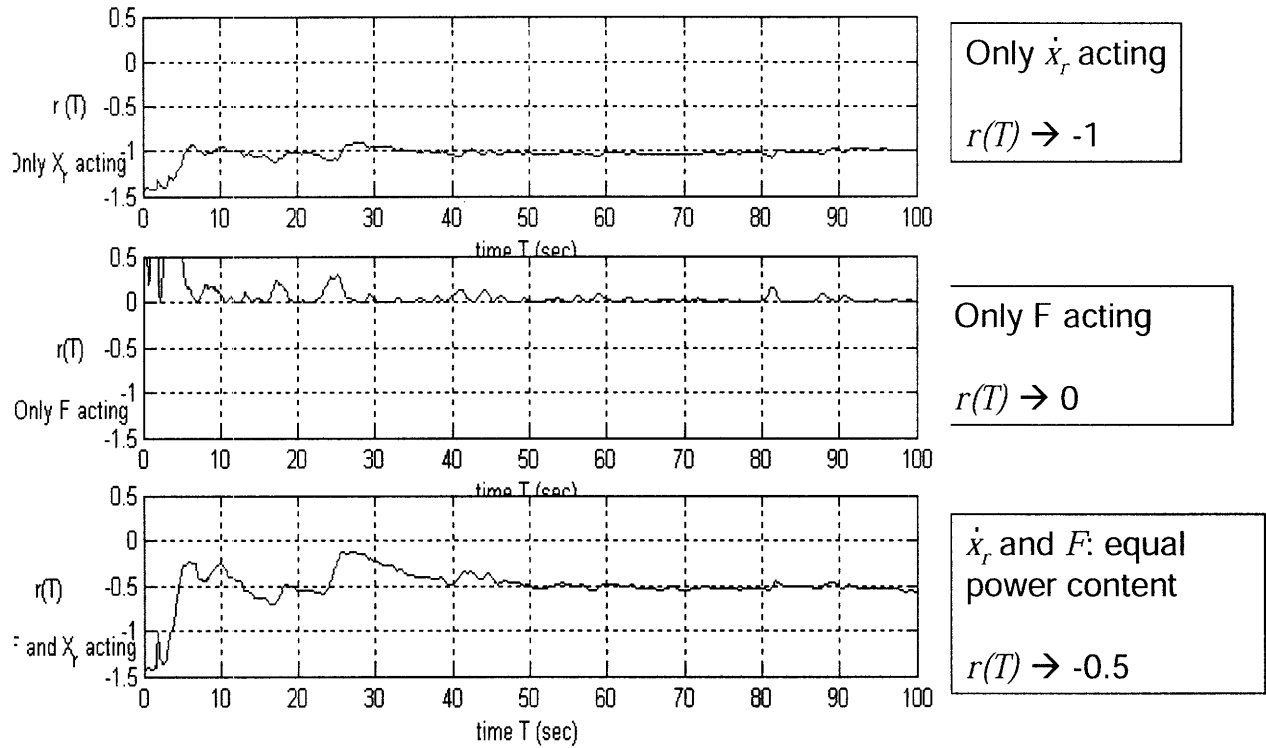


Figure 6-10: Performance of metric $r(T)$ to determine the source of disturbance

6.2.3 Exponential Forgetting

The metric $r(T)$ gives an excellent estimate of the source of the disturbance as well as the relative power content in the steady state disturbance input (No change in the relative power content of the disturbance inputs). But this metric is sluggish to respond to changing disturbance input conditions as illustrated in Figure 6-10. This is because the integrals get “hardened”, i.e., they do not forget old values. One way to speed up the disturbance estimator response is by implementing “exponential forgetting”. The intuitive motivation for this is that the past values should be discounted exponentially. Here we modify the integrals in the metric $r(T)$ by those shown in Equation (6.17). This modification actually makes the execution easier, as we can use a low-pass filter instead of an integrator. The improved response to changing disturbance conditions is shown in Figure 6-11.

$$r(T) = \frac{\int_0^T (x_s - x_r) \dot{x}_s e^{-a(T-\tau)} d\tau}{|\cos \phi_{eff}| \int_0^T |x_s - x_r| |\dot{x}_s| e^{-a(T-\tau)} d\tau} \quad (6.17)$$

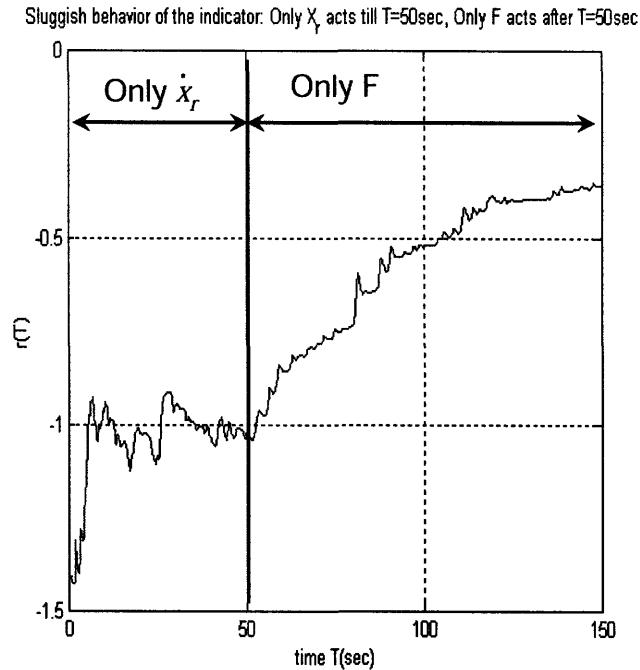


Figure 6-11: Sluggish behavior of the indicator $r(T)$

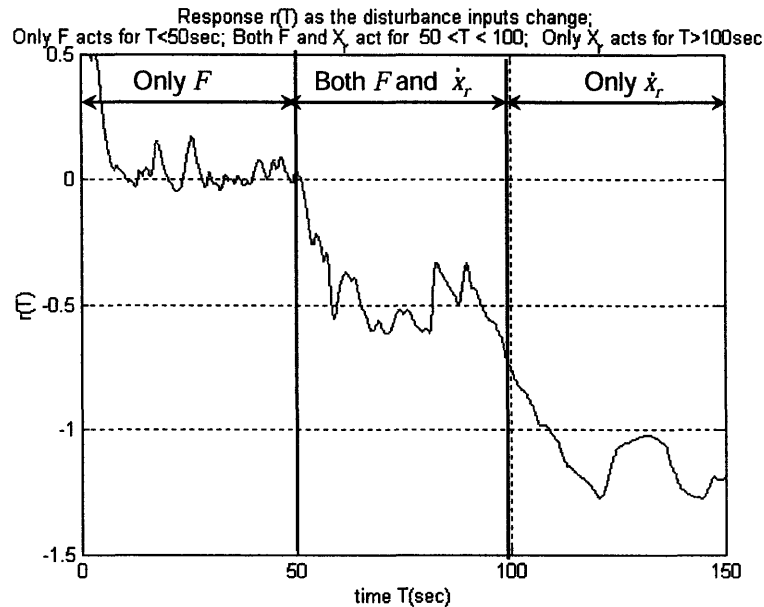


Figure 6-12: Improvement in response time of the indicator $r(T)$ after implementing exponential forgetting

6.2.4 Stiffness scheduling based on $r(T)$

The metric $r(T)$ can be used to determine the power content in each disturbance input and as the optimum stiffness depends on the disturbance input acting, we can switch the stiffness as a function of the metric $r(T)$. One possible switching algorithm can be given by Equation (6.18), as shown in Figure 6-13:

$$K = \begin{cases} K_{\max} = \alpha K_{\text{nom}} & \text{for } r(T) > -1/3 \\ K_{\text{nom}} & \text{for } -1/3 > r(T) > -2/3 \\ K_{\min} = K_{\text{nom}} / \alpha & \text{for } r(T) < -2/3 \end{cases} \quad (6.18)$$

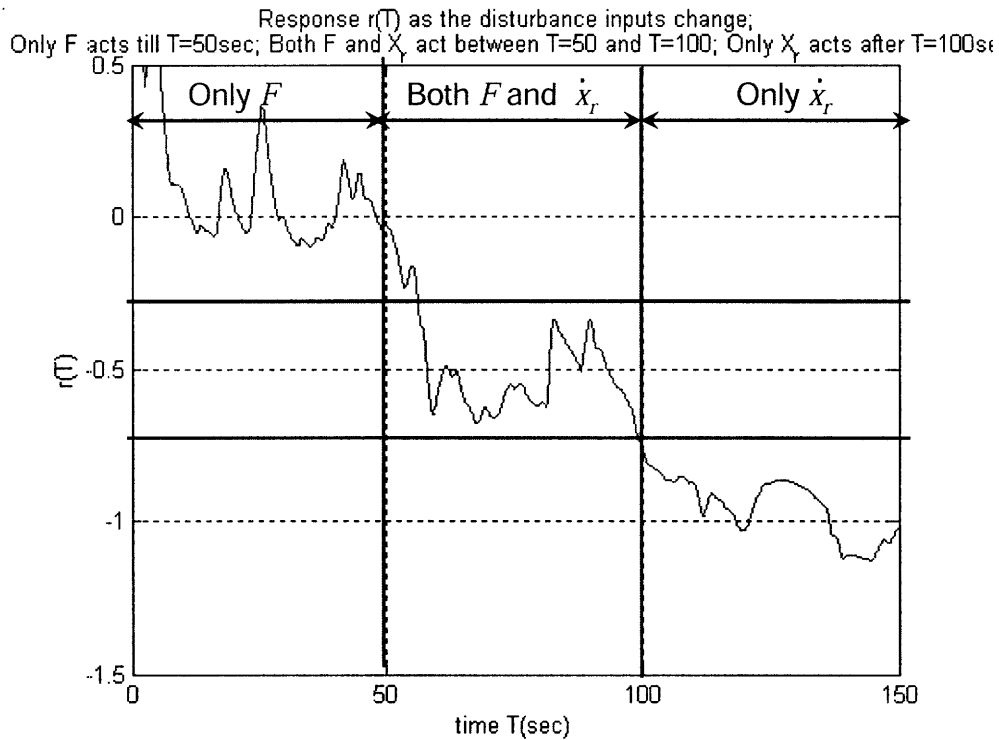


Figure 6-13: Stiffness scheduling using indicator $r(T)$

The simulation results in Figure 6-14 show the switching of stiffness and the resulting response x_s and \dot{x}_s of the system for different values of α . For this simulation, only disturbance F is acting for the first 50 seconds, both disturbances F and \dot{x}_r are acting with equal power-content for the next 50 seconds, and only disturbance \dot{x}_r is acting for the last 50 seconds. The algorithm identifies the type of disturbance input and also their relative power content and the stiffness switching is shown in Figure 6-14.

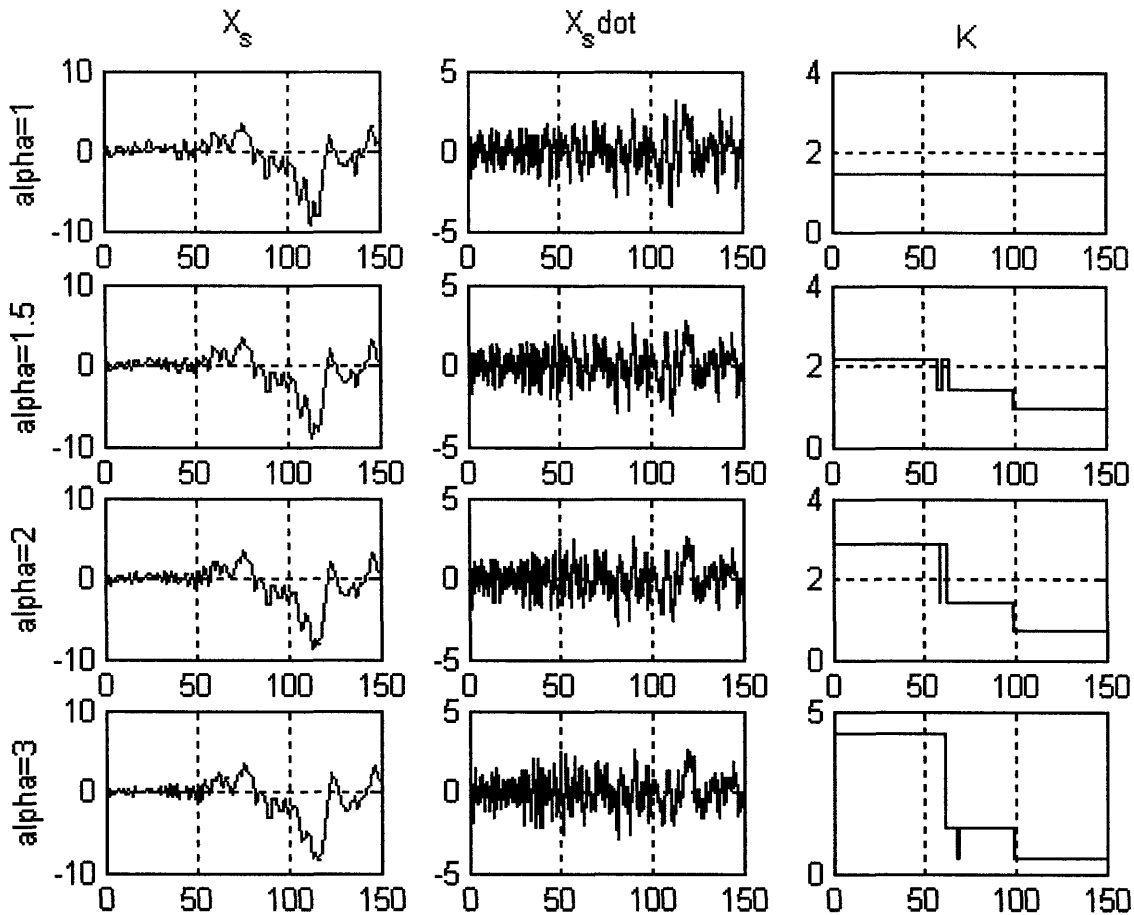


Figure 6-14 Simulation results for stiffness switching using $r(T)$ for different α values

During the first 50 seconds, when only disturbance input F is acting, the algorithm sets the stiffness to K_{max} . The improvement in the transfer function x_s/F , which is indicative of vehicle and wheel attitude changes due to inertial forces, is shown in Figure 6-15. The 2-norm of x_s reduces from 0.55 for $\alpha = 1$ (no stiffness switching) to 0.35 for $\alpha = 3$.

During the last 50 seconds, when only disturbance input x_r is acting, the algorithm sets the stiffness to K_{min} . The improvements in \dot{x}_r/\dot{x}_s , which is indicative of road-noise isolation, is shown in Figure 6-16 for $\alpha = 1$ (no stiffness switching) and $\alpha = 3$. The 2-norm of \dot{x}_s reduces from 1.18 for $\alpha = 1$ (no stiffness switching) to 0.87 for $\alpha = 3$.

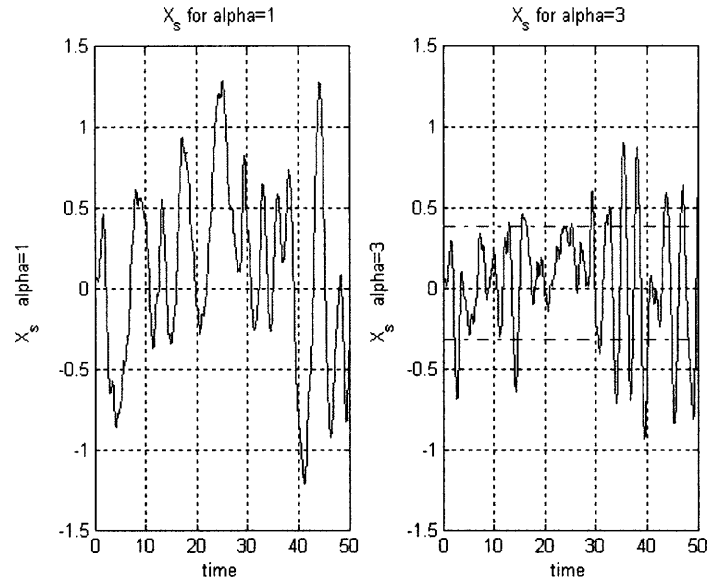


Figure 6-15 Improvements in x_s using the stiffness switching strategy ($\alpha=3$)

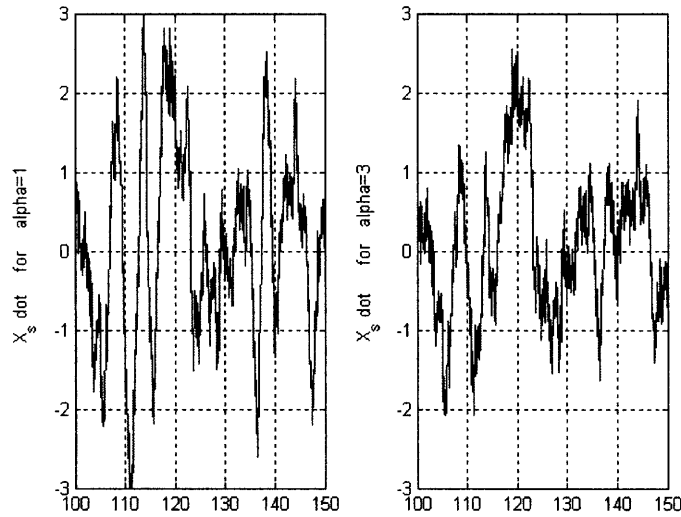


Figure 6-16 Improvements in \dot{x}_s using the stiffness switching strategy ($\alpha=3$)

The ultimate goal of this research is to come up with a non-linear control law of the form $K = K_1 + K_2 \operatorname{sgn}((x_s - x_r) \dot{x}_s)$. The motivation is that $(x_s - x_r) \dot{x}_s$ will keep changing sign when excited by force F and as a result the system will offer an effective stiffness of K_I . Whereas, $(x_s - x_r) \dot{x}_s$ will be negative most of the time when excited when by road noise x_r and as a result the system will offer an effective stiffness of less than K_I .

6.3 Summary

Ride-height control of the pneumatic suspension system is discussed. The response of this nonlinear system to the valve On-Off control has been modeled and a feedback control law is proposed for ride-height control. It is observed that a feedback control law using only position feedback leads to a limit cycle. A modified state feedback control law using position and pressure feedback is proposed to eliminate the limit cycle, and this leads to convergence to the equilibrium point

The optimum stiffness depends on the source of disturbance. An attempt is made to determine the source of disturbance and their relative power content from state measurements exploiting phase relations, and to set the stiffness to the optimum value based on the source of disturbance. Orthogonality of the states due to inertial force disturbance input is exploited to come up with a metric to determine the source of disturbance and their relative power content. The metric involving integral of product of states provides as excellent measure of the source of disturbance as well as their relative power content. But this metric is sluggish to respond to changing disturbance conditions as the integral gets “hardened”. Exponential forgetting is implemented by using a low-pass filter to improve the response of the metric to changing disturbance conditions and shows promising results. There is a trade-off involved in the selection of the cut-off frequency; a high cut-off frequency leads to significant oscillations of the metric, whereas a low cut-off frequency leads to a sluggish response to changing disturbance conditions. Future work involves optimization of the cut-off frequencies depending on the application and eliminating this trade-off through use of higher order filters and through a choice of a different metric. An example algorithm for switching stiffness to the optimum value using this metric has been illustrated and improvements in road-noise isolation as well as inertial-force isolation have demonstrated. Future work involves creation of a non-linear control law to combine the sensing as well as switching in the control law.

Chapter 7

Conclusions

Automotive suspension system design typically involves a trade-off between the conflicting requirements of comfort and handling. In this thesis, the application of Axiomatic Design Theory to eliminate these trade-offs is investigated.

1. Coupling in existing suspension system is manifest by the wheel alignment parameter changes due to suspension travel. A new six-bar Watt-I linkage suspension system is proposed to make the wheel alignment parameters independent of suspension travel, thereby eliminating the lateral destabilizing forces and excessive tire-wear. This allows the use of a lower stiffness spring without compromising on handling. A formulation for kinematic synthesis of the six-bar Watt-I linkage is outlined. This design has promise for improved comfort and handling and reduced tire-wear on straight-ahead driving conditions, but exhibits unfavorable camber change on cornering. This exercise indicates that altering the single degree of freedom suspension kinematics may have limited benefit in eliminating the coupling. It also indicates that it is essential to include inertial forces caused by maneuvering input as a disturbance input in addition to the road noise.
2. To avoid the trade-offs involved in comfort and handling, a novel design for a customizable automotive suspension system is proposed, that is capable of independent control of stiffness, damping and ride-height with low power input. This system is capable of providing the desired performance depending on user preference, road conditions and maneuvering inputs.
3. An electromechanical suspension prototype is designed and fabricated to demonstrate the concept. The suspension kinematics was assumed as given and the proposed modifications do not change the suspension kinematics.

4. Use of a linear stage on the lower control arm to achieve the stiffness change present cost, robustness and unsprung mass issues. Moreover, application of variable stiffness suspension system to improved vehicle dynamics suggests that much greater benefit could be derived if the stiffness change could be instantaneous (rapid) and if stiffness change did not affect ride-height.
5. A customizable pneumatic suspension system is proposed that has the potential of rapid stiffness change with limited power input and no effect on ride-height due to stiffness change. This is done by connecting the air-spring volume to auxiliary volumes through On-Off valves. By adequately choosing N unequal auxiliary volumes, this system can achieve 2^N stiffness settings.
6. Moreover, the proposed pneumatic isolation system is simple, inexpensive, robust and light, and as a result it is applicable to generic vibration isolation systems with conflicting or time-varying stiffness requirements. Application to systems with conflicting and time-varying stiffness requirements, such as isolation system for precision motion stage for semiconductor metrology and isolation for prosthetic limbs, is discussed.
7. A customizable pneumatic suspension system prototype has been designed and incorporated in a car and it demonstrates the concept well. A data acquisition system has been designed and incorporated in the car for testing the performance of the pneumatic suspension system.
8. A detailed thermodynamic model to incorporate the effect of air inertia and the pipe losses on the frequency response of the air-spring with auxiliary volumes is developed and it is shown that the air-spring with auxiliary volumes exhibits a low stiffness at low frequencies and high stiffness at high frequencies. This model matches well with experimental data for small displacements. This linearized model is used to study the effect of this frequency dependant stiffness behavior on the road-noise isolation performance of the system, and it is verified that the frequency dependant stiffness behavior has a negligible effect on the road-noise isolation performance.
9. For large displacements, significant deviations from the linear model are observed. A nonlinear model is developed and it explains the observed data well. Moreover this analysis reveals a counter-intuitive stiffness behavior for the air-spring in extension. The air-spring with higher effective volume is actually stiffer than the air-spring with lower

effective volume beyond a certain deflection. We have shown that this counter-intuitive behavior is due to the cross coupling between the two stiffness components K_A and K_T . This means that our original strategy of increasing effective volume to reduce stiffness needs to be modified. Further study of this asymmetric stiffness behavior is needed to account for, and possibly exploit this non-linear behavior.

10. With our proposed design, we can only reduce the thermodynamic stiffness K_T and this restricts the achievable range of stiffness if K_A is greater than K_T , which was the case in the prototype design. Two possible solutions for this problem are discussed. Reduction of area change stiffness K_A is possible only in limited operating range and is not acceptable as it makes the system coupled. Moreover it leads to a very low overall stiffness, and hence has to be accompanied by increase of thermodynamic stiffness K_T . The associated packaging and suspension travel issues are discussed and some potential solutions are proposed.
11. The applications of suspension systems capable of low bandwidth and high bandwidth (instantaneous) stiffness change are discussed. Optimum suspension performance over the entire speed range can be achieved by varying the adaptive suspension parameters as a function of speed. Strategies to minimize wheel and vehicle attitude changes due to maneuvering inputs by rapid stiffness change using the proposed system are discussed.
12. The application of variable stiffness to achieve real-time alteration of pitch and bounce motion centers, and real time alteration of anti-pitch and anti-dive characteristics is discussed. Moreover the possibility of ensuring stability through real-time alteration of understeer-oversteer characteristics is demonstrated on the pneumatic suspension prototype.
13. The response of constant area pneumatic suspension system to the valve On-Off control is modeled and a feedback control law is proposed for ride-height control. A feedback control law using only position feedback leads to a limit cycle and a modified state feedback control law using position and pressure feedback leads to convergence to the equilibrium point.
14. An algorithm for stiffness scheduling, based on the hypothesis that the optimum stiffness depends on the source of disturbance, is proposed. Determination of the disturbance source is done using only state-measurements. This algorithm computes a metric

involving integral of product of states which provides a measure of the source of disturbance as well as their relative power content. An example algorithm for switching stiffness to the optimum value using this metric has been illustrated and improvements in road-noise isolation as well as inertial-force isolation have been demonstrated. Future work involves coming up with a non-linear control law to combine the sensing as well as switching in the control law.

Bibliography

Ackermann, J., 1994, "Robust Decoupling, Ideal Steering Dynamics and Yaw Stabilization of 4WS car", *Automatica*, Vol. 30, No. 11, pp 1761-1768.

Ackermann, J., 1997, "Robust control prevents car skidding", 1996 Bode Lecture Prize Article, *IEEE Control Systems Magazine*, pp 23-31.

Anderson, O.W., 1967, *The Analysis and Design of Pneumatic Systems*, John Wiley and Sons.

Bachrach, B.I., and Rivin, E., 1983, "Analysis of a damped pneumatic spring". *Journal of Sound and Vibration*, Vol. 86 (2), pp 191-197.

Bastow, D., 1987, *Car Suspension and Handling*. Pentech, London.

Berg, M., 1999, "A three dimensional air-spring model with friction and orifice damping", *Proceedings of the 16th IAVSD Symposium*, The dynamics of vehicle on roads and tracks, Pretoria, South Africa.

Blickhan, R., 1989, "The spring-mass model for running and hopping", *Journal of Biomechanics*, Vol. 22, No. 11/12, pp 1217-1227.

Buma, S., 1988, Air Suspension, US Patent Number 4616811.

Chance, B.K., 1984, "Continental Mark VII/Lincoln Continental electronically controlled air-suspension system", *SAE Paper No. 840342*.

Cho, D., and Hedrick, J.K., 1985, "Pneumatic Actuators for Vehicle Active Suspension Applications", *Trans. A.S.M.E. Journal of Dynamic Systems, Measurement and Control*, Vol. 107, pp 67-72.

Corriga, G., Giua, A., and Usai, G., 1996, "An H2 Formulation for the Design of Passive Vibration-Isolation System for Cars", *Vehicle System Dynamics*, Vol. 26, pp 381-393.

Crosby, M.J., and Karnopp, D.C., 1973, "The Active damper- A New Concept for Shock and Vibration Control", *Forty-third shock and vibration bulletin*, Part-H, pp 119-133.

Deo, H. V., and Suh, N. P., 2004, "Axiomatic Design of a Customizable Automotive Suspension", *Proceedings of the Third International Conference on Axiomatic Design*, Seoul, Korea, June 21-24.

Deo, H.V., and Suh, N.P., 2004, "Mathematical Transforms in Design: Case Study on the Feedback Control of a Customizable Automotive Suspension System", *Proceedings of the CIRP General Assembly*, Krakow, Poland.

Deo, H. V., and Suh, N. P., 2005, "Variable Stiffness and Variable Ride-height Suspension System and Applications to Improved Vehicle Dynamics", *Transactions of the SAE 2005 World Congress*, Detroit, MI, April 11-14. (Also published in *SAE Transactions 2005-01-1924*)

Dixon, J.C., 1996, *Tires, Suspension and Handling*. Society of Automotive Engineers, Warrendale, PA, ISBN 0-340-67796-1.

Elbeheiry, E.M., Karnopp, D. C., Elaraby, M. E., and Abdelraaouf, A.M., 1995, "Advanced Ground Vehicle Suspension Systems – A Classified Bibliography", *Vehicle System Dynamics*, Vol. 24, pp 231-258.

Elbeheiry, E.M., Karnopp, D.C., Elaraby, M.E., and Abdelraaouf, A.M., 1996, "Suboptimal Control Design of Active and Passive Suspensions based on a Full Car Model", *Vehicle System Dynamics*, Vol. 26, pp 197-222.

Esmailzadeh, E., 1979, Servo Valve Controlled Pneumatic Suspensions, *Proc. of the Inst. Mech. Engrs.*, Journal of Mechanical Engineering Science, Vol. 21(1), pp 7-18.

Ferris, D.P., and Farley, C.T., 1997, "Interaction of leg stiffness and surface stiffness during human hopping," *The American Physiological Society*, pp 15–22.

Farley, C.T., Houdijk, H. H. P., Strien, C.V., and Louie, M., 1998, "Mechanism of leg stiffness adjustment for hopping on surfaces of different stiffnesses," *The American Physiological Society*, pp 1044–1055.

Ferris, D. P., Louie, M., and Farley, C. T., 1998, "Running in the real world: adjusting leg stiffness for different surfaces," in *Proc. Royal. Society of London*, Vol. 265, pp 989–993.

Firestone, 2005, *Engineering Manual and Design Guide for Airstroke Actuators and Airmount Isolators*, Indianapolis, IN.

Frydrych, D., Prasil, L., and Kracik, V., 2004, Numerical models of bellows air springs for calculation of geometrical characteristics , *Hydraulika a Pneumatika*, 2, pp 29-31.

Gillespie, T.D., 1992, *Fundamentals of Vehicle Dynamics*, SAE Inc., Warrendale, PA, ISBN 1-56091-199-9.

Hedrick, J.K., and Wormely, D.N., 1975, "Active Suspension for Ground Support Transportation –A Review", *ASME-AMD*, Vol. 15, pp 21-40.

Hoffman, D., and Rizzo, M., 1998, "Chevrolet C5 Corevette Vehicle Dynamic Control System", *SAE Technical Paper Series*, SAE-980223.

Hrovat, D., 1997, "Survey of Advanced Suspension Developments and Related Optimal Control Applications", *Automatica*, Vol. 33, pp 1781-1817.

Imani, Y., 1993, Air Suspension System, US Patent Number 5255935.

ISO, 2004, ISO 4138:2004, Passenger cars- Steady-state circular driving behavior: Open-loop test methods.

Jost, K., 1996, "Cadillac Stability Enhancement", *Automotive Engineering*.

Karnopp, D.C., 1983, "Active Damping in Road Vehicle Suspension Systems", *Vehicle System Dynamics*, Vol. 12, pp 291-316.

- Karnopp D.C., and Margolis D., 1984, "Adaptive Suspension Concepts for Road Vehicles", *Vehicle System Dynamics*, Vol. 13, pp 145-160.
- Karnopp, D.C., Margolis, D.L., and Rosenberg, R.C., 1990, *System Dynamics: A Unified Approach*, John Wiley and Sons, ISBN 0-471-62171-4.
- Karnopp, D.C., 1995, "Active and Semi-active Vibration Isolation", *Journal of Mechanical Design*, Vol. 117, pp 177-185.
- Klinger, D.L., and Calzado, A.J., 1977, "A pneumatic on-off vehicle suspension system", *Transactions of the ASME, Journal of Dynamic Systems, Measurements and Control*, pp 130-136.
- Kornhauser, A. A., Smith, J. L. Jr., 1993, "The effects of heat transfer on Gas Spring Performance", *Journal of Energy Resource Technology*, Vol. 115, pp 70-75.
- Kornhauser, A. A., 1994, "Dynamic Modeling of Gas Springs", *Journal of Dynamic Systems, Measurement and Control*, Vol. 116, pp 414-418.
- Leffler, H., Auffhammer, R., Heyken, R., and Roth, H., 1998, "New driving Stability Control System with reduced technical effort for compact and medium class passenger cars", *SAE Technical Paper Series*, SAE-980234.
- Li, T.H., and Kuo, P. Y., 2000, "Evolutionary algorithms for passive suspension systems" *JSME International Journal*, Series C 43, pp 537-544.
- Lin, Y., and Zhang, Y., 1989, "Suspension optimization by frequency domain equivalent optimal control algorithm" *Journal of Sound and Vibration*, Vol. 133, pp 239-249.
- Longhurst C. J., 2006, The Suspension Bible, http://www.carbibles.com/suspension_bible.html
- Maclaurin, E.B., 2003, Compound Strut and Planar Six-Bar Linkage Suspension System, *Proceedings of the Institution of Mechanical Engineers*, Vol. 217, Part D: Journal of Automobile Engineering, pp 215-219.
- McMahon, T.A., and Greene, P.R., 1979, "The influence of track compliance on running," *Journal of Biomechanics*, Vol. 12, pp 893-904.

- McMahon, T. A., 1985, "The role of compliance in mammalian running gaits," *Journal of Experimental Biology*, Vol. 115, pp 263–282.
- McMohan, T.A., and Cheng, G.C., 1990, "The mechanics of running: How does stiffness couple with speed?" *Journal of Biomechanics*, Vol. 23, pp 65-78.
- Melvin, J.W., and Suh, N.P., 2002, "Beyond the Hierarchy: System-wide Rearrangement as a Tool to Eliminate Iteration" *Proceedings of the International Conference on Axiomatic Design*. Cambridge, MA.
- Melvin, J.W., and Deo, H.V., 2002, "Axiomatically Designed Robustness", *American Supplier Institute 19th Annual Taguchi Methods Symposium*, San Diego, CA.
- Melvin, J.W., "Axiomatic System Design", 2003, *Doctoral Thesis*, Department of Mechanical Engineering, MIT, Cambridge, MA.
- Milliken, W.F., and Milliken, D.L., 1995, *Race Car Vehicle Dynamics*. Society of Automotive Engineers, Warrendale, PA, ISBN 1-56091-526-9.
- Oda, N., and Nishimura, S., 1969, "Dynamic Characteristics of air spring suspension and its design" (In Japanese), *Trans. Japanese Soc. Mech. Engr.*, Vol. 35, No 273, pp 996-1002.
- Olley, M., 1938, "National Influences on American Passenger Car Design", *Proceeding of the Institution of Automobile Engineers*, Vol. 32, pp 509-572.
- Pinkos, A., Shtarkman E., and Fitzgerald T., 1994, "An actively damped passenger car suspension system with low voltage eletro-rheological magnetic fluid", *Proceedings of Int. Symp. on Advanced Vehicle Control*, Tsukuba, Japan, pp 311-317.
- Prasil, L., Kracik, V., and Frydrych, D., 2005, "Shape medeling of Air Bellows Springs", *Proceedings of Algoritmy*, pp 142-149.
- Presthus, M., 2002, Derivation of air spring model parameters for train simulation, Masters Thesis, Lulea University of Technology.

- Quaglia, G., and Sorli, M., 2001, "Air Suspension Dimensionless Analysis and Design Procedure", *Vehicle System Dynamics*, Vol. 6, pp 443-475.
- Quaglia, G., and Guala, A., 2003, "Evaluation and Validation of an Air Spring Analytical Model", *International Journal of Fluid Power B*, Vol. 4, Issue 2.
- Reimpell, J., Stoll, H., and Betzler, J.W., 1996, *The Automotive Chassis*, Society of Automotive Engineers, Warrendale, PA.
- Robson, J. D., and Dodds, C. J., 1975, "Stochastic Road Inputs and Vehicle Response", *Vehicle System Dynamics*, Vol. 5, pp 1-13.
- SAE, 1981, Society of Automotive Engineers Passenger Car and Light Truck Steady State Directional Control Response Test Procedures, SAE Proposed Recommended Practice, XJ266, Warrendale, PA.
- SAE, 1996, Society of Automotive Engineers Manual for Incorporating Pneumatic Springs in Vehicle Suspension Designs, 1996, In Society of Automotive Engineering Spring Design Manual, 2nd Edition, Warrendale, PA, ISBN 1-56091-680-X.
- Sandor, G.N., and Erdman, A.G., 1989, *Advanced Mechanism Design: Analysis and Synthesis*, Vol. 2, Prentice-Hall, New Jersey.
- Sayers, M., and Gillespie, T.D., 1982, "The Effect of Suspension System Nonlinearities on Heavy Truck Vibrations", *The Dynamics of Vehicles on Roads and Tracks*, Proceedings, A. H. Wickens, Editors Swets and Zeitlander, Lisse, pp 154-166.
- Sharp, R.S., and Crolla, D.A., 1987, "Road Vehicle Suspension System Design –A Review", *Vehicle System Dynamics*, Vol. 16(3), pp 167-192.
- Sturk, M., Wu, X.M., and Wong, J.Y., 1995, "Development and evaluation of a high voltage supply unit for electro-rheological fluid dampers", *Vehicle System Dynamics*, Vol. 24, pp 101-121.

Suh, N.P., 2001, *Axiomatic Design: Advances and Applications*, CIRP Design Book Series, Oxford University Press, Oxford, NY, ISBN 0-19-504345-6.

Suh, N.P., 1990, *The Principles of Design*. Oxford University Press, New York.

Svartz, B.O., and White, D., 2005, Air Spring Stiffness Controller, US Patent Number 6883810.

Tener, D.R., 2004, "Overcoming the Ride/Handling Compromise - A Cockpit Adjustable Suspension System", *Transactions of the SAE 2005 World Congress*, Detroit, MI.

Timoshenko, S., Young, D. H., and Weaver, W., 1990, *Vibration Problems in Engineering*, John Wiley and Sons. ISBN 0-471-63228-7

Toyofuku, K., Yamada, C., Kagawa, T., and Fujita, T., 1999, "Study on Dynamic Characteristic Analysis of Air Spring with Auxiliary Chamber", *JSAE Review*, Vol. 20, pp 349-355.

White, F.M., 1999, *Fluid Mechanics*, McGraw Hill series in Mechanical Engineering, 4th ed. ISBN 0-07-069716-7.

Xiao, J., Kulakowski, B.T., 2003, "Sliding mode control of active suspension for transit buses based on a novel air spring model", *Proceedings of the American Control Conference*, Denver Colorado.

Zuo, L., Nayfeh, S.A., 2004, "Structured H2 Optimization of Vehicle Suspensions", *Vehicle System Dynamics*.